

Final Report
for the period
July 1985 to
July 1987

Flexible Structure Control Laboratory Development and Technology Demonstration

see 1473

January 1989

Authors:
H. C. Vivian
P. E. Blair
D. B. Eldred
G. E. Fleischer
C. Ih
R. E. Scheid
J. T. Wen

Jet Propulsion Laboratory
California Institute of Technology
4800 Oak Grove Blvd
Pasadena, CA 91103

JPL Publication 88-29
AFRPL 69006

AD-A210 577

DTIC
SELECTE
JUL 26 1989
S D CS D

Approved for Public Release

Distribution is unlimited. The AFAL Technical Services Office has reviewed this report, and it is releasable to the National Technical Information Service, where it will be available to the general public, including foreign nationals.

Prepared for the:

**Air Force
Astronautics
Laboratory**

Air Force Space Technology Center
Space Division, Air Force Systems Command
Edwards Air Force Base,
California 93523-5000

89 . 7 26 040


NOTICE

When U.S. Government drawings, specifications, or other data are used for any purpose other than a definitely related Government procurement operation, the fact that the Government may have formulated, furnished, or in any way supplied the said drawings, specifications, or other data, is not to be regarded by implication or otherwise, or in any way licensing the holder or any other person or corporation, or conveying any rights or permission to manufacture, use, or sell any patented invention that may be related thereto.

FOREWORD

This final report was submitted by the Jet Propulsion Laboratory on completion of work sponsored by the Air Force Astronautics Laboratory and the National Aeronautics and Space Administration. The AFAL Project Manager was Capt Tim Strange.

This report has been reviewed and is approved for release and distribution in accordance with the distribution statement on the cover and on the DD Form 1473.


TIMOTHY J. STRANGE, CAPT, USAF
Project Manager

FOR THE DIRECTOR


L. KEVIN SLIMAK
Chief, Subsystems Branch


ROBERT L. GEISLER
Director, Aerospace
Vehicle Systems Division

The research described in this publication was carried out by the Jet Propulsion Laboratory, California Institute of Technology, and was sponsored by the U.S. Air Force Astronautics Laboratory and the National Aeronautics and Space Administration.

Reference herein to any specific commercial product, process, or service by trade name, trademark, manufacturer, or otherwise, does not constitute or imply its endorsement by the United States Government or the Jet Propulsion Laboratory, California Institute of Technology.

REPORT DOCUMENTATION PAGE

Form Approved
OMB No. 0704-0188

1a. REPORT SECURITY CLASSIFICATION UNCLASSIFIED		1b. RESTRICTIVE MARKINGS	
2a. SECURITY CLASSIFICATION AUTHORITY		3. DISTRIBUTION / AVAILABILITY OF REPORT Approved for Public Release. Distribution is Unlimited.	
2b. DECLASSIFICATION / DOWNGRADING SCHEDULE			
4. PERFORMING ORGANIZATION REPORT NUMBER(S) 88-29		5. MONITORING ORGANIZATION REPORT NUMBER(S) AFAL-TR-88-093	
6a. NAME OF PERFORMING ORGANIZATION Jet Propulsion Laboratory	6b. OFFICE SYMBOL (if applicable)	7a. NAME OF MONITORING ORGANIZATION Air Force Astronautics Laboratory	
6c. ADDRESS (City, State, and ZIP Code) California Institute of Technology 4800 Oak Grove Drive Pasadena CA 91103		7b. ADDRESS (City, State, and ZIP Code) AFAL/VSSS Edwards AFB CA 93523-5000	
8a. NAME OF FUNDING / SPONSORING ORGANIZATION Air Force Astronautics Labor.	8b. OFFICE SYMBOL (if applicable) AFAL/VSSS	9. PROCUREMENT INSTRUMENT IDENTIFICATION NUMBER	
8c. ADDRESS (City, State, and ZIP Code) Edwards AFB CA 93523-5000		10. SOURCE OF FUNDING NUMBERS	
		PROGRAM ELEMENT NO. 62302F	PROJECT NO. 2864
		TASK NO. 00	WORK UNIT ACCESSION NO. DR
11. TITLE (Include Security Classification) Large Space Structure Figure Estimation and Control (U)			
12. PERSONAL AUTHOR(S) Vivian, H.; Blaire, P.; Eldred, D.; Fleischer, G.; Ih, C.; Nerheim, N.; Scheid, R.; Wen, J.			
13a. TYPE OF REPORT FINAL	13b. TIME COVERED FROM 85/7 TO 87/7	14. DATE OF REPORT (Year, Month, Day) 89/1	15. PAGE COUNT
16. SUPPLEMENTARY NOTATION			
17. COSATI CODES		18. SUBJECT TERMS (Continue on reverse if necessary and identify by block number)	
FIELD	GROUP	SUB-GROUP	
22	02		Structures, Modeling, Control, Algorithms, Experiments, Demonstrations, Space Antennas
22	03		
19. ABSTRACT (Continue on reverse if necessary and identify by block number) This report describes an experimental structure which has been constructed to demonstrate and validate recent and emerging technologies in the active control and identification of large flexible space structures. The configuration consists of a large, 20 foot diameter antenna-like flexible structure in the horizontal plane with a gimbaled central hub, a flexible feed-boom assembly hanging from the hub, and 12 flexible ribs radiating outward. Fourteen electrodynamic force actuators mounted to the hub and to the individual ribs provide the means to excite the structure and exert control forces. Thirty permanently mounted sensors, including optical encoders and analog induction devices provide measurements of structural response at widely distributed points. An experimental remote optical sensor provides sixteen additional sensing channels. A computer samples the sensors, computes the control updates and sends commands to the actuators in real time, while simultaneously displaying selected outputs on a graphics terminal and saving them			
20. DISTRIBUTION / AVAILABILITY OF ABSTRACT <input type="checkbox"/> UNCLASSIFIED/UNLIMITED <input checked="" type="checkbox"/> SAME AS RPT. <input type="checkbox"/> DTIC USERS		21. ABSTRACT SECURITY CLASSIFICATION UNCLASSIFIED	
22a. NAME OF RESPONSIBLE INDIVIDUAL Timothy J Strange, Capt, USAF		22b. TELEPHONE (Include Area Code) 805-275-5147	22c. OFFICE SYMBOL AFAL/VSSS

Block 17 (continued)

in memory. Several control experiments have been conducted thus far and are documented in this report. These include implementation of distributed parameter system control, model reference adaptive control, and static shape control. These experiments have demonstrated the successful implementation of state-of-the-art control approaches using actual hardware.

GENERAL	
STATUS	CRASH ✓
DATE	
TIME	
BY	
DESCRIPTION	
REMARKS	
INITIALS	
A-1	



EXECUTIVE SUMMARY

Extensive research has been conducted over the past decade in the control and identification of large flexible structures for civil and military applications in space. The Jet Propulsion Laboratory (JPL), under NASA sponsorship, has been actively involved since 1978 in the development of new theory, algorithms, software, and hardware in support of this research. Validation of these technologies by means of experimental demonstration of performance is an important element in these developments.

In recognition of this need and in order to facilitate the application of these technologies to both DOD and NASA programs, the Air Force Astronautics Laboratory (AFAL) and JPL undertook a joint effort with the objective of developing an advanced flexible structure ground test facility which duplicates, to a reasonable extent, the characteristics of a typical large space structure, and to conduct technology validation experiments. The desired characteristics of this system include: many low frequency, densely packed modes; low structural damping; and three-dimensional interaction among structural components. Included in the facility are the necessary transducers and computational capacity to acquire and process data both in real-time and off-line.

The program was undertaken as a four task effort consisting of: 1) a six month period for definition and preliminary design, 2) a seven month period for detailed design, 3) nine months for fabrication, installation, and alignment, and 4) four months for conducting the initial experiments and documenting them and the facility. Two teams were formed to implement the program, one responsible for developing the facility and the other responsible for developing the experiments. The teams worked closely together during the definition phase to select the final configuration and to optimize its design within available resources. Once working definitions of the facility and experiment programs were developed, the teams concentrated their efforts on their respective tasks--the facility team designing, fabricating, erecting, aligning, integrating and calibrating the demonstration system, and the experiment team detailing the experiment plans, refining algorithms and performing simulations, and developing and testing codes and procedures for conducting the experiments. Following shakedown tests and initial calibrations of the demonstration system, individual experimenters shared the use of the facility in conducting their respective experiments.

The selected configuration is a large (20 foot diameter), 12 rib circular antenna-like flexible structure with a gimbaled central hub and a long flexible feed-boom assembly. The ribs are very flexible in the vertical (out-of-plane) direction, and are coupled to one another by tensioned wires which dynamically simulate the coupling effect of a mesh on a real antenna. Simple pulley-counterweight suspension assemblies support the ribs which would otherwise droop excessively under their gravitational weights. For excitation and control, 14 actuators and 30 sensors are distributed throughout the experiment structure. In addition, displacements at up to 16 additional locations can be measured by SHAPES

(Spatial, High-Accuracy Position Encoding Sensor), an experimental remote optical sensor under development at JPL.

The facility is fully computer controlled. A MicroVAX computer handles this function. A major part of the facility development effort entailed writing software for this computer. Software was divided into two categories: system software, which provides functions common to all experiments such as communicating with transducers and displaying results; and experiment software, which implements the individual experiment algorithms. Ada was chosen as the system software language due to its highly structured programming style, concurrent task capabilities, and its forced self-documentation, all of which contributed to error-free code and future maintainability. The system software is implemented as a series of nested menus, which permits an experimenter to select various modes, change parameters, and display and analyze results. Because of the familiarity of experiment principal investigators with FORTRAN, the algorithms for implementing the individual experiments are coded as FORTRAN subroutines which link to the system software.

In order to accommodate the 30 sensors (not including SHAPES) and the 14 actuators, a custom-designed data acquisition system (DAS) was built. SHAPES communicates with the computer through a dedicated direct high speed interface. The main functions of the DAS are to sample the sensors and pass these data to the computer, and to pass commands from the computer to the actuators. The DAS includes the amplifiers, analog-to-digital and digital-to-analog converters along with power supplies and other circuitry required to operate and interface with the transducers. An 8088 microprocessor coordinates the sensing, actuation and the handling of data. Because a high degree of intelligence is built into the DAS, the computer can devote more of its available time to the computations related to the experiment algorithms, making possible implementation of larger and more complex controllers.

A finite element model of the experiment structure utilizing 308 degrees of freedom was developed in order to support the control synthesis and simulation tasks. Although the model uses mostly simple beam-type elements, it does include the effects of gravity and compression on various parts of the structure, to first order. By taking advantage of the high degree of symmetry in the structure and the bandedness in the mass and stiffness matrices, it was possible to reduce the dimension of the system and effect a very efficient solution algorithm. The resulting solution yields approximately 40 modes below 5 Hz (with the lowest frequency mode at about 0.09 Hz). By actuating only at the hub, only a small subset of all these modes is excited, and this property was used to implement the initial set of experiments.

A three year plan was developed which defines a sequence of increasingly advanced experiments in the fields of unified modeling and control design, adaptive control, static shape determination and control, and parameter identification. The requirements of this experiment program governed the configuration and specifications of the experiment structure. Experiments in each of these fields were chosen for initial demonstrations.

The objective of the experiment in unified modeling and control design was to demonstrate transient regulation utilizing linear quadratic gaussian (LQG) control methodology. Several different compensator designs were optimized to damp initial disturbance induced vibrations as rapidly as possible. A compensator based on the finite element system model was implemented first. Subsequent compensators based on 1) an improved system model which was obtained through a preliminary least squares system identification experiment, and 2) a more robust design utilizing loop transfer recovery (LTR) and robustness enhancement techniques, demonstrated successively improved closed loop behavior.

The adaptive control experiment was based on a model reference algorithm recently developed. Initial experiments encountered difficulties due to the lack of velocity inputs which the algorithm requires. It had been assumed that rates could be derived by differencing successive position measurements, providing that the outputs were nearly noise-free. This assumption was proved wrong, and the velocity estimates obtained were excessively noisy. A state estimator was implemented to provide noise-free rate estimates which yielded satisfactory algorithm performance. The adaptive control experiment has demonstrated the ability to design stable, robust controllers with high performance which do not require precise a-priori information of plant dynamics.

The static shape experiment demonstrated successful integration of the SHAPES optical sensor, the levitator position sensors, and the shape determination algorithms. This experiment determined the existence of structural asymmetry and the results were used to minimize these error effects by realigning the structure and modifying the tension of the coupling springs.

This report summarizes the development of the experiment facility and describes the results of the initial experiments. These experiments demonstrated the successful implementation of state-of-the-art control approaches using actual hardware. Preparations are now underway for implementing the Phase 2 and later generation experiments which will ultimately employ additional sensors and actuators and will push performance levels to new and greater theoretical limits.

ACKNOWLEDGEMENTS

The design, construction and operational checkout of the Large Flexible Structure Test Facility described in this report was sponsored by the U.S. Air Force Astronautics Laboratory (AFAL), formerly the Rocket Propulsion Laboratory (RPL) at Edwards Air Force Base, California, under the direction of Mr. Kevin Slimak, Dr. Alok Das and Lt. Tim Strange through AFRPL Task Order No. 69006, and was conducted by the Jet Propulsion Laboratory through NASA Task Re-182, Amendment 431.

The technology experiment program planning, and the development and execution of individual experiments described in this report were performed under the Control Technology Program sponsored by the NASA Office of Aeronautics and Space Technology (OAST), Information Sciences and Human Factors Division, Mr. Lee Holcomb, Director. The underlying research for the experiment program has been carried out under a continuing program at JPL also sponsored by NASA OAST.

The major participants responsible for the development of the test facility and the experiment program are:

Task Management and Systems Engineering	Howard C. Vivian
Facility Requirements and Experiment Planning	Daniel B. Eldred
Mechanical Engineering and Design	Gerald S. Perkins
Computer Hardware and System Software Development	Gerald E. Fleischer
Data Acquisition System	Patrick E. Blaire
SHAPES* System	Noble M. Nerheim
Dynamic Control Experiment	John T. Wen
Adaptive Control Experiment	Che-Hang Charles Ih
Static Shape Determination Experiment	Robert E. Scheid

Additional contributions were made by Robert Bamford, David Bayard, Randel Blue, Dhemitrios Boussalis, Brad Gibson, Fred Hadaegh, Donald McFarland, Deirdre Meldrum, Edward Mettler, Mark Milman, Mark Nelson, and Yeung Yam.

Valuable guidance and direction provided by Guillermo Rodriguez, Fernando Tolivar, and Shyh Jong Wang are gratefully acknowledged.

* SHAPES - Spatial High-Accuracy Position-Encoding Sensor.

CONTENTS

EXECUTIVE SUMMARY.....	iii
ACKNOWLEDGEMENTS.....	vi
ABSTRACT.....	vii
1.0 INTRODUCTION	
1.1 BACKGROUND.....	1-1
1.2 OBJECTIVES.....	1-1
1.3 APPROACH.....	1-2
2.0 EXPERIMENT PLAN AND TEST STRUCTURE DEFINITION	
2.1 EXPERIMENT PLAN.....	2-1
2.1.1 Phase 1 Experiments.....	2-1
2.1.2 Phase 2 Experiments.....	2-4
2.1.3 Phase 3 and 4 Experiments.....	2-7
2.2 EXPERIMENT STRUCTURE DESIGN PARAMETERS.....	2-7
2.2.1 Design Tradeoffs.....	2-7
2.2.2 Experiment Structure Design.....	2-9
3.0 DEMONSTRATION SYSTEM	
3.1 MECHANICAL SYSTEM.....	3-1
3.1.1 Backup Structure.....	3-2
3.1.2 Experiment Structure.....	3-5
3.2 COMPUTER SYSTEM.....	3-19
3.2.1 Hardware and Supporting Software.....	3-19
3.2.2 System Software.....	3-21

3.3	DATA ACQUISITION SYSTEM (DAS).....	3-38
3.3.1	Introduction.....	3-38
3.3.2	Interfaces.....	3-38
3.3.3	Timing Specifications.....	3-40
3.3.4	Hardware.....	3-42
3.3.5	Software.....	3-43
3.4	SPATIAL, HIGH-ACCURACY, POSITION-ENCODING SENSOR (SHAPES).....	3-45
3.4.1	Operating Principle.....	3-46
3.4.2	Optical System.....	3-48
3.4.3	Sensor Electronics.....	3-50
3.4.4	Software.....	3-53
4.0	SYSTEM MODELING	
4.1	FINITE ELEMENT DEGREES OF FREEDOM.....	4-1
4.2	GENERATING MASS AND STIFFNESS MATRICES.....	4-1
4.3	THE MATRIX EIGENVALUE PROBLEM.....	4-4
4.4	SOLUTION TO THE REDUCED ORDER EIGENVALUE PROBLEM.....	4-5
4.5	MODE SHAPES AND FREQUENCIES.....	4-7
5.0	EXPERIMENTS	
5.1	DYNAMIC CONTROL EXPERIMENT.....	5-1
5.1.1	Experiment Design.....	5-1
5.1.2	Algorithm Description.....	5-4
5.1.3	Results and Evaluation.....	5-11
5.1.4	Conclusions.....	5-52
5.2	ADAPTIVE CONTROL EXPERIMENTS.....	5-57
5.2.1	Experiment Description.....	5-57

5.2.2	Algorithm Description.....	5-60
5.2.3	Results and Evaluation.....	5-64
5.2.4	Conclusions.....	5-96
5.3	STATIC SHAPE DETERMINATION AND CONTROL.....	5-99
5.3.1	Experiment Description.....	5-99
5.3.2	Algorithm Description.....	5-103
5.3.3	Preliminary Results.....	5-106

Figures

2.0-1	Control Technology Demonstration Schedule.....	2-2
2.2-1	Experiment Structure.....	2-10
2.2-2	Transducer Locations and Labelling - Plan View.....	2-11
2.2-3	Frequencies of Dish Modes as a Function of the Number of Ribs.....	2-14
2.2-4	Frequencies of Boom-dish Modes as a Function of the Boom Length.....	2-14
2.2-5	Frequencies of Boom-dish Modes as a Function of the Feed Mass.....	2-15
2.2-6	Mode Shapes of Dish Modes - Radial Dependence...	2-15
2.2-7	Frequencies of Dish Modes as a Function of the Coupling Wire Tension.....	2-17
2.2-8	Rib Sag as a Function of Levitator Positions....	2-17
3.0-1	Mechanical System.....	3-0
3.0-2	Computer/DAS Operating Console.....	3-0
3.0-3	Plan View of Flexible Structure Test Facility Installation.....	3-3
3.1-1	Elevation View of Flexible Structure Test Facility Installation.....	3-3
3.1-2	In-process Photograph of Support Structure.....	3-4
3.1-3	Support Structure Rigging.....	3-4
3.1-4	Rib Root Arm Assembly - Underside View.....	3-7

3.1-5	Alignment Pins.....	3-7
3.1-6	Levigator Assembly.....	3-11
3.1-7	Rib-cable Attachments.....	3-11
3.1-8	Counterweight Test Fixture.....	3-13
3.1-9	Catch Cable Installation.....	3-13
3.1-10	Coupling Wire Attachments.....	3-15
3.1-11	Special Turnbuckle Tool with Calibration Base.....	3-15
3.1-12	Sensors.....	3-16
3.1-13	Actuators.....	3-18
3.2-1	Ada Listing of DEMO.....	3-24
3.2-2	System Control Task: CONTROL.....	3-24
3.2-3	DEMO Display Screen Layout.....	3-33
3.2-4	Main Menu.....	3-33
3.2-5	Hardware Checkout Menu.....	3-34
3.2-6	Scale Factor Parameter Table.....	3-34
3.2-7	Status Display.....	3-35
3.2-8	Real-Time Plot of Sensor Outputs.....	3-35
3.2-9	System Impulse Response.....	3-37
3.2-10	Sensor Test.....	3-37
3.3-1	Data Acquisition System Block Diagram.....	3-39
3.3-2	Time Line.....	3-41
3.3-3	DAS Cabinet - Rear View.....	3-41
3.4-1	Schematic of SHAPES Operating Principle.....	3-47
3.4-2	Schematic of SHAPES Optical Path.....	3-47
3.4-3	Top View of Optical Arrangement.....	3-49
3.4-4	Sketch of Optical Path Designed to Optically Rotate the Image by 90 Degrees.....	3-49
3.4-5	Block Diagram of CCD Timing, Readout and Processing Electronics.....	3-51

4.0-1	Finite Element Model Degrees of Freedom.....	4-2
4.0-2	Mode Shapes of Dish Modes - Radial Dependence.....	4-2
4.0-3	Mode Shapes	4-9
5.1-1	Archetypal Interconnected System.....	5-6
5.1-2	FFT of HS1.....	5-12
5.1-3	Simulated vs. Actual Response - HS1, Input Pattern 1.....	5-15
5.1-4	Simulated vs. Actual Response - HS10, Input Pattern 1.....	5-15
5.1-5	Simulated vs. Actual Response - HS1, Input Pattern 2.....	5-16
5.1-6	Simulated vs. Actual Response - HS10, Input Pattern 2.....	5-16
5.1-7	Decoupling Test - HA10, Input Pattern 1.....	5-18
5.1-8	Decoupling Test - HA1, Input Pattern 1.....	5-18
5.1-9	Decoupling Test - HA10, Input Pattern 2.....	5-19
5.1-10	Decoupling Test - HA1, Input Pattern 2.....	5-19
5.1-11	Open Loop Response - Input Pattern 1.....	5-23
5.1-12	Open Loop Response - Input Pattern 2.....	5-24
5.1-13	Time History Plots of Case 1 Controller with Analytic Model under Input Pattern 1.....	5-25
5.1-14	Time History Plots of Case 1 Controller with Analytic Model under Input Pattern 2.....	5-26
5.1-15	Time History Plots of Case 2 Controller with Analytic Model under Input Pattern 1.....	5-27
5.1-16	Time History Plots of Case 2 Controller with Analytic Model under Input Pattern 2.....	5-28
5.1-17	Time History Plots of Case 1 Controller with First Identified Model under Input Pattern 1.....	5-30
5.1-18	Time History Plots of Case 1 Controller with First Identified Model under Input Pattern 2.....	5-31

5.1-19	Time History Plots of Case 2 Controller with First Identified Model under Input Pattern 2.....	5-32
5.1-20	Time History Plots of Case 1 Controller with Second Identified Model under Input Pattern 1.....	5-34
5.1-21	Time History Plots of Case 1 Controller with Second Identified Model under Input Pattern 2.....	5-35
5.1-22	Time History Plots of Case 2 Controller with Second Identified Model under Input Pattern 2.....	5-36
5.1-23	Time History Plots of Case 3 Controller with Second Identified Model under Input Pattern 1.....	5-37
5.1-24	Time History Plots of Case 3 Controller with Second Identified Model under Input Pattern 2.....	5-38
5.1-25	Time History Plots of Case 4 Controller with Second Identified Model under Input Pattern 1.....	5-39
5.1-26	Time History Plots of Case 4 Controller with Second Identified Model under Input Pattern 2.....	5-40
5.1-27	Time History Plots of Case 6 Controller with Second Identified Model under Input Pattern 1.....	5-42
5.1-28	Time History Plots of Case 7 Controller with Second Identified Model under Input Pattern 1.....	5-43
5.1-29	Time History Plots of Case 8 Controller with Second Identified Model under Input Pattern 1.....	5-44
5.1-30	Time History Plots of Case 8 Controller with Second Identified Model under Input Pattern 2.....	5-45
5.1-31	Time History Plots of Case 1 Controller with Analytic Model and Case 7 Estimator with Second Identified Model under Input Pattern 1.....	5-47
5.1-32	Time History Plots of Case 7 Controller with Second Identified Model and Case 1	

	Estimator with Analytic Model under Input Pattern 1.....	5-48
5.1-33	Time History Plots of Case 7 Controller with Second Identified Model and Case 1 Estimator with Analytic Model under Input Pattern 2.....	5-49
5.1-34	Time History Plots of Case 8 Controller with Second Identified Model and Case 1 Estimator with Analytic Model under Input Pattern 1.....	5-50
5.1-35	Time History Plots of Case 8 Controller with Second Identified Model and Case 1 Estimator with Analytic Model under Input Pattern 2.....	5-51
5.1-36	Time History Plots of Case 8 Controller with Third Identified Model under Input Pattern 1.....	5-53
5.1-37	Time History Plots of Case 8 Controller with Third Identified Model under Input Pattern 2.....	5-54
5.2-1	Adaptive Control System Block Diagram.....	5-62
5.2-2	Quiescent Control Response.....	5-66
5.2-3	Open-loop Responses to 2-Sec Pulse of 1.5 N-m.....	5-67
5.2-4	Closed-loop Responses to 2-Sec Pulse of 1.5 N-m.....	5-71
5.2-5	Open-loop Responses to 1-Sec. Pulse of 1.5 N-m.....	5-75
5.2-6	Closed-loop Responses to 1-Sec Pulse of 1.5 N-m.....	5-78
5.2-7	Open-loop Responses to 3-Sec Pulse of 1.5 N-m.....	5-82
5.2-8	Closed-loop Responses to 3-Sec Pulse of 1.5 N-m.....	5-85
5.2-9	Open-loop Responses to Initial Deflection.....	5-88
5.2-10	Closed-loop Responses to Initial Deflection.....	5-91
5.3-1	Critical Point Directory.....	5-107
5.3-2	Rib No. 3 Profile... ..	5-107

5.3-3	Symmetry Analysis (9/21/87).....	5-108
5.3-4	Symmetry Shifts Over Time.....	5-108

Tables

2.2-1	Experiment Structure Design Parameters.....	2-19
3.2-1	Command Summary.....	3-26
4.0-1	Normal Modes.....	4-8
5.1-2	Identified Modal Frequencies Based on FFT Plots.....	5-11
5.1-3	Identified Modal Dampings Based on Least Square Fit in FFT Plots.....	5-13
5.1-4	Identified Model Based on Minimization of Output Prediction Error.....	5-13
5.1-5	Fine-Tuned Model Based on Matching of Time Response.....	5-14
5.1-6	Decoupling Test Result.....	5-17
5.1-8	Symmetry Test Result.....	5-17
5.1-9	Parameters for Controller Comparisons.....	5-21
5.1-10	Open Loop Performance.....	5-22
5.1-11	Performance of Analytic Model Based Controllers.....	5-22
5.1-12	Performance of First Identified Model Based Controller.....	5-29
5.1-13	Performance of Second Identified Model Based Controller (Cases 1-2).....	5-33
5.1-14	Performance of Second Identified Model Based Controller (Cases 3-4).....	5-33
5.1-15	Performance of Second Identified Model Based Controller (Case 6).....	5-41
5.1-16	Performance of Second Identified Model Based Controller (Cases 7-8).....	5-46
5.1-17	Performance of Analytic Model Based Controller and Second Identified Model Based Estimator.....	5-46

5.1-18	Performance of Second Identified Model Based Controller and Analytic Model Based Estimator.....	5-46
5.1-19	Performance of Third Identified Model Based Controller.....	5-52
5.2-1	Open-loop Responses to 2-sec Pulse.....	5-66
5.2-2	Closed-loop Responses to 2-sec Pulse.....	5-70
5.2-3	Open-loop/Closed-loop Ratio for 2-sec Pulse Excitation.....	5-70
5.2-4	Open-loop Responses to 1-sec Pulse.....	5-74
5.2-5	Closed-loop Responses to 1-sec Pulse.....	5-74
5.2-6	Open-loop/Closed-loop Ratio for 1-sec Pulse Excitation.....	5-74
5.2-7	Open-loop Responses to 3-sec Pulse.....	5-81
5.2-8	Closed-loop Responses to 3-sec Pulse.....	5-81
5.2-9	Open-loop/Closed-loop Ratio for 3-sec Pulse Excitation.....	5-81
5.2-10	Comparison of Open-loop to Closed-loop Outputs Y_p 's for Deflection Regulation.....	5-95
5.2-11	Open-loop Responses to Deflection Regulation.....	5-95
5.2-12	Closed-loop Responses to Deflection Regulation.....	5-95
5.2-13	Open-loop/Closed-loop Ratio for Deflection Experiment.....	5-96

SECTION 1

INTRODUCTION

1.1 BACKGROUND

Extensive research has been conducted over the past decade in the parameter identification and control of large flexible structures. This has been motivated in part by proposed space applications for large communications and radiometry antennas, reflectors for astronomy and space defense, large platforms for multiple experiments, large solar arrays, long stabilized or controlled booms, etc. The prohibitive cost of transporting large, rigid, heavy, precision structures into space necessitates the use of lightweight, compact deployable systems, which are then unfurled or assembled in orbit, and which take advantage of the weightless space environment.

The consequences of the large size and light weight characteristic of these structures are that they are very flexible, with multiple, closely packed modes of low frequency and low damping. As a result, any disturbances introduced into the system may cause undesirable vibrations which are detrimental to system performance or even destructive to the structure. To maintain acceptable vibration levels, active multi-point or distributed control is required. Because the exact structural characteristics may not be fully predictable prior to deployment in space, it may be necessary to apply parameter identification technology to identify the dynamic properties, such as natural frequencies, mode shapes, damping ratios, and mass properties, before an active vibration control system can be implemented. Structural properties, particularly mass distributions, may even change during the course of a mission. In this case, an adaptive control strategy would be appropriate for system damping control. Finally, if precision figure alignment is required of the structure such as would be the case with an antenna or optical reflector, some form of active shape control is required. Implicit is the need to identify the shape in the first place.

The Jet Propulsion Laboratory (JPL) has been actively involved since 1979 in the development of new identification and control theory, algorithms, software and hardware, including remote optical sensing systems, and distributed sensing and actuation systems. Validation by means of experimental confirmation of performance estimates is an important element of these developments.

1.2 OBJECTIVES

In recognition of this need and the application of this technology to both military and non-military programs, the Air Force Astronautics Laboratory (AFAL) (formerly Rocket Propulsion Laboratory) and JPL undertook a joint program with the objective of developing an advanced general utility ground test facility at JPL which duplicates, to a reasonable extent in a gravity and atmospheric environment, the characteristics of a typical large space structure. These include many low frequency modes, densely packed modes, low

structural damping, and three-dimensional interaction among components. Included in the facility are the necessary transducers and computational capacity to acquire and process data in real-time to validate and demonstrate existing identification and control technologies such as static and dynamic shape determination and control, unified modeling/control design, and adaptive control, as well as new technologies to be developed over the next three-to-seven years. The technologies to be demonstrated include hardware such as the SHAPES* sensor and distributed sensing and actuator systems such as PVF₂ piezo electric polymer film transducers. The validation of one or more identification or control technologies was also included as a program objective.

1.3 APPROACH

The program was undertaken as a four phase effort consisting of a six month definition and preliminary design phase, a seven month detailed design phase, a nine month fabrication/installation and alignment phase, and a four month experiment and report preparation phase. A facility development team and an experiment development team were formed to implement the program. The two teams worked closely during the definition phase to select the configuration and optimize the design of the facility and experiment programs within the available resources. Once working definitions of the facility and experiment programs were developed, the teams concentrated their efforts on their respective tasks - the facility team designing, fabricating, erecting, aligning, integrating and calibrating the demonstration system, and the experiment team detailing the experiment plans, refining algorithms and performing simulations, and developing and testing final coding and procedures for the experiments. Following shakedown tests and initial calibrations of the demonstration system, individual experimenters time-shared the use of the facility in rotation to conduct the experiments described in this report.

* SHAPES - Spatial High-Accuracy Position-Encoding Sensor.

SECTION 2

EXPERIMENT PLAN AND TEST STRUCTURE DEFINITION

Definitions of the experiment structure configuration and functional requirements were developed in conjunction with the development of a long-range control technology demonstration plan to ensure that the physical test facility would meet the validation needs of the control technology research programs for five or more years. The technologies initially selected for demonstration include: unified modeling/control/design; adaptive control; static shape control; and parameter identification, since these were major research thrusts at NASA/JPL during the development of the facility. Tradeoffs of technology validation needs, likely near-term applications, expandability, cost, development time and other factors led to the definition of a large (~20 foot dia.) 12 rib circular antenna-like flexible experiment structure with a gimballed central hub and long flexible feed-boom assembly having 20 or more closely packed boom/dish modes within a 2 Hz band. For excitation and control, a total capability of 14 actuators and 46 sensors (including SHAPES) distributed throughout the experiment structure was specified. The structure is described in Sec. 2.2.2 with diagrams of the basic configuration and transducer layout given in Figures 2.2-1 and 2.2-2 (pages 2-10 and 2-11).

2.1 EXPERIMENT PLAN

The long-range technology experiment plan was organized into a four phase program. The phasing plan is shown in Figure 2.0-1 and the experiments planned for each phase are described below.

2.1.1 Phase 1 Experiments.

Phase 1 is intended to demonstrate the basic technology of the research areas, exciting only the boom-dish modes (a small subset of all the system modes; see Section 4) and using a limited number of the many available sensors and actuators in closed loop. Early on, it was realized that attempts to tackle a more complicated problem (more modes, more sensors and actuators, more complex control objectives) would be frustrated by the intricacies of the hardware, software, and algorithms. This caution later proved to be justified in that experience showed that it was difficult to demonstrate even the Phase 1 experiments at a satisfactory performance level without refinement of experiment computer code. Phase 1 thus serves as a foundation upon which more advanced experiments can be built. As the Phase 2 and later experiments are scheduled for the future, results from only the Phase 1 experiments are included in this report.

2.1.1.1 Transient Regulation by Distributed Control. In this experiment transient regulation utilizing distributed parameter LQG (Linear Quadratic Gaussian) control design is performed. Excitation, sensing, and control actuation act through the hub only, and thus only the boom-dish modes are excited (see Section 4 for a definition of the boom-dish modes). The experiment is intended to validate the LQG methodology for transient and jitter regulation.

TECHNOLOGY AREA EXPERIMENT PHASE	STATIC SHAPE DETERMINATION & CONTROL	DYNAMIC MODEL IDENTIFICATION	UNIFIED CONTROL, MODELING DESIGN	ADAPTIVE CONTROL	μ -SYNTHESIS (PRESIDENT FUND)
PHASE 1	SHAPES INTEGRATION JUL. 1987 STATIC SHAPE DETERMINATION AND CONTROL SEP. 1987		TRANSIENT REGULATION VIA DISTRIBUTED CONTROL AUG. 1987	TRANSIENT/INITIAL DEFLECTION REGULATION SEP. 1987	
PHASE 2	ON-LINE SHAPE DETERMINATION AND CONTROL FILE IDENTIFICATION OF STIFFNESS AUG. 1988	DYNAMIC MODEL ID FEB. 1988 ON-LINE DISTURBANCE ID OCT. 1988	TRANSIENT REGULATION BY REDUCED ORDER AND ROBUST CONTROLLER APR. 1988	TRANSIENT/INITIAL DEFLECTION REGULATION WITH ADDITIONAL COLOCATED SENSORS AND ACTUATORS JUN. 1988	ROBUST CONTROL OF HUB MODES MAR. 1988 ROBUST CONTROL OF DISH MODES JUL. 1988
PHASE 3	STATIC SHAPE DETERMINATION OF MESH COUPLED STRUCTURE OCT. 1989	OPEN/CLOSED LOOP TRANSFER FUNCTION IDENTIFICATION MAY 1989	DISTURBANCE REGULATION WITH ENHANCED INSTRUMENTATION DEC. 1988	NON-LINEARITIES AND TIME DELAY ROBUST REGULATION FEB. 1989	
PHASE 4	FILE ID OF MESH-COUPLED STRUCTURE JUN. 1990	ON-LINE DYNAMIC MODEL IDENTIFICATION FEB. 1990	POINTING AND TRACKING BY DISTRIBUTED CONTROL APR. 1990	RECONFIGURATION CONTROL DEC. 1989	

Control Technology Demonstration Schedule
Figure 2.0-1

For this first experiment a succession of LQG compensators is developed. The first, a low gain compensator, is implemented to gain experience with the system and to establish a baseline performance level to which subsequent experiments can be compared. The bandwidth of the low gain controller is adjusted via manipulation of the LQG design parameters so that the control system acts primarily upon the first two bands of the boom-dish modes, for a total of four modes. The objective is to actively damp structural vibrations in the structure caused by an initial excitation (impulse or otherwise) in as short of a time period as possible. The controller gains are then increased, slowly, until the closed loop performance cannot be improved any further.

The compensators are derived using the principle of functional gain convergence to realize a match between performance objectives and model order selection. Briefly, the methodology consists of constructing an increasing sequence of approximating open loop models together with their respective optimal feedback gains. Under mild conditions, these feedback gains, or functional gains, are known to converge. The appropriate finite dimensional model is that which yields essentially converged functional gains. As with all LQG designs, there is considerable latitude for tuning by adjusting the performance weighting matrices in the LQG problem formulation. In general, an increase in performance objectives requires a higher order model.

2.1.1.2 Transient/Initial Deflection Regulation by Adaptive Control. The objective in this case is to demonstrate the use of an adaptive control algorithm to actively damp initial excitations and initial deflections. The specific algorithm targeted for demonstration is a model reference technique.

The basic idea behind many adaptive control algorithms is to make the output of an unknown plant asymptotically approach that of a reference model which has the desired performance of the plant. This is a reasonable objective and there are many adaptive control algorithms which attempt to attain it. However, lack of global stability (or at least proof of it) has always been a problem with adaptive control algorithms. A relatively recent proof shows that, under certain conditions, a particular formulation of model reference adaptive control will be globally stable. It is a variation of this which is demonstrated during Phase 1.

The design of the controller proceeds as follows. Initially, a reference model is designed whose response reflects the desired system output. The adaptive control algorithm is designed to track the reference model via adaptive rate plus position feedback. If the reference model is identically zero, then the controller becomes a regulator. In order to be effective, the reference model should have a small order and high damping. The main virtue of the algorithm is that there is no need to have prior knowledge of the actual system model. There are, however, several gain parameters relating to the speed at which the algorithm adapts; the selection of these parameters constitutes the tuning of the algorithm.

A limitation of the adaptive control algorithm is that rate feedback is required; in addition, the sensors must be collocated with actuators. Unfortunately, no suitable rate sensors for the experiment structure were located and the decision was made to derive rate by differencing successive position measurements. This turned out to be a severe

problem for the adaptive control algorithm, since the position measurements for the hub angle are rather noisy due to the small range of angular travel relative to the full scale range of the hub sensor. It became necessary to add an estimator to software to generate satisfactory rate estimates which were then passed to the algorithm. The results are described in detail in Section 5.2.

The objective of the first half of the Phase 1 active control experiment is to actively damp an initial disturbance as rapidly as possible. In this case, the reference model is maintained at zero throughout the experiment. The hub torquer is used to excite the structure, after which the adaptive controller is turned on and allowed to dissipate the energy of the system.

The objective of the second half of the adaptive control experiment is to perform initial deflection regulation. A reference model is created whose initial condition consists of an initial deflection and whose time response decays towards zero asymptotically. The actual structure is held in an initial configuration which is not necessarily identical to that of the reference model, and then released at the same moment that the adaptive controller is turned on. Ideally, the system follows the reference model, and the degree to which this occurs is an indication of how well the algorithm performs.

2.1.1.3 Static Shape Determination and Control. A number of applications in the technology of large space structures can be analyzed as static distributed systems. This approach is appropriate for systems where the time-dependent effects are negligible and where the control forces can be applied without significantly exciting the system dynamics. The objective of a controller in this case is to compensate for quasi-static disturbances; for example, gravitational and thermal effects. An important application for such technology is a large space based antenna, which the experiment structure strongly resembles (by intention).

In Phase 1, only static shape determination is to be performed, shape control being reserved for Phase 2. The static shape determination algorithm is based on a minimum variance (least squares) recursive estimator formulation of the distributed parameter system, and can also be related to a finite element model of the system. The hub for all static shape control experiments is clamped in a fixed orientation. Measurements taken using SHAPES, the levitator sensors, and the rib root sensors, for different loading conditions are processed off-line to synthesize the state estimates. The loading is established through a combination of rib-root actuator forces and weights placed manually about the structure. Comparison of the estimates gives a quantitative evaluation of the quality of the system model.

2.1.2 Phase 2 Experiments

Phase 2 is intended to be similar to Phase 1, but on an expanded scale. Up to 30 modes will be excited, and most if not all of the 46 sensors (including the SHAPES targets) and the 14 actuators will be used to simultaneously estimate and control them. Additional transducers may be added, notably accelerometers, rate sensors, and piezoelectric polymer distributed

actuators, depending on program constraints. Algorithms will be similar to those in Phase 1, but will almost certainly experience major difficulties owing to the huge increase in their respective operation counts and the more distributed nature of the sensing and actuation.

2.1.2.1 Transient Regulation by Reduced Order and Robust Controller. In this experiment, LQG controllers are derived under two sub-optimal conditions. In the first case, the compensator order is constrained to a small size, reflecting realistic software limitations which limit the number of computations which can be performed within a specified time period. In the second case, the model used for the compensator synthesis is intentionally degraded, reflecting the type of a priori modeling errors which can be expected with a large space-based system.

The reduced order compensator design is derived from a nominal LQG design using the functional gain convergence criterion described in the previous experiment. This nominal compensator is then reduced in dimension using the method of balanced realizations, an analytical technique which arranges the state space variables in order of relative contribution to the input-output properties of the closed loop system. Those states which contribute least are truncated.

In order to effect transient regulation on a system whose model is not well known, two robustness enhancement methods are applied. Each focuses on adjusting parameters in the estimator to achieve a more robust design. One approach which will be demonstrated is to adjust parameters in the Kalman filter design in a way that asymptotically recovers the loop gain of the full state feedback. This method is called loop transfer recovery (LTR). A variant of this approach called the algebraic loop recovery method has also been developed and investigated. The second approach consists of a sensitivity optimization of the eigenvalues of the closed loop system. A nominal LQG compensator is used as an initial condition, and pole placement techniques (which involve determining the eigenvalue sensitivities with respect to the control parameters) are used to select parameters which force the closed loop eigenvalues into pre-specified regions.

2.1.2.2 Transient/Initial Deflection Regulation with Additional Collocated Sensors and Actuators. The experiment in adaptive control for Phase 2 is essentially an extension of the Phase 1 experiment and builds upon the experience base of that experiment to control additional modes by the use of additional sensors and actuators. In this case, four collocated rib root sensors and actuators are used in addition to the two collocated hub sensors and hub actuators used in the previous experiment. The objective is to demonstrate the performance of the adaptive controller, this time also with parameter errors and model truncation errors, for a large number of initial excitations and deflections.

In the Phase 1 experiments, only the hub torquers and sensors are used, and thus only the boom-dish modes are excited. In the Phase 2 experiments, the additional rib root sensors and actuators will also excite the dish modes. Therefore, as many as 25 or more modes will play a significant role in the system dynamics and will have to be controlled. The operation count will increase by at least an order of magnitude, presenting a

challenge to streamline the algorithm software coding so that it can operate at approximately 20 Hz or faster. The challenge will be compounded if direct rate sensing at the rib roots is not available during Phase 2, and estimators are required to derive the rate information from the position sensors.

2.1.2.3 Static Shape Control and MLE Identification of Stiffness Parameters

The objective of the static shape control experiment is to maintain the shape of the structure in a reference configuration in a background of modeling error, measurement noise, and system disturbances. To do this, a three step process is implemented: the sensors are sampled, the existing shape is estimated (using the minimum variance estimator developed in Phase 1), and the control commands required to correct the shape are calculated (not necessarily in real time since there is no time pressure in a static shape control application). The control forces are achieved by using a combination of rib root actuators and calibrated weights placed manually about the structure at predetermined locations along the ribs and levitator counterweights. The RMS error in the shape is determined, and the process is iterated if necessary.

The objective of the off-line identification experiment is to identify the stiffness parameters of the physical structure. The algorithm proceeds as follows. A sequence of finite element models of the dish is generated by truncating various partial differential representations at different points of the system. Based on these models, an estimator based on the maximum likelihood principle (MLE) is developed. Different combinations of sensor measurements are processed off-line to yield state and parameter estimates. The latter are systematically compared with one another and with the a priori parameter values to effect a quantitative evaluation of the identification algorithm. The results will also be reconciled with the system model.

2.1.2.4 Dynamic Model and Disturbance Identification.

The objective of this experiment is to demonstrate identification algorithms which are applicable to the on-orbit identification of large space systems. Parameter identification owes its importance to the inaccuracies in modeling and the difficulty of testing such systems on the ground, due mainly to the presence of gravity and the inherent flexibility of such systems, and also the need for configuration verification in space. A secondary application of parameter identification is to incorporate it into an LQG controller such that the combination will adaptively adjust to a changing configuration, a common need with large space systems.

The first experiment will identify the modal frequencies, damping ratios, and mode shapes of the structure using maximum likelihood identification parameter estimation (MLE). Excitations of the structure which maximize the identifiability of these parameters will be chosen using optimal input design techniques. Virtually all the sensors will be used to collect response data, and these data will be processed off-line to extract the desired parameter values. The resulting identified model will likely be used by other experiments to synthesize control algorithms.

The other identification experiment demonstrates the ability to reconstruct the location and time history profile of an impulsive disturbance which is applied at some unknown point on the structure. For this experiment,

it is assumed that an accurate model of the physical structure is available. The basic approach is to use multiple hypothesis testing detection algorithms to locate the input disturbance, and inverse filtering/smoothing algorithms to recover the input force profile.

2.1.2.5 Other Phase 2 Experiments. An additional experiment is planned which will demonstrate the ability to reconstruct three-dimensional position information based on two-dimensional images of it obtained with a video camera, which are fed into a computer and processed.

A second experiment will demonstrate the performance of control algorithms derived via the mu-synthesis technique, in actively damping transients in both the boom-dish modes and the dish modes.

2.1.3 Phase 3 and 4 Experiments

In Phases 3 and 4, the control algorithms will be tuned to their maximum potentials; as many modes as possible will be estimated and controlled and performances will be increased to the maximum extent possible. Somewhere in between Phases 3 and 4, fairly major structural configuration changes will be made to accommodate the planned experiments, though the precise scope and nature of these changes will not be refined until the completion of Phase 2. One candidate is to add additional levitators (perhaps changing their design as well), to give the structure a behavior more characteristic of a distributed parameter system; another is to replace the coupling wires with a mesh type membrane, which would considerably complicate the coupling between adjacent ribs. Almost certainly, different or additional sensors and actuators will be implemented. Highlights of these experiments include: implementation of the MLE identification algorithm in real time; pointing and tracking via the Unified Modeling/Control/Design algorithm; and adaptive control of a system whose mass properties change with time.

2.2 EXPERIMENT STRUCTURE DESIGN PARAMETERS

This section describes some of the considerations and analyses which contributed to a final specification of the experiment structure. Most parametric studies were performed using the finite element model described in Section 4.

2.2.1 Design Tradeoffs

The experiment structure is intended to replicate the properties of a large space structure which are relevant to the control technologies which will be demonstrated on it. These properties are not necessarily compatible, and are summarized below.

The experiments in Static Shape Determination and Control require a structure with a large surface which can be described as a highly coupled, distributed parameter system, even if the finite element method is used to model it. The theory behind these experiments was originally targeted towards controlling antennas, so the structure would ideally at least resemble an

antenna. A typical experiment would impose a loading on the surface, measure its deflection, calculate its shape, and perhaps iterate the process to achieve a target surface shape or to identify stiffness parameters. In order that the surface can be adequately estimated and controlled, sensors and actuators should be distributed about the surface. Static Shape Determination and Control is not concerned with system dynamics, and accordingly any vibrations introduced during the course of an experiment are allowed to damp out completely before any measurements or other actions are taken. The desirable properties for Static Shape Determination and Control thus include: large, coupled surface; many sensors and actuators distributed about the surface; and relatively high damping, or at least a short settling time.

The Adaptive Control experiments aim to actively damp structural vibrations while tracking a reference model. Thus, a dynamic multimode structure is required. The theory behind the algorithm assumes that each actuator used for control be collocated with a sensor. Furthermore, the sensors should provide velocity information. The algorithm becomes computationally prohibitive if too many sensor/actuator pairs are used, and hence can only use a small set of sensor/actuator pairs (about 4 to 6), as long as observability/controllability are achieved.

The experiments in Distributed Control theory are nominally based on Kalman filtering and optimal control. Though new methods are used to obtain the control law formulations, this type of controller has been demonstrated on a variety of different facilities throughout the research community. What has not been demonstrated is the control of a large number of modes (more than, say, 20) simultaneously. It was deemed important that at least this many modes be prominent in the system dynamics. Additionally, a complete set of sensors and actuators should be provided which guarantees observability and controllability conditions. Computational speed limits can affect how many sensors and actuators can be used within the real time loop, but with efficient organization of the algorithm, quite large problems can be handled satisfactorily.

The objective of the Maximum Likelihood Identification algorithm is to identify as many flexible modes as possible. The relevant requirements on the structure are that many flexible modes (20 or more) exist, that there be enough actuators or other means of exciting these modes, and that there be an overabundance of sensors for measuring the response. Since computation will be performed off-line, at least in the initial identification experiments, there are no restrictions relating to speed.

One of the important objectives of the experiment program is to demonstrate the SHAPES sensor in a simulated operational setting. The SHAPES sensor is designed to make simultaneous ranging measurements of multiple targets (16 at the present) distributed over a large surface. It is designed to accommodate a range of motion of about 10 cm, the precise value depending on the optics used. The sensor cannot sample faster than about 10 Hz, since this is the fastest rate at which the information stored on the CCD, an integral part of the sensor, can be retrieved. By the sampling theorem, no modes faster than 5 Hz can be observed by a sensor sampling at 10 Hz. Thus, 5 Hz is a firm upper limit on the normal mode frequencies of the structure. Ideally, the modal frequencies should be much lower than this. Modal frequencies should be as low as possible to allow the control computer sufficient time to complete control calculations, as well.

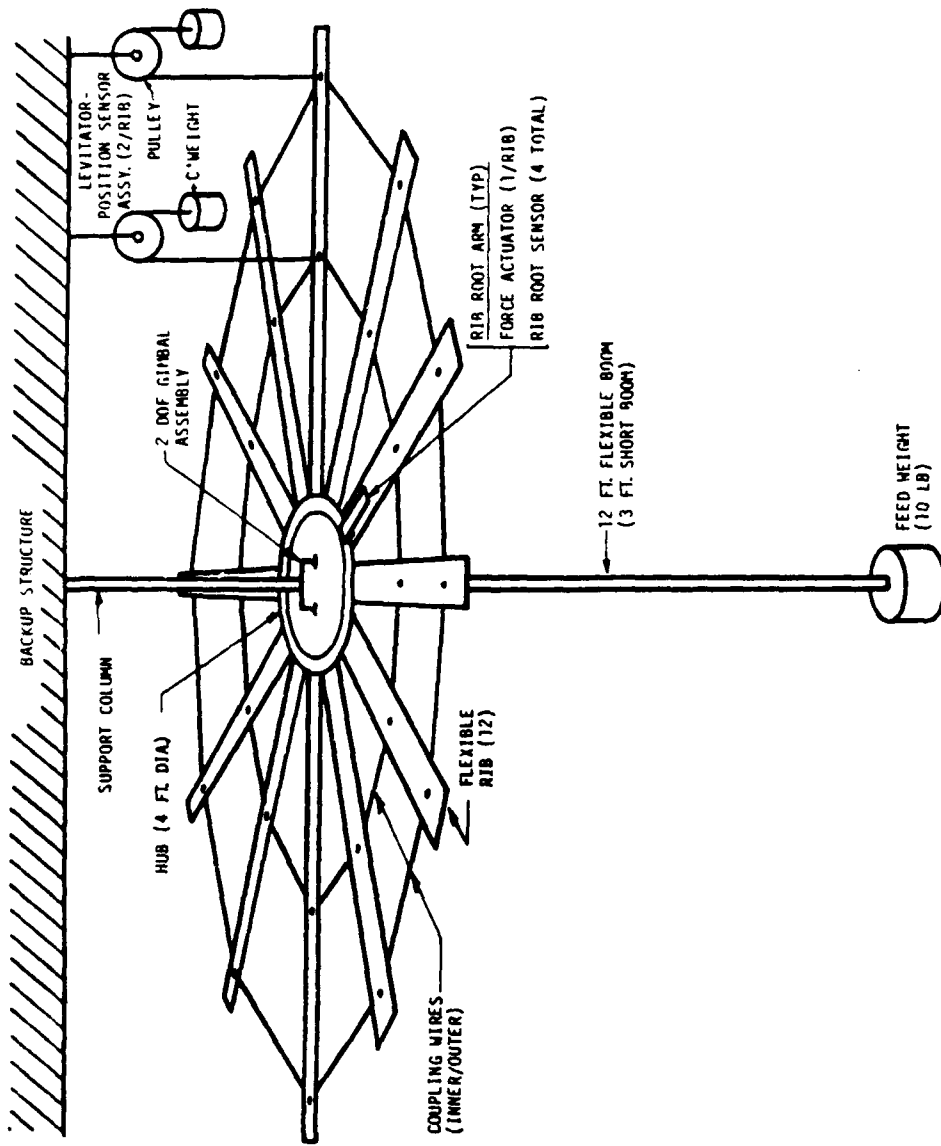
Another objective of the system is to physically demonstrate the use of control technologies in a highly visible way. To achieve this aim, motion of the structure should be easily visible to an observer, about +/- 5 cm. A conflicting consideration which effectively prohibits larger motion is that the range of motion should be restricted to values which would be small relative to the size of the structure, so that linearity is maintained; a number of terms in the model go non-linear if too much motion is allowed.

In summary, the general requirements developed for the experiment structure are that it should have a large surface, preferably in the shape of an antenna, with coupling in both horizontal directions. The range of motion should be about +/- 5 cm. There should be at least 20 lightly damped modes with frequencies as low as possible, but certainly lower than 5 Hz. Multiple sensors and actuators should be distributed throughout the structure. And, there should be 4 to 6 collocated velocity sensor/actuator pairs, for the Adaptive Control experiment.

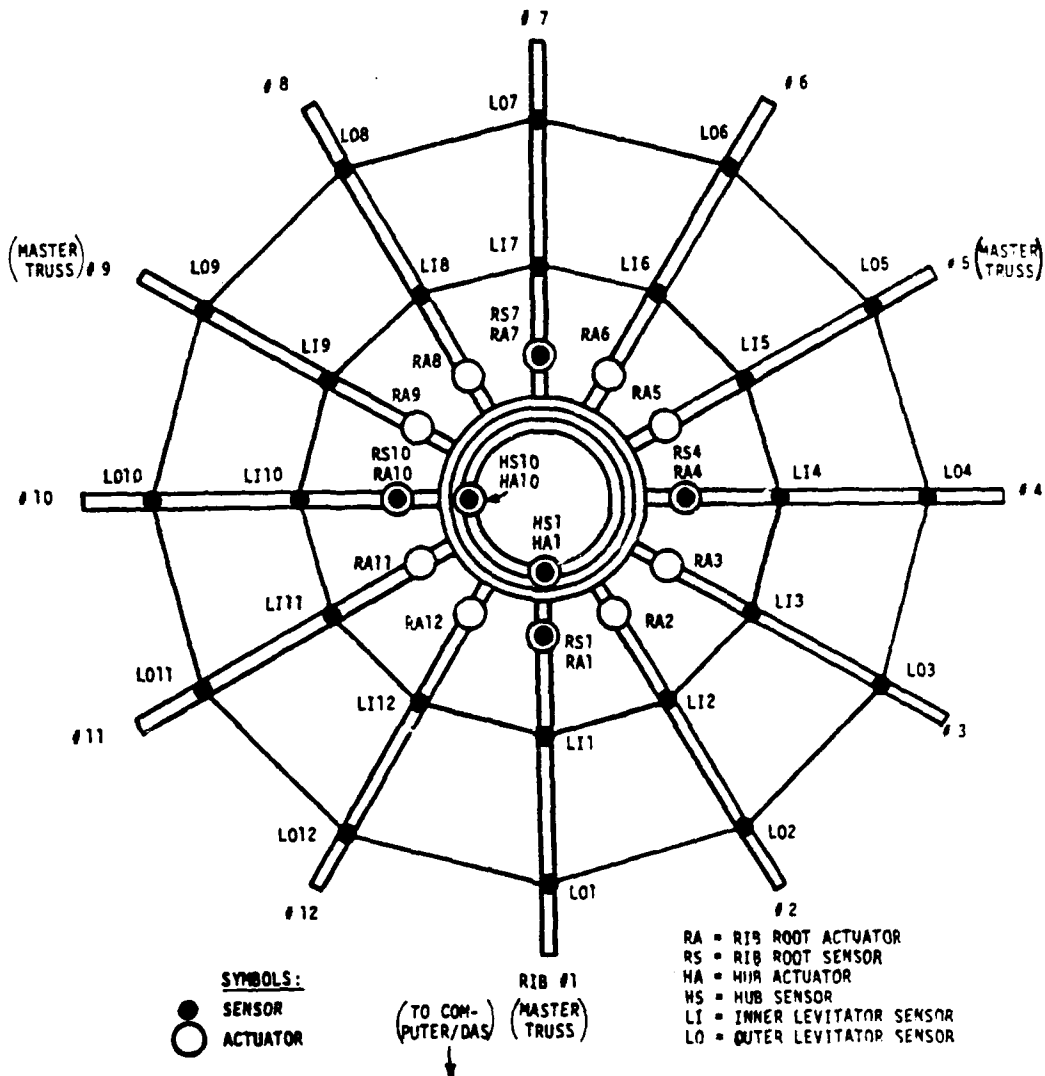
2.2.2 Experiment Structure Design

2.2.2.1 Configuration. The configuration selected for the experiment structure is shown in Figure 2.2-1. The backup structure, which provides a base for mounting the levitators and the gimbal bearings, is not shown. The main component of the apparatus consists of a central hub to which 12 ribs are attached. The diameter of the dish-like structure is slightly less than about 19 feet, the large size being necessary to achieve the low frequencies desired. The ribs are coupled together by two rings of wires which are maintained under nearly constant tension. Functionally, the wires provide coupling of motion in the circumferential direction which would otherwise occur only through the hub. The ribs, being quite flexible and unable to support their own weight without excessive droop, are each supported at two locations along their free length by levitators. A levitator assembly consists of a pulley, a counterweight, and a wire attached to the counterweight which passes over the pulley and attaches to the rib. The hub is mounted to the backup structure through a gimbal arrangement, so that it is free to rotate about two perpendicular axes in the horizontal plane. A flexible boom is attached to the hub and hangs below it, and a feed weight, simulating the feed horn of an antenna, is attached at the bottom end of the boom. The original boom was 12 feet long, but the desirability of conducting experiments at the floor position so that the structure is accessible resulted in a second, 3 foot long boom being used for the Phase 1 experiments instead.

Actuation of the structure is as follows. Each rib can be individually manipulated by a rib-root actuator mounted on that rib near the hub. A rib root actuator reacts against a mount which is rigidly attached to the hub, and thus, is functionally similar to the rib root torquers which are being considered for future 20-meter class space antennas. In addition, two actuators are provided which torque the hub about its two gimbal axes. The hub torquers do not provide torque directly, but rather are linear force actuators which produce torque by pushing (or pulling) at the outer circumference of the hub. The torque provided is equal to the force times the lever arm about the axis of rotation. The placement of these actuators guarantees good controllability of all of the flexible modes of motion. The locations of the actuators are shown in Figure 2.2-2.



Experiment Structure
Figure 2.2-1



Transducer Locations and Labeling -- Plan View
 Figure 2.2-2

The sensor locations are also shown in this figure. First, each of the 24 levitators is equipped with a sensor which measures the relative angle of the levitator pulley. The levitator sensors thus provide, in an indirect manner, the measurement of the vertical motion of the corresponding ribs at the points where the levitators are attached. They also provide the distributed sensing over the surface of the structure required by the Shape Control experiments. Four position sensors measure rib displacement at the rib-root actuator locations to satisfy the collocated sensor requirement of the Adaptive Control experiments. As was stated previously, the Adaptive Control experiments require velocity feedback, but, as no suitable velocity sensors were located, it was decided to use position sensing instead and difference successive measurements to obtain velocity, perhaps using a digital filter if necessary. Sensing for the hub consists of two rotation sensors which are mounted directly at the gimbal bearings. Again, hub rate for the Adaptive Control experiment is obtained by differencing. Finally, up to 16 targets for the SHAPES sensor can be mounted at any of 120 equally spaced locations on the ribs (10 locations per rib), or virtually anywhere else on the structure.

2.2.2.2 Rib Design Requirements. Because the ribs constitute the major portion of the mass of the experiment structure, they largely determine the dynamic properties of the system. By changing the physical properties of the ribs, it is possible to tailor the frequency distributions of the normal modes to approximate the desired target values. Making the ribs more flexible or more massive will decrease the modal frequencies of the system, while making them stiffer or lighter will have the opposite effect. Ribs can be made stiffer, relative to their other properties, either by increasing their thicknesses or by decreasing their lengths. On the other hand, they can be made more massive, relative to their other properties, by attaching weights along their lengths or on both sides of a levitator pulley.

Since the experiment requirements call for modal frequencies being as low as possible, and certainly less than about 5 Hz, the ribs were made as long as possible. The practical limit is dictated by the space available in the Celestarium, about 20 feet in diameter. Two other considerations also limit the maximum allowable length of the ribs. First, a longer rib requires more levitators, or else it will sag excessively under its own weight (more than about .5 cm). As the levitators and their associated hardware constitute a major expense item, it was desired to keep their number to a minimum. Second, the modal frequencies should be kept as high as possible to minimize the effect of the damping in the levitator bearings. This damping is Coulomb damping, which affects the lower frequency modes much more severely than the higher frequency modes. A compromise was made and the final rib length was chosen such that the frequency of the first cantilevered mode of a rib with levitators was about 0.2 Hz. This roughly corresponds to the frequency of the first band of dish modes. A dish mode is a mode which would result from the hub being clamped, and it turns out that the vast majority of modes are of this type, even when the hub is free to move; see Section 4 for more details. The frequency of the second cantilevered mode is about 1.2 Hz, which roughly corresponds to the frequency of the second band of dish modes.

While the length of the ribs determines the approximate frequencies of the modes, the number of ribs determines how many modes there are. Were no coupling wires present, each band of dish modes would have a degeneracy equal

to the number of ribs. The coupling wires, since they provide weak coupling among ribs, split this degeneracy, and a given band consists of a group of closely packed modes approximately centered about the frequency of a cantilevered rib. Figure 2.2-3 shows the grouping of modes as a function of the number of ribs. The frequencies of the bands drop as fewer ribs are used. The reason for this is that from geometric considerations, with fewer ribs, there is greater compression in the ribs caused by the coupling wires. Due to the cyclic symmetry of the structure, most of these modes are two-fold degenerate, the exceptions being the lowest and highest frequency modes. Since the final configuration for the experiment structure contains 12 ribs, there are about 24 dish modes which are lower than about 2 Hz.

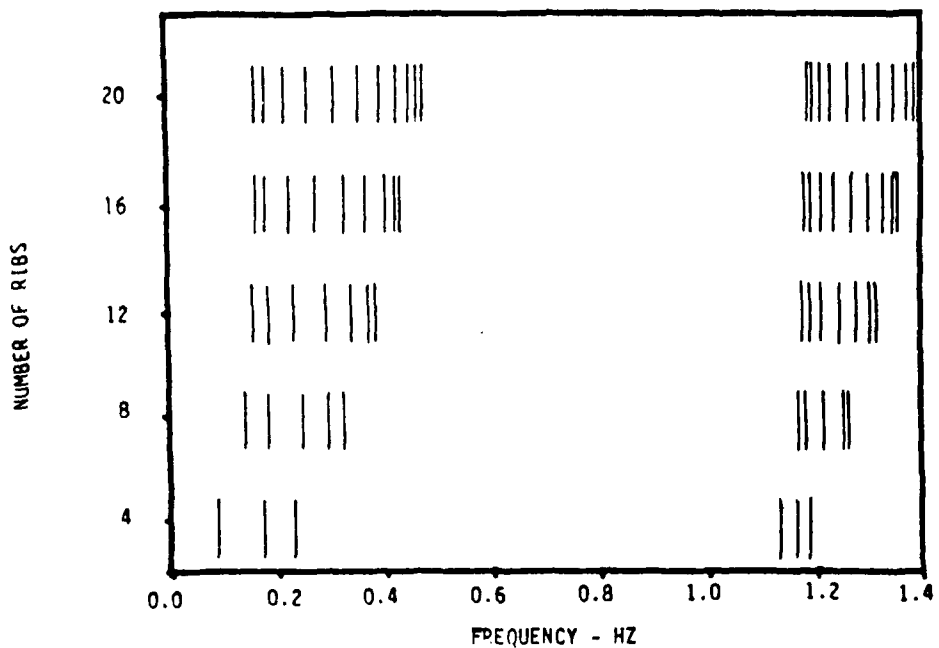
2.2.2.3 Boom and Feed. An important problem in antenna control which will be addressed in future experiments is that of controlling the feed relative to the antenna, while simultaneously controlling the antenna surface as well. This problem is significant because the antenna and the feed are generally connected together via a long, flexible boom with its own dynamics. The feed on the experiment structure is intended to replicate the feed horn of a space antenna, while the boom should be long and flexible and have dynamics within the control bandwidth.

The pendulum effect of the feed weight also has the desirable effect of providing a restoring force which tends to return the structure back to its equilibrium position. Without this restoring force, there would be a rigid body mode and the uncontrolled structure would run into its stops.

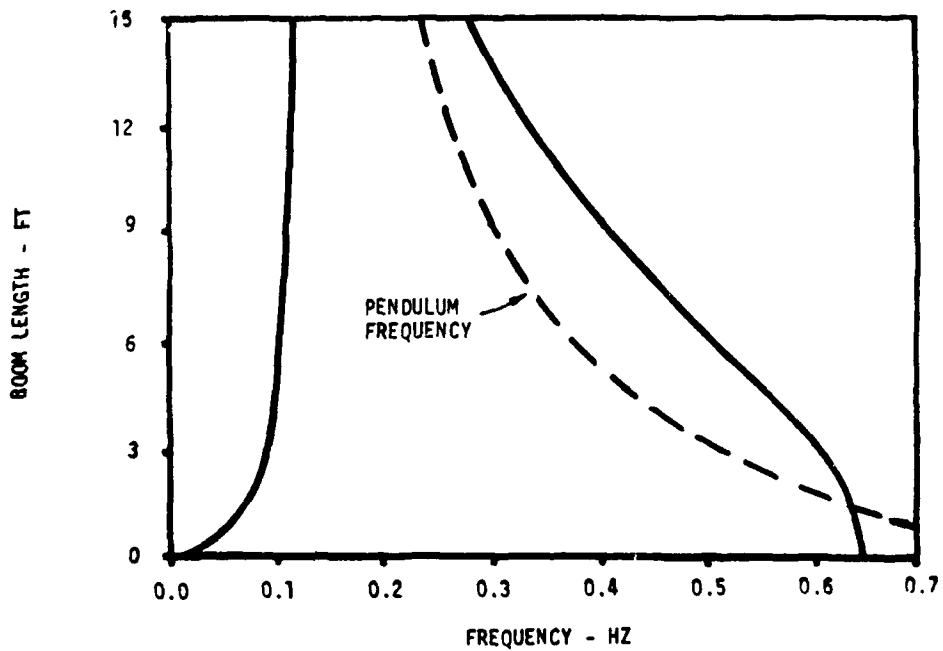
A number of parametric studies were performed to determine what effects on the modal frequencies changes in the boom stiffness, length, and the feed mass have, and to determine their final values. The only modes affected are the boom-dish modes; these are the modes which involve hub motion, and are described in Section 4. Figure 2.2-4 shows how the frequencies of the first two boom-dish modes vary according to boom length. As expected, a rigid body mode appears when the boom length is reduced to zero. As the boom is lengthened, the frequency of the first mode rises, rapidly at first and then more slowly. Figure 2.2-5 shows how the frequencies of the first two boom-dish modes vary according to the mass of the feed for a 12 foot boom. As the feed mass is reduced towards zero, the first mode tends towards a rigid body mode, not quite reaching it because the mass of the boom still provides a pendulum effect.

2.2.2.4 Coupling Wires. The function of the coupling wires is to couple motion of the ribs in the circumferential direction. The primary issues concerning their design are how many to use, where to put them, and how much to tension them.

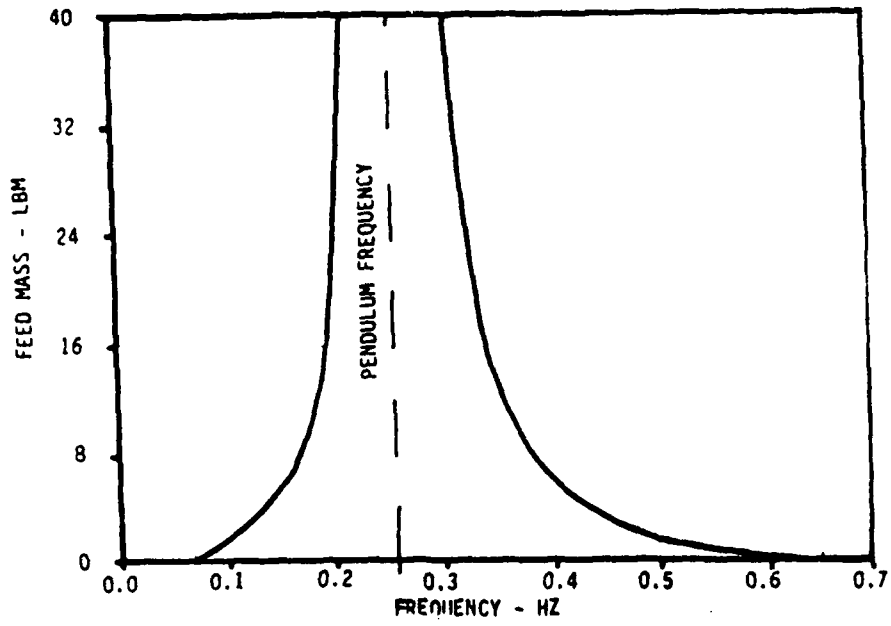
The decision to use two sets of coupling wires and to attach them to the ribs at the levitator attachment points was made by studying the mode shapes of the dish modes, Figure 2.2-6. In order to achieve maximum coupling between ribs, the coupling wires should be located close to points of maximum modal amplitude. The outer levitator position is roughly the location of the first mode maximum amplitude while the maximum amplitude of the second mode occurs near the inner levitator. The first two mode bands, corresponding to these mode shapes, are the primary ones of interest for the control



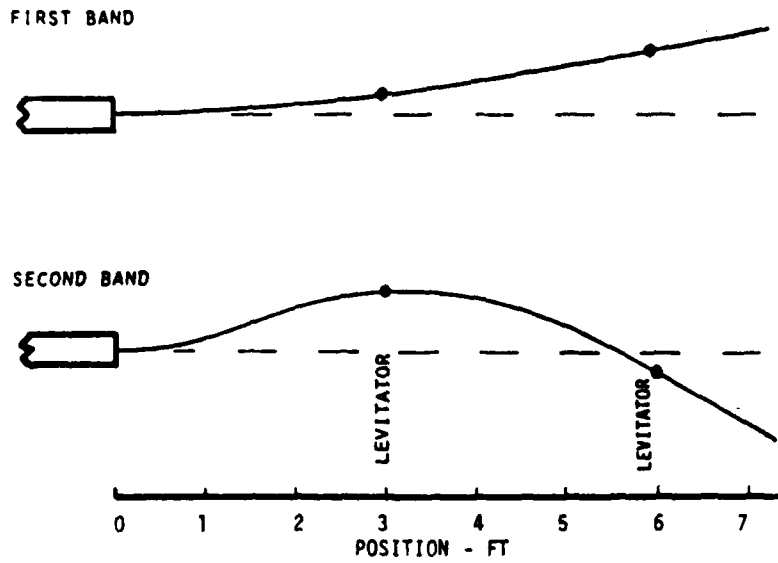
Frequencies of Dish Modes as a Function of the Number of Ribs
Figure 2.2-3



Frequencies of Boom-dish Modes as a Function of the Boom Length
Figure 2.2-4



Frequencies of Boom-dish Modes as a Function of the Feed Mass
Figure 2.2-5



Mode Shapes of Dish Modes - Radial Dependence

Figure 2.2-6

experiments and hence higher modes are not considered for the placement of coupling wires.

The coupling between adjacent ribs is directly proportional to the level of tension in the coupling wires. However, tension in the coupling wires has the undesirable side effect of causing compression within the ribs, only a part of which can be incorporated into a linear model. Enough compression in a rib will cause it to buckle. Thus, the criterion for selecting the tension was to use enough tension to cause noticeable coupling between the ribs, as determined by the splitting of the degeneracy in the dish modes, while at the same time using far less tension than that which would cause buckling of the ribs.

The tension which causes rib buckling also depends on where the coupling wire is attached. The outer coupling wire will cause buckling at less than half the tension of the inner coupling wire. Thus, the tension of the outer wire was set at one half that of the inner wire. Figure 2.2-7 shows how the frequencies of the dish modes depend on the tension in the coupling wires, when this 1 to 2 ratio is maintained. The buckling limit is the point at which the frequency of the first mode goes to zero. The selected tension values are 1 lb. for the inner wire and 0.5 lb. for the outer wire.

2.2.2.5 Levitators. The purpose of the levitators is to support the weight of the ribs so that they remain approximately horizontal. The design issues associated with the levitators are: how many to use per rib, where to place them, and what size counterweights to use. An associated issue is what friction level to allow within the bearings.

The displacement of a given rib in terms of its finite element degrees of freedom, (see Figure 4.0-1), is given by,

$$x = K^{-1} (f_g + B f_1),$$

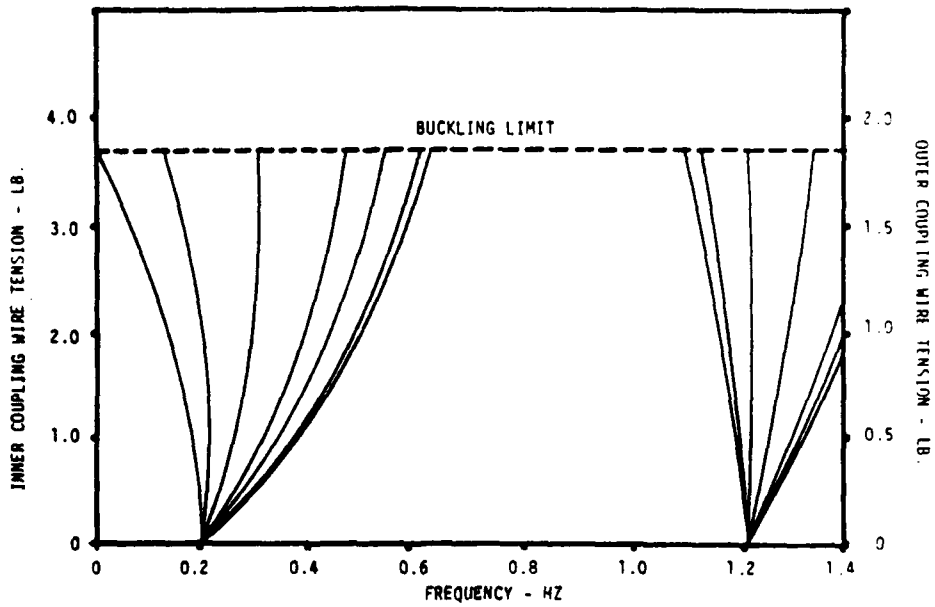
where K is the finite element stiffness matrix for a rib, x is the vector consisting of the finite element degrees of freedom, f_g is a vector of known forces which are due to the rib being under the influence of gravity, f_1 is the unknown vector of opposing levitator forces, and B is the control distribution matrix which determines the locations where the levitators can be located. The levitator forces are determined from the optimization problem which minimizes the functional,

$$x^T D x,$$

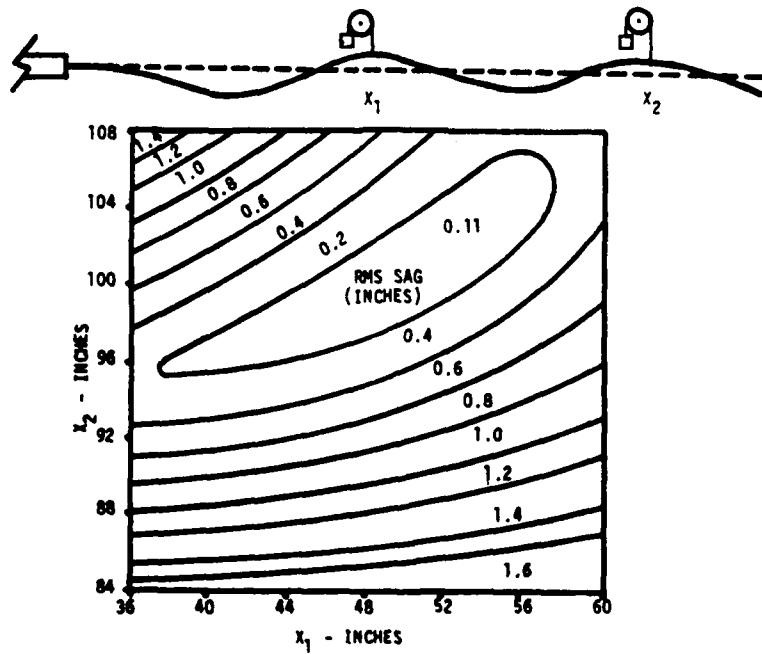
where D is a diagonal weighting matrix which has 1's along the diagonal positions corresponding to finite element displacements, and 0's at positions corresponding to finite element slope degrees of freedom. Minimizing this cost functional results in the minimum rms displacement of a rib from nominal. The solution to the minimization problem is given by

$$f_1 = -(B^T K^{-1} D K^{-1} B)^{-1} B^T K^{-1} D K^{-1} f_g.$$

While this formula gives the optimal levitator forces to apply, it does not provide any insight into where to place the levitator or levitators. It was immediately apparent that a rib could not be adequately supported by



Frequencies of Dish Modes as a Function of the Coupling Wire Tension
Figure 2.2-7



Rib Sag as a Function of Levitator Positions
Figure 2.2-8

just one levitator, but that two would likely be adequate. To determine the best locations for two levitators, the two-dimensional map shown in Figure 2.2-8 was calculated. It shows that with the levitator positions conveniently located at 40% and 80% of the rib length from the hub, the rms sag in the ribs is close to its global minimum.

The damping in the levitators was a serious concern from the start. Other sources of damping, such as air resistance and internal dissipation, have much less effect. For this reason, frictionless levitator designs using air bearings were pursued but were abandoned due to technical problems. The damping from the levitators is mostly due to bearing friction, though some additional damping comes from the friction of the counterweight wires passing over the pulleys. It can be shown, and it was demonstrated experimentally with a test setup, that the damping is Coulomb type, and for a given mode is approximately proportional to the bearing friction and inversely proportional to the modal frequency squared, its amplitude, and the radius of the levitator pulley. Coulomb damping is particularly undesirable because it is nonlinear. To minimize the damping, a combination of four things can be done: 1) use the best bearings possible consistent with their loading; 2) use the largest diameter pulley possible, keeping in mind that a larger pulley requires more resolution of the levitator sensors; 3) make the modal frequencies as high as possible; and 4) work with relatively large amplitudes of motion. Effective compromises were reached and it was estimated that damping of several percent could be achieved. Considerably higher levels of damping were seen in the structure once it was constructed, in the range of 15-20% for the boom-dish modes. The damping in the dish modes has not yet been measured (it will in the Parameter Identification experiment), but appears to be less than this. Undoubtedly some of the damping comes from unanticipated sources, such as the transducer cabling and joint friction, but the levitators remain the most likely primary cause of friction. Checks on 6 of the levitators indicated that they exceeded the specified friction level by as much as 100%. Additional work is planned to reduce levitator friction by decreasing bearing preloads, replacing bearings with lower friction units or redesigning the assemblies entirely.

2.2.2.6 Summary Design Parameters. Design parameters for the experiment structure design are given in Table 2.2-1. These served as a foundation for the hardware design but were relaxed in some cases where technical, schedule or cost limitations precluded full compliance. The impact of these waivers on system performance are noted where applicable throughout this report.

I.	<u>Experiment Apparatus</u>		IV.	<u>Gimbal mechanism</u>	
	Rib thickness	0.21 cm		Stiction torque	2.0E-2 N-m
	Rib width	7.62 cm		Restoring torque	0.2 N-m
	Rib length	2.25 m		Tilt range	+/- 4 Deg.
	Rib material	RC45 steel	V.	<u>Levitation Sensors</u>	
	Rib density	1.28 kg/m		Displacement range	140 deg. rotation
	Max. initial deformation	0.5 cm		Resolution	0.25 mm
	Inner levitator position	0.9 m from hub		Bandwidth	30+ Hz
	Outer levitator position	1.8 m from hub		Noise level	0.25 mm
	Inner wire position	0.9 m from hub	VI.	<u>Rib Root Sensors</u>	
	Outer wire position	1.8 m from hub		Location	0.225 m from hub
	Coupling wire material	Small gauge wire		Number	4 (every 90 deg.)
	Hub outer diameter	1.22 m		Displacement range	+/- 1 cm
	Hub inertia (4-10 axis)	4.29 kg-m ²		Resolution	0.10 mm
	Hub inertia (1-7 axis)	3.55 kg-m ²		Bandwidth	30+ Hz
	Hub mass	22.8 kg		Noise level	0.10 mm
	Inner gimbal mass	19.0 kg	VII.	<u>Hub Angle Sensors</u>	
	Boom wall thickness	0.079 cm		Location	At gimbal axes
	Boom length (long)	3.66 m		Number	2
	Boom length (short)	0.91 m		Displacement range	+/- 4 Deg.
	Boom material	Stainless Steel		Resolution	0.02 deg.
	Boom tube density	0.25 kg/m		Bandwidth	30+ Hz
	Feed mass	4.52 kg		Noise level	0.02 deg.
	Retro locations	10 per rib	VIII.	<u>Rib Root Actuators</u>	
	Retroreflector mass (ea.)	0.03 kg		Locations	0.225 m from hub
II.	<u>Backup Structure</u>			Number	12 (one per rib)
	Vertical resonance	12 Hz or more		Force range	+/- 1.0 N
	Horizontal resonance	4 Hz or more		Displacement range	+/- 1.0 cm
	Isolation from building	Vertical		Bandwidth	25+ Hz
III.	<u>Levitator Mechanism</u>		IX.	<u>Hub Actuators</u>	
	Pulley diameter	15.24 cm		Locations	On outer gimbal ring
	Pulley material	Aluminum		Number	2
	Pulley inertia	1.15E-3 kg-m ²		Force range	+/- 1.5 N
	Pulley mass	307 gm		Displacement range	+/- 4 deg.
	C'weight mass, inner	1.61 kg		Bandwidth	25+ Hz
	C'weight mass, outer	1.30 kg			
	Allowable stiction	1.0E-5 N-m			
	Maximum displacement	+/- 5 cm			
	Wire diameter	0.35 mm			

Table 2.2-1 Experiment Structure Design Parameters

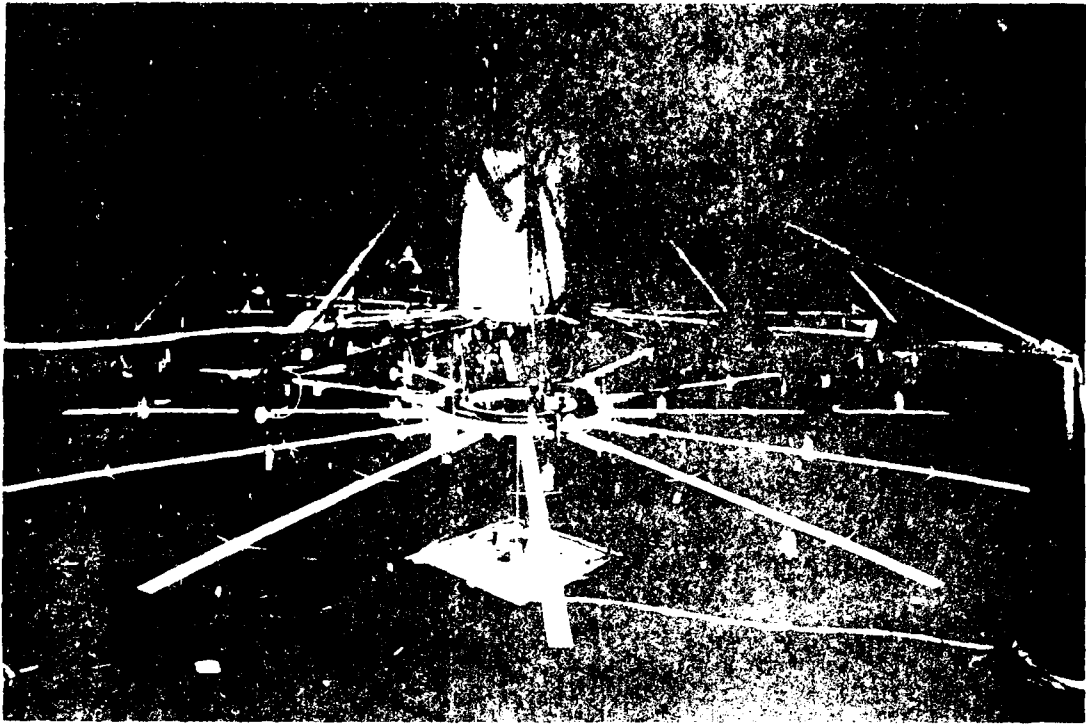


Figure 3.0-1 Interferometer

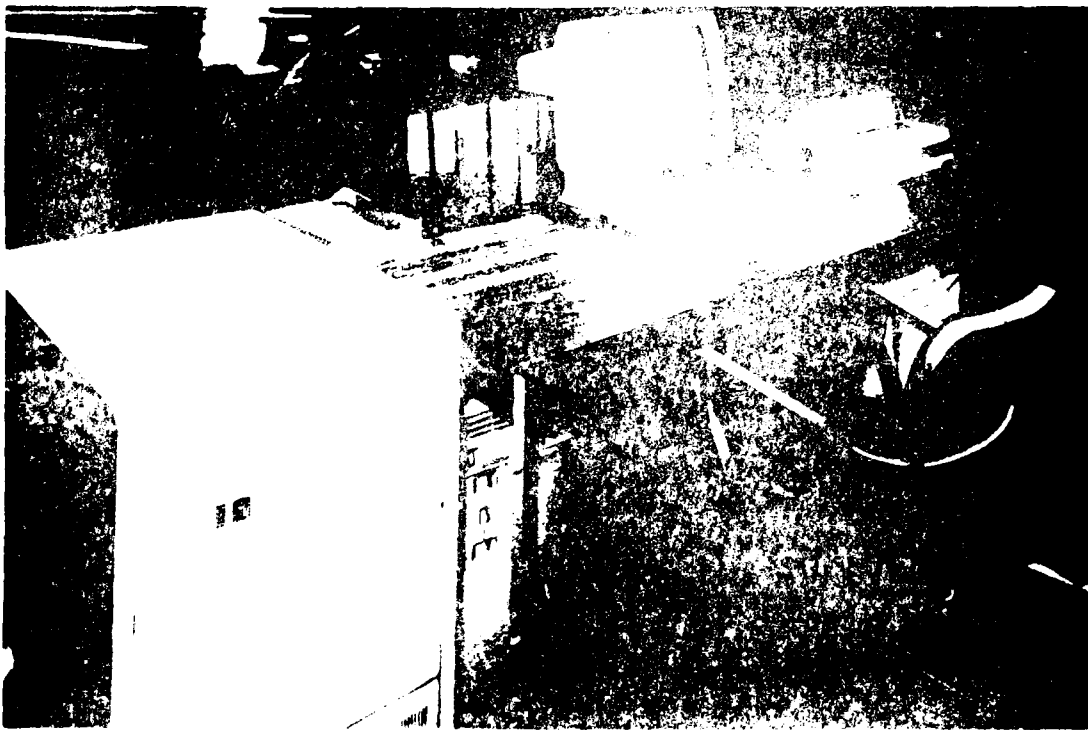


Figure 3.0-2 Computer/IAS Console

SECTION 3

DEMONSTRATION SYSTEM

The demonstration facility is comprised of four major subsystems; 1) the mechanical system including the experimental apparatus, its support structure and transducers; 2) the data acquisition system (DAS); 3) the system computer, and 4) the SHAPES system. The entire facility is installed in the Celestarium (Bldg. 199) at JPL. Photographs of the mechanical system and the computer/DAS operation console are shown in Figures 3.0-1 and 3.0-2. A plan view of the installation is shown in Figure 3.0-3.

The Celestarium is a special purpose building dedicated to optical system testing and calibrations, and to experimental validation of multi-axis control systems, particularly those utilizing optical sensors. The central test room has a hemispherical interior surface which is treated to be highly absorptive to visible light by the application of flat black painted honeycomb material. The room is 40 feet in diameter and 26 feet high, with the hemispherical section beginning 6 feet above the floor level.

There are three intermittently used test systems in the room which support JPL flight and research programs. These are a heliostat which is mounted above the ceiling in the center of the test room and projects a 30 inch diameter stationary collimated beam of sunlight to the floor directly below, a Canopus star secondary standard calibration system which mounts on one of two cranes which circle the room, and a ten foot diameter rack on which moving targets are mounted for use in SHAPES multi-target dynamic tests. The flexible structure demonstration facility must share the room and be compatible with occasional uses of these systems.

Detailed descriptions of the four major subsystems comprising the demonstration facility are given throughout this section.

3.1 MECHANICAL SYSTEM

The mechanical system consists of the experiment apparatus, backup structure, lifting winch and post-column assemblies. The arrangement of these assemblies is shown in the interior elevation view of the facility of Figure 3.1-1.

The experiment apparatus and backup structure are designed to operate at either a floor position or elevated position. Operation at the floor position enables checkouts, adjustments and alterations to be made at a convenient working height. In this position, a short boom is used to provide a pendulous restoring moment to the experiment apparatus. Operation in the elevated position allows the long (12 ft.) boom to be used for a more representative simulation of antenna system dynamics, and also minimizes interference with other activities in the Celestarium. Except for differences in dynamics resulting from the different boom lengths, operation is functionally identical at the two working heights. In the floor position, the backup structure rests directly atop five foot high floor mounted posts and obtains all vertical, lateral and torsional support from the rigidly attached posts. The experiment structure hangs 24 inches below and the 36 inch boom/feed

assembly just clears the floor. In the elevated position, the backup structure is supported vertically by three floor columns which rest atop the floor posts. But lateral and torsional support is obtained from the building structure. The orientation of the post floor column pattern was chosen to avoid interference with one SHAFES test head and the retroreflecting targets installed in the test rack on the opposite side of the room.

Because the experiment apparatus must be extremely flexible (hence fragile) to meet the performance requirements for low natural frequencies, the need for a rigid integral backup structure became apparent to provide multiple support points and to permit handling the apparatus as an integral assembly. The backup structure also serves as a reference coordinate system to interrelate measurements made throughout the apparatus to a common framework.

3.1.1 Backup Structure

The backup structure assembly consists of the supporting structure, gimbal assembly, winch system, and support post and columns.

3.1.1.1 Supporting Structure. The supporting structure supports all attachment points to the experiment apparatus through three master trusses and nine slave trusses all attached to a center tube. The center tube configuration was dictated by the need to provide clear passage for the 30 inch diameter Celestarium heliostat beam through the backup structure and experiment apparatus without significant encroachment of either structure. Upper and lower machined flanges are riveted to the center tube to carry hoop loads and provide attachment points for the master and slave trusses. Three bipods bolt to the upper and lower flanges. The upper bipods have hollow guide pins welded at their apexes which enter mating guide holes in brackets welded to the inner surface of a heliostat tube which fastens to the building structure at the top of the Celestarium dome. These pins align the backup structure to the building in the elevated position and transfer any backup structure torsional or translational loads to the building structure. The backup structure is raised by three lift cables which attach to the bottom flange of the backup structure center tube and pass through the upper bipod hollow guide pins to a three drum hand powered winch located above the Celestarium dome. A guide pulley assembly fastened to the floor of the dome routes the lift cables around components of the heliostat mounted directly above the heliostat tube opening. A photograph of the (pre-rigged) backup structure is shown in Figure 3.1-2 which illustrates the design and assembly of the master trusses, slave trusses, center tube and upper bipods. Conical spuds are seen at the tips of the master trusses. These insert into the support columns and serve as pin joints when the system is in the elevated position. They insert into the floor posts when the system is at the floor position and transfer lateral and torsional as well as vertical loads to the floor.

To minimize weight, the support structure is constructed of thin wall aluminum tubing and formed sheet metal connection plates with blind rivet fasteners used for all permanent connections. To maintain structural natural frequencies well above the test frequencies of interest, all loads attach at the intersections of truss members so that loading is in tension or compression rather than bending. Proof load deflection tests made on the

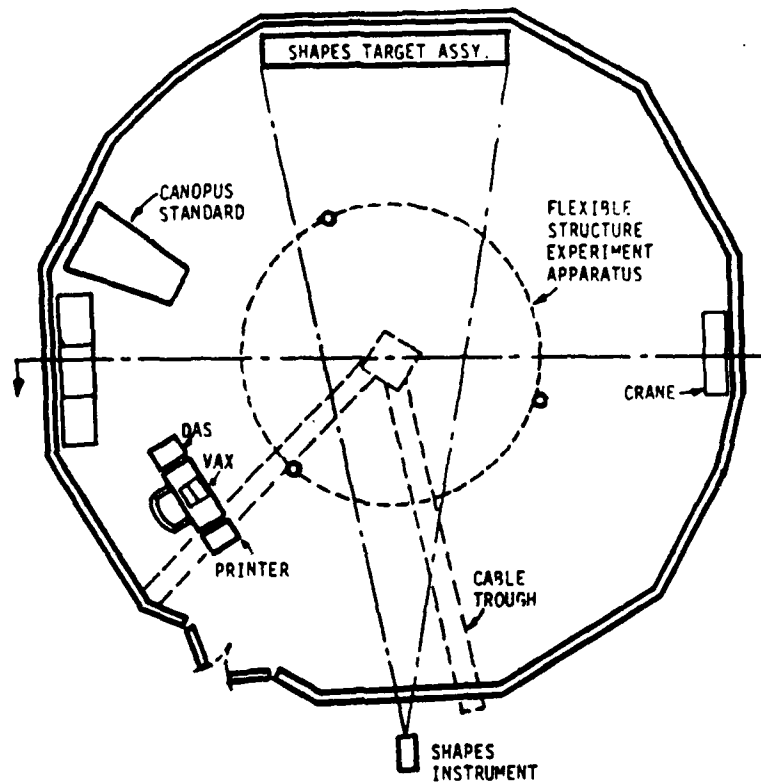


Figure 3.0-3 Plan View of Flexible Structure Test Facility Installation

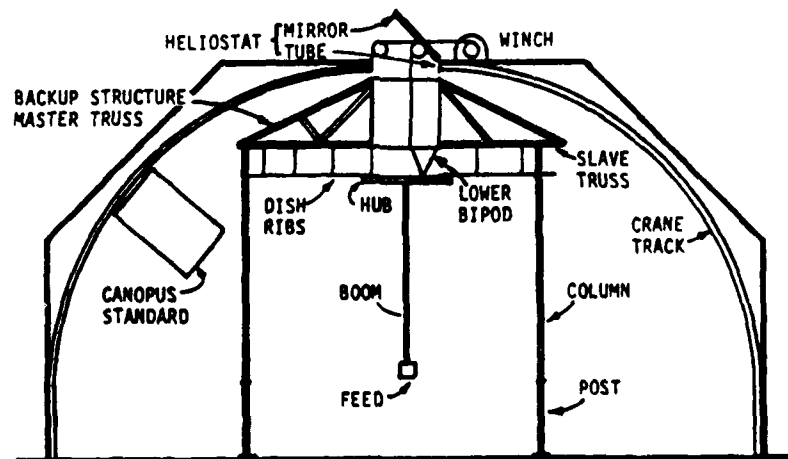


Figure 3.1-1 Elevation View of Flexible Structure Test Facility Installation

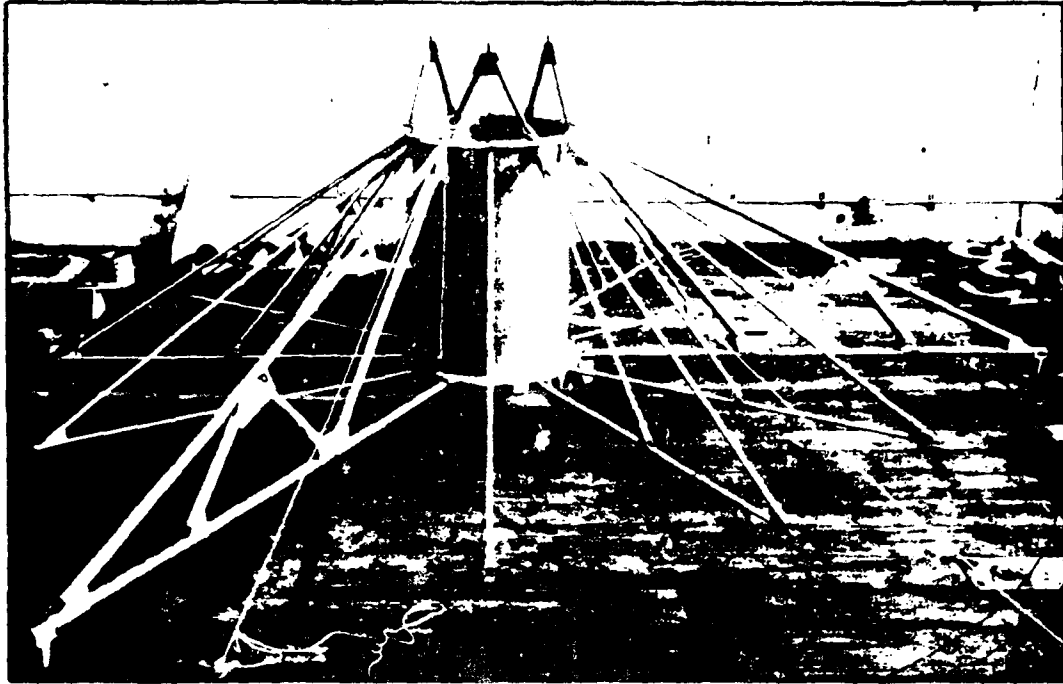


Figure 3.1-2 In-process Photograph of Support Structure

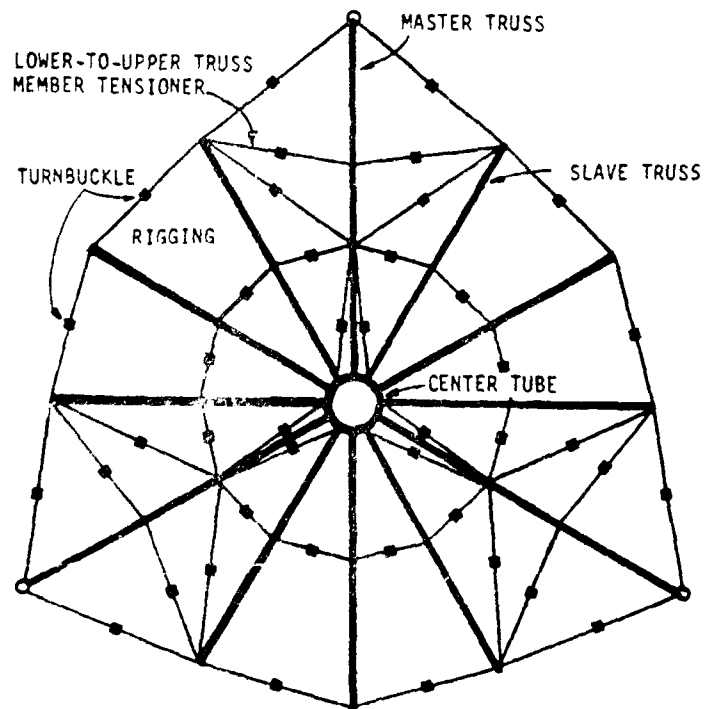


Figure 3.1-3 Support Structure Rigging

completed support structure indicated a fundamental natural frequency in the vertical direction of 13 Hz. Lateral and torsional rigidity are obtained by a cable rigging system interconnecting both upper and lower truss members. Each rigging cable incorporates a turnbuckle to accommodate dimensional variations. The rigging configuration is shown in Figure 3.1-3. Master truss rotational alignment cables were installed first and tensioned to accurately establish the three point base mounting pattern and provide torsional stiffness to the structure. Outer and inner ring cables were then added and adjusted to accurately space the slave trusses around the structure. Cross brace cables were then installed and carefully tightened to avoid distorting the alignment of the structure.

3.1.1.2 Gimbal Assembly. The support structure carries the gimbal-hub assembly which attaches through three lower bipods to the lower flange of the support structure center tube. A two gimbal system is used which permits hub freedom about two orthogonal tilt axes. The system is composed of an inner, center and outer ring. The inner ring is fixed to the lower bipods and supports the center ring via two Bendix limited motion flexural bearings mounted diagonally opposite each other. Flexural bearings were chosen for this application because of their complete absence of stiction. (The torsional spring characteristic of this type of bearing is permissible because the supported assembly is self restoring due to its pendulousity.) The center ring supports the hub (outer ring) through two flexural bearings mounted opposite each other and displaced by 90 degrees from the center ring support bearings. Each ring was formed by rolling thin wall steel tubing into a ring of proper diameter and welding the free ends together. Milled housings to support the flexures, actuators and sensors, and pads to support the ribs and boom spider were then jig welded to the rings at all attachment points and the rings were stress relieved before painting and final assembly.

3.1.2 Experiment Structure

The experiment structure consists of the ribs, rib root arm assemblies, levitator assemblies, rib support cables and attachments, counterweights and catch cables, coupling wires, boom-feed assembly, and transducers.

3.1.2.1 Ribs. The twelve ribs are made of 0.083 in. thick steel strap, 3.0 in. wide by 88.58 in. (2.25 m) long. Early laboratory tests indicated that the flexible ribs could be accidentally bent if not handled with extreme care. To alleviate this problem, very tough band saw steel (used in large lumber mill saws) was mill cut to the required width from the standard 10 inch width and delivered on special order to JPL in 11 foot lengths carefully crated to protect against shipping damage. On removal from the crate, each rib was taped to a one inch pine board, three inches wide to provide protection during handling, trimming, drilling, painting and mounting. These boards have been retained for use on future occasions when the ribs are removed from the structure.

The ribs bolt to equally spaced pads welded around the lower face of the hub gimbal ring. The pads were ground clean to remove burrs and slag after welding but were not faced to a common surface plane. As a consequence, it was later necessary to custom fit tapered shims to align the ribs to a

common mounting plane. Fitting was accomplished by clamping the hub in the level position and then using a bubble level and test shims to determine the coarse shimming necessary to level each rib in the radial direction. Final shimming was done with the ribs installed in place by sliding shim material between the coarse shim shoulders and hub pads, again using a bubble level and test shims for measurement. Because there is a 40:1 magnification between the shim thickness and rib tip displacement, it was necessary to shim to an accuracy of 0.001 in. to maintain the rib tip plane parallel to, and within 0.040 in. (1 mm) of its correct position relative to the hub plane. It was not necessary to shim in the cross-radial direction since fabrication tolerances were tighter, no displacement magnification occurs, and displacements in this plane are not of significant interest to the experiments. Shim design details are shown in the rib root assembly diagram of Figure 3.1-4.

Shape determination and control experiments impose a requirement for installing SHAPES targets at any of ten locations along the free length of each rib. To accommodate this requirement, each rib is drilled at ten percent intervals along its length and "dummy" retroreflectors are available to exchange with real retroreflectors as they are moved from one location to another. The stainless steel dummy retros are accurately trimmed to the average weight of the real retros so that relocations from one position to another will not cause significant shape changes in the affected ribs. Rib root actuator and sensor mounting hole patterns are also provided at ten, fifteen and twenty percent locations along the free length of the ribs, and coupling wire anchor clip holes are drilled just outboard of the levitator support points at the forty and eighty percent points. Including four mounting pad holes and two guide pin holes, a total of twenty three holes is drilled in each of the twelve ribs.

3.1.2.2 Rib Root Arm Assembly. The rib root arm assembly consists of the arm, mounting spacer with guide pins, dual clamp and the rib root sensor and actuator. An exploded view of the assembly is shown in Figure 3.1-4. Since the 0.1 in. radial clearance between the transducer cores and stators is fully consumed as the rib travels through its specified range, the initial stator alignments relative to core mounting holes drilled in each rib are critical. To maintain close tolerances, a drill template with hardened inserts was made for use in drilling the rib (in the rib root area), arm, spacer with guide pin holes, and clamp. Guide pin holes drilled in the rib, spacer, and arm, align these components with sufficient accuracy that they can be disassembled and reassembled with only visual adjustment. Eighth inch diameter roll pins used as guide pins are pressed into the mounting spacer so that they protrude 0.083 in. on each side to engage guide holes in the rib and rib-root arm.

The most critical dimensions are the center-to-center distance between the transducer stator holes in the clamp and the corresponding center-to-center distance between the transducer core shaft mounting holes in the rib. Oversize clamp screw mounting holes in the rib-root arm allow rotational and lateral adjustment of the clamp assembly. Alignment is accomplished with the aid of two alignment pins shown in Figure 3.1-5 which mount in the clamp in place of the transducer stators and enter the rib core shaft mounting holes. The alignment pins are dimensioned to provide the proper distance between the arm and rib, and to provide close fits to the clamp and rib holes. Once the alignment pins are inserted into the rib, the clamp-to-arm mounting

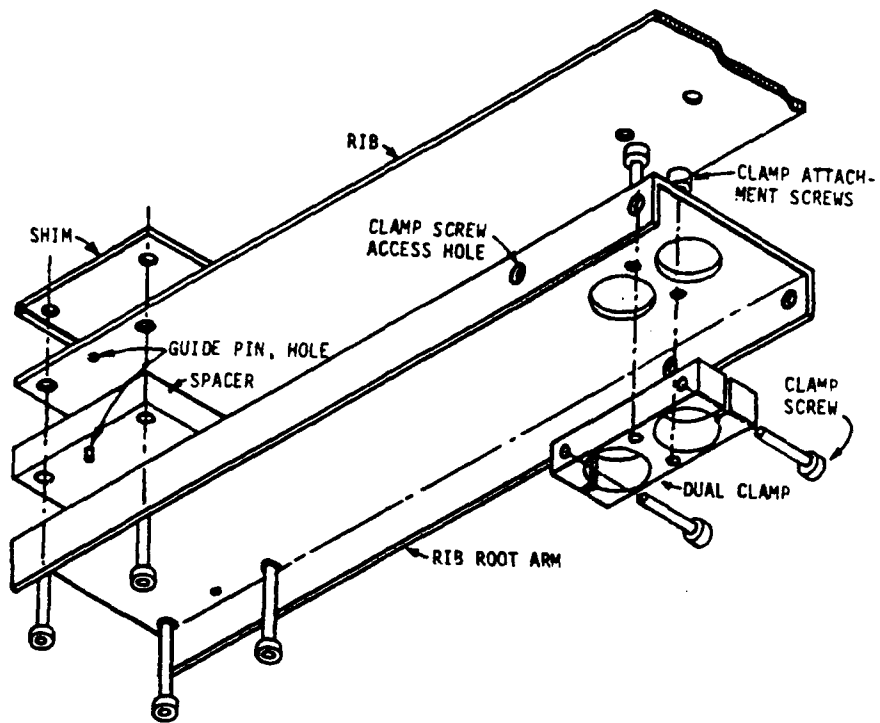


Figure 3.1-4 Rib Root Arm Assembly - Underside View

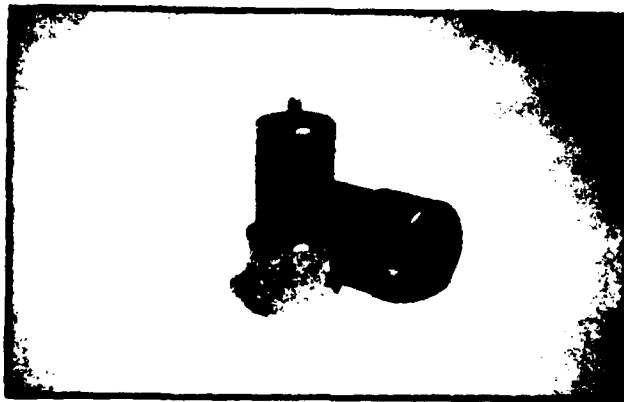


Figure 3.1-5 Alignment Pins

screws are tightened, the alignment pins are removed, and the cores and stators are installed.

3.1.2.3 Levigator Assemblies. Twenty-four levigator assemblies are required to support each of the twelve ribs in two places. The support locations were calculated to minimize the rms shape deviation along the rib from the root to the tip. The calculations were confirmed by laboratory experiments which showed that supporting the free length of the rib at the 40% and 80% points results in a 0.11 in. (2.8 mm) rms sag.

Important characteristics for the levigator are that it have very low friction, provide precise levitation force independent of displacement, and be affordable. Other desirable characteristics are that dynamic interactions with the test structure be minimum, (i.e., low effective added mass or external spring force), and that a displacement readout be incorporated as an accessory function of the levigator assembly.

Several experimental designs based on the concept of an integral air bearing guided air piston assembly were built and tested in the laboratory. These configurations had advantages of very light moving mass, extremely low viscous friction, and total absence of stiction. However, numerous difficulties were encountered with the experimental designs including insufficient bearing radial load capacity, bearing instability, piston/regulator stability interaction, limited axial travel, high sensitivity to supply pressure and extremely tight machining tolerance requirements (hence, high cost). While most of these problems could have been overcome with further development, it became apparent that these developments could not be carried out within programmatic constraints.

The selected levigator concept, based on a straightforward pulley-counterweight approach was analyzed and evaluated in the laboratory using instrument grade ball bearings for the pulley. This simple configuration offers low viscous damping, insensitivity of levitation force to rib position, stability of the levitation force, ease of adjustment, and ease of integrating a displacement sensor into the design, simplicity, reliability and low cost. In trade for these features, bearing stiction force is unavoidable with the use of ball bearings, and a significant amount of moving mass is added to the test apparatus. The stiction is the most serious shortcoming of these since it introduces a nonlinear effect on the structure. Analysis determined that the effects of bearing stiction would be minimized by the use of a large pulley diameter. Laboratory tests utilizing a six inch diameter pulley confirmed that bearing friction is the predominant source of dissipation in the system (e.g., viscous friction, cable scuffing and hysteresis, and air damping are insignificant by comparison), but that a damping ratio of less than 2% can be attained in a dual levigator, 0.1 Hz system by careful design and bearing selection. This level of performance was considered satisfactory for the final design.

To avoid added losses by the use of redundant bearings, the final design utilizes the shaft and bearings of an optical encoder to support the pulley. The encoder also provides the desired displacement readout signal. As shown in the cross-section view of the levigator assembly in Figure 3.1-6, the pulley drum extends inward of the shaft so that the cable hangs directly below the support truss and straddles the encoder internal bearings to equally

distribute the load between the two bearings. By equalizing the bearing loads, the total radial load (hence shaft friction) is minimized and excessive front bearing load is eliminated. Except for the mounting clamps and tee-rail brackets, all parts of the master and slave truss levitator assemblies are interchangeable. The clamp mounting arrangement allows the levitator assembly to be rotated and shifted along the support truss so that the pulley shaft lies horizontally and the cable hangs vertically.

3.1.2.4 Rib Support Cables and Attachments. Monofilament line was specified for the levitator cables to avoid the possibility of interstrand friction in stranded or braided line. Also, because cable stretching must be minimized to maintain displacement sensor calibration, the use of music wire was preferred over that of a non-metallic line.

Having identified music wire as the preferred cable material, experiments were undertaken to determine the optimum wire diameter and to develop reliable termination techniques. Nine mil music wire was used in initial experiments to develop a termination method using crimped copper or brass ferrules. Initially, ferrules were made by cutting 12 gauge copper wire into one-eighth inch lengths, facing the ends and through-drilling 0.030 in. holes on a jeweler's lathe. Later, ferrules were made by cutting 1/8 in. diameter brass tube (0.030 in. I.D.) into 1/8 in. sections without end facing. Vise-grip pliers were used for crimping the ferrules. Samples successfully passed 15 lb. proof load tests (~250,000 psi wire tensile load), but notch failures occurred in a few samples and wire slippage occurred in several others. The use of heavier gauge (14 mil) wire and an extra loop through the ferrule overcame these problems. The final design of the support cables incorporated small wire hooks or split rings as termination hardware to facilitate connections with joining parts. All support cables were made with the use of simple jigs that enabled like cables to be made to precise lengths for interchangeability, and aided in the fabrication of tight slip-free terminations.

To limit the amount of twist imparted to ribs as the hub gimbals rotate about their flexures, the inner levitator attachments to the ribs allow universal angular freedom with minimum resistance to small tilt motions about the horizontal plane. As shown in Figure 3.1-7(a), tilt freedom is accommodated by universal flexure of the support wire in its mounting socket formed as a part of the support attachment screw fitting. The outer levitator rib attachments are designed to hold the ribs level about the twist axes, hence all twist caused by rotation of the hub takes place between the hub and outer rib attachment. The attachment detail is shown in Figure 3.1-7(b).

3.1.2.5 Counterweights and Catch Cables. Each counterweight is individually matched to its specific rib and levitator position. Individual matching was required primarily because of small but significant differences in the relaxed shapes of the ribs due to internal forming stresses. The counterweighting criterion used in trimming the weights was to maintain a flat rib plane coincident with the plane of the hub. This required that the counterweights not only offset the free weight of the ribs, but also compensate for variations in the relaxed shapes of the ribs. The consequence of this is that slight differences in rib mass properties are created by the

amount of counterweight mass required to compensate for their shape variations. Other matching criteria are possible with different consequences.

Individual counterweight determinations were made using the special fixture shown in Figure 3.1-8. The fixture uses a straight 78 in. length of 3 in. x 3 in. heavy wall square aluminum tubing as a base to which the test rib is securely bolted using the regular hub mounting holes. The rib is clamped between an upper plate and two half inch thick spacers which separate the rib from the base. This mounting arrangement closely simulates the rib-hub mounting configuration on the demonstration structure. The test rib is loaded with dummy retroreflectors bolted in the correct locations except at the 40% and 80% levitator support positions where special brass dummy retros are mounted on the under side of the rib. Regular levitator rib attachment hardware is used at the two support points.

When making the inner counterweight measurement, a knife edge support is placed exactly beneath the outer support position. The height of the knife edge support is the same as that of the mounting spacer (1 in.). The knife edge is cut out to straddle the special brass dummy retro, and contacts the rib near both edges to prevent twisting. A special electrical contactor mounted on an insulated base is placed under the inner levitator support attachment. The combined height of the special brass dummy retro and the single point contractor in combination with the knife edge support arrangement duplicates the desired support conditions for the rib when it is mounted to the hub in the demonstration structure and supported at the two levitator support points.

To measure for the correct amount of counterweight required to levitate the rib at the inner support location, a pulley cable is coupled to the inner levitator rib attachment ring, passed over a carefully balanced 6 in. diameter pulley mounted in precision bearings, and coupled to a hanging weight tray. An ohmmeter is connected between the insulated electrical contactor and the base to detect continuity. Laboratory balance scale weights are then placed on the weight tray until the rib just lifts off the inner contactor as indicated by a break in electrical continuity. The total weight of the hanging tray and scale weights is the correct weight for the counterweight including its attachment hardware. The test fixture pulley-cable assembly was built to the same design and quality standards as used for comparable parts employed in the demonstration structure. To simplify measurements and reduce the possibility of error, a hanging weight tray weighing exactly one kilogram was built and used.

To measure for the correct amount of counterweight at the outer levitator position, the knife edge and electrical contactor support positions are exchanged, and the pulley assembly and ohmmeter are moved to the outer support position. The trial balance procedure is repeated at this position.

The threshold of the counterweight measurement procedure is approximately one gram, and the final counterweights were trimmed to comparable accuracy by rough machining 2 in. diameter cold rolled steel blanks to lengths slightly greater than the estimated finish dimensions and trimming on the basis of scale measurements. The determinations of the final counterweight amounts included adjustments for the counterweight attachment hardware and for the weights of the coupling wire assemblies whose weights are also supported by the levitators.

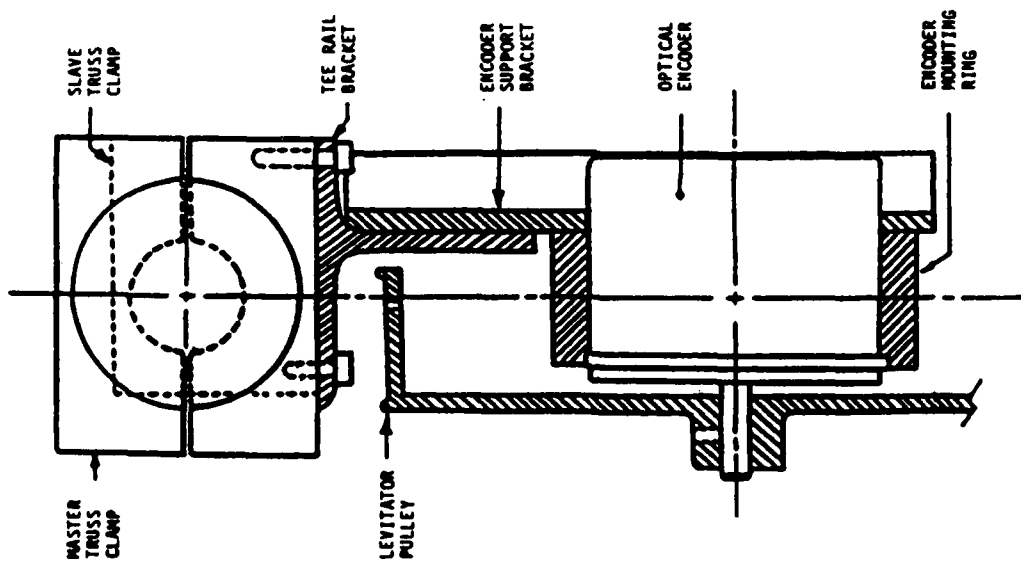
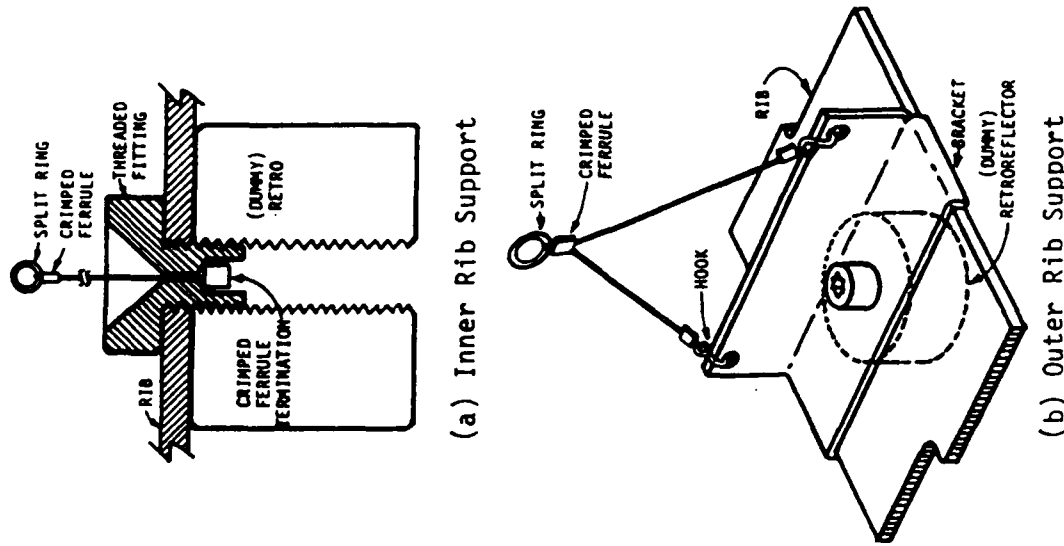


Figure 3.1-6 Levitator Assembly



(a) Inner Rib Support

(b) Outer Rib Support

Figure 3.1-7 Rib-cable Attachments

Catch cables are installed on each of the counterweights to protect persons underneath the structure from a falling counterweight in the event that a levitator cable breaks. Electrical cable lacing material is used for the catch cables and shock relief springs are used to minimize the shock load on the cables. To provide damping to the spring-mass combination, the catch cable loops through the counterweight eye with one end tied to the support structure and the other end tied to the free end of the spring. As shown in Figure 3.1-9, the fixed end of the spring is also tied to the support structure. Considerable damping force is created as the catch cable drags through the counterweight eye when the weight drops due to levitator cable breakage.

3.1.2.6 Coupling Wires. The motions of each rib are coupled to its neighbors' by two sets of constant force coupling wires which ring the demonstration structure at the inner and outer levitator support locations. These wires simulate the motion coupling effects of RF reflective mesh installed over the rib frame of a real deployable antenna. The demonstration structure functional specifications called for the coupling wires to be (1) tensioned within 5% of each other, (2) have near-constant force over the range of rib motions, and (3) attach to the ribs in a manner that minimizes the creation of twist forces on ribs due to out-of-plane motions of adjacent ribs. These specifications were met by (1) carefully calibrating the tension springs, (2) using "soft" springs stretched to their near-limit, and (3) employing the free-pivot attachment arrangement shown in Figure 3.1-10 in which attachment hooks from adjacent rib coupling wires hook through the same hole in the rib. Rib twist torque is limited to the vertical component of coupling wire force acting through one-half the diameter of the attachment hole (approx. 1/8 in.).

The coupling springs in the inner ring are tensioned to one pound force whereas those in the outer ring are tensioned to one-half pound force. The rib attachment holes are drilled 3/4 in. outboard of the levitator support points and are countersunk on each side to provide a knife-edge pivot contact line for the end hooks.

Each spring has a relaxed length of approximately one inch and is stretched to approximately double that length when installed. Two springs are used for each coupling wire, thus the total stretched spring length is approximately 4 in. The springs were pre-calibrated by measuring and recording the total extension of each two-spring pair when stretched by a half or one pound weight. Each coupling wire set consisting of two end hooks, two calibrated springs and a connecting wire was custom fitted in place on the demonstration structure using a clamp bar to maintain precise rib separation during the fitting process and the special turnbuckle shown in Figure 3.1-11 to provide the correct calibrated spring set end-to-end extension. The connecting wires are made with crimped ferrule terminations as are the levitator support cables, and their lengths are custom tailored to their location in the demonstration structure during the fitting process. Each assembly is marked to identify its position in the structure. Accordingly, if the rib hub mounting bolts are loosened or removed allowing the rib to shift in its mounting, it is necessary to refit the four coupling wire assemblies to the affected rib.

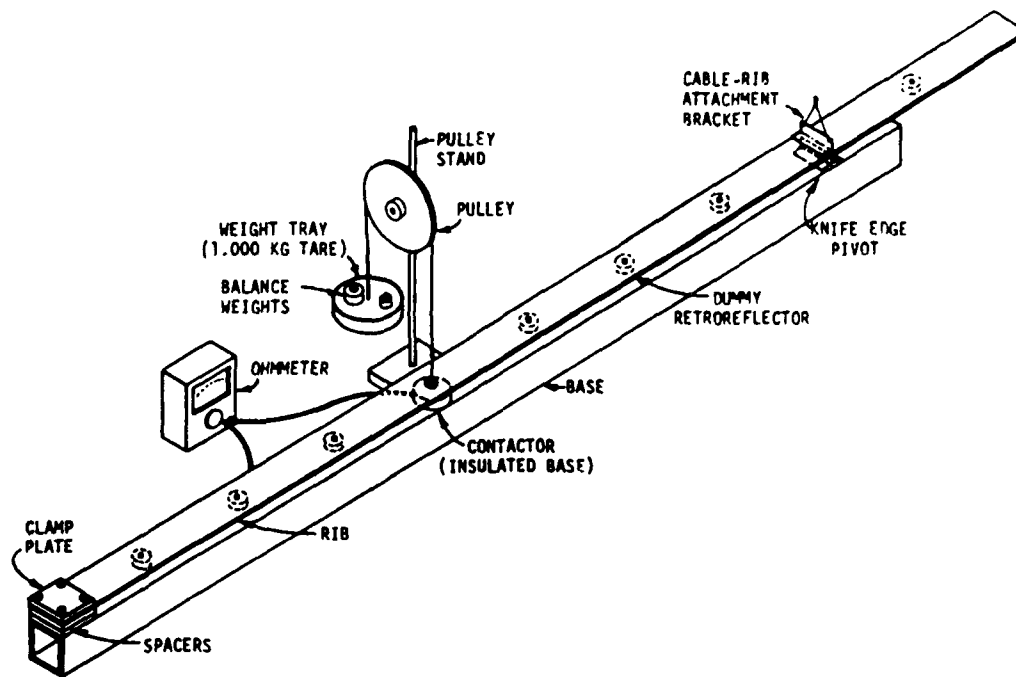


Figure 3.1-8 Counterweight Test Fixture

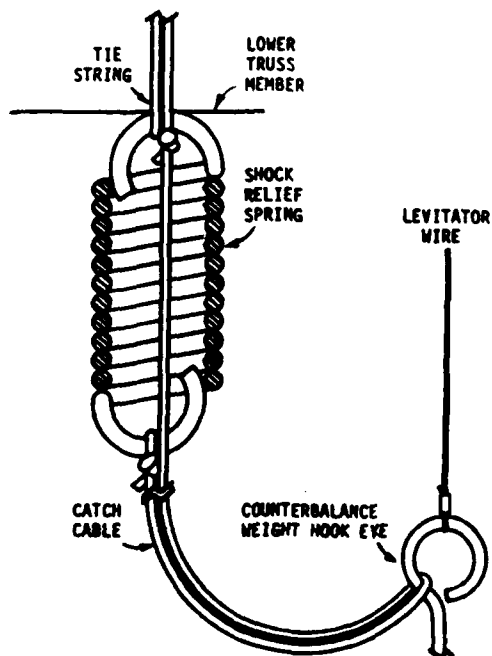


Figure 3.1-9 Catch Cable Installation

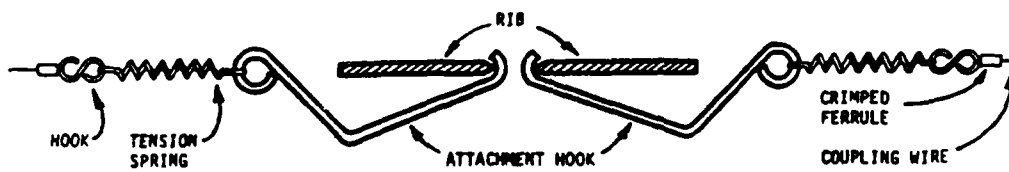


Figure 3.1-10 Coupling Wire Attachments

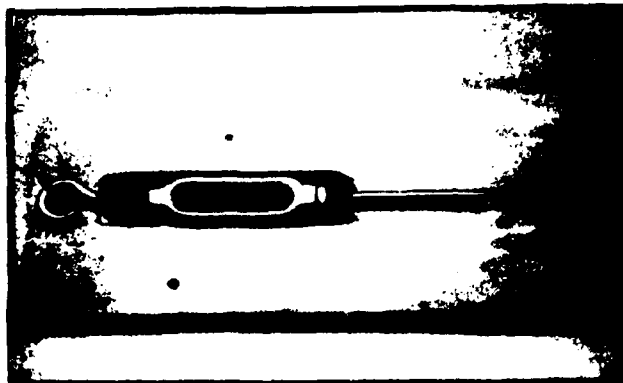


Figure 3.1-11 Special Turnbuckle Tool with Calibration Base

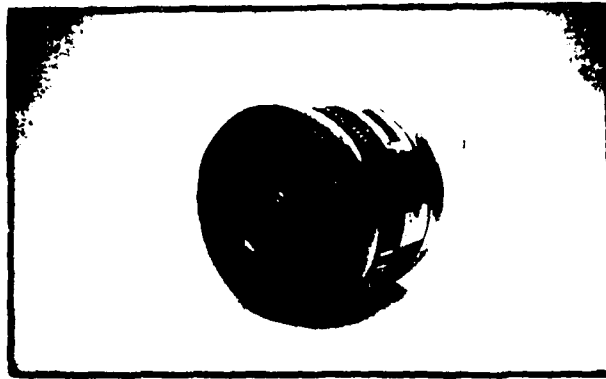
3.1.2.7 Boom-Feed Assembly. The boom attaches to the hub through a spider which bolts to the hub in three places. The standard twelve foot long boom is used when the structure is raised to its operating position. To simplify installation of the boom, a Morse taper coupling is used which locks into a play-free joint when the male and female sections are mated. The female section is machined into a spool shaped part which installs in the center of the spider. The male section is machined as an end fitting which is pinned to the upper end of the boom. The sections lock automatically under the weight of the feed when they join as the structure is raised to the operating position. The sections unlock automatically when the feed weight strikes the floor as the structure is lowered. A short, three foot long boom is used when the structure is operated at the floor level. Both booms are made of 1/2 in. diameter 1/32 in. wall stainless steel tubing.

A ten pound cylindrical weight threaded into a fitting pinned to the lower end of the boom simulates the mass of the antenna feed. While no transducers are installed to move or sense the motion of the boom or feed, tapped holes are provided at 90 degree spacings around the perimeter of the feed to accommodate retroreflectors for SHAPES displacement measurements.

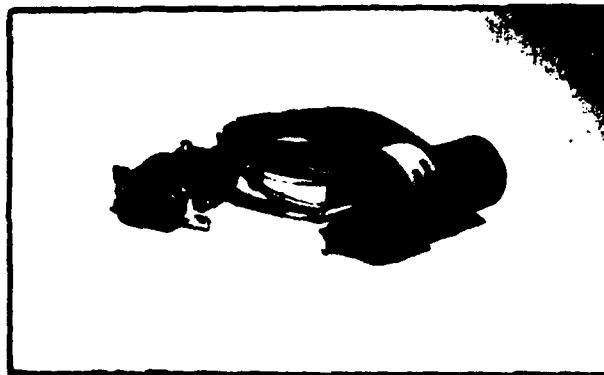
3.1.2.8 Transducers. A total of 44 electromechanical sensors and actuators are distributed around the demonstration structure for use by experimenters in monitoring and controlling the displacements of the various members of the structure. The SHAPES sensor also provides for an additional 16 sensing positions whose locations on the structure can be changed with a minimum of realignment and recalibration effort. All sensors measure displacements (e.g., no rate or acceleration sensors are used), and all actuators produce pure force, independent of displacement within their linear range.

In the selection of transducers, preference was given to those types which are free of mechanical friction in their operation. Other selection criteria included sensitivity, linearity, scale factor stability and cost. Due to cost considerations, all sensors were chosen from the wide array of available off-the-shelf units. On the other hand, no suitable off-the-shelf actuators were found, and it was necessary to procure custom actuators designed to JPL specifications.

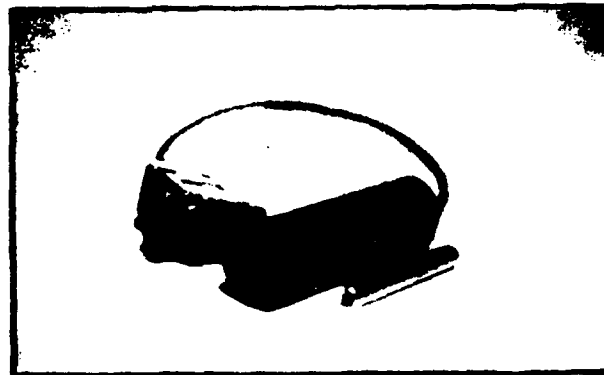
3.1.2.8.1 Sensors. Because the incremental optical encoder bearings also support the levitator pulleys, the shaft load capacity and bearing stiction characteristics are important factors in the selection of these sensors. Baldwin Motion Systems Model L25G servo mount, two phase, 1800 cycles-per-revolution units were selected as the most suitable off-the-shelf encoders for this application. The sensors were ordered to a specification of 0.05 in-oz. breakaway torque for an 8 lb. radial shaft load. An offset pulley design is used with the encoder to equalize bearing loading and thereby minimize breakaway torque. Incremental encoders were selected in preference to absolute units in part because of cost considerations, but also because it was concluded that the majority of anticipated experiments require knowledge of displacement relative to initial position rather than to an absolute datum plane. However, the encoders are equipped with an index output which, if calibrated relative to a reference plane, can be used to determine absolute position relative to the reference plane. A photograph of the encoder model is shown in Figure 3.1-12(a).



(a) Optical Encoder - Levitator
Position Encoder



(b) RVDT - Hub Angle Sensor



(c) LVDT - Rib Root Position Sensor

Figure 3.1-12 Sensors

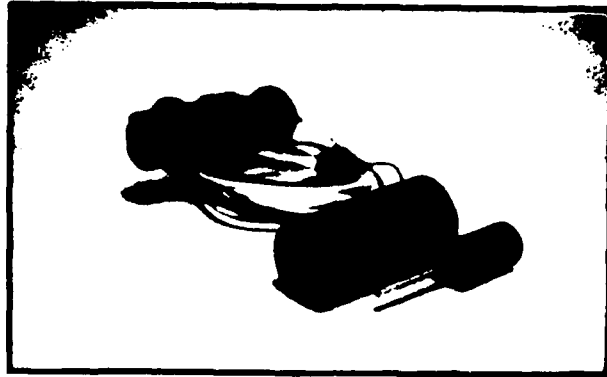
Schaevitz Model R30D rotary variable differential transformers (RVDT) are used as the hub sensors. These are non-modular servo mount units with internal bearings. Since torque levels are high at the hub, the small amount of stiction characteristic of these bearings is insignificant. However, since flexible shaft couplings are not used due to physical space and access limitations in the installation housing, shaft alignment relative to the gimbal flexural bearing axis must be carefully adjusted to prevent radial loading of the RVDT bearings. A Schaevitz Model SMS/GPM signal conditioner is used with each of the sensors which produces ± 10 volt dc full scale output for supply inputs of ± 15 volts dc. Because the RVDTs operate over an angular range of ± 4 degrees, an external dc line amplifier with a gain of ten is installed in each signal conditioner housing to boost the output level. This arrangement has been the source of excessive electrical noise in the sensor system, and modifications are under consideration to overcome this problem. A photograph of the RVDT model is shown in Figure 3.1-12(b).

Off-the-shelf linear variable differential transformer (LVDT) sensors are used for the four rib-root sensors. The Schaevitz Model 200 HR LVDT was chosen for this application because of its large core-to-bore diametrical clearance of 0.125 in. which is required to accommodate the large arc that the core travels through as the rib bends outboard of the hub clamp hinge line. Even with the extra clearance of this model, the core must be carefully centered to prevent core-to-bore bottoming at the extremes of rib travel. Schaevitz Model SMS/GPM signal conditioners are also used with the LVDTs. External line amplifiers are not required, however, because the 0.20 in. rated range of the LVDTs closely matches the maximum expected rib motion travel. A photograph of this model is shown in Figure 3.1-12(c).

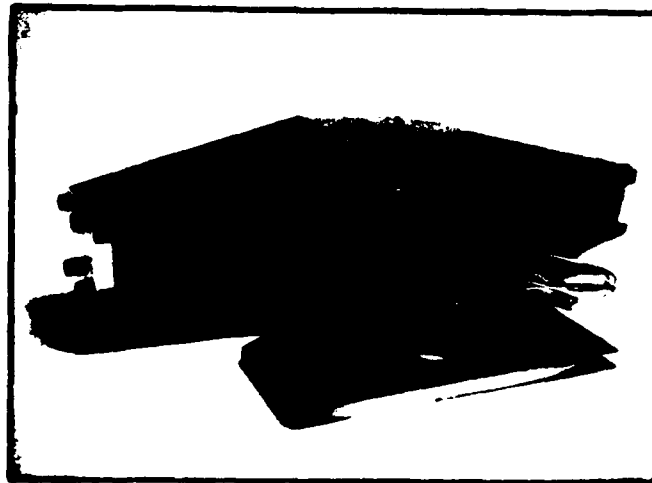
3.1.3.8.2 Actuators. Custom designed permanent magnet force actuators are used for hub torquers and rib root actuators. While both types produce a continuous rated force output of 6 oz., the rib root actuator operates over a ± 0.25 in. maximum travel whereas the maximum range of the hub actuator is ± 1.5 in. Both produce full rated force at 24 volts dc input with a current of less than 300 milliamperes. Because of the different stroke requirements, substantially different design configurations are used for the two applications.

The rib root actuator is a solenoid design which employs a 0.5 in. diameter cylindrical permanent magnet core moving axially within the bore of a 7/8 in. OD stator solenoid coil. The stator coil is sheathed by a backiron sleeve with end rings to minimize the magnetic path reluctance and provide high force-per-ampere performance. The diametral clearance between the core and stator is 0.10 in. and, as with the rib root sensors, the core must be carefully centered within the bore to prevent bottoming at the extremes of travel. Even with careful adjustment, in-service experience has shown that core to stator magnetic attraction causes undesirable nonlinear effects when the core is not perfectly centered. Because of the suspension geometry, the core is always non-centered when the rib is not in its neutral position. To date, the extent of these effects has not been fully evaluated. This actuator is illustrated in the photograph of Figure 3.1-13(a).

The hub gimbal actuator is a knife configuration in which a pancake wound air core armature coil passes between the poles of a large (13 lb.) permanent magnet stator. Although the gimbal assembly must be counterbalanced



(a) Rib Root Actuator



(b) Hub Actuator

Figure 3.1-13 Actuators

to offset the heavy weight of the stator, the high force scale factor of 40 oz/amp is also attributable to use of a heavy magnet. Because of the large coil surface (1.5 in. x 4.0 in.), close gap (0.05 in.) and large travel (± 1.5 in.), a tedious multi-axis alignment process is required to maintain coil clearance throughout the travel. A three axis alignment of the stator is performed first with the aid of an alignment plate and dial indicator. Next, the coil is installed and visually aligned by adjusting the three screws of its tripod mounting base. Experience has proven the stability of the mounting and alignment schemes under the stress of numerous occasions in which the hub assembly has been driven to its stops, both by accidental impact and by malfunction of an experiment program. The photograph in Figure 3.1-13(b) shows the components of the hub actuator.

3.2 COMPUTER SYSTEM

3.2.1 Hardware and Supporting Software

3.2.1.1 General Requirements. The functional and performance requirements that influenced the selection of the system computer hardware and development of its supporting software were derived by the system software developer with the inputs and support of the experimenters. Programmatic considerations were also factored into the requirements.

The key requirements are that the system shall:

1. Be suited in architecture and operating system software to real-time data acquisition, process control and applications software development.
2. Provide a minimum capability of 300,000 floating-point operations per second with provisions also for double-precision floating point operation.
3. Execute dynamic control experiments at a rate of at least 10 frames/second with capability for up to 30 frames/second operation.
4. Contain a high-resolution video display supported by ANSI GKS standard software subroutines for generating two-dimensional graphics.
5. Graphically plot up to 6 dynamic variables simultaneously in real-time on the video display.
6. Provide an I/O bus for transmission of data to and from the experiment system devices, including the SHAPES sensor.
7. Contain a minimum of 1 Mbyte of RAM for each of the three major users of memory space: (a) operating system, compiler, linker, and debugger, (b) applications programs, and (c) I/O data buffers with expanding capability at 6 Mbytes.

8. Include magnetic tape cartridge or reel storage.
9. Support the ANSI FORTRAN 77 standard language with a high-speed, optimizing compiler and a comprehensive symbolic debugging tool.
10. Support the ANSI Ada standard language with a fully validated, high-speed, optimizing compiler and a comprehensive symbolic debugging tool.
11. Allow FORTRAN program elements to be invoked by Ada program elements or vice versa. Mixed-language programs must be compatible with the comprehensive symbolic debugging tool.
12. Include a modem for off-line telephone transmission of experiment data to an IBM PC-AT computer.

3.2.1.2 Implementation. The hardware and supporting software items selected to satisfy these general requirements are listed and briefly described as follows:

1. DEC VAXstation II computer system (SV-LV55B-EK) consisting of:

MicroVAX II Central Processing Unit (CPU), 5 MB of main memory, and Floating-Point Coprocessor Unit (FPU).

System enclosure (BA123) for up to four mass storage devices and 12 Q-bus backplane slots for memory, controllers, or other special-purpose interface logic modules.

RD53 5.25 in. hard disk drive and RQDX3 controller with 71 MB of formatted capacity.

TK50 streaming cartridge tape subsystem including TQK50 controller with 95 MB of formatted capacity, microprocessor control, automatic error correction and self-calibration.

RX50 dual 5.25 in. floppy disk drives with a total formatted capacity of 819.2 KB.
2. Video terminal consisting of:

VCB01 1K by 2K bit-mapped video graphics system.

VR260 19" monochrome landscape monitor with a resolution of 1024 by 864 pixels (78 dots per inch) and a non-interlaced screen refresh rate of 60 Hz.

LK201 standard keyboard.

Mouse.

3. Printer/plotter consisting of:

LA210 dot-matrix desktop printer with high-speed draft, near-letter quality, and high-resolution graphics (72+ dots per inch) printing modes.

4. VAX software consisting of:

MicroVMS (Version 4.3) real-time and general purpose operating system.

MicroVMS workstation software (Version 2.0) supporting multi-windowing.

Graphical Kernel System (GKS/OB, Version 1.2) package of subroutines for producing two-dimensional graphics, also includes software emulation of DEC VT100 and Tektronix 4014 terminals.

VAX Ada (Version 1.2) language; a government validated implementation of the ANSI-MIL-STD-1815-A-1983 Ada language.

VAX FORTRAN (Version 4.4) language.

Language Sensitive Editor (LSE) (Version 1.2).

5. IEEE-488 Bus Interface:

National Instruments (GPIB11V-2) Direct Memory Access (DMA) interface controller board with MicroVMS handler software for data transfer between the IEEE-488 bus and the DEC Q-bus.

6. Data Acquisition System (DAS) Interface:

DEC (DRV11-WA) general purpose DMA 16-bit parallel digital interface board for the Q-bus, with DEC-supplied DRV11-WA software driver (XADRIVER).

7. Communications Interface:

DEC (DHV11) eight-line, asynchronous, DMA multiplexer for the DEC Q-bus with modem control on all lines; supports Bell 100 and 200 series modems and their equivalents; also compatible with EIA RS-232-C/CCITT V.28 terminals/systems.

3.2.2 System Software

3.2.2.1 General Requirements. The system software is required at a minimum to carry out those functions that are common to all of the experiments and needed by each of them. These include:

1. User command processing
2. Data acquisition control

3. Timing, sequencing, and mode control
4. I/O data processing
5. Graphical display
6. Hardcopy production
7. Experiment data management

In order to perform this minimal set of functions in an efficient and reliable way, it is also necessary to add the requirements for:

8. System status reporting
9. System error reporting

The system software, written primarily in Ada, is distinguished from the experiment software that will be tested and "validated" by the system experiments. The latter are exclusively FORTRAN subroutines written to evaluate algorithms for shape determination, shape control, state estimation, parameter and input identification, pointing control, adaptive vibration damping, etc.

3.2.2.2 Program Overview. The software program that was implemented to carry out the system experiments and meet the general requirements listed here, is called DEMO. DEMO consists of 55 separate modules (not including the experimenters' FORTRAN subroutines) of which 28 are written in Ada and 27 in FORTRAN. FORTRAN was used solely for easier interfacing to VAX windowing (graphics and text display) utility software and to the driver routines for the DRV11-WA and GPIB11V-2 bus interface cards. The breakdown of program source lines between the two languages is as follows:

Program DEMO

Ada source lines	= 4239
FORTRAN source lines	= 1331

Total (including comments)	= 5570 lines

In addition to DEMO, several utility programs and numerous test drivers were also written. One of the more important utilities, called VIBES, is an interactive program written in Ada to sample and record real-time data from the system's hub and levitator sensors in response to a physically applied disturbance to the boom. These data are then used by the experimenters to perform a modal survey of the structure using the Fast Fourier Transform (FFT).

Two other utilities, DAS_TEST and TIME_DAS, are used to test the Data Acquisition System (DAS) built for the system by Vista Controls Corporation. Both are written in FORTRAN. DAS_TEST is designed to test all the DAS functions, one transaction at a time, in an interactive mode. The results of the single transaction between the DAS and the VAXstation are displayed on the monitor at the bit level, including register contents of the interface board, error status bits, etc. This software proved to be very valuable in the DAS checkout and integration testing phase. TIME_DAS was used to perform a timing measurement on the DAS' block read/write cycle to verify that design specifications had been met.

Source code line counts on these three utilities are as follows:

<u>Utility Programs</u>	<u>Source Lines</u>
VIBES (Ada)	520
DAS_TEST (FORTRAN)	835
TIME_DAS (FORTRAN)	42

Total (including comments)	1397 lines

Including the software test drivers, more than 8000 source lines (in Ada and FORTRAN) were written and tested to support the demonstration system, exclusive of the experiment software.

3.2.2.2.1 Top-Level Structure. The fundamental structure of program DEMO can be seen from the Ada listing of its top-level procedure in Figure 3.2-1. This procedure (also called DEMO) consists of (1) its specification part, which defines the two primary functions -- INTERACT_WITH_USER and CONTROL, and (2) its body (or executable part), where INTERACT_WITH_USER is executed. CONTROL is assigned an execution priority of 10, higher than the default priority of 7 assigned to DEMO and its dependent -- INTERACT_WITH_USER. Thus, INTERACT_WITH_USER, which processes user input from the VAXstation keyboard, can only run when CONTROL is not running or is temporarily suspended.

Note the VAX Ada library units that are imported by means of the Ada "with" and "use" statements in Figure 3.2-1. These resources are thus made available to DEMO, CONTROL, INTERACT_WITH_USER, and all the Ada subprograms defined by these units.

One other major Ada unit must be considered to be at the top-level of the DEMO program. It is the Ada package called CMD_PROCESSING and is the only package specified and referenced by the program DEMO. CMD_PROCESSING can be thought of as the program's global data pool. As its name suggests, it primarily contains declarations of data types and objects used to represent user command parameters, command menus, and related command processing variables. However, it also contains a variety of other data types and object declarations that are common to more than one Ada module.

3.2.2.2.2 User Commands. When executing, the procedure INTERACT_WITH_USER is an endless loop consisting of prompts to the user for command menu selections and the acquisition of the user's keyboard entries. Command menus are displayed at two levels - the main menu at Level 1 and 6 possible menus of command categories at Level 2. At Level 3 (the lowest command entry level), an indexed list or table of command parameters and their current values is displayed. At this level the user is invited to select a particular command parameter to be changed and to supply its new value. The user may change as many parameters in the table as he wishes until he types in the "exit" choice; at this point he will return to the next higher level's menu display. All new parameter value entries are immediately displayed for user verification. Unexpected characters (e.g. alphabetic) will cause an exit back to the next higher level.

```

                                DEMO

with SYSTEM                    : use SYSTEM
with CALENDAR                  : use CALENDAR
with FLOAT_MATH_LIB           : use FLOAT_MATH_LIB
with TEXT_IO                   : use TEXT_IO
with INTEGER_TEXT_IO          : use INTEGER_TEXT_IO
with FLOAT_TEXT_IO            : use FLOAT_TEXT_IO
with LONG_FLOAT_TEXT_IO       : use LONG_FLOAT_TEXT_IO
--
procedure DEMO is
--
    task CONTROL is
        pragma priority (10);
    end CONTROL;
    task body CONTROL is separate;
    procedure INTERACT_WITH_USER is separate;
--
begin
--
    INTERACT_WITH_USER;
--
end DEMO;

```

Figure 3.2-1 Ada Listing of DEMO

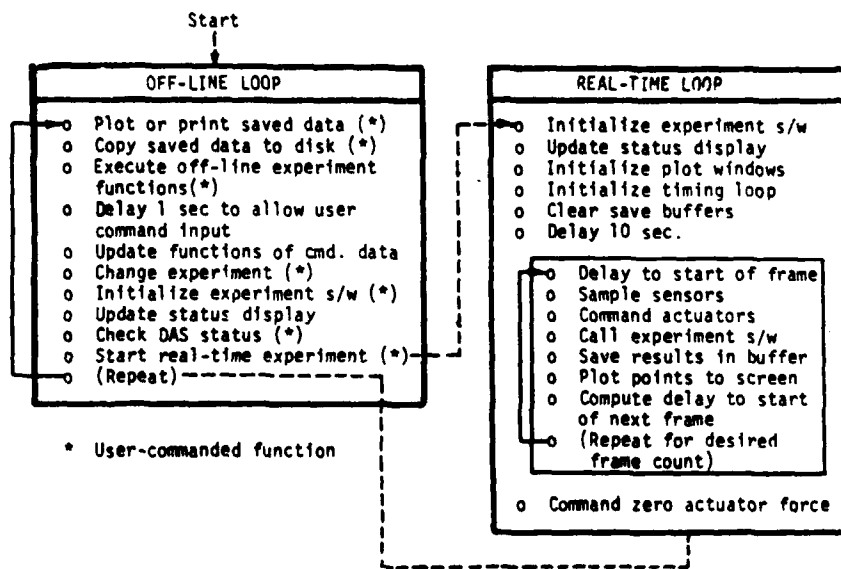


Figure 3.2-2 System Control Task: CONTROL

The main menu provides 6 possible choices of second level menus. These are:

- o Experiment 1 -- Vibration Control
- o Experiment 2 -- Static Shape Determination
- o Experiment 3 -- Adaptive Control
- o System Execution Control
- o Data Display Control
- o System Hardware Checkout

While the number of Level 1 choices can be easily extended beyond 6, the current DEMO program provides a command menu for each of the three currently defined experiment types as well as three menus for controlling various elements of the system software.

A variety of command parameter data types are supported, including single-precision floating-point, integer, character string, and Boolean. In all cases, the command parameters are transmitted to the CONTROL task for the purpose of controlling system or experimental software functions. Typically, the Boolean command parameters are used to immediately enable or disable some functional activity in CONTROL or in the experimental software subroutines called by CONTROL. These types of commands, as well as all the other types, are briefly summarized in Table 3.2-1.

In total, 44 different command options are provided to the user, 29 of which control elements of the system program DEMO. The remaining 15 command options (five for each experiment type) are used to set the values of parameters that are eventually passed to the experimental software by means of an initialization call.

The 29 system command options provide the capability to change 330 separate system parameter values (278 floating-pt., 30 Booleans, 21 integers, and 1 string), while the experiment command options affect 51 different experiment parameter values (45 floating-pt., 3 Booleans, and 3 strings).

3.2.2.2.3 Real-Time Controller. Like the procedure INTERACT_WITH_USER, the task CONTROL consists basically of an endless processing loop. However, CONTROL continually examines (rather than updates) the incoming command parameters to determine what action should be taken next. One of CONTROL's prime functions is to execute a real-time experiment, for which it must establish and regulate the timing, sample the sensors, command the actuators, activate the experimental software algorithms, save dynamic data, display some dynamic data on the monitor, and check for errors. However, this real-time mode of operation is not the only mode that CONTROL is designed to carry out. One of the experiment types, i.e. Static Shape Determination, uses the real-time mode only for accumulating sensor data samples and not for control. And, in fact, static shape determination experiments are carried out in a "one-shot", step-by-step, non-real-time approach.

Basically then, CONTROL requires only an outer loop for continuous servicing of commands and activation of off-line (i.e. non-real-time) system functions and experiments, and an inner loop for carrying out real-time experiments or system tests. Figure 3.2-2 shows a simplified flow-chart of CONTROL's processing activity.

1-1	(1 BOOLEAN)	ENABLE EXPERIMENT #1 SOFTWARE SELF-INITIALIZATION. *
1-2	(1 STRING)	NAME THE DISK FILE CONTAINING EXPERIMENT #1 SOFTWARE PARAMETERS.
1-3	(14 FLOAT)	SET THE HUB/RIB ACTUATOR DISTURBANCE TORQUE/FORCE LEVEL.
1-4	(14 FLOAT)	SET THE HUB/RIB DISTURBANCE TORQUE/FORCE DURATION.
1-5	(1 FLOAT)	SELECT EXPERIMENT #1 MODE OF OPERATION.
1-6	(1 BOOLEAN)	ENABLE THE STORAGE OF EXPERIMENT RESULTS IN A DISK FILE. *

EXPERIMENT 1 -- VIBRATION CONTROL

4-1	(1 INTEGER)	SELECT EXPERIMENT TYPE
4-2	(6 BOOLEAN)	SELECT SYSTEM EXECUTION MODE. *
4-3	(2 FLOAT)	SET REAL-TIME EXECUTION SAMPLING INTERVAL AND TOTAL RUN-TIME
4-4	(3 BOOLEAN)	ENABLE USE OF ACTUATORS, DAS OR SHAPES SENSOR
4-5	(2 BOOLEAN)	ABORT THE REAL-TIME EXPERIMENT OR EXIT THE PROGRAM. *
4-6	(1 STRING)	NAME THE DISK FILE CONTAINING SIMULATED HUB SENSOR DATA
4-7	(1 BOOLEAN)	ENABLE SIMULATED HUB SENSOR DATA TO BE USED DURING A REAL-TIME EXPERIMENT
4-8	(1 BOOLEAN)	ENABLE THE STORAGE OF SAMPLED SENSOR DATA IN A DISK FILE. *

SYSTEM EXECUTION CONTROL

2-1	(1 BOOLEAN)	ENABLE EXPERIMENT #2 SOFTWARE SELF-INITIALIZATION. *
2-2	(1 STRING)	NAME THE DISK FILE CONTAINING EXPERIMENT #2 SOFTWARE PARAMETERS.
2-3	(1 FLOAT)	SET THE NUMBER OF SHAPE MEASUREMENTS TO BE AVERAGED.
2-4	(1 FLOAT)	SELECT EXPERIMENT #2 MODE OF OPERATION.
2-5	(1 FLOAT)	SET THE SHAPE ESTIMATE RESOLUTION (POINTS PER RIB).
2-6	(2 BOOLEAN)	ENABLE THE STORAGE OF EXPERIMENT RESULTS IN A DISK FILE. *
2-7	(2 FLOAT)	SET THE SHAPE CONTROL FORCE APPLICATION PARAMETERS.

EXPERIMENT 2 -- STATIC SHAPE DETERMINATION

5-1	(200 FLOAT)	ENABLE DISPLAY OF SY. SAVE TABLE; ALSO, CHANGE PLOT SCALE FACTORS. *
5-2	(-)	ENABLE PRINTING OF THE SYSTEM SAVE TABLE. *
5-3	(7 BOOLEAN)	SELECT THE DISPLAY MODE. *
5-4	(2 INTEGER)	SELECT THE VARIABLES FOR A SINGLE TIME PLOT TO SCREEN (2 VARIABLES)
5-5	(6 INTEGER)	SELECT VARIABLES FOR STRIP-CHART TIME PLOT TO SCREEN (6 VARIABLES)
5-6	(2 INTEGER)	SET RIB SHAPE PROFILE DISPLAY PARAMETERS (RIB NUMBER AND PLOT MODE)
5-7	(8 INTEGER)	SELECT 7 VARIABLES FOR PRINTING AND THE PRINT INTERVAL.
5-8	(2 INTEGER)	SELECT STATUS DISPLAY PAGE. *

DATA DISPLAY CONTROL

3-1	(1 BOOLEAN)	ENABLE EXPERIMENT #3 SOFTWARE SELF-INITIALIZATION. *
3-2	(1 STRING)	NAME THE DISK FILE CONTAINING EXPERIMENT #3 SOFTWARE PARAMETERS.
3-3	(6 FLOAT)	SET THE HUB/RIB ACTUATOR DISTURBANCE TORQUE/FORCE LEVEL.
3-4	(6 FLOAT)	SET THE HUB/RIB DISTURBANCE TORQUE/FORCE DURATION.
3-5	(1 FLOAT)	SELECT EXPERIMENT #3 MODE OF OPERATION.
3-6	(1 BOOLEAN)	ENABLE THE STORAGE OF EXPERIMENT RESULTS IN A DISK FILE.

EXPERIMENT 3 -- ADAPTIVE CONTROL

6-1	(2 FLOAT)	SET ACTUATOR TEST TORQUE LEVEL
6-2	(12 FLOAT)	SET RIB-ROOT ACTUATOR TEST FORCE LEVEL
6-3	(2 FLOAT)	SET SINE-WAVE FREQ OR PULSE WIDTH OF HUB/RIB ACTUATOR TEST SIGNAL
6-4	(12 FLOAT)	SET SENSOR/ACTUATOR SCALE FACTORS; SET SENSOR RESPONSE LIMITS
6-5	(16 FLOAT)	SET 'SHAPES' SENSOR RANGE MEASUREMENT BIAS LEVEL
6-6	(24 FLOAT)	SET LEVITATOR SENSOR POSITION MEASUREMENT BIAS LEVEL
6-7	(4 FLOAT)	SET RIB-ROOT SENSOR POSITION MEASUREMENT BIAS LEVEL
6-8	(2 FLOAT)	SET HUB SENSOR ANGULAR POSITION MEASUREMENT BIAS LEVEL
6-9	(6 BOOLEAN)	ENABLE DAS CONTROL/TEST FUNCTIONS; ALSO, CLEAR DAS ERROR INDICATORS *

SYSTEM HARDWARE CHECKOUT

* IMMEDIATE EXECUTION

Table 3.2-1 Command Summary

The functions followed by asterisks in Figure 3.2-2 are conditionally executed based on the presence of a user command to do so. After execution, the function's command flag is then cleared until the user again requests that type of activity.

The time delay of 1 second inserted into the off-line loop of CONTROL serves to suspend execution of CONTROL so that the lower priority task (DEMO) can service terminal keyboard inputs using INTERACT_WITH_USER. The speed of the VAX is such that CONTROL will usually spend the vast majority of its time suspended by this delay when executing in the off-line mode. (The only exception to this is the rather lengthy function of copying experiment data from RAM buffers to disk files.)

A time delay is also built into the processing sequence that is used to make the transition from off-line mode to the real-time mode. Here, the purpose of the delay is to provide a time buffer, for example, to allow screen displays to settle, or allow the structure to be manually disturbed, or simply give the operator/user time to gather his wits, before starting a real-time run.

The real-time run itself consists of a fixed number of iterations or frames, determined in advance from the user-specified control/sampling interval and total run time. Again, the Ada DELAY statement is employed to control the repetition interval (or frame time) in the standard textbook fashion. The VAX interval timer is used as the absolute timing reference for calculating the necessary delay time to the start of the next frame. No hardware interrupts are used.

One benefit of having computed the explicit value of the frame's "dead-time" (i.e. the unused time from the finish of the last frame's processing to the start of the next frame) is that it can be saved as part of the real-time run's dynamic data and displayed in a real-time screen plot or after the run. It is obviously very important that the dead-time always remain positive if the user-specified control/sampling frequency is to be kept constant and accurate. It is prudent to always check for this at the end of a run by plotting unused frame time vs. time.

The requirement to provide a 30 Hz. control/sampling interval (see 3.2.1.1) is not difficult for CONTROL to accomplish. However, in the worst case, i.e. when both the DAS and the SHAPES sensor are being used, at best only 10-15 ms. of the total frame time of 33 ms. can be made available to the experimental software algorithm. Thus, a successful 30 Hz. control experiment is heavily dependent on VAX processing speed, data acquisition speed, and control algorithm complexity.

Even though two of the experiment types are real-time oriented and the third is not, the use of a common calling format for all experimental subroutines has been entirely successful. CONTROL calls each of the three FORTRAN subroutines using the same set of CALL statement arguments.

It is obviously in the interest of the experimenter to get as much information as possible about the performance of his algorithms and the experiment results. With only 5 Mbyte of RAM totally available in the VAXstation (1.2 Mbyte of which is occupied by MicroVMS alone), some reasonable limit must be placed on the amount of RAM allocated for temporary

storage of dynamic data from the real-time run. The limit chosen was 800 K bytes, based on saving a maximum of 200 floating-pt. variables (4 bytes each) and a maximum of 1000 time samples for each variable. If the total number of real-time frames will not exceed 1000, then 200 sampled variables are buffered to RAM at the end of each frame (i.e. after the experimental subroutine is called and its SAVE_STATE vector is returned). However, if the maximum frame count does exceed 1000, CONTROL will automatically save the 200 samples in every other frame, or every third frame, etc., so that the total number of saved numbers does not exceed 200,000.

The set of 200 dynamic variables selected for storage during a real-time run is as follows:

1...50	System sensor measurements
51...70	System actuator commands
71...100	System software variables
101...200	Experiment software variables

Currently, only about half of this allocated storage capacity has been used. For example, only two of the 30 available system software slots are used -- one for the value of the independent variable, TIME, and one for the unused frame time.

A variation to this standard approach to data saving has been incorporated for the benefit of the static shape determination experiment software. Since this experiment does not run in real-time, except for sampled sensor data acquisition, its SAVE_STATE vector is not buffered to RAM during that real-time acquisition mode. And because its primary output is the shape of each structural rib, with up to 100 shape values for each of the 12 ribs, its SAVE_STATE output vector has been necessarily expanded to a length of 2741. The rib shape functions are then extracted from SAVE_STATE for display in the off-line mode of CONTROL's operation.

The system execution modes recognized by CONTROL, and activated by the user command 4-2, require some further explanation. First and foremost in terms of the computer system resources used is the REAL-TIME mode. It has already been described from the point of view of running experiments and performing all the functions shown in Figure 3.2-2. But, some of the functions can be bypassed for the purposes of test, and three submodes have been created to accomplish this.

One submode is the SENSOR TEST mode. With only this submode enabled (using command 4-2), real-time execution bypasses experiment subroutine calls completely (including initialization) and displays the current sampled value of each sensor numerically rather than graphically. Only actuator commands to apply zero force/torque are sent out through the DAS. This mode of real-time execution is useful for checking and calibrating sensor devices. However, the sampling frequency must be kept below 1 Hz. because of the relatively slow speed inherent in writing text to the screen in real-time.

Another submode is the ACTUATOR TEST mode. With only this submode enabled (using command 4-2), real-time execution again bypasses all experiment subroutine calls and displays a graphical plot of any one of the 200 available saved variables. (Of course, none of the experiment software's variables will

be of any interest.) In this mode, actuator test commands are enabled to drive the system. Depending on the user's previous commands, any actuator can be programmed to apply a constant level or a pulse of force/torque. And if a third submode, the SINE DRIVE mode, is enabled also, a sinusoidal test signal can be applied by any actuator. All actuator levels, pulse widths, sinusoid frequencies, and sinusoid amplitudes are user-selectable from commands 6-1, 6-2, and 6-3.

The two submodes SENSOR TEST and ACTUATOR TEST can be enabled simultaneously to both stimulate the actuators and get the real-time numerical sensor output display. The constraint on sampling frequency still applies however.

3.2.2.2.4 Data Acquisition. As indicated in Section 3.2.1.2, data transmission between the VAXstation and external devices (sensors and actuators) takes place via the MicroVAX II I/O bus (Q-bus). The decision to accommodate SHAPES sensor data acquisition from an IBM PC-AT using the IEEE-488 or General Purpose Interface Bus (GPIB) protocol required the use of a special Q-bus-to-GPIB interface and GPIB bus controller (the National Instruments GPIB11V-2 DMA board). The remainder of the system I/O is carried out by the DAS. The DAS designer, Vista Controls Corp., specified that the VAXstation's interface to the DAS should be a DEC DRV11-WA general purpose DMA 16-bit parallel digital interface board.

All of the sensor data acquisition functions that normally take place in a real-time experiment are executed at the start of the real-time frame. They are immediately followed by the actuator command outputs. This ensures that the measurement sampling as well as the control commands are as perfectly periodic and as nearly "simultaneous" as it is possible to make them. Further, the DAS functions and the SHAPES functions are independently enabled by user command 4-4, so that experiments need not operate with both types of I/O. Independent control also makes testing and timing of the separate DAS and SHAPES I/O functions much easier.

All of the raw incoming sensor measurement data must be converted to engineering units by the system software before passing it on to the experimental software. Likewise, the experimental software's commands to the actuators must also be converted from engineering units to binary counts before passing them on to the DAS. The engineering units used are milliradians (angular position), millimeters (linear position), Newtons (force), and Newton-meters (torque).

As a safety precaution, all actuators are commanded to apply zero force/torque immediately following a real-time run of any kind, except a static shape determination experiment. Since the DAS' digital-to-analog converters will hold an actuator command indefinitely, the zero command will remain in force until the next real-time run. One other safety precaution taken by the system software is to zero all actuator forces/torques whenever an error in VAXstation processing occurs, whenever a DAS I/O processing error is detected, or whenever a SHAPES data acquisition error is detected.

SHAPES data transmission to the VAXstation via the GPIB bus consists of 16 measurement samples, each formatted as a 32-bit (4 byte) floating-point variable in DEC F-format. Thus, 64 bytes are sent serially

down the GPIB bus by the IBM PC in response to the high-level "READ" function code issued from the VAXstation system software via the GPIB11V-2 bus controller. The data transmission mode is then ended by issuing a low-level "COMMAND" function from the VAX to place the IBM PC in the "un-talk" mode (i.e. unaddressed for talking), and the cycle is then repeated for each block of 64 bytes to be read. Initialization of the bus and SHAPES device is carried out at the beginning of each real-time run simply by activating the GPIB "TRIGGER" function, a high-level function call to the board driver software. SHAPES is switched off-line at the end of a real-time run using the GPIB "DEVICE CLEAR" command message.

Details of the DAS operation are discussed in the next section of this report. However, highlights of the data interface with the VAXstation are touched on here from the point-of-view of the system software. The DAS' several functions, including RESET, STATUS, BLOCK SAMPLE, BLOCK OUTPUT, and DIAGNOSTIC are commanded from the system software by sending a 3-bit code as part of the SYSSQIOW call.

The combined execution time on the VAX of the DAS BLOCK SAMPLE and BLOCK OUTPUT function pair was specified in the DAS performance requirements as 8 ms. (including VMS handling of the QIO request, MACRO driver execution, and DAS processing). Based on measurements taken by the utility program TIME_DAS, this was just barely achieved. The read/write function pair was executed 1000 times in a loop with the total execution time of exactly 8 seconds.

The DAS BLOCK SAMPLE function always returns 30 16-bit words to the VAX. Of these, 24 are rib levitator encoder measurements, accumulated in digital counters and delivered in the form of 2s complement binary words. The remaining 6 measurements are analog signals converted to digital offset binary form; they must therefore be further transformed to a usable 2's complement binary form by the FORTRAN subroutine, READ_DAS.

The DAS BLOCK OUTPUT function accepts 14 actuator commands in the form of 2s complement integers (16-bit) from the VAX and passes these to a 12-bit (plus sign) digital-to-analog converter. Thus, the system software automatically limits these outputs to absolute values less than 2048.

All sensor measurements supplied by SHAPES or by the DAS are not only subject to unit conversion (i.e. scaling) by the system software, but can also be biased. The default values used by the system software for measurement or command scale factors as well as sensor input biases can all be modified by exercising user commands 6-4, 6-5, 6-6, 6-7, and 6-8.

3.2.2.2.5 Diagnostics. Program DEMO provides diagnostic information (i.e. error messages, error codes, error counts, status flags, etc.) concerning several types of execution errors. These error types are:

- o I/O errors
- o User command input errors
- o Standard VAX Ada exceptions
- o Experimental software's internal errors

The FORTRAN subroutines developed by experimenters generally take advantage of the opportunity provided by the standard call statement argument, STATUS. The experimenters have used at least 8 or more of the Boolean elements in the STATUS vector, to pass error status indicators back to the calling subprogram, CONTROL. For the most part, the flags are used to signal errors in the number or value of various parameters being input to the experimental software by CONTROL (i.e. by the user) or by external disk files. In some cases, an error flag is used to signal an estimation or search algorithm's failure to converge. Error flags are also used to signal various disk file access errors. Whatever the purpose of the error flag, its TRUE or FALSE value is displayed in the STATUS window of the VAXstation's graphics display monitor. However, since the STATUS display is not updated during the real-time mode, real-time execution errors can only be seen there after the run has concluded.

In order to handle other run-time or execution errors that the VAX system would normally detect, i.e. rather serious errors that cause interruption of the expected execution paths, six exception handlers are installed at the end of task CONTROL. Five of these handlers are designed to recognize the 5 standard Ada predefined exceptions:

- o NUMERIC_ERROR
- o CONSTRAINT_ERROR
- o PROGRAM_ERROR
- o STORAGE_ERROR
- o TASKING_ERROR

and in each case, the handler will issue an error-identifying message, zero all actuator forces and torques, and finally exit the task CONTROL. The sixth exception handler is included to handle all other system-detected errors, and its response is the same -- error message, zero forces/torques, and exit CONTROL. Exiting CONTROL means DEMO cannot restart CONTROL, and the entire program must be stopped and restarted from scratch (hopefully after the problem has been fixed).

Another very likely error source are the commands (i.e. menu selections and parameter values) typed in by the user at the VAXstation keyboard. These errors are detected at the very lowest level, i.e. in the module that is designed to accept the required character type, by using a "catchall" exception handler. When any kind of error occurs, the handler prints the short message "ERROR" and exits the routine, thus causing a return to the next highest menu level. This allows the user another chance at making a correct input.

By far, the bulk of the error diagnostic software designed into program DEMO is devoted to I/O operations, i.e. DAS and SHAPES I/O. For both types of I/O, the approach used is to detect the error at the lowest program level and then pass an error-identifying code to the high-level program element which is using that particular I/O function. This code can then be used to trigger the appropriate actions. In the case of SHAPES I/O, three functions are called from the task CONTROL -- START, READ, and STOP. Since START and READ are embedded in the real-time loop, any errors diagnosed in these operations are used to first issue an error message (to the screen), including the error code value for identification. The real-time loop is then immediately exited, thus aborting the run and returning to the off-line or

command mode. The STOP function error case only issues a screen message, since it is only called at the end of a real-time run.

For the case of DAS I/O, the approach is much the same, although 6 functions are called from CONTROL -- READ, WRITE, STARTUP, STATUS, DIAGNOSE, and CALIBRATE. In those instances where the function is embedded in the real-time loop (READ, WRITE), the programmed response to DAS I/O errors is to exit and thereby abort the real-time loop. The additional programmed response to all DAS I/O function errors is to simply record the error type and count it. No DAS I/O error messages are ever generated. The DAS error types and the error count are displayed, however, in the STATUS window of the graphics display monitor. Only one error count is maintained for all the DAS function types, but an error type indicator is used for each function type. When necessary, the user can clear all DAS I/O error indicators (including the count) to zero by using command 6-9.

3.2.2.2.6 Display Features. A major portion of DEMO is concerned with the display of system information in textual or graphical form on the VAXstation monitor. The task of implementing such displays is made relatively easy by virtue of the VAXstation II's Workstation Software, a graphics package included with the MicroVMS operating system software. This software provides a graphics interface to the user for creating and manipulating windows, displaying multiple styles and sizes of text, receiving input, and drawing graphics objects in the created windows. All of this can be accomplished by calling a variety of routines in the User Interface Services (UIS) graphics software package. And all of these callable UIS routines can be accessed from a high-level programming language -- FORTRAN in our case.

The standard screen layout used by DEMO on the 11x14 inch landscape monitor is sketched in Figure 3.2-3. Three non-overlapping windows are placed on the screen. In the upper left-hand corner is the terminal window, emulating a DEC VT100 terminal. The VT100 window is of course also used when DEMO is not executing, for example for file editing or for any other usual VAXstation terminal functions. While DEMO is executing, however, the VT100 window is used to display user command menus, keyboard input, and error messages in a scrolled (bottom-up) manner.

Figure 3.2-4 shows DEMO's main menu. If, for example, selection 9 -- SYSTEM HARDWARE CHECKOUT -- is chosen, the menu of Figure 3.2-5 scrolls up into Window #1. And if selection 4 -- DEVICE SCALE FACTORS -- is chosen, the parameter table shown in Figure 3.2-6 appears with a prompt to choose one of the list of 12 for updating. The MIN and MAX columns are intended to remind the user of any constraints imposed on the range of a particular parameter's values. After a new value is entered, the entire list is displayed again to show the new value.

Window #2 of the screen layout shown in Figure 3.2-3 is used exclusively for displaying the status of the program. The window's display space is divided evenly between the system software's status and the experimental software's status. And each of these status tables are divided evenly between floating-pt. variables and Boolean variables (8 each). An example of a status display window is shown in Figure 3.2-7.

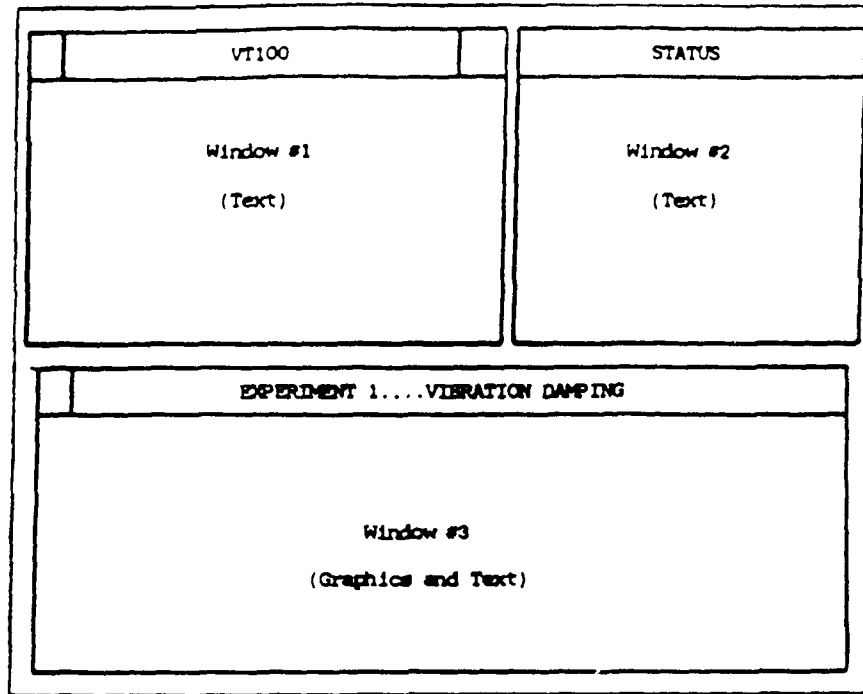


Figure 3.2-3 DEMO Display Screen Layout

```

*****
*
*   WELCOME TO THE CONTROL TECHNOLOGY   *
*   DEMONSTRATION PROGRAM               *
*
*****

Main Menu:
-----

0....EXIT
1....EXPERIMENT #1 -- VIBRATION CONTROL
2....EXPERIMENT #2 -- STATIC SHAPE DETERMINATION
3....EXPERIMENT #3 -- ADAPTIVE CONTROL
4....UNUSED
5....UNUSED
6....UNUSED
7....SYSTEM EXECUTION CONTROL
8....DATA DISPLAY CONTROL
9....SYSTEM HARDWARE CHECKOUT

SELECTION ==>

```

Figure 3.2-4 Main Menu

```

*****
*                                     *
*                               HARDWARE CHECKOUT                               *
*                                     *
*****

```

Command parameter change menu:

- ```

0....EXIT
1....HUB GIMBAL TORQUE
2....RIB ROOT FORCE
3....HUB/RIB TEST PARAMETERS
4....DEVICE SCALE FACTORS
5....SHAPES SENSOR BIAS CONTROL
6....LEVITATOR SENSOR BIAS CONTROL
7....RIB SENSOR BIAS CONTROL
8....HUB SENSOR BIAS CONTROL
9....DAS CHECKOUT COMMANDS

```

SELECTION ==> █

Figure 3.2-5 Hardware Checkout Menu

| INDEX | NAME                | UNITS      | MIN         | MAX         | VALUE        |
|-------|---------------------|------------|-------------|-------------|--------------|
| ----  | ----                | -----      | ---         | ---         | -----        |
| 1     | SHAPES SCALE FACTOR | (mm/bit)   | 0.00000E+00 | 0.00000E+00 | 1.00000E+00  |
| 2     | HS1 SENSOR SCALE    | (mrad/bit) | 0.00000E+00 | 0.00000E+00 | -7.65000E-02 |
| 3     | HS10 SENSOR SCALE   | (mrad/bit) | 0.00000E+00 | 0.00000E+00 | 7.26000E-02  |
| 4     | RIB SENSOR SCALE    | (mm/bit)   | 0.00000E+00 | 0.00000E+00 | -1.55500E-03 |
| 5     | LEV SENSOR SCALE    | (mm/bit)   | 0.00000E+00 | 0.00000E+00 | 2.66000E-01  |
| 6     | HA10 ACTUATOR SCALE | (bits/N-m) | 0.00000E+00 | 0.00000E+00 | -5.04800E+02 |
| 7     | HA1 ACTUATOR SCALE  | (bits/N-m) | 0.00000E+00 | 0.00000E+00 | -1.05600E+02 |
| 8     | RIB ACTUATOR SCALE  | (bits/N)   | 0.00000E+00 | 0.00000E+00 | -2.04700E+03 |
| 9     | LEV POSITION LIMIT  | (mm)       | 0.00000E+00 | 1.00000E+02 | 1.00000E+04  |
| 10    | HUB POSITION LIMIT  | (mrad)     | 0.00000E+00 | 7.00000E+01 | 1.00000E+04  |
| 11    | RIB POSITION LIMIT  | (rad)      | 0.00000E+00 | 7.00000E+01 | 1.00000E+04  |
| 12    | D/A CONVERT. LIMIT  | (bits)     | 0.00000E+00 | 2.04700E+03 | 2.04700E+03  |

ENTER INDEX OF PARAMETER TO BE UPDATED (0=exit) ==> █

Figure 3.2-6 Scale Factor Parameter Table

| SYSTEM       |   |          |                  |
|--------------|---|----------|------------------|
| interval     | = | 0.100    | realtim_go = F   |
| max_time     | = | 100.000  | encoder_cal = F  |
| max_count    | = | 1001.000 | actuatr_test = F |
| print_intrvl | = | 1.000    | sensor_test = F  |
| save_intrvl  | = | 0.100    | sin_drive_on = F |
| i/o_errors   | = | 0.000    | actuators_on = T |
| experiment   | = | 1.000    | DAS_io_on = F    |
| cmd_count    | = | 0.000    | SHAPES_io_on = F |
| EXPERIMENT   |   |          |                  |
| Control mode | = | 1.000    | Error = F        |
| Converg time | = | 0.000    | File error = F   |
| HA10 disturb | = | 0.000    | Order error = F  |
| HA1 disturb  | = | 0.000    | Illegal i.c. = F |
| RA1 disturb  | = | 0.000    | Save variabl = F |
| RA2 disturb  | = | 0.000    | I/O number = F   |
| RA3 disturb  | = | 0.000    | I/O item = F     |
| RA4 disturb  | = | 0.000    | Actuator lim = F |

Figure 3.2-7 Status Display

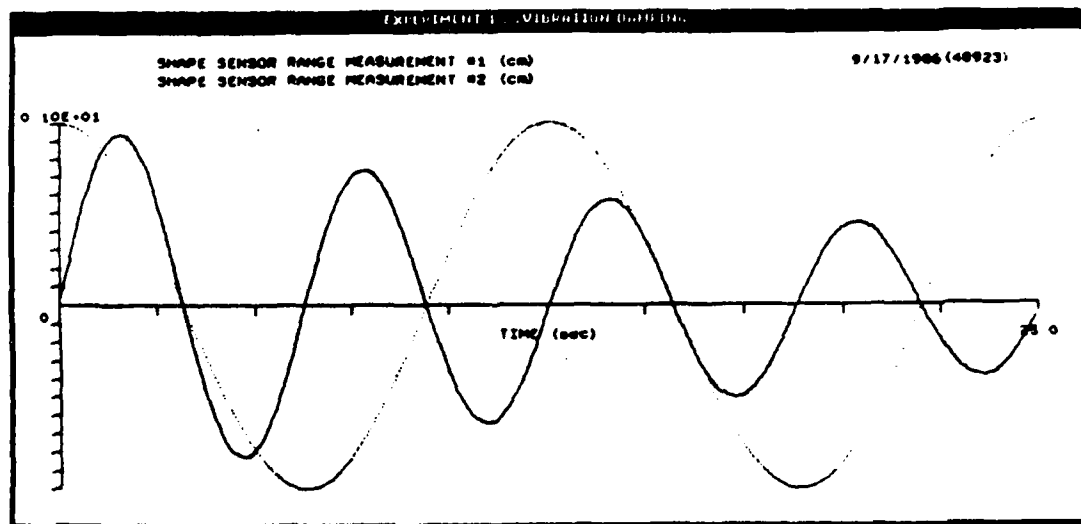


Figure 3.2-8 Real-Time Plot of Sensor Outputs

A quick glance at the status window can tell the user about the on/off state of the major execution and functional modes of the program, the real-time mode's timing parameters, which experiment is on call, and whether any I/O errors have occurred. With respect to the experiment, the Booleans are generally used to indicate internal errors, and the floating pt. variables can show operating mode, convergence time, and input disturbance levels, as shown in the example. The status display is also paged so that the user can call an additional 32 variables (per page) to the screen for as many pages as he wishes to define. User command 5-8 changes the status page.

Window #3 of the screen layout is used primarily for graphical display of experiment results, either in the real-time mode or in the off-line mode. Typically system variables are plotted vs. time as shown in Figure 3.2-8, which is a plot of simulated SHAPES sensor range measurements made during a real-time run. This example of a window display shows the window header with an experiment title. In a real-time run, two variables can be plotted simultaneously vs. time, while in the off-line mode, only one variable is plotted. In either case, the vertical scale can be set by user command 5-1, and any one (or two in real-time) of the 200 possible variables defined in the Save Table can be selected for plotting using command 5-4. The variables chosen are listed by name at the top of the window. If two variables are being plotted, they share the plot scale selected for the first (which is listed on top). The solid-line curve is the first variable, and the dotted-line curve is the second. Note also the text in the upper right-hand corner of the window, which shows the date and, in parentheses, the number of seconds since midnight when this real-time run started. The latter acts as an effective run identifier, and all plots or printouts of a particular run's results will have this same number attached to it.

Figure 3.2-9 shows the response at the inner and outer levitators of rib #1 to an impulse applied to the boom of the system. Some nonlinear effects are in evidence from one of the levitator weights hitting a mechanical stop. This particular test did not include rib ties, and the impulse was delivered by manually striking the short boom's tip weight.

As an example of using Window #3 for displaying text, Figure 3.2-10 shows the display used for the SENSOR TEST mode. In this mode, real-time sampling of the sensors takes place at a slow rate so that the sample values can be displayed as numerical text and be easily read. In the example shown in Figure 3.2-10, the SHAPES sensor was not operative. Units are not shown since it is understood that levitator and rib-root measurements are in millimeters, and hub gibal angles are in milliradians.

One other significant display feature is the strip chart, which can be activated by user command 5-3. In this display mode, six windows, each containing a time plot of a single variable, are stacked on top of one another to cover the entire screen. The window headers and borders are removed to give an appearance similar to that of a strip-chart recorder's. The format of each window is exactly the same as in Figure 3.2- , and the six variables chosen for plotting (in real-time or off-line) are input through user command 5-5.

Another slight variation of the single time-plot display window is used for plotting rib shape profiles. In this case the independent variable

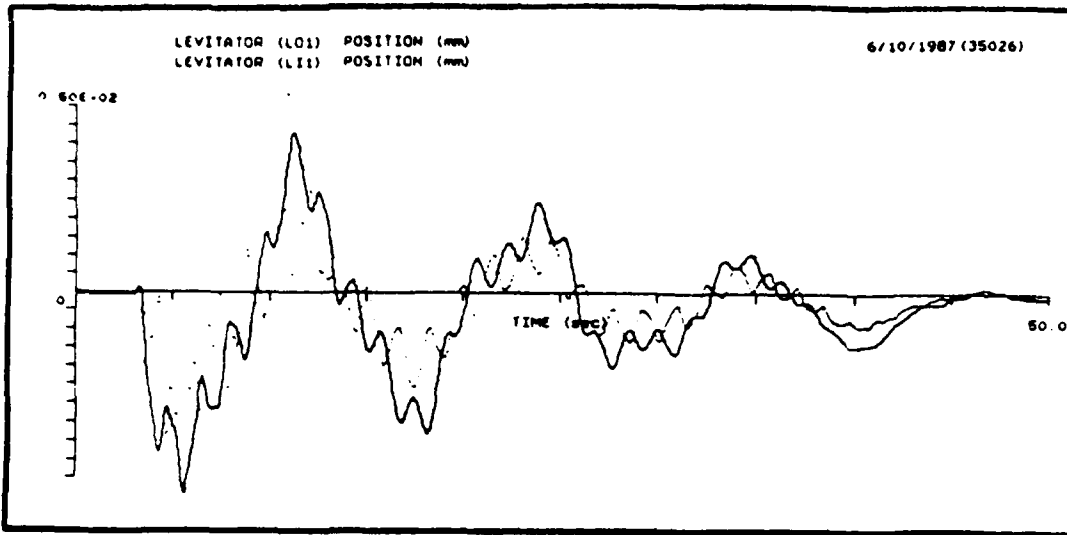


Figure 3.2-9 System Impulse Response

| SENSOR STATES |        |           |         |
|---------------|--------|-----------|---------|
| SHAPES        |        | LEVITATOR |         |
| 1.....        | 0.000  | 9.....    | 0.000   |
| 2.....        | 0.000  | 10.....   | 0.000   |
| 3.....        | 0.000  | 11.....   | 0.000   |
| 4.....        | 0.000  | 12.....   | 0.000   |
| 5.....        | 0.000  | 13.....   | 0.000   |
| 6.....        | 0.000  | 14.....   | 0.000   |
| 7.....        | 0.000  | 15.....   | 0.000   |
| 8.....        | 0.000  | 16.....   | 0.000   |
| MODE SIGNAL   |        | RIB ROOT  |         |
| MS1.....      | -3.136 | RS1.....  | -1.140  |
| MS10.....     | 12.996 | RS4.....  | -1.499  |
|               |        | RS7.....  | -1.662  |
|               |        | RS10..... | -2.026  |
| LI1.....      | 0.000  | LO1.....  | 2.660   |
| LI2.....      | -6.064 | LO2.....  | -9.044  |
| LI3.....      | -8.320 | LO3.....  | -11.970 |
| LI4.....      | -7.448 | LO4.....  | -14.630 |
| LI5.....      | -6.384 | LO5.....  | -12.236 |
| LI6.....      | -3.468 | LO6.....  | -9.676  |
| LI7.....      | -0.632 | LO7.....  | -1.862  |
| LI8.....      | 2.660  | LO8.....  | 5.320   |
| LI9.....      | 6.660  | LO9.....  | 10.640  |
| LI10.....     | 6.660  | LO10..... | 13.832  |
| LI11.....     | 6.384  | LO11..... | 14.364  |
| LI12.....     | 3.468  | LO12..... | 7.448   |

Figure 3.2-10 Sensor Test



plotted on the horizontal axis is distance (along the rib) from the hub, rather than time.

All the screen graphics displays can be copied to the dot-matrix printer. The VAXstation mouse is used to select the screen copying option from a menu and is also used to outline the portion of the window that is to be copied. Each copy takes approximately 2-3 minutes, depending on the amount of detail in the picture. A copy cannot be made of more than one window's contents at a time.

### 3.3 DATA ACQUISITION SYSTEM (DAS)

#### 3.3.1 Introduction

The primary functions of the DAS are to sample the sensors and to send commands to the actuators under MicroVAX II control. Upon receipt of a command by the MicroVAX II, the DAS first samples the sensors and passes these data back to the MicroVAX, and then sends drive signals computed in the previous time frame to the actuators. A block diagram of the system architecture is shown in Figure 3.3-1. The Digital Equipment Corporation (DEC) VAXstation II (MicroVAX II) computer has authority over all system operations.

The DAS hardware and software, including all sensor and actuator power supplies and cabling, were designed, fabricated, installed and tested as a complete system to JPL specifications by Vista Controls Corporation of Valencia, CA. The STD bus computer system is employed in the DAS and all subsystem electronics are assembled on boards that slide into the STD bus card cages which are installed and interwired in a custom designed rack. The system contains sufficient volume, power, cooling and connector cutouts to support expansion of data acquisition and command channels by 30% of the number currently installed. The DAS software is also capable of accommodating these additional I/O channels.

#### 3.3.2 Interfaces

3.3.2.1 Computer Interface. A 16-bit parallel interface standard is used for communication between the DAS and the DEC MicroVAX II. This is accomplished using a DEC DRV 11-WA interface board plugged into the DEC MicroVAX and cabled to the DAS. All data passed between the DAS and the MicroVAX is transmitted in a format consistent with the DRV 11-WA 16-bit (data) parallel interface hardware and with the standard 22-bit DEC Q-bus of the MicroVAX.

3.3.2.2 Sensor Interfaces. There are 24 12-bit optical position encoders, 4 linear position (LVDT) sensors and 2 angular position (RVDT) sensors. The optical encoders are of the incremental type, which requires that the DAS contain up-down counters (in hardware) for each of the encoders. In order to establish an absolute reference when required by the experiments, the experiment structure is driven through a motion routine that ensures that each

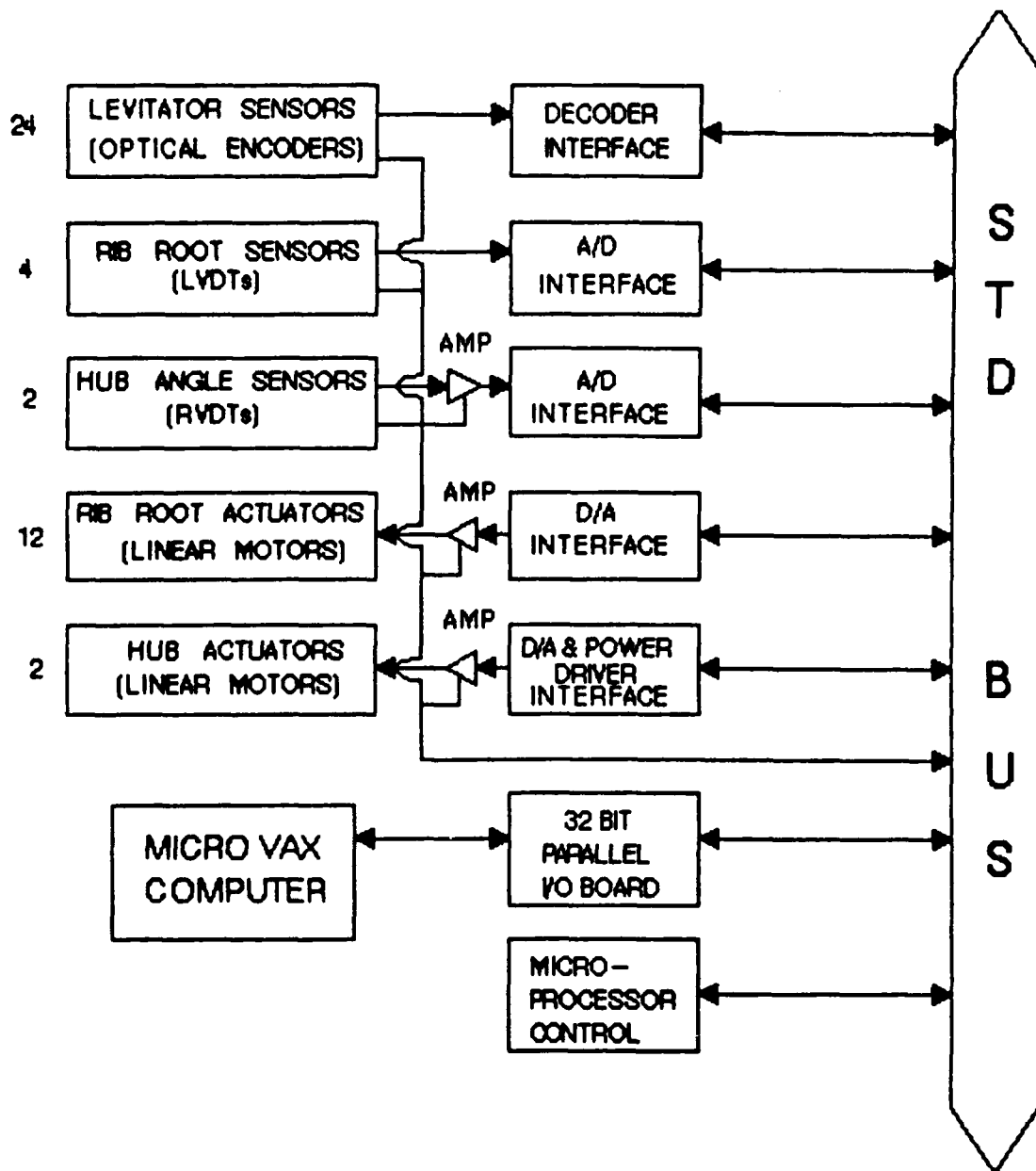


Figure 3.3-1 Data Acquisition System Block Diagram

encoder passes through an index position which provides a marker pulse to the DAS. The DAS monitors the indexing routine and sends a pass/fail status word to the MicroVAX. The LVDT and RVDT sensors are self contained with their own internal electronics for generating excitation carriers and demodulating sensor signals to provide low impedance d.c. analog output voltages. However, because the RVDTs operate over very small portions of their maximum ranges, in-line output voltage amplifiers (x10) are mounted in the electronics packages. The DAS A/D converters process the LVDT and RVDT outputs to digital signals. The DAS also provides  $\pm 12$  volt excitation power to the analog sensors and +5 volt power to the optical encoders.

3.3.2.3 Actuator Interfaces. The fourteen force actuators mounted on the experiment structure are all controlled through DAS current drivers. Twelve of these actuators are rib-root actuators which require analog drive currents of  $\pm 300$  ma. at  $\pm 24$  volts to produce maximum rated force outputs. The other two are hub actuators which are linear motors of a different design that require analog drive currents of  $\pm 150$  ma. at  $\pm 24$  volts to produce rated outputs. The DAS driver amplifiers utilize current feedback loops to maintain accurate drive levels independent of temperature effects on actuator coil resistances, and to minimize the force-current time constant.

3.3.2.4 DAS-Sensor/Actuator Cabling. Individual cables connect each sensor and actuator to the DAS. Each cable contains excitation and signal wires with appropriate ground wires and shielding, and mates with its individual connector at the DAS rear panel. All cables and connectors have identification tags on each mating connector. While connector type and indexing does not preclude mis-mating sensors or actuators of the same type, it is not possible to mis-mate cables to transducers of different types.

### 3.3.3 Timing Specifications

Figure 3.3-2 is a time line which shows a typical data acquisition cycle. The sequence for reading the 30 sensors proceeds as follows. First, the MicroVAX II sends a command to the DAS telling it to start sensing. Upon receipt of this command, the DAS samples all the sensors and sends the sensor data back to the MicroVAX II. The total time for sensing, including the command to the DAS, is approximately 4 ms.

The sequence for sending signals to the 14 actuators proceeds similarly. First, the MicroVAX II sends a command to the DAS, this time telling it to prepare to receive actuator data. When the DAS is ready, the MicroVAX II transmits these data to the DAS which in turn converts them to the proper signal levels for the actuators. Total time for actuation including the command from the MicroVAX is approximately 4 ms.

The MicroVAX is preoccupied with other computations associated with the individual control demonstrations and is not available for DAS processing at all other times.

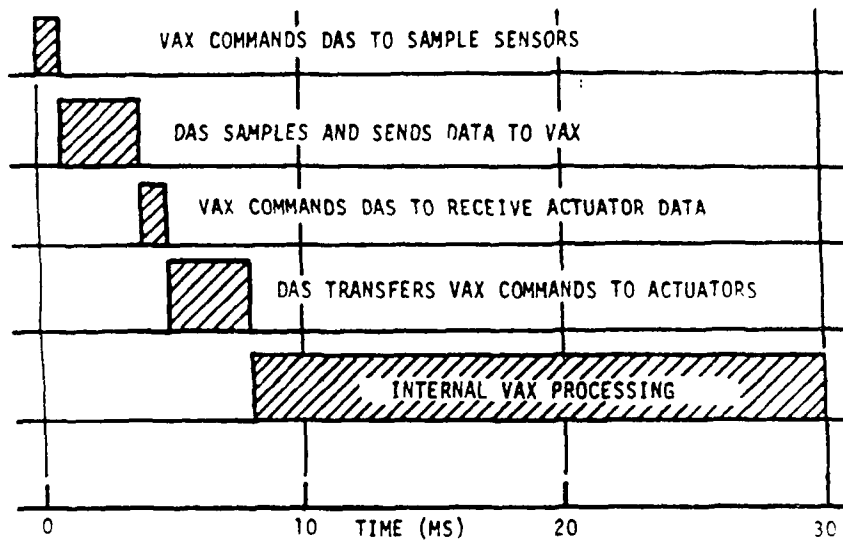


Figure 3.3-2 Time Line

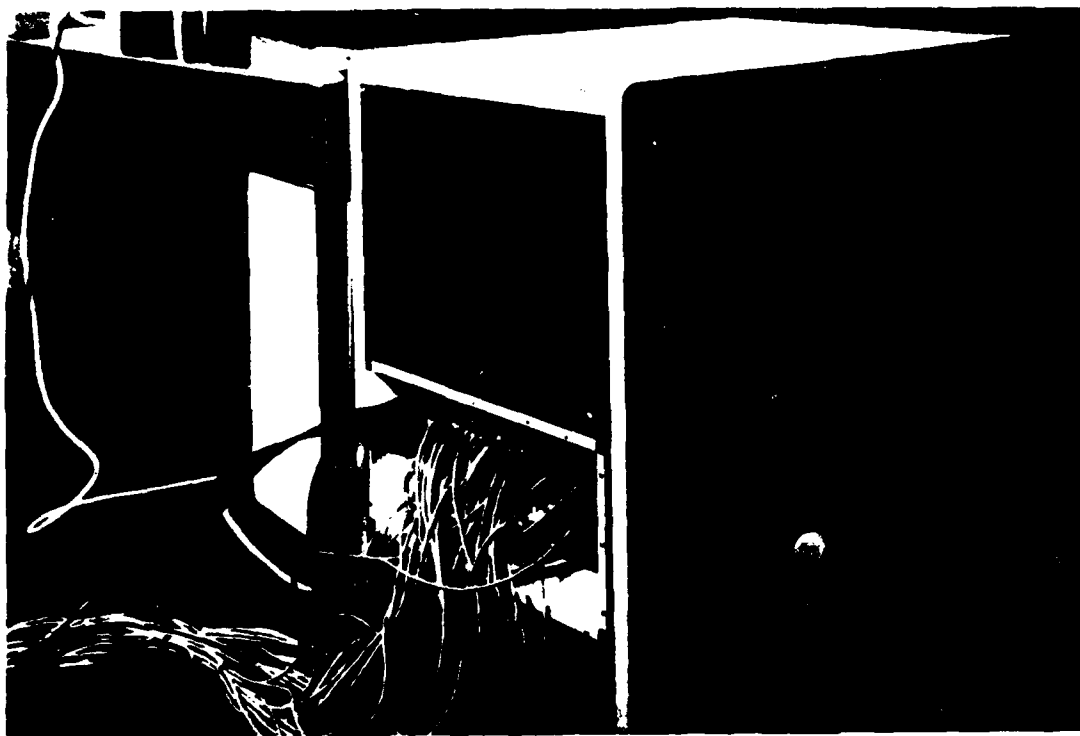


Figure 3.3-3 DAS Cabinet - Rear View

### 3.3.4 Hardware

The data acquisition system is assembled using STD bus computer modules mounted in a custom cabinet with power supplies for operating all transducers as well as the DAS components. Sufficient cooling is provided to permit continuous operation of all drivers at maximum specified power. The system components are installed in a standard 30 in. high floor cabinet with all transducer cable connectors mounted in the rear hinged door. All system cards, power supplies and intercabling are accessible through the rear door. A rear view photograph of the DAS is shown in Figure 3.3-3. Brief descriptions of the system components are given below.

3.3.4.1 DAS Controller Card. The DAS controller is an Octagon 880 multi-function CPU manufactured by Octagon Systems Corporation of Westminster, CO. The Octagon 880 uses the Intel 8088 microprocessor with an eight-level interrupt priority controller, 16 parallel I/O channels, and five 8-bit counters (useful for counting, timing and signal generation). It contains embedded ROBASIC language. The 880 board controls all other boards in the STD computer system.

3.3.4.2 Encoder Cards. Each of the 12 Amtek STD 2500 optical encoder cards decode two quadrature incremental optical encoders. The cards receive A and B phase pulses and an index pulse from each encoder. Counters are included on these cards to calculate velocity and position information.

3.3.4.3 Analog-to-Digital Converter Cards. Three Amtek STD 2200 LVDT/RVDT cards are used to convert the  $\pm 5$  volt rib root and hub sensor analog outputs to 12-bit digital signals. The card accepts eight separate analog inputs and multiplexes them into a single A/D converter.

3.3.4.4 Power Driver Cards. Seven dual channel Amtek STD 1200 power driver cards convert VAX digital actuator commands to  $\pm 500$  ma analog current drives for the hub and rib root actuators. The cards operate from a  $\pm 24$  volt source and employ current feedback to maintain current scale factor calibration independent of thermally induced load resistance variations. The cards include adjustable current limiters for each channel.

3.3.4.5 Parallel I/O Card. A Prolog parallel I/O card is employed to enable 32-bit (16-bit input and 16-bit output) communication using the DRV11-WA protocol standard. This card is used as a communication link between the STD bus computer system and the DEC MicroVAX II computer system.

3.3.4.6 System Power Supplies. The DAS system includes four separate power supplies for supplying d.c. voltages to the STD bus boards and sensors mounted on the experiment structure. A 5 volt supply provides all power to the DAS computer components and optical encoders. A dual  $\pm 12$  volt supply provides d.c. excitation voltage to the LVDT rib-root and RVDT hub sensors. Separate 24 volt, 12 ampere d.c. supplies are ganged to provide  $\pm 24$  volt actuator drive power.

### 3.3.5 Software

The DAS software consists of a program set residing in Octagon 880 CPU memory. These programs are stored in EPROM and execute automatically in response to a POWER ON RESET condition.

The 880 includes a high-level, multi-tasking language called ROBASIC and its supporting operating system in 64K of on-board ROM. For peripheral I/O, the 880 is compatible with the STD Bus and allows 64K of STD Bus memory space. In addition, 64K of user EPROM space is available on the CPU board.

The DAS program set is comprised of a main program written in ROBASIC and a collection of subprograms written in 880 assembly language. The ROBASIC program can perform all of the real-time and off-line DAS functions as well as interact with a terminal user (for the purposes of development and test) by generating menus, displaying I/O data and control signals at the bit level, and showing diagnostic messages. When a terminal is not connected to the 880 (i.e., during normal operational use of the DAS), the assembly language subprograms are called from the ROBASIC main program to execute the DAS' real-time Block Sample and Block Output functions at the maximum possible speed.

Eight different DAS functions can be commanded by the MicroVAX II. These are:

- o Reset
- o Block Sample
- o Block Output
- o Status
- o Diagnostic
- o Block Sample (calibration)
- o Block Output (calibration)
- o Calibrate

The ROBASIC program that implements these functions as well as the interactive terminal functions consists of 600 source code lines (including comments). The assembly language routines that execute the Block Sample and Block Output functions total 370 lines (including comments).

- o RESET

Upon detection of the Reset command from the MicroVAX, the DAS is initialized to a known state and ready condition. All actuator command outputs are set to zero, all optical encoder counts are set to zero, internal software constants and parameters are reset to their default values, and the read-only memory contents are checksummed (if not already done previously). This function is also activated in response to a system power-up. The total time required for this activity is 1 second.

- o BLOCK SAMPLE

Upon receipt of the Block Sample command from the MicroVAX, the DAS samples all the digital encoder output counters (24), and then samples (using a single A-D converter) the analog signals coming from the Rib Root sensors (4) and Hub angle sensors (2). These 30 16-bit words are passed to the MicroVAX via the DRV11-WA DMA interface board, with the DAS software handling the interface control protocol. The total time allotted for this function (including VMS and DRV11-WA software driver overhead) is 4 msec.

- o BLOCK OUTPUT

The Block Output command from the MicroVAX causes 14 actuator command words (16-bits each) to be passed via the DRV11-WA interface controller to the DAS. These include the 12 rib-root actuator commands and the inner and outer hub gimbal actuator commands. Actuator command inputs are applied using D/A converters supplemented by power driver electronics. The total time allotted for this function (including VMS and DRV11-WA software driver overhead) is 4 msec.

- o STATUS

For each buffer of data transferred between the MicroVAX and the DAS (via the 16-bit input and output data registers), the DRV11-WA driver software allows for the exchange of an additional 6 bits of information (via the Control/Status Register). Three of these bits are the so-called FUNCTION bits and are used to transmit the MicroVAX's command for one of the eight possible DAS functions. The other three bits, called the STATUS bits, are accessible to the DAS for transmitting coded status information back to the MicroVAX upon the completion of all transfers. (Neither the VAX/VMS operating system nor the DRV11-WA modifies the FUNCTION and STATUS bits in any way. Both 3-bit fields are defined solely to suit the DAS functional requirements.)

Only two of the 3 available STATUS bits are defined for use by the DAS. The most significant bit (STATUS A) is used to signal a DAS system failure, i.e., a bad checksum of the read-only memory. Another bit (STATUS B) is used to indicate a failure in the command interface with the MicroVAX (e.g., if an unrecognized command is received). All 3 bits are normally set to "1", so that when the Status command is issued by the MicroVAX, the returned 3-bit status word with no indicated errors will read as a '7' when interpreted as an unsigned binary number.

- o DIAGNOSTIC

Upon detection of the Diagnostic command from the MicroVAX, the DAS will perform a checksum of the entire fixed portion of the DAS system software residing in EPROM (i.e., instructions and

fixed data). The results of this diagnostic can be obtained by requesting the Status function at least 10 seconds after the Diagnostic command was sent.

o BLOCK SAMPLE (CALIBRATION) - BLOCK OUTPUT (CALIBRATION)

If the DAS user is only interested in obtaining a relative frame of reference for the measurements taken by the rib levitators' optical encoders, then the Block Sample and Block Output functions described previously should be used as pairs in any real-time sequence. The zero position reference would be established by commanding the Reset function at the appropriate time before the real-time experiment.

On the other hand, if an absolute frame of reference for these position measurements is needed, the user can instruct the DAS to zero the position counters only when a special index mark (etched onto the encoder wheel) rotates past the sensor. This is accomplished from the MicroVAX by using the Block Sample (Calibration) and Block Output (Calibration) function commands as pairs in a real-time sequence. (Of course, in this case, the Reset function should not be used.)

o CALIBRATION

The final function provided by the DAS allows the results of the attempts to establish absolute reference frames for all 24 levitator encoders to be seen. When the DAS receives this command, it returns two 16-bit calibration status words to the MicroVAX, each of which shows 12 bits (4 bits not used) representing the pass/fail status of 12 encoder devices. A zero value indicates an encoder that did not pass through the zero-position index mark.

### 3.4 SPATIAL, HIGH-ACCURACY, POSITION-ENCODING SENSOR (SHAPES)

SHAPES is an optoelectronic range sensor that is capable of ranging to a number of moving targets simultaneously with submillimeter accuracy. SHAPES makes use of a streak tube camera to determine range from time-of-flight correlations of short optical pulses returned from retroreflector targets. Target illumination is provided by semiconductor laser diodes that are pulsed at a rate of  $10^8$  pulses per second and produce pulses with a duration of about 35 ps. A common 100 MHz sinusoidal signal is used to time the laser pulsing and to drive the streak tube deflection plates in "Synchroscan" mode. The streak tube output, from which the range data is derived, is recorded on a CCD detector. The CCD readout is accomplished by means of custom electronics that offer a number of options for the data processing. The CCD output is collected by a microcomputer which calculates the target position and then transmits the data to the Control Technology Facility Vax computer in real-time.

In its present configuration, SHAPES is capable of obtaining and transmitting range data from 16 targets at a data update rate of 10 Hz.



### 3.4.1 Operating Principle

Figure 3.4-1 is a schematic that demonstrates the SHAPES operating principle. The optical pulses returned from each target are collected by a camera lens and focused onto the streak tube photocathode. The photoelectrons produced by each pulse are accelerated away from the photocathode by a high voltage grid and, at zero deflection plate voltage, focused to a unique spot on the phosphor screen by focusing electrodes. The fluorescence produced at the phosphor screen by the impinging electron packets become, in turn, an optical source which is then focused onto a CCD detector by a transfer lens. With zero drive voltage applied to the deflection plates, the scene on the photocathode is imaged on the phosphor screen in a manner analogous to optical imaging.

When the sinusoidal streak tube drive voltage is turned on, the photoelectron packet produced by each return optical pulse is deflected by an amount determined by the instantaneous voltage on the deflection plate. Because the drive voltage is synchronized with the laser pulsing, the range may be inferred from the amount of the deflection. Thus, the measurement of the time-of-flight is replaced by a measurement of distance on the CCD. A necessary adjunct to this scheme is the use of a second, reference retroreflector target placed at a known range. The location of the reference image on the CCD serves to establish the relation between range and the phase of the streak tube drive voltage.

3.4.1.1 Signal Averaging. The targets are typically illuminated for a period of about 10 ms during each data acquisition (framing) period. This means that about  $10^6$  pulses are collected during each exposure. As noted above, the streak tube drive and the laser pulsing are synchronized; therefore, the deflection plate voltage is exactly the same as each succeeding pulse is returned from a stationary (or slow moving) target. Consequently, each photoelectron packet strikes the screen at the same point and the effect is to average  $10^6$  pulses and thereby essentially eliminate the effect of laser firing jitter on the spot centroid.

3.4.1.2 Range Ambiguities. Because there are a number of pulses in the optical path at any time, there is an ambiguity associated with the range measurement. At an operating frequency of 100 MHz, the pulses emitted from each laser diode are separated by 3m as indicated in Figure 3.4-1. This means that the pulses returned from two targets separated by 1.5m (and illuminated by a common laser) would arrive at the sensor at the same time. Furthermore, because the amount by which the electron packet is deflected is double-valued during each drive period (one cannot tell if a spot was produced during the positive-going or the negative-going portion of the drive waveform), the results are ambiguous unless the targets are constrained to move no more than  $\pm 37.5$  cm from a known position. Fortunately, the target motion of all targets of the present experiments is limited to about  $\pm 5$  cm from a nominal position.

3.4.1.3 Maximum Number of Targets. The maximum number of targets that can be viewed simultaneously depends on the spot size of target image on the CCD and the size of the CCD. To see this, consider that the CCD is oriented with its rows (and serial register) parallel to the streak tube sweep direction.

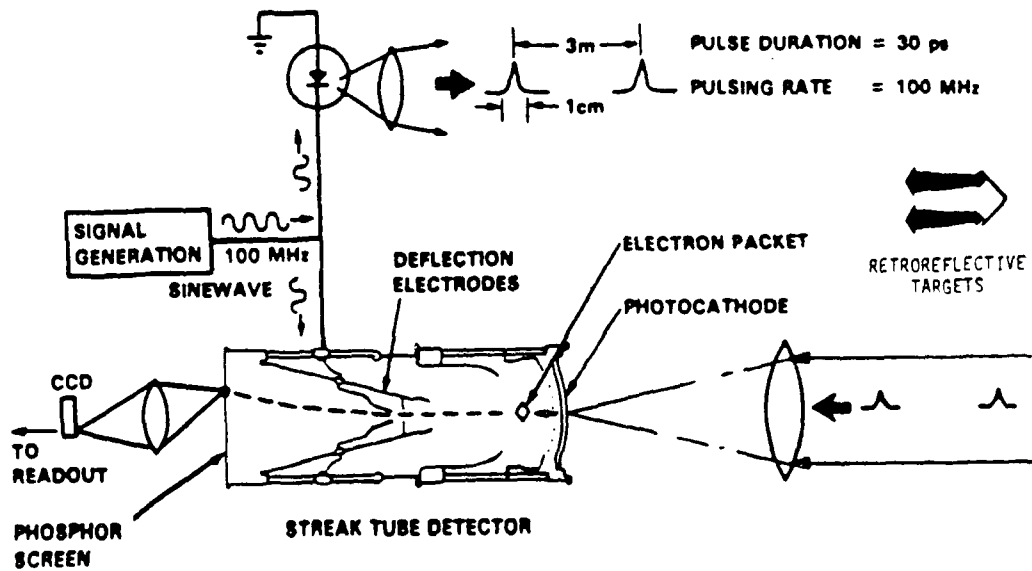


Figure 3.4-1 Schematic of SHAPES operating principle. Time-of-flight correlations to obtain range are obtained from the location of the image on the CCD. A reference target, not shown, placed at a known range is necessary for absolute range measurements.

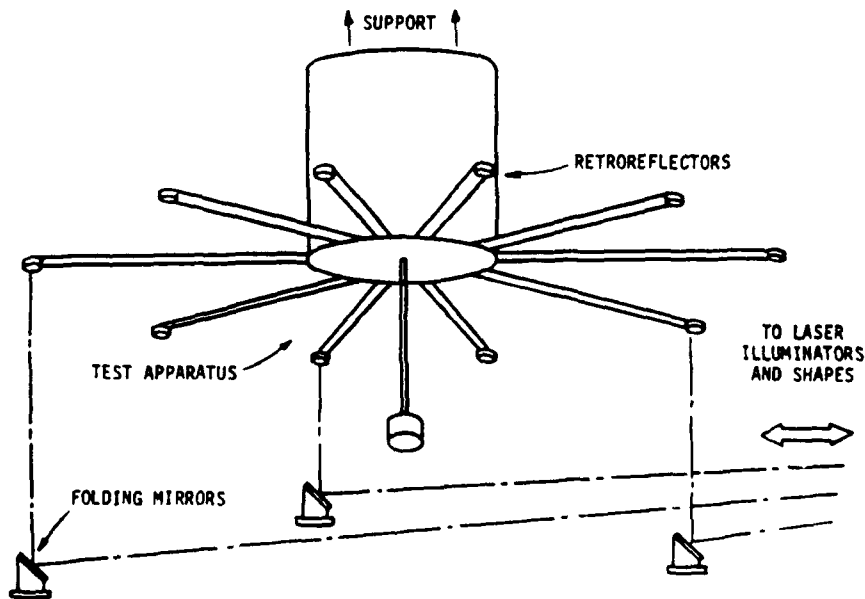


Figure 3.4-2 Schematic of SHAPES optical path. A plane mirror is placed directly below each target to direct the retro return to the sensor.

The spot deflection is thus anyplace along a CCD row, at a position that depends on the target range and the amplitude of the drive voltage. The number of rows needed to contain the spot is termed the height of the target "window". Image overlap is not allowed. Therefore, it follows that one limitation to the number of targets that can be viewed is that not more than one image can occupy a window on the CCD row. For a fixed CCD size, then, the limit to the maximum number of targets that can be viewed simultaneously is the required number of the rows assigned to each window.

For the present configuration of SHAPES, the required image separation is roughly 10 rows. With a 256-row CCD, 25 targets could be successfully imaged on the CCD without spot overlap. However, the practical limitations on the number of targets is the SHAPES readout electronics package which, at present, is designed to process the returns from a maximum of 16 targets during each frame.

### 3.4.2 Optical System

3.4.2.1 Optical Path with Folding Mirrors. A schematic diagram of the optical arrangement is depicted in Figure 3.4-2. As indicated in the figure, the optical path between each target and the sensor is folded by a plane mirror located on the floor below each target. The folded optical path arrangement was used because direct viewing of the target area, by placing SHAPES below the test apparatus with its optical axis vertical, was deemed to be impractical.

As shown in the figure, each target is illuminated by a separate laser, and the folding mirrors are located directly below the target to provide a vertical light path. Because the target motion is always vertical, the target motion and the optical path are parallel and there is no lateral motion of the target relative to the optical path. Consequently, each retroreflector may be illuminated with a narrow laser beam and the measurements provide range directly with no correction for target lateral motion required. The range measurement, relative to a horizontal plane, can be made with the test apparatus at any height above the floor.

One of the disadvantages of the folding mirror optical arrangement is that although the displacements of each retroreflector can be measured with great precision, it becomes very difficult to accurately measure the range of all targets relative to a common reference. This is because the optical path depends critically on the 3-dimensional position of the folding mirror. A workable calibration procedure that would produce range measurements of all targets relative to a common horizontal plane just above the folding mirrors has been devised; however, the cost to implement the concept greatly exceeded the available resources.

3.4.2.2 Rotation of Image Plane. Because the line of sight is not normal to the target array, the view of the target array as seen by SHAPES tends to be elliptical with the major axis horizontal and therefore, parallel to the streak tube sweep direction. The image separation is greatly reduced by this geometry; however, normal image separation is restored by optically rotating the image on the photocathode by  $90^\circ$ . To fix ideas, assume the

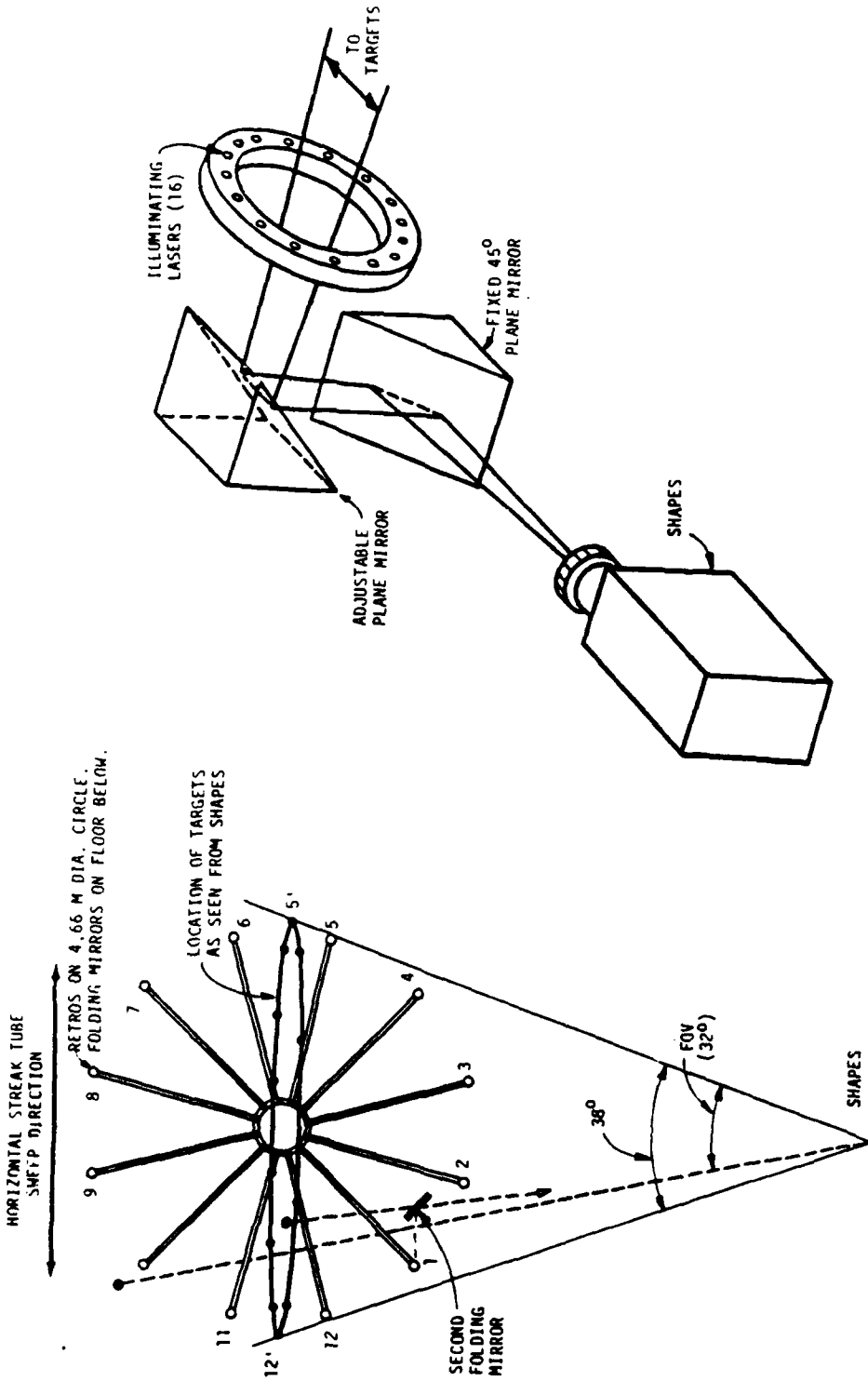


Figure 3.4-3 Top view of optical arrangement. The sensor is 1.5 m above the floor at a distance of 7.3 m from the center of the pattern.

Figure 3.4-4 Sketch of optical path designed to optically rotate the image by 90 degrees.

retroreflectors are placed at the outer location of each rib. The diameter of the circle containing these points is 4.66 m. The sensor is located in an adjoining room with its camera lens 1.5 m above the floor and 7.3 m from the floor location directly below the center of the experimental apparatus. The view of the targets at the camera lens is outlined by the distorted ellipse shown in Figure 3.4-3. It may be seen that the target separation in the direction normal to the sweep direction is highly compressed and therefore the image separation on the CCD is drastically reduced. To overcome this problem, two plane mirrors, placed close to the camera lens and oriented at approximately  $45^\circ$  to vertical, were placed in the optical path to rotate the image on the photocathode by  $90^\circ$ . This optical path is shown in Figure 3.4-4. With the image of the target area rotated by  $90^\circ$ , the major axis of the ellipse becomes vertical on the photocathode, perpendicular to the sweep direction, and the image separation on the CCD becomes manageable.

3.4.2.3 Sensor Field of View. The camera lens is a Canon 14 mm, F/2.8 35-mm camera lens. The diameter of the usable portion of the photocathode is about 8 mm. Thus, the camera FOV is about 32 degrees. With the camera at 7.3 m from the center of the target area,  $32^\circ$  is insufficient to include all possible target locations. Targets normally exterior to the camera FOV are imaged on the CCD by including a second folding mirror in their optical path and locating it within the FOV.

3.4.2.4 Semiconductor Diode Lasers. Each target is illuminated by an individual laser. The lasers are Mitsubishi Model ML 4102 that produce 3 mw of cw power at a wavelength of 780 nm. The laser drive current consists of a dc bias supply superimposed on a 100 MHz rf signal. The very short laser pulses are produced by passing the rf drive through a comb generator (Hewlett Packard Model 32003 Coaxial Step Recovery Diode Modules). The laser drive circuit causes one laser pulse to be emitted during each period of the rf signal. The laser is turned on and off by switching the bias supply on and off. The lasers are mounted as shown in Figure 3.4-4.

### 3.4.3 Sensor Electronics

3.4.3.1 Streak Tube and CCD. The streak tube camera is a Hadland Photonics Imacon 500 designed to operate in synchroscan mode at 100 MHz. This camera normally comes equipped with an input lens and slit and with a film pack to record the phosphor screen image. As described above, the lens and slit were replaced with a wide angle lens and the film pack was replaced with the CCD detector. The only streak tube parameter under the operator's control is the amplitude of the drive signal. The drive amplitude determines the streak tube scale factor and therefore requires calibration. This is discussed below.

The CCD is RCA Model SID501. It has 320 columns and 512 rows with one serial register. Although the full CCD can be exposed, only 256 rows are used in the present configuration. The CCD is cooled with a Peltier cooler to reduce thermal noise and is housed in a vacuum chamber to avoid condensation. The CCD clocking and readout signals are supplied by custom electronics described below.

As mentioned above, it is necessary to calibrate the streak tube/CCD combination as a function of the streak tube drive voltage amplitude. This is accomplished by ranging to a pair of reference retroreflectors that are placed a known distance apart. The calibration targets are located in the FOV such that the unswept image location is very near the row center at pixel number 160. When the sweep is turned on, each image moves to a location along the CCD row that depends on the target range, the drive amplitude, and the value of the phase difference between the laser firing and the streak tube drive. A phase modulator in the circuit allows the phase between the laser firing and the streak tube drive to be varied. During calibration, the phase is adjusted to place the swept image of one of the targets at its unswept location. The separation of the two images is then measured and divided by the known separation to provide a scale factor with units of pixels per cm.

3.4.3.2 Processing Electronics. The SHAPES custom electronic circuits control the CCD readout and perform some of the data processing steps. The circuits are designed for a maximum of 16 targets. Prior to obtaining quantitative range data, the targets are illuminated and the CCD is scanned to locate the images on the CCD array. The image location is specified by placing a "window", described below, around each image. The purpose of the use of windows is to speed up the CCD readout by processing only the data that are located within a window.

A window is a designated set of adjacent rows of CCD pixels that contain an image of one of the retroreflector targets. The window is specified by a CCD row number and the number of rows that comprise the window height. The CCD readout electronics are designed to process but a single image in each window. To obtain maximum sensitivity, the number of rows in the window must be enough to fully contain each image within the window.

A "guard band" is associated with each window. It consists of one or more CCD rows adjacent to the window on the side closer to the readout serial register. Its purpose, as described below, is to insure the serial register is free of any extraneous charge before quantitative data from pixels are obtained.

A block diagram of the CCD clocking and readout electronics is shown in Figure 3.4-5. Each block represents a circuit board which was designed and fabricated at JPL. The function of each board is described below.

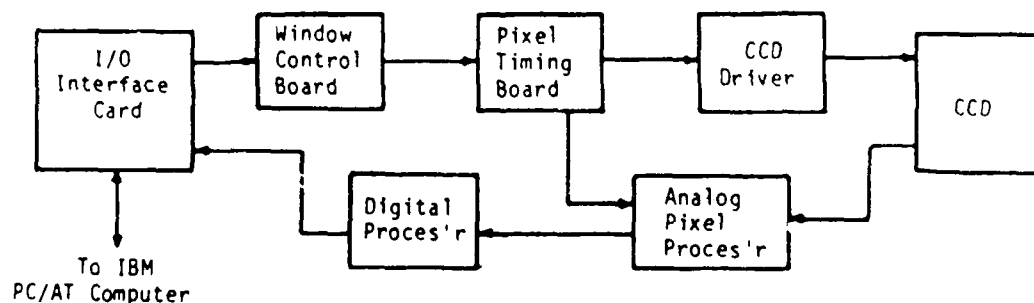


Figure 3.4-5 Block Diagram of CCD Timing, Readout and Processing Electronics

3.4.3.2.1 I/O Interface Board. The SHAPES custom CCD hardware circuits were fabricated on boards which plug into a S-100 bus rack. The interface between the SHAPES hardware and the IBM PC/AT computer includes two interface chips (Intel 8255 Peripheral Interface Adapters), located on a PC expansion board, that serve as a command port and as a data input port. The laser diode bias control circuits are also interfaced to the computer through the S-100 bus. This interface allows the target illumination period to be fixed by the SHAPES software.

3.4.3.2.2 Window Control Board. Once the images have been located, each window coordinate (CCD row number) is stored in the window control circuit along with the number of rows selected for the window height. The window control board uses the window coordinate information to control the CCD line (a "line" is a CCD row of pixels) and pixel clocking sequences during data processing.

For each window, the sequence is as follows:

- (1) Flushing mode. Line clocking with continual pixel clocking until the guard band has been clocked into the serial register. Pixel clocking is at the faster of two pixel clocking rates.
- (2) Guard band mode. The guard band pixels are clocked out at the fast rate and the output discarded. This insures that the serial register is completely clear for the charge associated with the image.
- (3) Summing mode. All rows of the window are clocked into the serial register. Thus, the charge from all rows in each column of the window is summed.
- (4) Process mode. The serial register is clocked out at the slower rate. This is the data used to determine the image centroid location.

3.4.3.2.3 Pixel Timing Board. The Pixel Timing Board synchronizes the 3-phase shifting of the CCD lines and pixels at the proper rates and in the proper sequence based on the signals generated by the window control board. Timing signals are directed to the CCD Drive Board and also to the Analog Processor to control the sequence of analog processing.

3.4.3.2.4 CCD Driver Board. The CCD Driver Board conditions the TTL voltage level signals received from the Pixel Timing Board to the proper CCD voltage levels.

3.4.3.2.5 Analog Processor Board. The Analog Processor input is the CCD readout signal. It integrates and digitizes each analog pixel signal level. A 12-bit A/D converter is used to digitize the data.

3.4.3.2.6 Digital Processor Board. The digital processor detects the threshold pixel level that marks the beginning of an image ( $x_0$ ) and then produces the two sums  $\sum p_i x_i$  and  $\sum p_i$  where  $p$  represents the pixel charge and  $x$  is the pixel number measured from the threshold location,  $x_0$ . The three values,  $\sum p_i x_i$ ,  $\sum p_i$ , and  $x_0$  are output to the computer.

#### 3.4.4 Software

A IBM PC-AT computer is used to accept the CCD readout data from SHAPES, calculate the range data and transmit the calculated result to the Control Technology Facility Vax computer. The interface between SHAPES and the IBM computer is a pair of Intel Peripheral Interface Adapters and that between the IBM and the Vax is a IEEE-488 General Purpose Interface Bus (GPB).

The SHAPES data are processed real-time and transferred to the Vax at a rate of ten frames of 16 centroids per second.

The SHAPES software accomplishes four main tasks as follows:

- (1) Initialize the SHAPES hardware.
- (2) Read and process the SHAPES data.
- (3) Initialize the interface between the IBM and Vax computers.
- (4) Transfer the data to the Vax.

These tasks, which were written in Intel 80286 assembly language, are described in more detail below. The program listing is available on request.

3.4.4.1 Initialization of SHAPES. The interface between SHAPES and the IBM computer is implemented with a pair of Intel 8255 Peripheral Interface Adapters (PIA). The first initialization task is to configure one 8255 PIA as a command output port to SHAPES and the other 8255 PIA as a data input port from SHAPES. The SHAPES hardware is then initialized by sending commands through the command port using the Send\_Command subroutine. The software first loads a CCD exposure time, which determines the amount of time that the lasers are on, and a pixel intensity threshold level, which determines when the digital processing hardware will be activated. The next step in SHAPES initialization is to place windows around images on the CCD. A window is a region on the CCD, 5-10 rows wide, which defines the areas where CCD data will be processed. Windows are set on the CCD by the subroutine Find\_Windows. This routine scans the CCD one row at a time and searches for images from the retroreflector targets. When an image is located, the corresponding CCD row number is stored in an array. After the entire CCD has been scanned, the CCD row numbers containing target images are loaded into the SHAPES hardware. The entire initialization procedure takes about ten seconds to complete.

3.4.4.2 Reading and Processing SHAPES Data. SHAPES outputs data for each window loaded in the hardware. The data include the 16-bit pixel location



( $x_0$ ) where the pixel intensity threshold was exceeded, a 32-bit sum of pixel intensities in the image ( $\Sigma p$ ), a 32-bit sum of the products of the pixel intensities and the pixel position ( $\Sigma px$ ) where  $x$  is measured from  $x_0$ . Only pixels with intensities greater than threshold are included in these summations. The centroid of the image, which corresponds to the target, is then found by the formula:

$$\text{Centroid} = \frac{\Sigma px}{\Sigma p} + x_0$$

This calculation is performed by using the Intel 80287 math co-processor. The resulting 32-bit centroid is in the IEEE-754 standard for floating point numbers.

3.4.4.3 Initialization of the SHAPES/Vax Interface. The transfer of data from the SHAPES IBM computer to the Control Technology Facility Vax is over the IEEE-488 GPIB. A National Instruments GPIB interface card is installed in both computers. The Vax is configured as a system controller for GPIB operations. The SHAPES software first reads the device parameters of both computers and then takes steps to insure synchronization of the first bus operation. The SHAPES software then goes into a wait state until it receives a trigger signal from the Vax to begin a SHAPES data acquisition cycle.

3.4.4.4 Transfer of SHAPES Data to the Control Technology Facility Computer. The SHAPES software is ready to begin the data transfer process after all of the previously described initialization procedures have been completed. The SHAPES software now waits for the computer to request SHAPES data. If a valid request for data is detected, the software will issue a start command to SHAPES to begin the next data frame. While the SHAPES hardware is exposing the CCD, the SHAPES software writes the current frame of data to the GPIB. After writing the data, the software then calls the routine Find\_Centroids to read and process the next frame of SHAPES data. The software then waits for the next request of data from the Control Technology Facility Vax.

## SECTION 4

### SYSTEM MODELING

This section describes the modeling of the experiment apparatus. The objective in developing the model is to obtain the mode shapes and their corresponding frequencies for those modes which fall within the expected control bandwidth of the experiments. These modes are used in the synthesis of the control laws to calculate the appropriate control parameters and to simulate the behavior of the structure in open and closed loop situations. The model was also used extensively in the initial design phase of developing the facility, to assist in selecting the physical dimensions of the structure by determining their effect on the structural dynamics. In order to support the design of the facility during the early stages of its development, it was also critical that the model should be economical with respect to computation, because many different cases would have to be analyzed.

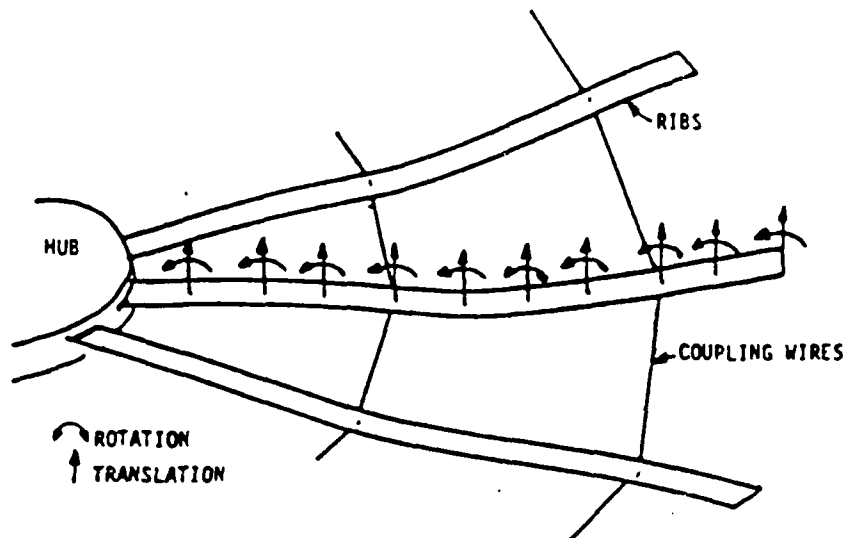
#### 4.1 FINITE ELEMENT DEGREES OF FREEDOM

The finite element method was used to obtain the system modes. While the method is standard procedure and is amply described in numerous references, some of the subtleties of modeling the experiment structure warrant the description which follows. As usual, a set of degrees of freedom for the structure is designated, as shown in Figure 4.0-1. The vertical displacements and slopes of the ribs at 10 equally spaced intervals constitute the rib degrees of freedom. The hub, for its part, is modeled as a very stiff circular ring which is constrained to rotate about the two perpendicular gimbal axes. The boom is modeled similarly to the ribs in that it is divided into 10 elements of identical length, except that motion is horizontal and can occur along either of the two horizontal axes.

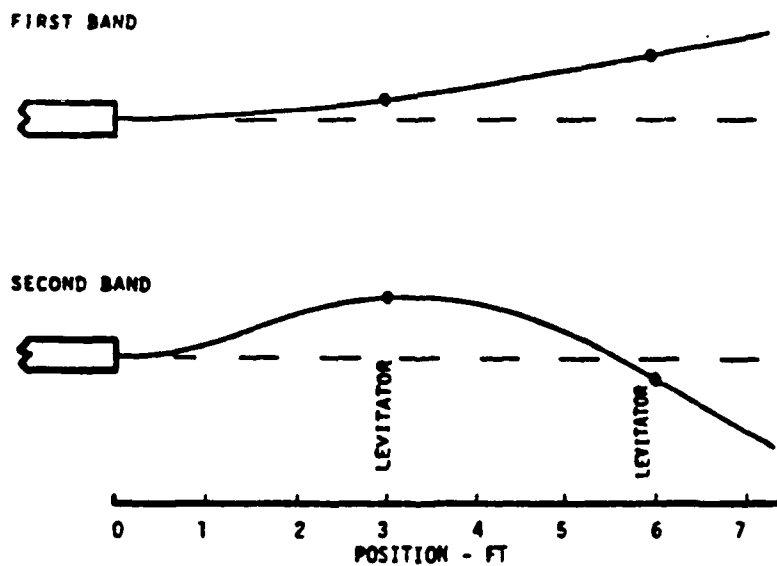
The displacements of the elements between these degrees of freedom, or nodes, as they are called, are approximated by appropriate interpolation functions. The requirements on these functions are that they must have sufficient order to satisfy boundary conditions, and they must not violate physical conditions such as continuity and compatibility. In this particular case, cubic splines are perhaps the simplest functions which satisfy these requirements and therefore are used as interpolation functions. The spline function for a given element is completely specified by the boundary conditions of that element, e.g. the finite element degrees of freedom. Thus, the displacement at any point along the structure can be expressed in terms of the finite element degrees of freedom. The significance of this is that the displacement of the continuous, infinite degree of freedom system can be represented in terms of this finite and manageable set of variables. Instead of solving a partial differential equation or, equivalently, an integral equation, to obtain the eigensystem, it becomes possible to work with finite dimensional matrices, for which powerful numerical algorithms have been developed.

#### 4.2 GENERATING MASS AND STIFFNESS MATRICES

To obtain the normal modes of the system, it is necessary to obtain expressions for the mass and stiffness matrices and then to solve the



Finite Element Model Degrees of Freedom  
Figure 4.0-1



Mode Shapes of Dish Modes - Radial Dependence  
Figure 4.0-2

resulting generalized eigenvalue problem. The mass and stiffness matrices are obtained from the matrix quadratic expressions which approximate, respectively, the kinetic and potential energies of the continuous parameter system in terms of the finite element degrees of freedom. The mass and stiffness matrices so obtained are consistent; the common practice of lumping the mass matrix into a diagonal form, which simplifies subsequent computations but detracts from accuracy, is not used. Lumping, though it is regularly applied with apparent success if small enough elements are used, is born more out of convenience than out of mathematical rigor, since the resulting eigenvalue problem is much easier to solve if the mass matrix is lumped. When the mass matrix is created using a consistent formulation, a more difficult generalized eigenvalue problem must be solved, but the results are more accurate.

Part of the key to the success of the finite element method is that it is possible to assemble the mass and stiffness matrices from the smaller (4 by 4) mass and stiffness matrices developed for a single element, since only a few different element types are present and therefore the elemental matrices do not have to be rederived for each different element. Generation of the consistent mass matrix for an element, and thereafter, for the structure, is fairly straightforward. The stiffness matrix is, however, somewhat more complex to generate for a given element, since it implicitly includes the effects of compression caused by the coupling wires or of gravity in the boom. The rib dynamics, incidently, are not affected to first order by gravity since the rib weight is precisely balanced by the levitator counterweights and motion is parallel to the gravitational field.

In developing the mass matrix, the dynamics of the levitator pulleys and counterweights cannot be ignored and in fact have a significant effect on the system's dynamics, since they move in correspondence with the rib motion and therefore share in the system's kinetic energy. From the standpoint of modeling, each counterweight is dynamically equivalent to a lumped mass attached rigidly to the rib at the point where the levitator wire attaches to it. Since the attachment points correspond to nodal locations on the ribs, these equivalent masses appear as terms along the diagonal of the mass matrix. The rotary inertias of the levitator pulleys themselves add additional equivalent masses to the ribs at these locations.

The stiffness matrix for any element located along the boom is determined in large part by the presence of gravity, since gravity places the boom under tension due to its own weight, and in fact the boom is made stiffer because of it. The tension varies along the length of the boom, being equal to the weight of the feed at its lower end and equal to that plus the weight of the boom itself at its upper end. Unfortunately, a rigorous accounting of the linearly varying tension in the analysis requires rederivation of a different stiffness matrix for each element within the boom. Furthermore, these elemental stiffness matrices cannot be determined analytically in terms of commonly used functions. The simplifying assumption is therefore made that tension within a given element is constant, but it is allowed to vary from element to element. The result of this approximation is that the stiffness matrix for a boom element can be expressed as the sum of two matrices: a bending stiffness matrix which is the same for all boom elements, and a tension stiffness matrix, which is added in proportion to the average tension in the element.

The presence of the tensioned coupling wires on the dish structure has a similar effect on the stiffness matrix for a given rib, but in reverse. From geometric considerations, a component of the coupling wire tension causes compression in the ribs. Compression can be considered as negative tension, and therefore causes a decrease in stiffness, as compared to the increase in stiffness for the boom due to gravity. In this case, no approximation has to be made; the stiffness matrix for a rib element can be expressed as the difference between a bending stiffness matrix and a tension stiffness matrix (compression being the reverse of tension), subtracted in proportion to the compression in the element. It is interesting to note that neither the elemental nor global stiffness matrix is guaranteed to be non-negative if compression is present, and in fact the stiffness matrix will take on negative eigenvalues if the rib compression increases beyond some value. Physically, a negative stiffness matrix would be the result of overtensioning the coupling wires, and would manifest itself in the unstable compressive buckling of the structure. It is therefore important to keep the tension in the coupling wires well below some critical value.

Finally, each rib is coupled directly to its two adjacent neighbors by the coupling wires. Accordingly, terms representing this type of coupling are added to the otherwise assembled stiffness matrix.

#### 4.3 THE MATRIX EIGENVALUE PROBLEM

Once the overall mass and stiffness matrices are obtained, the normal modes and their frequencies can be obtained by solving a generalized eigenvalue problem in standard form:

$$Kx - \omega^2 Mx$$

where "K" is the system stiffness matrix, "M" is the system mass matrix, and "x" is the system eigenvector with angular frequency  $\omega$ . While this is a standard problem and presents no special difficulties for the many solution algorithms available (e.g., QR, Jacobi, inverse iteration, power method, and variations of these), the problem is large and its solution can be expensive computationally. With each of the ribs and the boom divided into 10 elements, there can be as many as 308 degrees of freedom, the precise number depending on how the rib to hub interface is handled. The parametric studies used in the initial analysis of the structure required solving for the eigensystem repeatedly, for different combinations of physical parameters. Clearly, it was desirable to make solution to the eigenproblem as efficient as possible.

Fortunately, this can be accomplished through the use of cyclic reduction. Due to the cyclic symmetry of the dish structure, it is possible to separate variables and express a given mode's shape as the product of two terms: a shape function, which is independent of the rib location and a scalar function which depends on the rib location. The scalar term can be written by inspection, and has the following form:

$$\sin \left( \frac{2\pi ik}{n} + \phi_k \right)$$

where "i" is an index indicating rib location (counted sequentially), "n" is the number of ribs in the dish structure (12 in this case), and "k" is the circular wave number for a given mode, and " $\phi_k$ " is a phase angle. The mode shape, on the other hand, is determined by solving the much reduced order eigenvalue problem for a system with one "equivalent" rib. The dimension of the resulting generalized eigenvalue problem is just 44 by 44 instead of 308 by 308 which would have resulted from solving the full order eigenvalue problem. Even though this eigenvalue problem must be resolved for each different circular wave number k, the computational savings are considerable due to the much lower dimensionality. A mode is thus completely specified by its frequency, circular wave number, phase angle, and mode shape. It can be shown that for 12 ribs k = 0 and k = 6 each generates a single reduced order eigenvalue problem whereas k = 1, 2, 3, 4 and 5 each generates two distinct eigenvalue problems.

Furthermore, it can be shown that for circular wave number k equal to 0, 2, 3, 4, 5 or 6, all reaction forces on the hub caused by rib motion cancel out, and thus neither hub nor boom moves. Such modes, which are called the "dish modes", behave as if the hub were clamped into a fixed position even though it is not. The dish modes corresponding to k = 2, 3, 4, and 5 are each two-fold degenerate, from symmetry. The eigenvalue problem associated with solving the dish modes could be reduced to a 20 by 20 system by eliminating degrees of freedom associated with the hub and boom, though this was not done due to the difficulty of maintaining separate programs.

For circular wave number k equal to 1, the reaction forces on the hub do not cancel, and these modes are characterized by hub and boom participation and hence are called "boom-dish" modes. These modes have planes of symmetry which pass through the principal axes of the hub, which is not quite symmetric.

#### 4.4 SOLUTION TO THE REDUCED ORDER EIGENVALUE PROBLEM

In order to solve the eigenvalue problem, an appropriate algorithm must be chosen. It is interesting to note that the QR algorithm, widely recognized as best for solving a complete eigensystem, is not optimal in this case. First of all, the eigenvalue problem must be put into standard form for the QR algorithm to work; this involves determining the (non-unique) square root factors of either the mass or stiffness matrices and then rearranging terms, roughly as follows:

$$L^{-T}KL^{-1}(Lx) = \omega^2(Lx), \text{ where } L^T L = M$$

In any case, any bandedness of the system which might have been present is completely destroyed, and the QR algorithm must solve a fully populated 44 by 44 eigensystem. As the operation count for the QR algorithm is proportional to  $n^3$ , where n is the dimension of the system (44 in this case), the computation time can be significant, especially when it is considered that the system must be resolved for each value of k = 0 .. 6, though certainly the computation time is still much improved over that required to solve the full order system (308 by 308).

Instead, a modified power method utilizing Schmidt orthogonalization is used to obtain the first several modes of the system. The iteration scheme for finding the  $j^{\text{th}}$  eigenvector  $x^j$  is outlined below:

- |    |                                                           |                                                                            |
|----|-----------------------------------------------------------|----------------------------------------------------------------------------|
| 1. | Choose a random vector                                    | $y_0$                                                                      |
| 2. | Iterate                                                   | $y_{i+1} = K^{-1} M y_i$                                                   |
| 3. | Normalize with respect to known eigenvectors              | $y_i = y_i - \sum_{k=1}^{j-1} y_i^T M x^k$                                 |
| 4. | Normalize with respect to mass matrix                     | $y_i = \frac{y_i}{\sqrt{y_i^T M y_i}}$                                     |
| 5. | Compute the eigenvalue                                    | $\lambda_i = y_i^T K y_i$                                                  |
| 6. | Check for convergence, and go to Step #2 if not converged | $\left  \frac{\lambda_i - \lambda_{i-1}}{\lambda_i} \right  \leq \epsilon$ |
| 7. | Converged; update                                         | $x^j = y_i$                                                                |

The power method has a number of important advantages in this case. First, it is efficient; even though convergence is linear (compared to cubic for QR and inverse iteration, and quadratic for the Jacobi method), with proper structuring of the algorithm the number of operations per iteration of the power method is proportional to  $n$ , the dimension of the system, for a banded system such as this, vs  $n^3$  for the other algorithms. Second, the power method delivers modes in sequential order starting first with those of lowest frequency, and iterations can be halted once enough modes are obtained. With the QR method, all the modes must be obtained simultaneously. Third, accuracy of the modes is better, since the original matrices are left essentially intact, while with the QR method the original matrices are modified by a succession of similarity transformations. Finally, storage of the matrices is efficient since they remain banded. It can be argued that Schmidt orthogonalization tends to fall apart numerically if too many eigenvectors are involved, but in this case only the first few modes are required for a given circular wave number  $k$ . With all the simplifications and efficiencies resulting from the cyclic reduction and the modified power method, it was possible to perform virtually all of the model analysis on a personal computer.

As an aside, it should be mentioned that it is possible to solve for the dish modes, though not for the boom-dish modes, analytically, but this method has limited utility because the resulting frequency equation in this case includes, as one of its terms, the determinant of a 10 by 10 matrix. The frequency equation can be solved in a straightforward, if time consuming, way using bisection of Newton's method. Unfortunately, the number of algebraic terms involved makes the method unwieldy, and worse yet, terrific numerical errors can creep into the solution unless one is extremely careful to scale the problem properly. Nevertheless, the dish modes were modeled analytically while different modeling methods were being considered, and the results were used as a check of the finite element model before the method was abandoned.

#### 4.5 MODE SHAPES AND FREQUENCIES

The parameters used in the system model are listed in Table 2.2-1. In most cases, the physical properties were determined by weighing and measuring individual parts. Occasionally, parameters were obtained indirectly; for example, the rib stiffness was calculated based on the deflection of a short section of rib under a known load, and the pulley and hub inertias were calculated from their oscillation frequencies when attached to known springs.

The system modes below 10 Hz are summarized in Table 4.0-1. The boom-dish modes, which depend on the boom properties, are listed separately for the two different system configurations which will be used to conduct experiments; namely, the short boom and the long boom. Note, however, that the configuration using the short boom is used for all of the experiments discussed in this report. Each boom-dish mode has associated with it a unique pivot axis, defined in terms of the ribs which lie along this axis (See Figure 2.2-2 for the definition of the rib numbering). The dish modes, which are independent of the boom dynamics, are also listed separately together with their circular wave numbers.

Shapes for the first 12 boom-dish modes and the first 20 dish modes are shown in Figure 4.0-3. The boom-dish mode shapes corresponding to the 1-7 pivot axis are nearly identical to those corresponding to the 4-10 axis, and hence only one set of figures is shown for the boom-dish modes along these two pivot axes. The shapes for two degenerate dish modes with the same circular wave number (i.e., circular wave number of 2, 3, 4 or 5) are exactly identical, except have a different phase angle.

#### References

- [1] Eldred, D., Y. Yam, D. Boussalis and S. J. Wang, "Large Flexible Structure Control Technology Experiment and Facility Design", Fourth IFAC Symposium on Control of Distributed Parameter Systems, Los Angeles, June, 1986.
- [2] Yam, Y., "System Model for the RPL/JPL Ground Test Facility", JPL Engineering Memo #347-86-191 (Internal Document), 1986.
- [3] Wen, J., "Derivation of the Analytical JPL/AFRPL Antenna Model", JPL Engineering Memo #347-86-187 (Internal Document), 1986.
- [4] Scheid, R., Jr., "The Use of Cyclic Symmetry in the Distributed Model of a Large Dish Antenna", JPL Engineering Memo #347-83-146 (Internal Document), 1983.
- [5] Strang, G. and Fix, G. J., An Analysis of the Finite Element Method, Prentice-Hall, Englewood Cliffs, N.J., 1973.
- [6] Stewart, G. W., Introduction to Matrix Computations, Academic Press, New York, 1973.



I. Boom-Dish Modes  
(Short Boom Config.)

| <u>Frequency<br/>(hz)</u> | <u>Pivot<br/>Axis</u> |
|---------------------------|-----------------------|
| 0.091                     | 4-10                  |
| 0.091                     | 1-7                   |
| 0.616                     | 4-10                  |
| 0.628                     | 1-7                   |
| 1.685                     | 4-10                  |
| 1.687                     | 1-7                   |
| 2.577                     | 4-10                  |
| 2.682                     | 1-7                   |
| 4.858                     | 4-10                  |
| 4.897                     | 1-7                   |
| 9.822                     | 4-10                  |
| 9.892                     | 1-7                   |

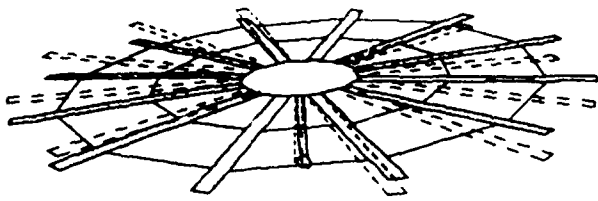
II. Boom-Dish Modes  
(Long Boom Config.)

| <u>Frequency<br/>(Hz)</u> | <u>Pivot<br/>Axis</u> |
|---------------------------|-----------------------|
| 0.112                     | 4-10                  |
| 0.113                     | 1-7                   |
| 0.332                     | 4-10                  |
| 0.332                     | 1-7                   |
| 0.758                     | 4-10                  |
| 0.774                     | 1-7                   |
| 2.264                     | 4-10                  |
| 2.354                     | 1-7                   |
| 4.724                     | 4-10                  |
| 4.726                     | 1-7                   |
| 4.926                     | 4-10                  |
| 4.967                     | 1-7                   |
| 9.018                     | 4-10                  |
| 9.886                     | 1-7                   |

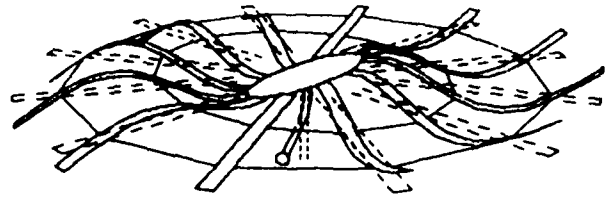
III. Dish Modes

| <u>Frequency<br/>(Hz)</u> | <u>Circular<br/>Wave<br/>Number</u> |
|---------------------------|-------------------------------------|
| 0.210                     | 0                                   |
| 0.253                     | 2                                   |
| 0.253                     | 2                                   |
| 0.290                     | 3                                   |
| 0.290                     | 3                                   |
| 0.322                     | 4                                   |
| 0.322                     | 4                                   |
| 0.344                     | 5                                   |
| 0.344                     | 5                                   |
| 0.351                     | 6                                   |
| 1.517                     | 0                                   |
| 1.533                     | 2                                   |
| 1.533                     | 2                                   |
| 1.550                     | 3                                   |
| 1.550                     | 3                                   |
| 1.566                     | 4                                   |
| 1.566                     | 4                                   |
| 1.578                     | 5                                   |
| 1.578                     | 5                                   |
| 1.583                     | 6                                   |
| 4.656                     | 0                                   |
| 4.658                     | 2                                   |
| 4.658                     | 2                                   |
| 4.660                     | 3                                   |
| 4.660                     | 3                                   |
| 4.661                     | 4                                   |
| 4.661                     | 4                                   |
| 4.662                     | 5                                   |
| 4.662                     | 5                                   |
| 4.663                     | 6                                   |
| 9.474                     | 0                                   |
| 9.474                     | 2                                   |
| 9.474                     | 2                                   |
| 9.474                     | 3                                   |
| 9.474                     | 3                                   |
| 9.474                     | 4                                   |
| 9.474                     | 4                                   |
| 9.475                     | 5                                   |
| 9.475                     | 5                                   |
| 9.475                     | 6                                   |

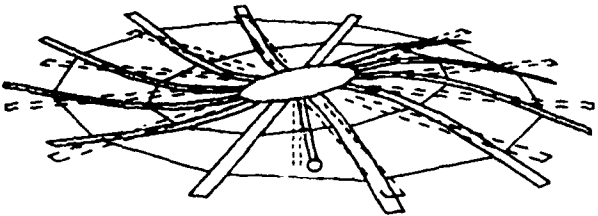
Normal Modes  
Table 4.0-1



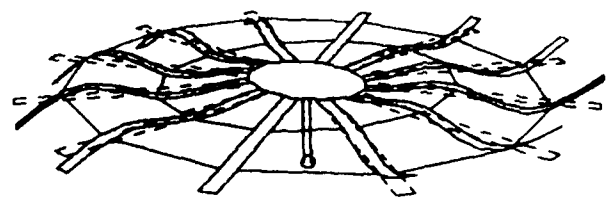
(a) 0.09 Hz



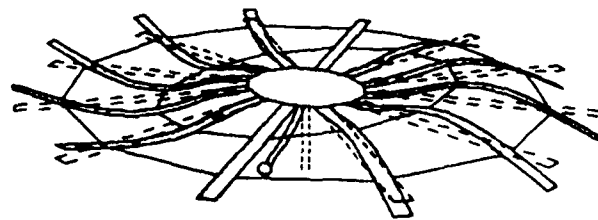
(d) 2.7 Hz



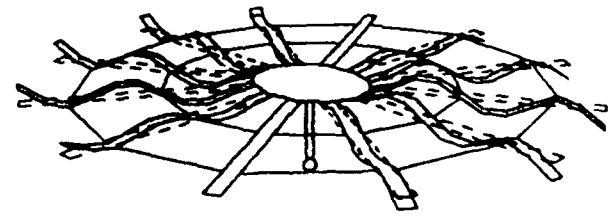
(b) 0.6 Hz



(e) 4.9 Hz



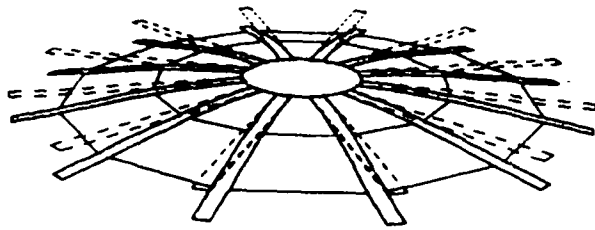
(c) 1.6 Hz



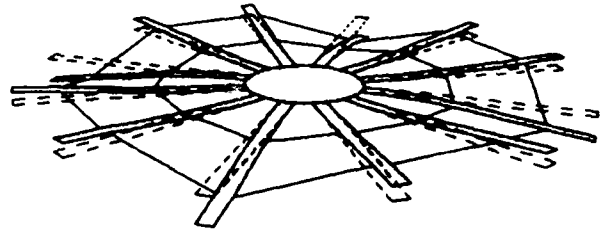
(f) 9.9 Hz

I. Boom-Dish Modes (Circular wave number  $k = 1$ )

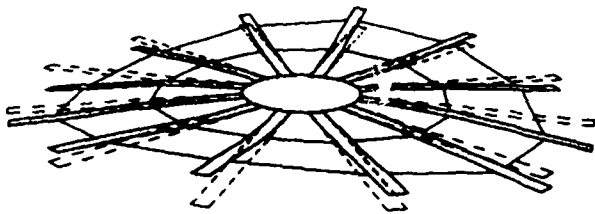
Figure 4.0-3 Mode Shapes



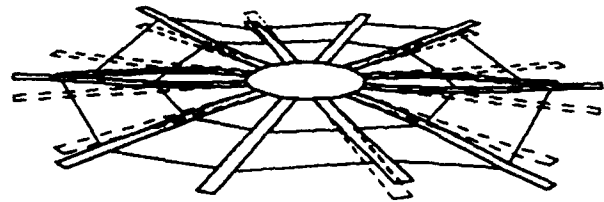
(a) 0.210 Hz,  $k^* = 0$



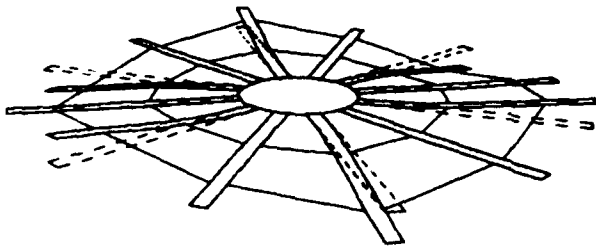
(d) 0.322 Hz,  $k = 4$



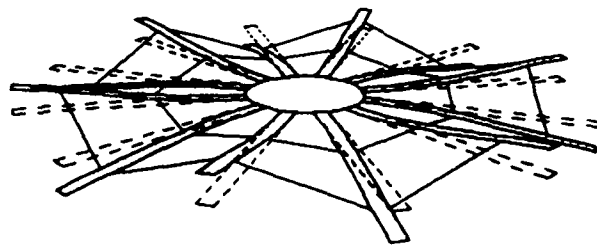
(b) 0.253 Hz,  $k = 2$



(e) 0.344 Hz,  $k = 5$



(c) 0.298 Hz,  $k = 3$

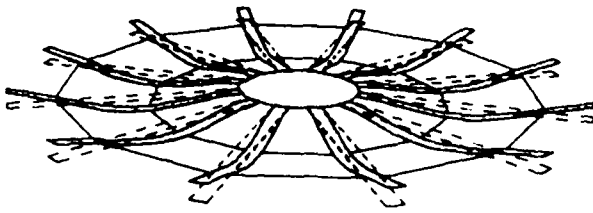


(f) 0.351 Hz,  $k = 6$

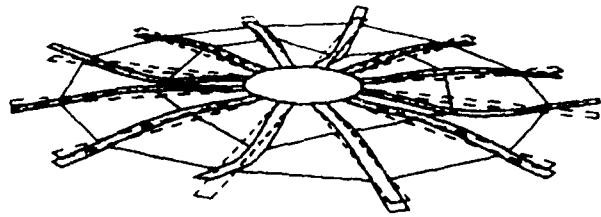
\*  $k$  = Circular wave number

## II. Dish Modes - First Band

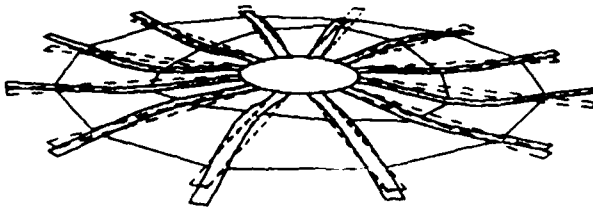
Figure 4.0-3 Mode Shapes (Continued)



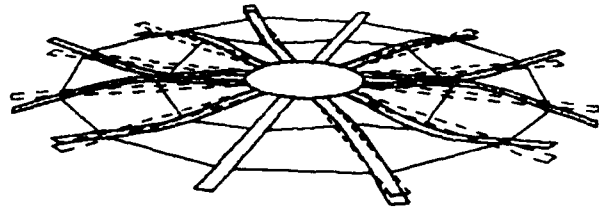
(a) 1.517 Hz,  $k = 0^*$



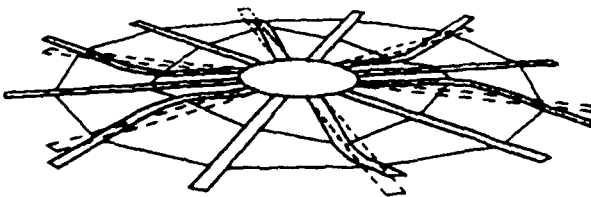
(d) 1.566 Hz,  $k = 4$



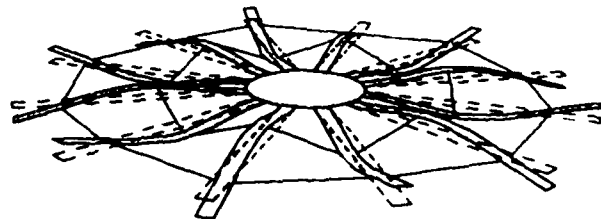
(b) 1.533 Hz,  $k = 2$



(e) 1.578 Hz,  $k = 5$



(c) 1.550 Hz,  $k = 3$



(f) 1.583 Hz,  $k = 6$

\*  $k$  = Circular wave number

### III. Dish Modes - Second Band

Figure 4.0-3 Mode Shapes (Continued)

## SECTION 5

### EXPERIMENTS

Experiments in vibration damping, adaptive control and shape determination were undertaken as part of the Phase 1 experiment program. The experiment designs and procedures, algorithm developments, and results and conclusions are discussed in this section.

#### 5.1 DYNAMIC CONTROL EXPERIMENT

##### 5.1.1 Experiment Design

5.1.1.1 Introduction. The infinite dimensional LQG theory represents the most mature methodology for the control of distributed parameter systems. The associated approximation theory and the numerical tools (to solve finite dimensional Riccati equations) are well developed and readily available. The objective of the Phase 1 dynamic control experiment is to validate the LQG methodology for transient regulation of structures. For this initial pathfinding phase, only the hub 2-axis torquers and hub 2-axis angle sensors are used for the control and estimation purpose. The use of the full set of instrumentation is deferred until future phases.

5.1.1.2 Modes of Operation. The Phase 1 experiment consists of exciting the structure with a train of pulses of specified duration and strength. The open loop and the closed loop responses under different control laws are then compared. There are six possible modes of operation:

- (1) state estimation
- (2) state estimation with initial excitation
- (3) control without initial excitation
- (4) control with initial excitation
- (5) control with initial excitation and high performance state estimation
- (6) offline state estimation

For Phase 1, mainly Modes 2 and 4 are exercised. Mode 2 is used to produce the open loop response and Mode 4 is used to generate the closed loop response.

5.1.1.3 Instrumentation. It is assumed that the dish is spatially and dynamically symmetrical and that there is no coupling between orthogonal sensing and control. The control loop utilizes hub torquers HA1 and HA10\* and sensors HS1 and HS10. The HA1 torquer is mounted on Rib 1 and effects a rotation about Rib 4-10 axis with the angle of rotation measured by HS10. The HA10 torquer is mounted on Rib 10 and effects a rotation about Rib 1-7 axis with the angle of rotation measured by HS1. The symmetry assumption of the

---

\* Figure 2.2-2

dish and the application of excitation and control action exclusively through the hub allows consideration of only the hub-boom modes. The assumption that the dynamics along the 1-7 axis and 4-10 axis are decoupled further simplifies the control problem to one involving two single-input/single-output systems (HA10-HS1 and HA1-HS10). The levitator sensors' signals are not used in the state estimation. They are mainly used to check the estimator performance and to verify the validity of the dish symmetry assumption. The full set of instrumentation will be incorporated into the future phases of the experiment.

5.1.1.4 Experimental Parameters. The experimental parameters are stored in text files (in ASCII format) and can be changed easily through a text editor. The most important parameters that are changed for different experiments are:

- (1) Specification of the initial excitation
  - o Number of excitation channels
  - o Number of excitation bands for each channel
  - o Length of each band
  - o Amount of excitation in each band
- (2) Control law and estimator parameters (stored in separate files)

5.1.1.5 Experiment Sequence. For Phase 1, the experiments are sequenced as follows:

- i. Perform control experiments based on the analytical model.
- ii. Identify parameters using both nonparametric and parametric techniques.
- iii. Rerun control experiments based on the updated model.

The spatial symmetry and hub axes decoupling assumptions are also tested. As experience was gained on the experimental apparatus, steps (ii) and (iii) were iterated with a more refined identification technique based on the output prediction error method with ARMAX parameterization (see [1]).

5.1.1.6 Initial Excitations. To see how the controller performs under different initial excitation patterns, different pulse frequencies are used to pump energy into different modes and the same set of controllers are used to study the closed loop performance. The excitation pattern is selected to excite mainly the first two modes. Because of the low excitability and the lack of accuracy of the higher order modes, a meaningful control experiment could not be formulated. It is anticipated that the effect of higher order dynamics will be more pronounced once the full set of instrumentation is used in the future phases of the dynamic control experiment series. For Phase 1, the following initial excitation patterns are used:

- (1) Single pulse with duration  $\sim$  5 sec and amplitude = 1.5 N-m in both HA1 and HA10.
- (2) Eight pulses with duration of each pulse = 0.8 sec, amplitude alternates between 1 N-m and -1 N-m in both HA1 and HA10.

Based on the sensor responses and simulation data, the amount of excitation in each mode is observed. In Pattern 1, mainly the first mode and some of the second mode are excited. In Pattern 2, mainly the second mode and some of the first mode are excited.

5.1.1.7. System Identification. The first pass identification is based on the response with manual pulse excitation along HA1. Frequency response is examined to spot the resonant frequencies. Then curve fitting is used to find the damping coefficient. The second pass identification is based on the output prediction error method with ARMAX parameterization. Various orders of polynomial are tried to obtain the most reasonable fit (as compared to the analytic model). With this more refined identification method, the entire model, including modal frequencies, damping coefficients and the influence matrix for the modes that are strongly excited can be obtained. A final fine tuning of the model, based on excitation Patterns 1 and 2, is also performed to obtain a reasonable match of the time responses.

To check the decoupling assumption, pulse excitation is fed into HA1 and then HA10 individually, and responses of HS1 and HS10 are compared. Good decoupling is indicated by large response differences. For the verification of the symmetry assumption, the levitator responses from the above two initial excitation patterns are transformed to the spatial modal coordinate by using the cyclic transformation (see Section 4.3, [2] and [3]). Response differences between the hub-boom modes and the dish modes should be large for good symmetry.

5.1.1.8. Controller Discretization. Four different discretization schemes for the continuous-time compensators were tried. They are based on the sample and zeroth order hold approximation of system output, sample and zeroth order hold of the control input and the system output, bilinear transformation and first order backward differencing. Performances were compared in simulations and the first three schemes were found to be adequate. The second scheme was used in the experiment.

The sampling rate is set at 10Hz since it provides ample time for control law computation and enough bandwidth for the modes that are controlled.

5.1.1.9. Controller Parameters. The controller design is based on the distributed parameter LQG methodology. Different weightings are used to penalize the RMS deflection error, hub angle error and levitator sensor errors. For higher gain controllers,  $\alpha$ -shift is used to guarantee stability margins. Not surprisingly, the control design parameters need to be modified as the system model is updated through the identification stage in order to maintain the same level of performance. Due to the inaccuracy of the model and the presence of instrument noise and system nonlinearities (actuator saturation, stiction, Coulomb friction, etc.), robustness is an intrinsic component of the controller design. Several weighting parameters need to be selected for the robust controller design. The parameters that can be adjusted are listed below:

|          |                                                                                                                                           |
|----------|-------------------------------------------------------------------------------------------------------------------------------------------|
| N        | - order of estimator (= 2 x number of modes)                                                                                              |
| $\beta$  | - scale down coefficient for the input vector                                                                                             |
| q0       | - penalty on individual modal displacements and velocities                                                                                |
| q1       | - penalty on RMS deflection error                                                                                                         |
| q2       | - penalty on hub angle output error (also serves as loop transfer recovery coefficient with respect to output channel, see Section 5.1.2) |
| q11      | - penalty on inner levitator sensor output error                                                                                          |
| q12      | - penalty on outer levitator sensor output error                                                                                          |
| qr       | - rib tip output error                                                                                                                    |
| qb       | - boom tip output error                                                                                                                   |
| r        | - control penalty weighting                                                                                                               |
| m1       | - coefficient on the identity state noise covariance                                                                                      |
| m2       | - loop transfer recovery coefficient with respect to input channel (see Section 5.1.2)                                                    |
| n1       | - output noise covariance                                                                                                                 |
| $\alpha$ | - guaranteed stability margin                                                                                                             |
| qa1      | - coefficient for state noise covariance modification (for robustness enhancement with respect to system matrix perturbation)             |
| qa2      | - coefficient for state penalty modification (for robustness enhancement with respect to system matrix perturbation)                      |
| H1       | - output influence map of uncertain system matrix                                                                                         |
| H2       | - input influence map of uncertain system matrix                                                                                          |
| a1       | - lower bound of uncertain system matrix                                                                                                  |
| $\sigma$ | - scaling parameter for the input matrix                                                                                                  |

Table 5.1-1 List of Controller Parameters

## 5.1.2 Algorithm Description

5.1.2.1. Introduction. In this section, the theoretical background of the control algorithm development is discussed. Detailed discussion of the theory is avoided. Instead, formal reasoning is used to highlight key ideas. For the Phase 1 experiment, only the stability issue is addressed. The systematic testing of robust control techniques is deferred until future phases. However, due to the limited knowledge of the system structural characteristics, the control algorithms in this phase must be robust. Therefore, some discussion on robust control is also included.

As stated earlier, the dynamic control experiment in Phase 1 is intended to validate the distributed parameter LQG methodology for the structural control problem. The basic idea of functional gain convergence is used to address the spillover effect in the low order compensator design. The precise degree of required convergence for stability is characterized by a new measure of robustness, the  $\nu$ -index. The  $\nu$ -index is also employed to deal with parameter uncertainties.

5.1.2.2. Analytic Model. The analytical model is generated based on the finite element analysis using the known material properties and the experimental configuration (see [4] and [5] for detail). The small displacement assumption is used throughout to ensure approximate linearity of



the system. The twelve ribs give rise to twelve spatial modes with only modes 2 and 12 coupling to the hub-boom assembly. As is usually true in analytic characterization of structural systems, the knowledge of the damping term, which is assumed to be modal to maintain the linear structure of the problem, is very crude. The outcome of the analytic modeling is a linear state space model in the modal coordinate. However, the system contains two prominent sources of nonlinearity, namely, the instrument saturation as manifested by control torque saturation and levitator pulleys hitting the stops, and the nonlinear friction effects such as Coulomb friction and stiction. For the purpose of algorithm design, the nonlinear effects are considered as perturbations of the nominal linear system.

5.1.2.3. Controller Design Methodology. As a result of the finite element analysis, the structure is modeled as a continuous-time linear time invariant system. In the state space form (in the modal coordinate), the model is given by:

$$\begin{aligned} M \ddot{x} + D \dot{x} + K x &= B u \\ y &= C x \end{aligned} \tag{5.1.1}$$

where  $x \in X$ ,  $X$  is an infinite dimensional Hilbert Space. In Phase 1, the actuators (hub torquers) and sensors (hub angle sensors) are collocated, hence,  $C = B^T$ . For a rigorous interpretation of (5.1.1), see [6]. As in the finite dimensional case, a separation principle [7,8] allows the compensator design to be decoupled to a full state feedback regulator problem and a state estimation problem. In the Phase 1 experiment, we consider only the optimal quadratic regulator design and minimum variance (Kalman filter) type of state estimator. For this problem, the optimal controller has the form:

$$\begin{aligned} u &= -G \hat{x} \\ G &= R^{-1} B^T P \end{aligned} \tag{5.1.2}$$

where  $P$  solves the algebraic Riccati equation

$$A^T P + P A + Q - P B R^{-1} B^T P = 0 \tag{5.1.3}$$

The estimated state  $\hat{x}$  is generated by the state estimator

$$\dot{\hat{x}} = A \hat{x} + B u + K(y - C\hat{x}) \tag{5.1.4}$$

where  $K$  is given by

$$K = H C^T N^{-1} \tag{5.1.5}$$

and  $H$  solves the dual Riccati equation

$$A H + H A^T + M - H C^T N^{-1} C H = 0 \tag{5.1.6}$$

It can be shown that provided that  $(A, Q^{1/2})$ ,  $(A, C)$  are detectable and  $(\cdot, B)$ ,  $(A, M^{1/2})$  are stabilizable the Riccati equations (5.1.3) and (5.1.6) have unique positive solutions and the closed loop system is exponentially stable. However, the implementation of this controller involves an infinite dimensional compensator and the precise knowledge of the open loop system, neither of which are realistic assumptions. This then necessitates the

approximation theory for the former and the robust control design problem for the latter. Both are elaborated below.

5.1.2.3. Infinite Dimensional Compensator Approximation. It has been shown in [9] that for the finite dimensional modal approximation system, i.e., projection of A, B, C onto the modal subspace, with Q, R, M and N replaced by their modal projections also, then the solutions of reduced order Riccati equations,  $P_N$  and  $H_N$  converge strongly to the infinite dimensional solutions, P and H. This implies that the gain operators,  $G_N$  and  $K_N$ , will converge in norm to the infinite dimensional gains, G and K. For the single actuator, single sensor case, G and K can be identified with elements in the Hilbert Space, X. For this experiment, they are functions of one spatial variable. These gains are called the functional control gain and functional estimator gain, respectively. For the multiple actuators and sensors case, there is a pair of functional gains for each actuator and each sensor. The convergence of  $G_N$  and  $K_N$  are called the functional gain convergence [6]. Once the functional gains have converged, the approximate controller will perform essentially as well as the infinite dimensional controller and the infinite dimensional plant is stabilized despite the presence of the "spillover" modes that are not modeled.

5.1.2.4. Spillover Issue. How is it known when functional gain has converged? The way this issue is approached is to regard the unmodeled modes as a perturbation of the nominal reduced order system that is used for controller design. To study stability of the nominal, low order controlled system under unmodeled dynamics, it is necessary to quantify the ability to maintain stability under modeling errors. There are several possible ways to characterize robustness margins with respect to perturbations. A common measure is the  $H_\infty$ -norm. Let the nominal closed loop system and the perturbation be put into the feedback block diagram as in Fig. 5.1-1, with the forward system  $T_1$  and feedback system  $T_2$  (both exponentially stable). If

$$\|T_2\|_\infty \leq \|T_1\|_\infty^{-1} \quad (5.1.7)$$

where  $\|\cdot\|_\infty$  denotes the  $H_\infty$ -norm, i.e.,

$$\|T\|_\infty = \sup_{\omega} \|T(j\omega)\|_2 \quad (5.1.8)$$

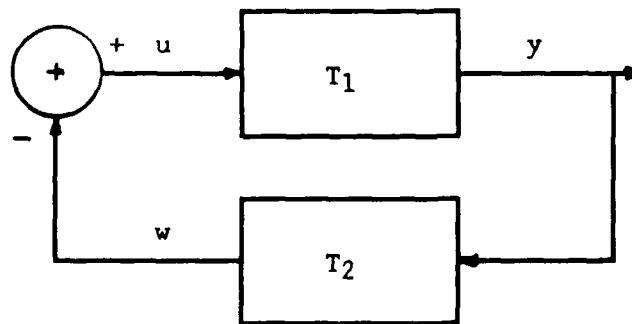


Figure 5.1-1 Archetypal Interconnected System

then the perturbed system is exponentially stable [10]. The assumption that both  $T_1$  and  $T_2$  are exponentially stable is a reasonable one since the nominal closed loop is stable by design and has already captured all the instabilities. The  $H_\infty$  criterion is based on the small gain theorem [11]. A different criterion based on the passivity theorem can also be formulated. The idea is very simple: if the perturbation dissipates more energy than the nominal system can generate, then the perturbed system is stable. A class of energy dissipating systems is called the positive real systems which is defined as the solvability of a set of equations called the Lur'e equations [12]. The amount of energy that a system can dissipate or generate is then quantified by an index, called the  $\nu$ -index, which measures the "closeness" between the system and positive realness. More specifically, the  $\nu$ -index is the least amount of parallel dissipation (a positive scalar system) needed to render a system positive real. The  $\nu$ -index, as has been stated, is a time domain quantity and is in general difficult to compute directly. It can be shown via the positive realness theorem that the  $\nu$ -index can be equivalently characterized in the frequency domain as

$$\nu(T) = -\inf_{\omega} \inf_w w^* T(j\omega)w \quad (5.1.9)$$

where  $w^*$  denotes the conjugate transpose of  $w$  and  $T$  is any complex valued square matrix analytic in the right half complex plane. Again consider the same interconnected feedback diagram as in Fig. 5.1.1. If

$$\begin{aligned} \nu(T_2) &< 0 \\ \frac{\|T_2\|_\infty}{\nu(T_2)} &< \frac{1}{\nu(T_1)} \quad (\nu(T_1) > 0) \end{aligned} \quad (5.1.10)$$

(the second condition can be dropped if  $\nu(T_1) \leq 0$ )

then the interconnected system is exponentially stable. Specifically in terms of application to finite dimensional compensator design for infinite dimensional systems (for details, see [12]), if the input matrix used in the controller design is replaced by  $B/\beta$  and the control gain is implemented as  $G/\beta$ , then

$$\frac{\nu(T_1)}{\beta} (\|\Delta T\|_\infty + \nu(\Delta T)) < 1/4 \quad (5.1.11)$$

where  $T_1$  denotes the nominal closed loop system with respect to the additive channel perturbation, would ensure closed loop stability. As the order of approximation of the infinite dimensional system increases,  $\nu(T_1/\beta)$  converges to some value and both  $\|\Delta T\|_\infty$  and  $\nu(\Delta T)$  converge to zero. Hence, a sufficient criterion for functional gain convergence can be stated as the satisfaction of (5.1.11).

5.1.2.5. Robustness Issue. The  $\nu$ -index is also used in the robustness margin calculation and robust controller design. When the uncertain parameter,  $p$ , is memoryless, possibly nonlinear time varying (NTV), the stability margin is given by

$$\inf_y \frac{y^T p(y)}{\|y\|^2} > 0 \quad (5.1.12a)$$

$$\sup_y \frac{\|p(y)\|^2}{y^T p(y)} < \frac{1}{\nu(T)} \quad (5.1.12b)$$

where  $T$  is the nominal closed loop transfer function around the uncertain element. When  $p$  is linear and symmetric, then (5.1.12) can be replaced by a more general condition:

$$p \geq 0 \quad (15.1.13a)$$

$$\|p\| < 1/\nu(T) \quad (5.1.13b)$$

Based on this argument, it can be shown [12] that the full state linear quadratic regulator and the Kalman filter possess  $[1/2, \infty]$  gain margin and  $[-60^\circ, 60^\circ]$  phase margin (with respect to perturbations in the control channel and output channel, respectively). For the dynamic output feedback case with LQG compensator, such as the case being considered now, the gain and phase margins are in general much more inferior than the full state feedback case. For a minimum phase system (which the system is for the first phase), a procedure termed loop transfer recovery ([13], [10]) can be used to systematically drive the loop shape closer to that of the full state feedback case. Basically, the procedure consists of modifying the noise covariance matrix  $M$  to

$$M = M_0 + q_1 B B^T \quad (5.1.14)$$

for input loop transfer recovery and modifying the state penalty weighting matrix  $Q$  to

$$Q = Q_0 + q_0 C^T C \quad (5.1.15)$$

for output loop transfer recovery. As  $q_1$  or  $q_0$  are increased, the recovery holds over wider bandwidth. However, it has been noted that simultaneous recovery of both the input and output loop transfer functions is in general not possible. The loop recovery is only accomplished for the low frequency band, the width of which is determined by the magnitude of  $q_1$  and  $q_0$ . For a robustness margin close to the full state feedback case, the loop recovery must hold over the closed loop bandwidth of the transfer functions with respect to the input and output channel perturbations, respectively. As  $q_1$  and  $q_0$  are both increased, the closed loop bandwidth also increases. Hence, it is possible that the loop can never recover fully over the closed loop bandwidth and the desired robustness margin is not obtained. For the Phase 1 experiment, the structure is described by two decoupled SISO systems. Then the input and output perturbations can both be lumped into the input channel or the output channel since the perturbation is a scalar quantity. The controller design models input channel perturbation only and uses the  $Q$  modification associated with the output channel perturbation (as in (5.1.15)) for performance enhancement.

A further advantage of using the  $\nu$ -index to characterize robustness is that nonlinear perturbations are included in the formulation since the derivation is based on Lyapunov theory rather than Nyquist plot arguments.

Thus, the gain and phase margin enhancement described in the previous paragraph holds for nonlinear effects in the actuators (such as Coulomb friction and stiction) and sensors (such as sensor noise), also. What about the actuator saturation? It is considered as a nonlinear perturbation in the input channel with slope bounded in the interval (0,1]. Even in the full state feedback case, only the nonlinearity with slope in [0.5,∞) can be tolerated. As a consequence, pointed out in [14], local, instead of global, exponential stability is achieved. The domain of convergence is determined by the [0.5,∞) stability margin. To increase the domain of convergence further, for the full state feedback case, a method has been proposed in [12] to effectively reduce the gain. This is achieved by replacing the input matrix B by  $\sigma B$  in the LQR design, then the robustness margin is widened to  $[\sigma, \infty)$ . As  $\sigma \rightarrow 0$ , the domain of convergence can be made arbitrarily large, i.e., the stability can be made close to global. To obtain wider margin for the LQG case, the loop transfer recovery should be used in conjunction with the modified design for LQR.

When the suspected sources of perturbation occur elsewhere in addition to the input and output channels, for example, uncertain modal frequencies, damping coefficients and mode shapes, gain and phase margins are no longer reliable measures of robustness and loop transfer recovery is not useful in general.

For this case, a design procedure based on the  $\nu$ -index can be formulated. Assume the system parameter matrices A, B, C and D are perturbed (the feedforward matrix D, in this case, is nominally zero and the perturbation is due to the unmodeled dynamics) as:

$$A = A_0 + H_1 \Delta A H_2 \quad (5.1.16a)$$

$$B = B_0 + F_1 \Delta B F_2 \quad (5.1.16b)$$

$$C = C_0 + J_1 \Delta C J_2 \quad (5.1.16c)$$

$$D = D_0 + L_1 \Delta D L_2 \quad (5.1.16d)$$

Suppose the specified lower bounds of the perturbation matrices are denoted by  $a_1$ ,  $b_1$ ,  $c_1$  and  $d_1$ , respectively. An  $H_2$ -based heuristic (see [15], [12]) provides a set of rules that is similar to the loop transfer recovery technique for modifying the penalty weightings and noise covariances:

$$Q = Q_0 + H_2^T H_2 + J_2^T J_2 \quad (5.1.17a)$$

$$R = R_0 + F_2^T F_2 + L_2^T L_2 \quad (5.1.17b)$$

$$M = M_0 + H_1 H_1^T + F_1 F_1^T \quad (5.1.17c)$$

$$N = N_0 + J_1 J_1^T + L_1 L_1^T \quad (5.1.17d)$$

It is interesting to note that this set of heuristics reduces to the LTR rules if perturbations in the input and output channels are considered. To ensure that the lower bounds of the perturbations are within tolerance, LQG design is performed with the modified system parameters:

$$A = A_0 - H_1 a_1 H_2 \quad (5.1.18a)$$

$$B = B_0 - F_1 b_1 F_2 \quad (5.1.18b)$$

$$C = C_0 - J_1 c_1 J_2 \quad (5.1.18c)$$

$$D = D_0 - L_1 d_1 L_2 \quad (5.1.18d)$$

The weightings are adjusted until robustness margins, as determined by  $\nu$ -index, include the upper bounds of the possible variations.

5.1.2.7. Guaranteed Stability Margin via  $\alpha$ -shift. An additional design parameter in the LQG framework described above is the guaranteed closed loop eigenvalue stability margin, denoted by  $\alpha$ . The A matrix used in the compensator design is replaced by  $A+\alpha I$ . The new system is called the  $\alpha$ -shifted system. The closed loop stability of the  $\alpha$ -shifted system then implies all the closed loop eigenvalues of the original system are to the left of the  $-\alpha+j\omega$  axis. When unmodeled modes are present, to ensure all closed loop eigenvalues, not just those in the reduced order model, have a stability margin of  $\alpha$ , functional convergence must hold for the full order  $\alpha$ -shifted system. Similarly, when the  $\nu$ -index is calculated, the  $\alpha$ -shifted system matrix must be used in the computation to ensure all the perturbed systems will not violate the  $\alpha$  stability margin requirement.

5.1.2.8. Discretization Schemes. So far, the discussion has been limited to the control law design, synthesis and analysis in the continuous time, i.e., the signal transmission is assumed instantaneous and the Kalman filter is implemented in continuous time. Since the control law calculation is performed in the computer, the closed loop system is actually a sampled data system. Hence, the control law must be implemented in discrete time. The true closed loop system is now described by:

$$\begin{aligned} \dot{x} &= Ax - BGS_1(\hat{x}) \\ \dot{\hat{x}} &= S_2((A-KC)\hat{x} - BGS_3(\hat{x}) + KS_4(y)) \end{aligned} \quad (5.1.19)$$

where  $S_1, S_2, S_3$  and  $S_4$  represent the effects of discretization. Typically,  $S_i, i=1,2,3,4$ , is composed of a sample and a hold of some order. Then the second equation can be implemented in the computer as a difference equation. Note that if  $S$  is a sample and zeroth order hold operator with sampling rate  $T$ ,

$$S(x(t)) = x(nT) \quad \text{if } nT \leq t < (n+1)T \quad (5.1.20)$$

Four different discretization algorithms were compared:

- (1) Impulse invariance transformation and hold with process output. (Treat  $y$  into the Kalman filter as a sample and hold process.)  
 $S_1, S_4$  = sample and zeroth order hold  
 $S_2, S_3$  = identity
- (2) Impulse invariance transformation and hold with process input and output. (Treat  $u$  and  $y$  into the Kalman filter as sample and hold processes.)  
 $S_1, S_3, S_4$  = sample and zeroth order hold  
 $S_2$  = identity
- (3) Bilinear transformation.  
 $S_1$  = sample and zeroth order hold  
 $S_2, S_3, S_4$  = Two-sample average ( i.e.,  $S(x(t)) = (x(nT)+x((n+1)T)) / 2$ , for  $nT \leq t < (n+1)T$ )
- (4) Backward difference.  
 $S_1, S_2, S_3, S_4$  = sample and zeroth order hold

The first three schemes all worked well in various cases tested in the simulation. The fourth scheme did not work well at all. In the Phase 1 experiment, Scheme 2 was used. Note that with  $S_i$ ,  $i = 1, 2, 3, 4$ , regarded as perturbation of the nominal (i.e. identity), a robustness analysis can also be performed with respect to these perturbations using the same tools discussed before. For Schemes 1 and 2, the perturbations occur in the input and output channels only. Therefore, it is expected that LTR will provide good robustness margins. A more detailed analysis of the effect of discretization will be carried out in future phases of the experiment.

5.1.2.9 Model Identification. As mentioned in Section 5.1.1.7, three different stages of model identification were performed. The first stage involved taking the FFT of the HS1 output under manual excitation at HA10 and fitting each observed resonant peak with the second order model characteristics. It has been assumed that the excitation is sufficiently close to a pulse that the spectrum of the input over the low frequency range is essentially flat. The second stage of identification involves using three different input excitation patterns and performing output prediction error minimization based on ARMAX parameterization of the model. Finally, the model parameters are fine tuned to give a good visual match between the simulated and actual responses. Separate and more detailed identification work has been slated for the structure in the future, at which time the controller will be updated based on the new model.

### 5.1.3 Results and Evaluation

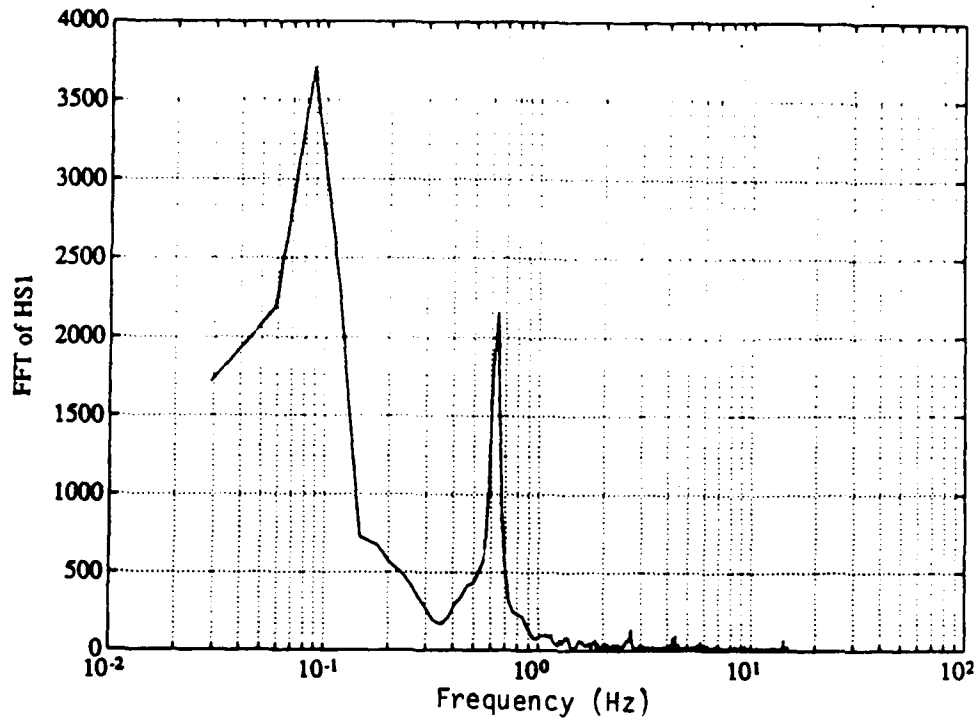
5.1.3.1. Introduction. This subsection is divided into three parts. The first part discusses the result of the preliminary identification efforts described earlier. The structure symmetry and hub decoupling assumption are examined in the second part. In the last part, the performance of the estimators and the controllers based on different plant models (analytic vs. identified), design parameters and input excitations is evaluated.

5.1.3.2. Preliminary Identification Test. The first stage of identification consists of manually exciting HA10 with a pulse-like input and then identifying the resonant peaks of the output in HS1. The excitation is assumed to be sufficiently close to an impulse that over the low frequency range (0-5 Hz) the resonant peaks correspond to a single second order mode. The FFT of the HS1 signal is shown in Fig. 5.1-2. The locations of the resonant peaks are listed in the table below:

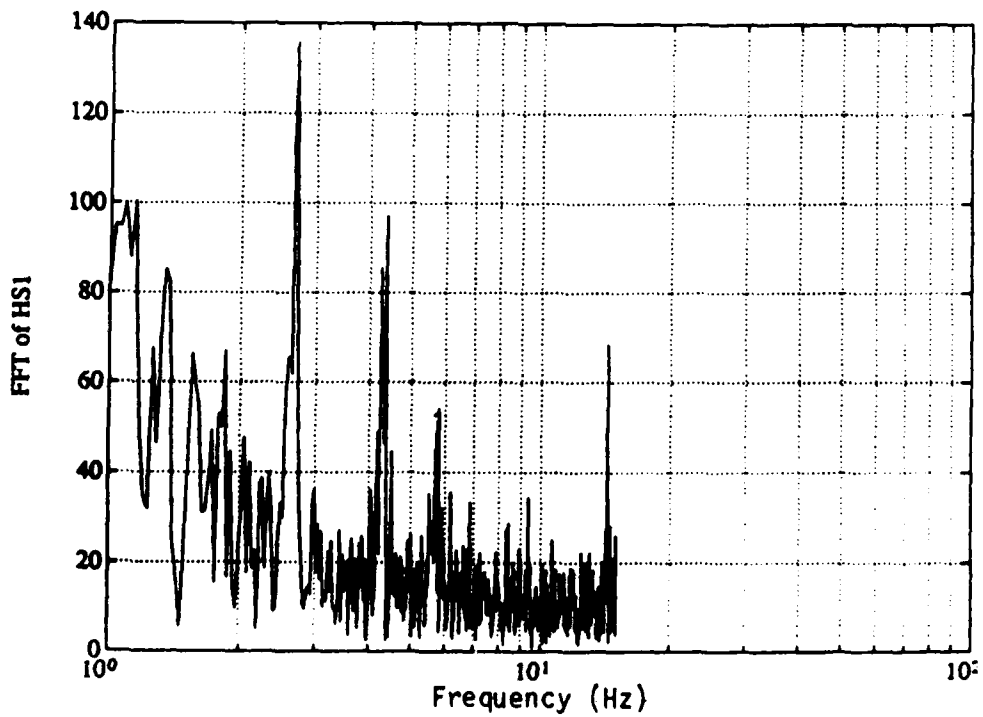
| Mode | Frequency |
|------|-----------|
| 1    | .12       |
| 2    | .64       |
| 4    | 2.70      |
| 5    | 4.37      |

Total number of points used in FFT = 1024  
 The frequency uncertainty (due to sampling)  
 =  $30 \text{ Hz} / 1024 = .03 \text{ Hz}$

Table 5.1-2 Identified Modal Frequencies Based on FFT Plots



(a) Complete Spectrum



(b) Expanded View of High Freq. Range

Figure 5.1-2 FFT of HS1



The third mode is buried in the noise which prevents clear identification of its location. A least squares fit is then performed to calculate the damping coefficient. The result is summarized below (again Mode 3 is not excited sufficiently for clear identification).

| Mode | Number of points used in the fit | Damping coefficient |
|------|----------------------------------|---------------------|
| 1    | 3                                | 17 %                |
|      | 4                                | 13 %                |
| 2    | 21                               | 18 %                |
|      | 16                               | 41 %                |
|      | 14                               | 37 %                |
|      | 12                               | 10 %                |
| 4    | 11                               | 5 %                 |
|      | 9                                | 2 %                 |
| 5    | 21                               | 5 %                 |

Table 5.1-3 Identified Modal Dampings Based on Least Squares Fit in FFT Plots

With this nonparametric method, the influence coefficients and readout coefficients (i.e., the B and C matrices) are not identified.

The next stage of identification involves the parametric method. The model is parameterized as an ARMAX model, i.e., the transfer function between the input and output is assumed to be of the form

$$A(q) y(t) = B(q) u(t-1) + C(q) e(t) \quad (5.1.21)$$

where  $y(t)$ ,  $u(t)$  and  $e(t)$  are output, input and white noise, respectively, A, B, and C are polynomials, and  $q$  corresponds to 1 time sample delay. The identification algorithm selects the coefficients of A, B, and C polynomials to minimize

$e^2(t)$ , where

$$e(t) = C(q)^{-1} ( A(q) y(t) - B(q) u(t-1) ) \quad (5.1.22)$$

based on the experimental data from the open loop response. By using various initial excitation patterns and experimenting with the orders of the A, B, and C polynomials, the following updated model is arrived at:

For HS1-HA10 modes

| Mode | Frequency | Damping | Influence coeff |
|------|-----------|---------|-----------------|
| 1    | .089      | 30%     | 4               |
| 2    | .63       | 3%      | 33              |
| 3    | 1.78      | 10%     | 2               |
| 4    | 2.00      | 12%     | 35              |
| 5    | 4.10      | 7%      | 100             |

Table 5.1-4 Identified Model Based on Minimization of Output Prediction Error

For HS10-HA1 modes

| Mode | Frequency | Damping | Influence coeff |
|------|-----------|---------|-----------------|
| 1    | .083      | 20%     | 4               |
| 2    | .61       | 0.75%   | 29              |
| 3    | 1.70      | 1%      | 3               |
| 4    | 2.00      | 38%     | 23              |
| 5    | 4.27      | 3%      | 10              |

Table 5.1-4 Identified Model Based on Minimization of Output Prediction Error (Continued)

The influence coefficient denotes the scalar multiplier associated with the transfer function of each mode, i.e., if the transfer function of Mode 1 is of the form

$$\frac{s}{s^2 + 2\zeta_i\omega_i s + \omega_i^2}$$

The influence function is the parameter a. Information on Modes 3-5 is very rough since they are not strongly excited and usually decay quickly into the noise level.

It is noted later that the updated model ensures closed loop stability but the performance under certain initial excitation patterns is poorer than the analytic model. Fine tuning of the model is carried out by adjusting frequencies, damping ratios and influence coefficients for good time history match. Agreement between output FFT divided by input FFT at the resonant frequency and the theoretical expectation is maintained as much as possible. A reasonable match is only obtained for the first two modes (see Figures 5.1-3 - 5.1-6); more refined ID techniques for the higher order modes are required to resolve the model with any confidence. A final refined model is summarized below:

For HS1-HA10 modes

| Mode | Frequency | Damping | Influence coeff |
|------|-----------|---------|-----------------|
| 1    | .0975     | 13.5%   | 3.2             |
| 2    | .635      | 2.5%    | 29.5            |

For HS10-HA1 modes

| Mode | Frequency | Damping | Influence coeff |
|------|-----------|---------|-----------------|
| 1    | .095      | 11%     | 5.2             |
| 2    | .615      | 0.9%    | 39              |

Table 5.1-5 Fine-tuned Model Based on Matching of Time Response

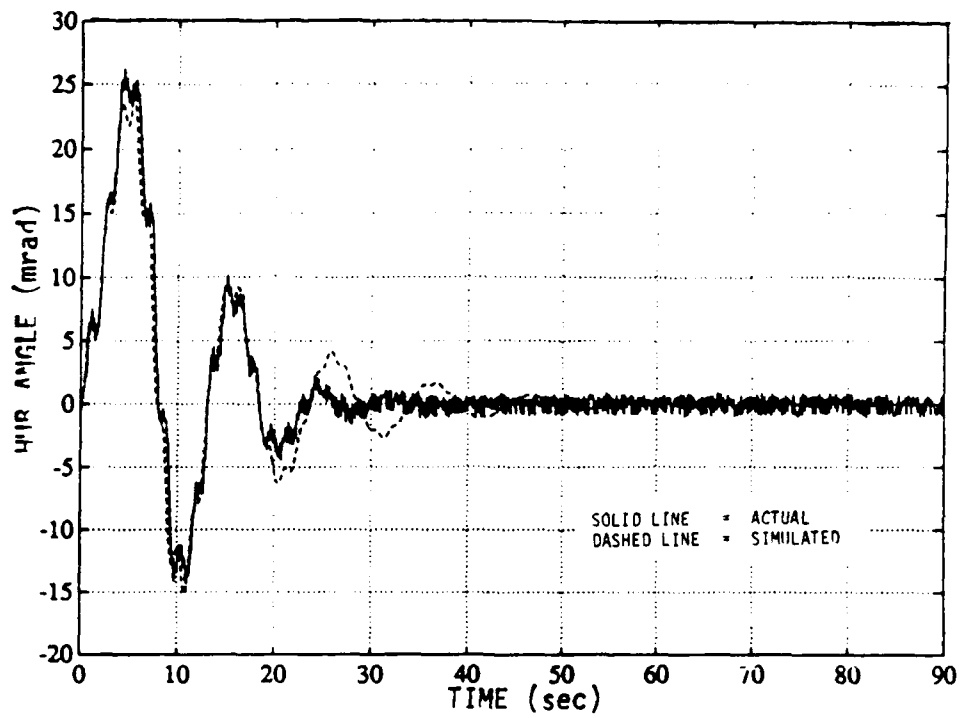


Figure 5.1-3 Simulated vs. Actual Response - HS1, Input Pattern 1

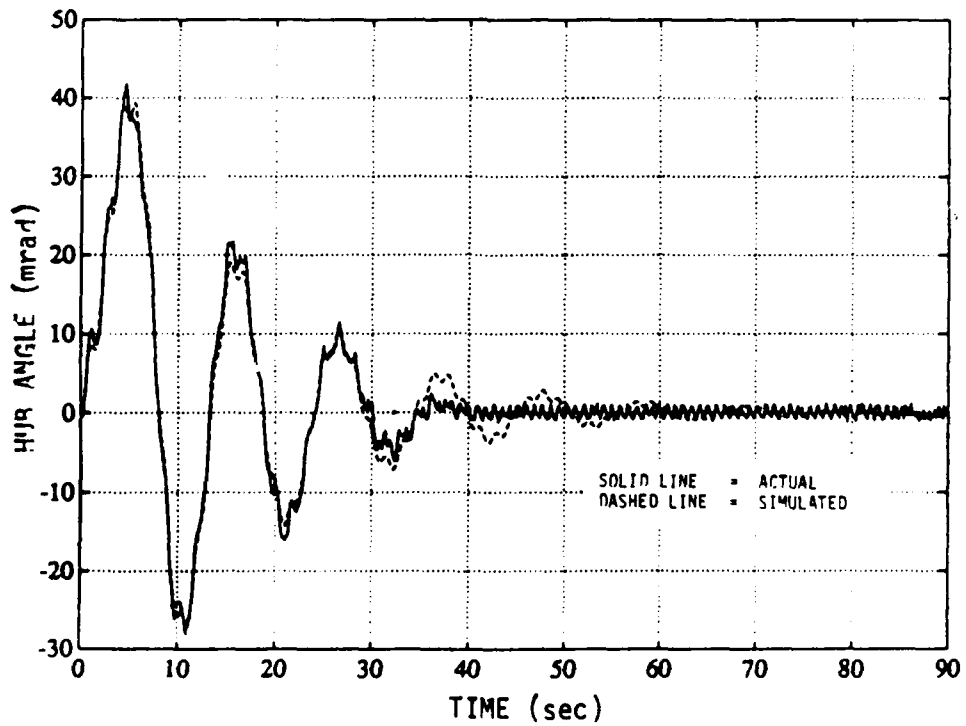


Figure 5.1-4 Simulated vs. Actual Response - HS10, Input Pattern 1

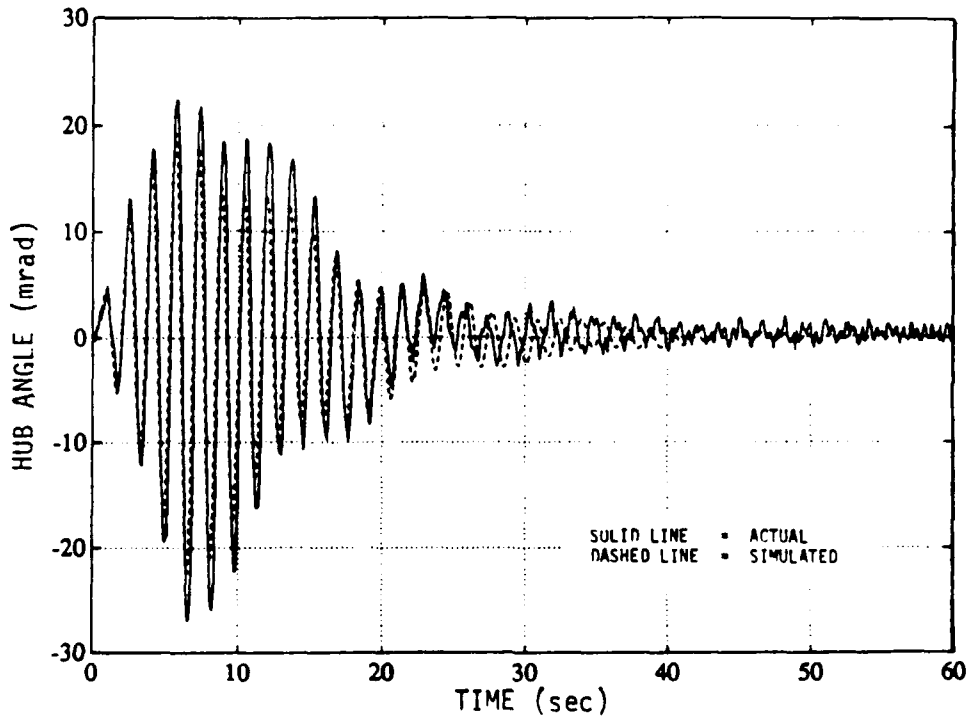


Figure 5.1-5 Simulated vs. Actual Response - HS1, Input Pattern 2

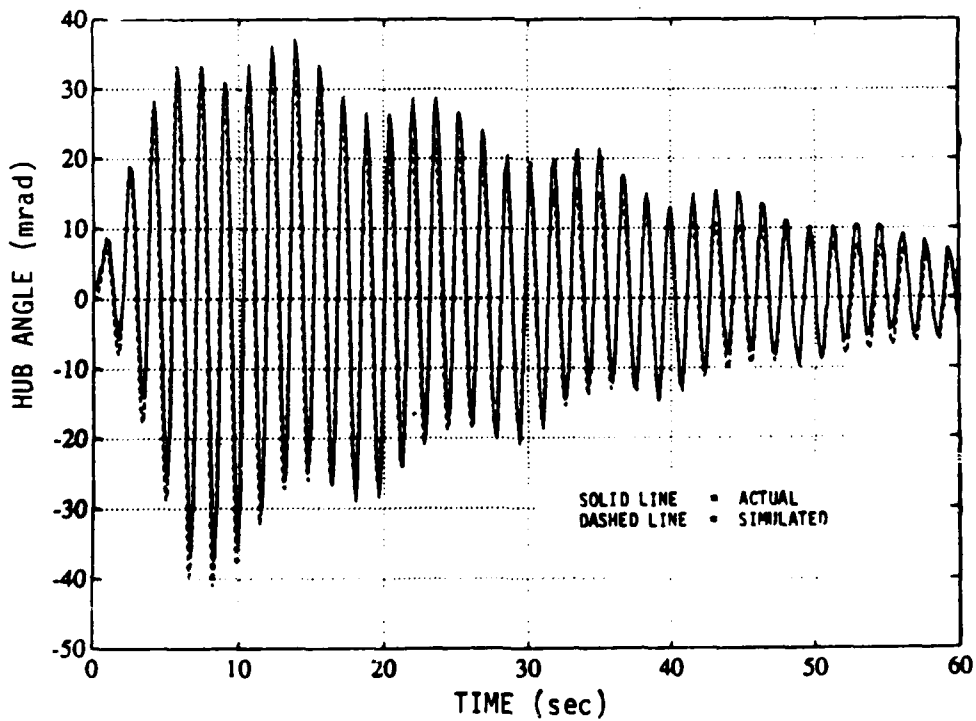


Figure 5.1-6 Simulated vs. Actual Response - HS10, Input Pattern 2

5.1.3.3. Hub Orthogonal Axes Decoupling Test. As mentioned in previous sections, the symmetry assumption (i.e., the ribs are of identical properties, symmetrically spaced around the hub) and the decoupling assumption (the sensors and actuators are mounted on the two orthogonal axes of the hub and the dynamics along the axes do not interact) are fundamental in the controller design. To check the validity of these assumptions, HA1 and HA10 are excited separately with input Patterns 1-3, and the response of HS10 and HS1 are compared. As shown in Figures 5.1-7 - 5.1-10, the amplitude of the dominant sensor response is much bigger, showing good decoupling. The comparative peak amplitudes are given below:

Only HA10 excited

| Input Pattern | Peak HS10 (mrad) | Peak HS1 (mrad) |
|---------------|------------------|-----------------|
| 1             | 21               | 3.5             |
| 2             | 30.8             | 3.6             |

Only HA1 excited

| Input Pattern | Peak HS10 (mrad) | Peak HS1 (mrad) |
|---------------|------------------|-----------------|
| 1             | 2                | 36.5            |
| 2             | 1.6              | 38.5            |

Table 5.1-6 Decoupling Test Result

5.1.3.4. Structure Symmetry Test. To test the symmetry assumption, the levitator measurements with input excitation Patterns 1-2 are cyclically transformed. Since the excitation is through the hub, only the boom modes should be excited. The amount of the 10 dish modes present is due to the asymmetry of the structure. In the table below, Mode 2 and Mode 12 are the boom modes. Large comparative peak amplitudes between the boom modes and the dish modes shown in the table below show good symmetry.

Input Pattern 1

| Spatial mode number | Inner levitator peak response | Outer levitator peak response |
|---------------------|-------------------------------|-------------------------------|
| 1                   | 4.9                           | 17.3                          |
| 2                   | 102.8                         | 167.6                         |
| 3                   | 8.4                           | 19.1                          |
| 4                   | 5.3                           | 13.5                          |
| 5                   | 3.4                           | 10.5                          |
| 6                   | 4.2                           | 12.4                          |
| 7                   | 4.1                           | 10.9                          |
| 8                   | 2.8                           | 6.3                           |
| 9                   | 4.5                           | 13.2                          |
| 10                  | 4.1                           | 12.0                          |
| 11                  | 5.4                           | 13.4                          |
| 12                  | 381.0                         | 640.0                         |

Table 5.1-8 Symmetry Test Result

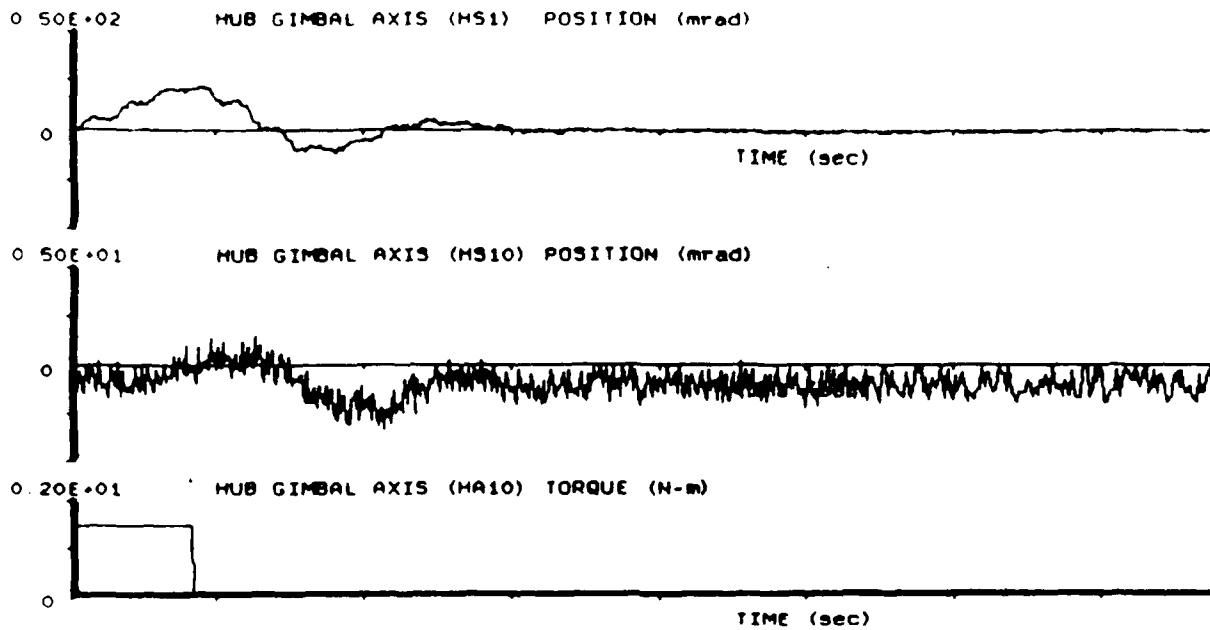


Figure 5.1-7 Decoupling Test - HA10, Input Pattern 1

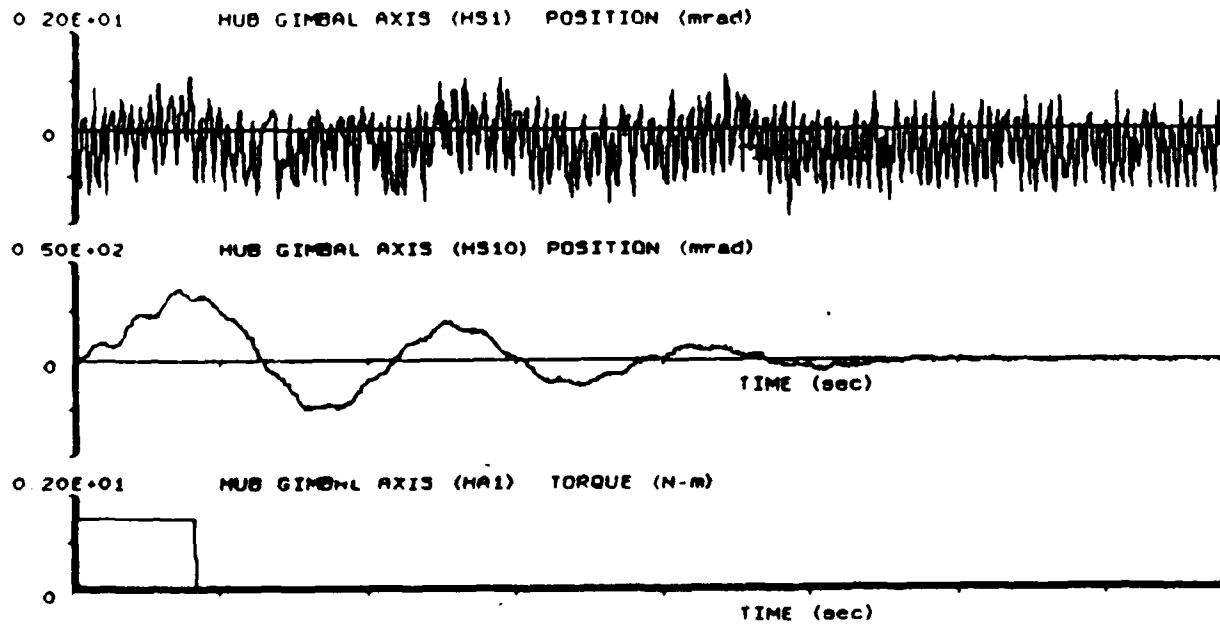


Figure 5.1-8 Decoupling Test - HA1, Input Pattern 1

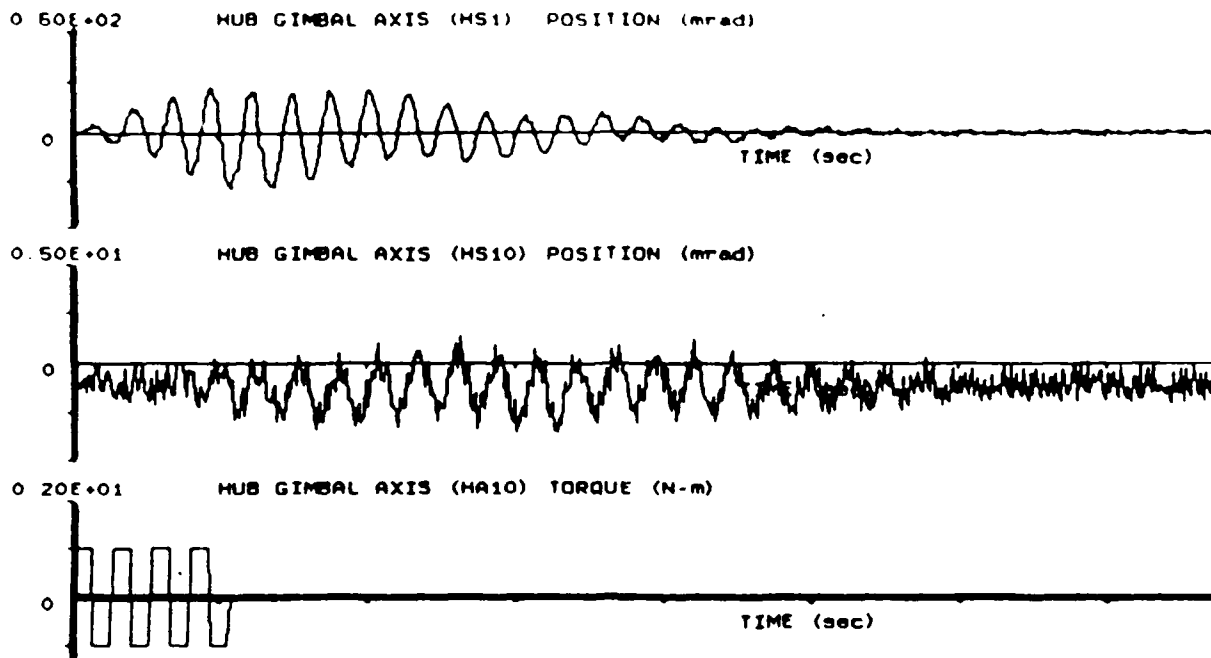


Figure 5.1-9 Decoupling Test - HA10, Input Pattern 2

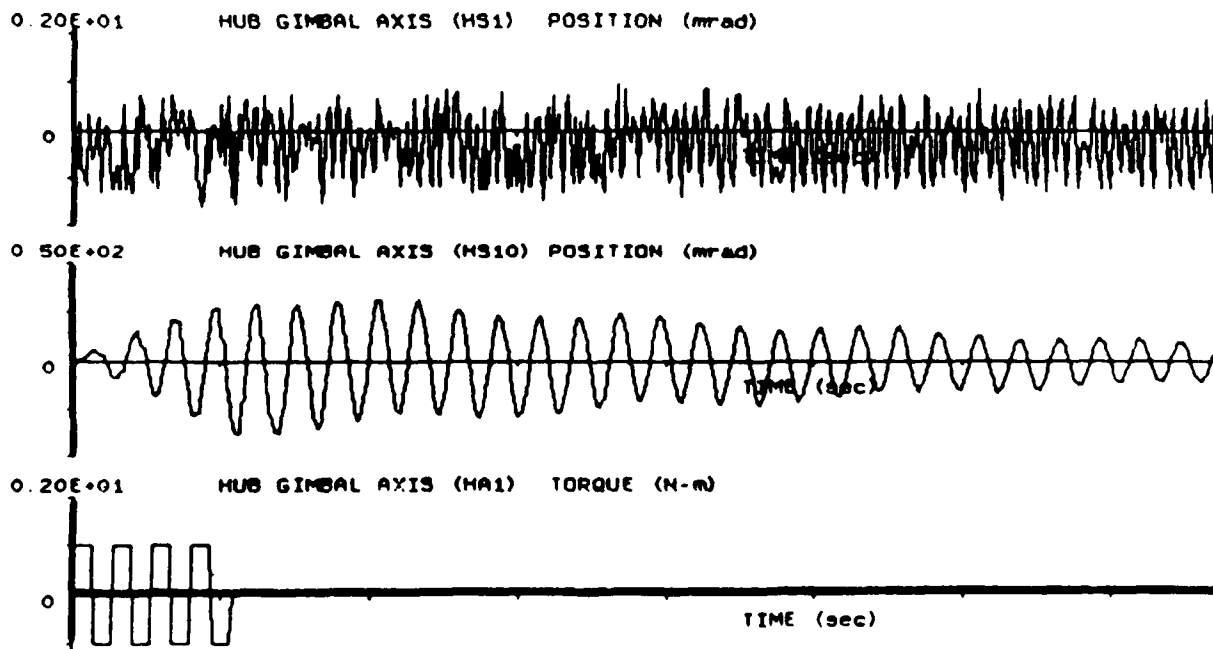


Figure 5.1-10 Decoupling Test - HA1, Input Pattern 2

Input Pattern 2

| Spatial mode number | Inner levitator peak response | Outer levitator peak response |
|---------------------|-------------------------------|-------------------------------|
| 1                   | 4.1                           | 10.5                          |
| 2                   | 74.7                          | 70.1                          |
| 3                   | 3.2                           | 4.1                           |
| 4                   | 1.9                           | 4.5                           |
| 5                   | 1.6                           | 2.6                           |
| 6                   | 4.1                           | 4.4                           |
| 7                   | 2.4                           | 4.1                           |
| 8                   | 2.7                           | 2.8                           |
| 9                   | 1.8                           | 4.5                           |
| 10                  | 1.7                           | 5.1                           |
| 11                  | 3.0                           | 6.4                           |
| 12                  | 201.5                         | 228.7                         |

Table 5.1-8 Symmetry Test Result (Continued)

5.1.3.5. Controller Performance Comparison. The testing of the control algorithms is closely related to the identification. Controllers are designed based on the analytic model and the identified models (three of them). They are then compared. The LQG-based algorithms mentioned in Section 5.1.2 allow many possible choices of parameters (especially coupled with robustness enhancement techniques). Before a controller was implemented on line, extensive simulation was performed to ensure good performance with respect to the model used. The actual performance was then observed and recorded. Some representative cases are highlighted here. The parameters associated with these cases are summarized in Table 5.1-9.

The modal frequencies and mode shapes (evaluated at the hub, levitators, boom tip and rib tips) of the analytic model are derived based on the finite element method. They are usually not too far off from the actual values. Damping ratios, however, are based on very crude guesses. Therefore, for the controllers based on the analytic model, good performance is not normally expected. It was found, surprisingly, that the analytic model is quite adequate for controller design, even superior to some of the identified models. This can be attributed to the fact that without performing a detailed ID experiment, the identified model may incur more error than the analytic model. The comparison between the performance of various controllers and the open loop response is based on two figures of merit:

- (1) Maximum overshoot
- (2) 10% settling time

The percentage improvement of the closed loop figures to open loop figures is calculated based on:

$$\left[ \frac{(\text{open loop settling time} - \text{length of initial excitation}) - (\text{closed loop settling time} - \text{length of initial excitation})}{(\text{open loop settling time} - \text{length of initial excitation})} \right] \div$$

$$\left[ \frac{\text{open loop overshoot} - \text{closed loop overshoot}}{\text{open loop overshoot}} \right] \div$$



Analytical Model

| Case no. | N | B | q1 | q2   | q11  | q12  | qr   | qb   | r | m1 | n1  | m2 | α |
|----------|---|---|----|------|------|------|------|------|---|----|-----|----|---|
| 1        | 2 | 1 | 10 | 1E-5 | 1E-6 | 1E-6 | 1E-5 | 1E-5 | 1 | 1  | 1E6 | 0  | 0 |
| 2        | 3 | 5 | 10 | 1E-5 | 1E-5 | 1E-5 | 1E-4 | 1E-4 | 1 | 1  | 1E6 | 0  | 0 |

First Identified Model

| Case no. | N | B | q1 | q2   | q11  | q12  | qr   | qb   | r | m1 | n1  | m2  | α   |
|----------|---|---|----|------|------|------|------|------|---|----|-----|-----|-----|
| 1        | 2 | 5 | 10 | 1E-5 | 1E-5 | 1E-5 | 1E-4 | 1E-4 | 1 | 10 | 1E6 | 0   | .30 |
| 2        | 3 | 5 | 10 | 1E-5 | 1E-5 | 1E-5 | 1E-4 | 1E-4 | 1 | 10 | 1E6 | 1E4 | .25 |

Second Identified Model

| Case no. | N | B | q1 | q2   | q11  | q12  | qr   | qb   | r | m1 | n1  | m2  | α   |
|----------|---|---|----|------|------|------|------|------|---|----|-----|-----|-----|
| 1        | 2 | 5 | 10 | 1E-5 | 1E-5 | 1E-5 | 1E-5 | 1E-5 | 1 | 10 | 1E6 | 0   | .20 |
| 2        | 3 | 5 | 10 | 1E-5 | 1E-5 | 1E-5 | 1E-5 | 1E-5 | 1 | 10 | 1E6 | 0   | .20 |
| 3        | 2 | 5 | 10 | 1E-5 | 1E-5 | 1E-5 | 1E-5 | 1E-5 | 1 | 10 | 1E6 | 1E3 | .10 |
| 4        | 2 | 5 | 10 | 1E-5 | 1E-5 | 1E-5 | 1E-5 | 1E-5 | 1 | 10 | 1E6 | 1E3 | .15 |
| 5        | 2 | 5 | 10 | 1E-5 | 1E-5 | 1E-5 | 1E-5 | 1E-5 | 1 | 10 | 1E6 | 1E5 | .15 |
| 6        | 2 | 5 | 50 | .50  | 1E-5 | 1E-5 | 1E-5 | 1E-5 | 1 | 10 | 1E6 | 1E5 | .10 |
| 7        | 2 | 1 | 20 | .50  | 1E-5 | 1E-5 | 1E-5 | 1E-5 | 1 | 50 | 1E6 | 1E5 | 0   |
| 8        | 2 | 1 | 40 | .25  | 1E-5 | 1E-5 | 1E-5 | 1E-5 | 1 | 50 | 1E6 | 1E5 | 0   |

Additional Parameters for Second Identified Model

| Case no. | qa1  | qa2 | qa0         | a1                 | σ   |
|----------|------|-----|-------------|--------------------|-----|
| 3        | 1E-3 | 1E3 | 0           | diag[.8 .2]        | 1   |
| 4        | 1E-3 | 1E3 | 0           | diag[.8 .2]        | 1   |
| 5        | 1E-3 | 1E3 | 0           | 0                  | 1   |
| 6        | 0    | 0   | [0 0 30 30] | 0                  | 1   |
| 7        | 0    | 0   | [0 0 20 20] | 0                  | .01 |
| 8        | 0    | 0   | 0           | diag[.35 .5 .1 .1] | .01 |

The robustness characterization matrices H1, H2 (see Section 5.1.2) for cases 3 and 4 are

$$\text{For HS1-HA10, } H_1 = \begin{bmatrix} 0 & 0 \\ 0 & 0 \\ 0 & 0 \\ -.24 & -3.96 \end{bmatrix} \quad H_2 = \begin{bmatrix} 0 & 0 & 0 & 1 \\ 0 & 0 & 3.96 & 0 \end{bmatrix}$$

$$\text{For HS10-HA1, } H_1 = \begin{bmatrix} 0 & 0 \\ 0 & 0 \\ 0 & 0 \\ -.06 & -3.83 \end{bmatrix} \quad H_2 = \begin{bmatrix} 0 & 0 & 0 & 1 \\ 0 & 0 & 3.83 & 0 \end{bmatrix}$$

For Case 10, H1 and H2 are

$$\text{For HS1-HA10, } H_1 = \begin{bmatrix} 0 & 0 & 0 & 0 \\ -.17 & 0 & -.61 & 0 \\ 0 & 0 & 0 & 0 \\ 0 & -.20 & 0 & -3.99 \end{bmatrix} \quad H_2 = \begin{bmatrix} 0 & 1 & 0 & 0 \\ 0 & 0 & 0 & 1 \\ .61 & 0 & 0 & 0 \\ 0 & 0 & 3.99 & 0 \end{bmatrix}$$

$$\text{For HS10-HA1, } H_1 = \begin{bmatrix} 0 & 0 & 0 & 0 \\ -.13 & 0 & -.60 & 0 \\ 0 & 0 & 0 & 0 \\ 0 & -.07 & 0 & -3.86 \end{bmatrix} \quad H_2 = \begin{bmatrix} 0 & 0 & 0 & 0 \\ 0 & 0 & 0 & 1 \\ .60 & 0 & 0 & 0 \\ 0 & 0 & 3.86 & 0 \end{bmatrix}$$

Fine Tuned Identification Model - (Combination of the cases above)

Table 5.1-9 Parameters for Controller Comparisons

These attributes are related to the outputs used in the compensators, namely, Hub Angles HS1 and HS10. The performance of the open loop responses (shown in Figures 5.1-11 - 5.1-12) under initial excitations 1 and 2 are:

| Input pattern | Maximum overshoot |      | 10% settling time |      |
|---------------|-------------------|------|-------------------|------|
|               | HS1               | HS10 | HS1               | HS10 |
| 1             | 13.5              | 27   | 21.9              | 41.5 |
| 2             | 23.1              | 32.7 | 33.8              | 74.7 |

Table 5.1-10 Open Loop Performance

The HA10-HS10 axis is much more disturbable and has lower damping than the HA10-HS1 axis. The signal in HS10 appears cleaner also.

The controllers based on the analytical model generally work adequately: the settling time improvement ranges from 20% to 70% and the overshoot improvement 10% to 100%. The time history is given in Figures 5.1-13 - 5.1-16. The hub angle sensor and hub torquer plots as well as the estimated states are included. The labeling of the plots requires some explanation. If a two-mode controller is used, then estimated Modes 1 and 2 correspond to the HS1-HA10 dynamics and estimated Modes 3 and 4 correspond to the HS10-HA1 dynamics. For three modes, estimated Modes 1-3 are for HS1-HA10 and 4-6 are for HS10-HA1. The beat pattern in the estimated mode three displacement and velocity indicate significant error in the model and actual frequencies. The specific performance relating to the Cases 1 and 2 is given below.

Case 1

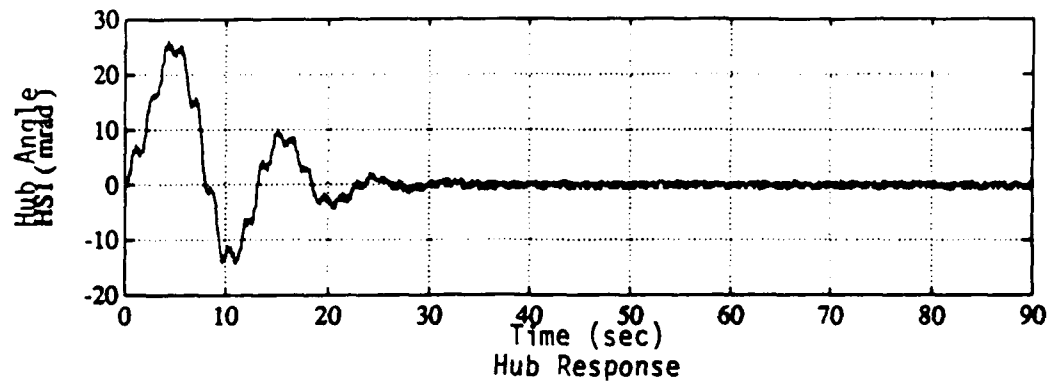
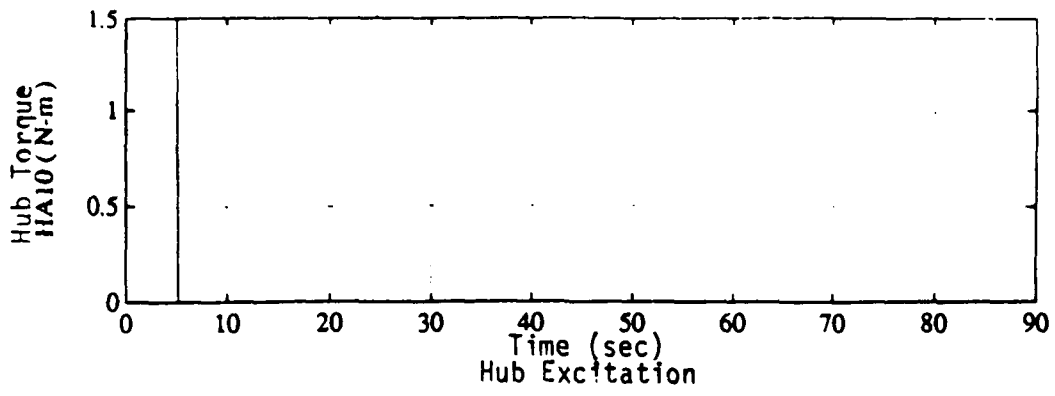
| Input pattern | Maximum overshoot (mrad) |           | 10% settling time (sec) |           |
|---------------|--------------------------|-----------|-------------------------|-----------|
|               | HS2                      | HS10      | HS1                     | HS10      |
| 1             | 5.5(59%)                 | 10.5(61%) | 14.5(44%)               | 18.7(62%) |
| 2             | 21.1(9%)                 | 28.8(12%) | 27.9(22%)               | 39.6(51%) |

Case 2

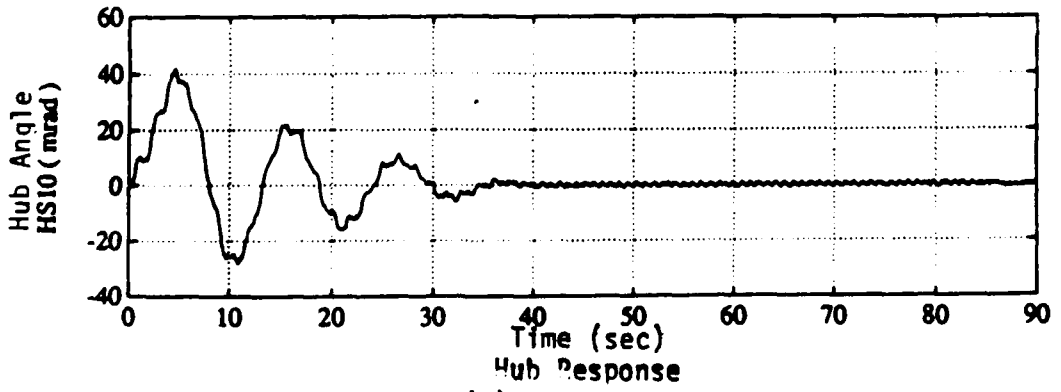
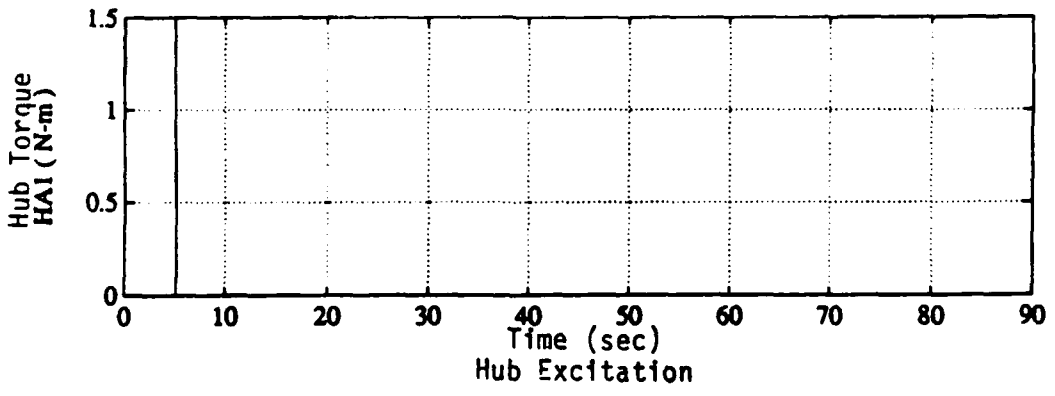
| Input pattern | Maximum overshoot (mrad) |           | 10% settling time(sec) |           |
|---------------|--------------------------|-----------|------------------------|-----------|
|               | HS1                      | HS10      | HS1                    | HS10      |
| 1             | 0(100%)                  | 0(100%)   | 14.7(43%)              | 14.9(73%) |
| 2             | 21.1(9%)                 | 28.8(12%) | 46.6                   | 59.0(23%) |

Table 5.1-11 Performance of Analytic Model Based Controllers

Values in the parentheses are the percentage improvements over the open loop responses. If the performance is actually worse than the open loop, then no value is given. It is evident that the performance is enhanced, especially in

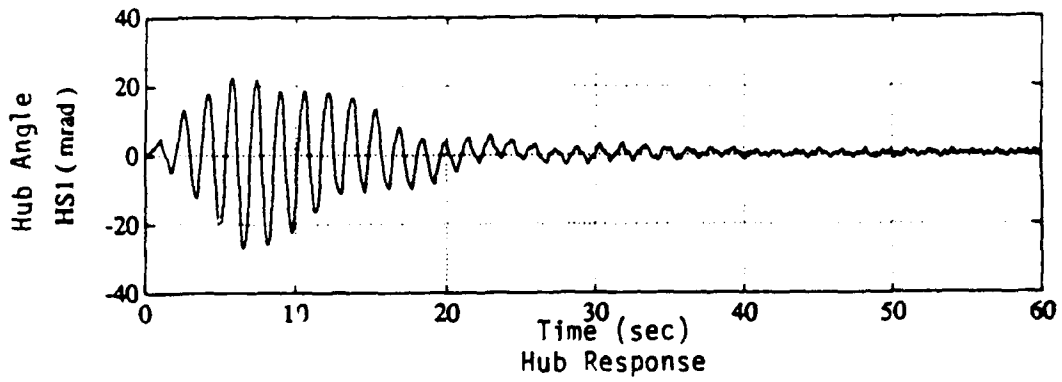
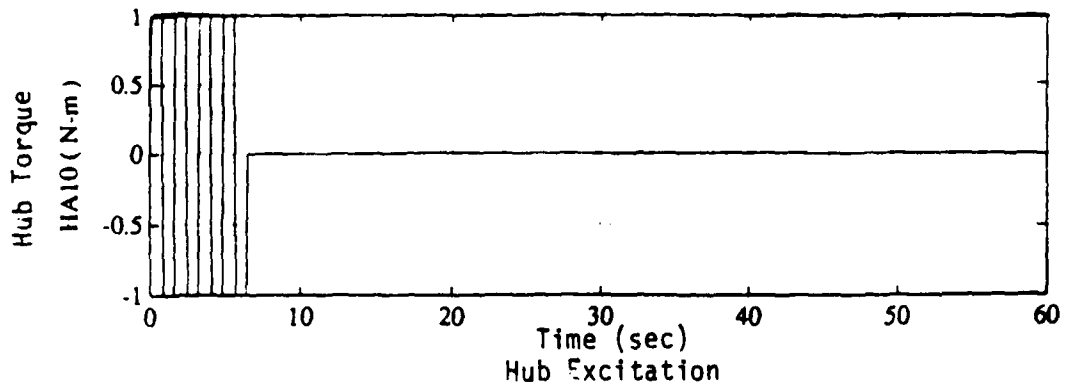


(a) HA10 - HS1 Axis



(b) HA1 - HS10 Axis

Figure 5.1-11 Open Loop Response - Input Pattern 1



(a) HA10 - HS1 Axis

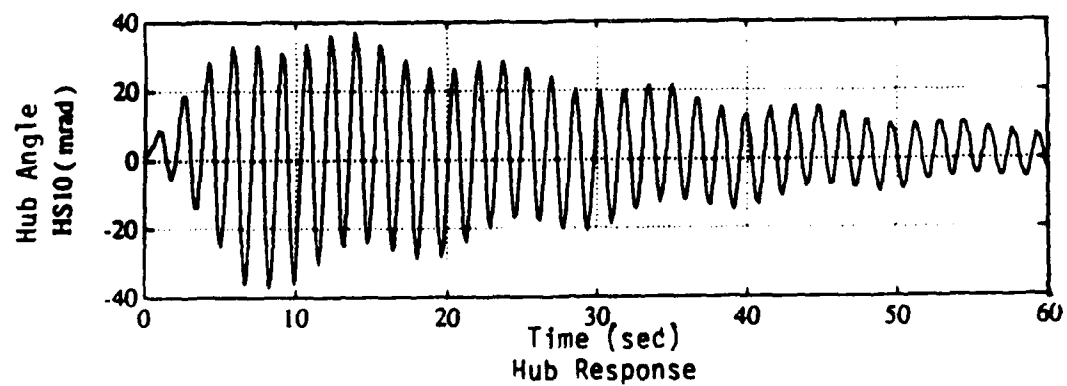
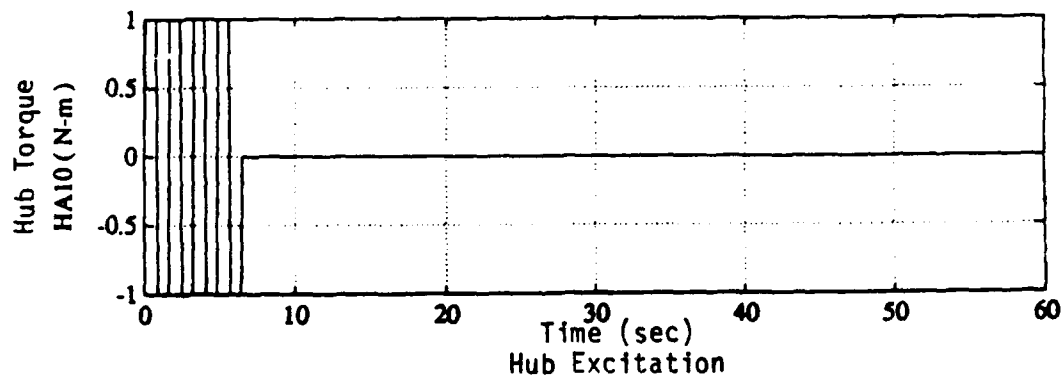


Figure 5.1-12 Open Loop Response - Input Pattern 2

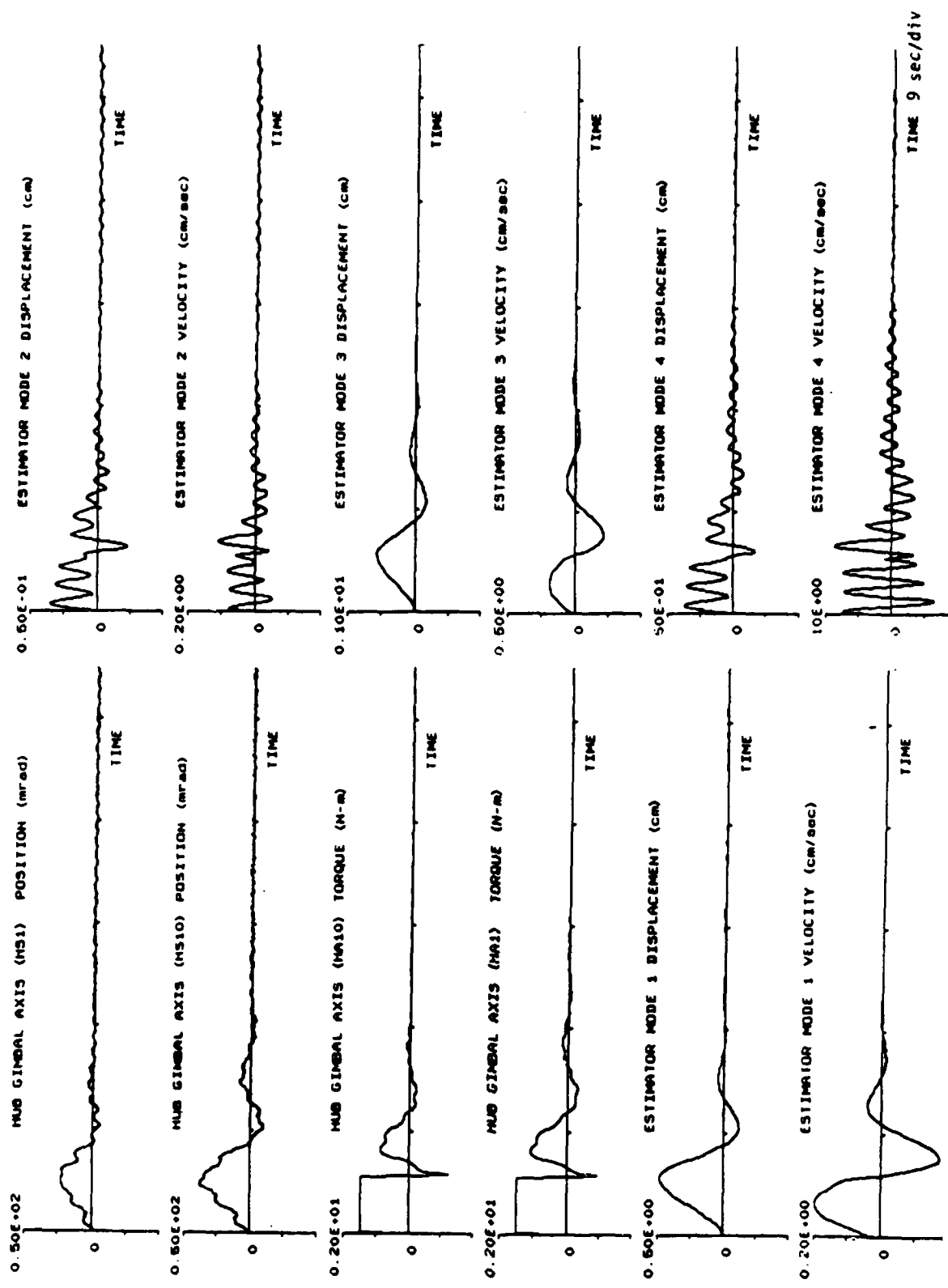


Figure 5.1-13 Time History Plots of Case 1 Controller with Analytic Model under Input Pattern 1

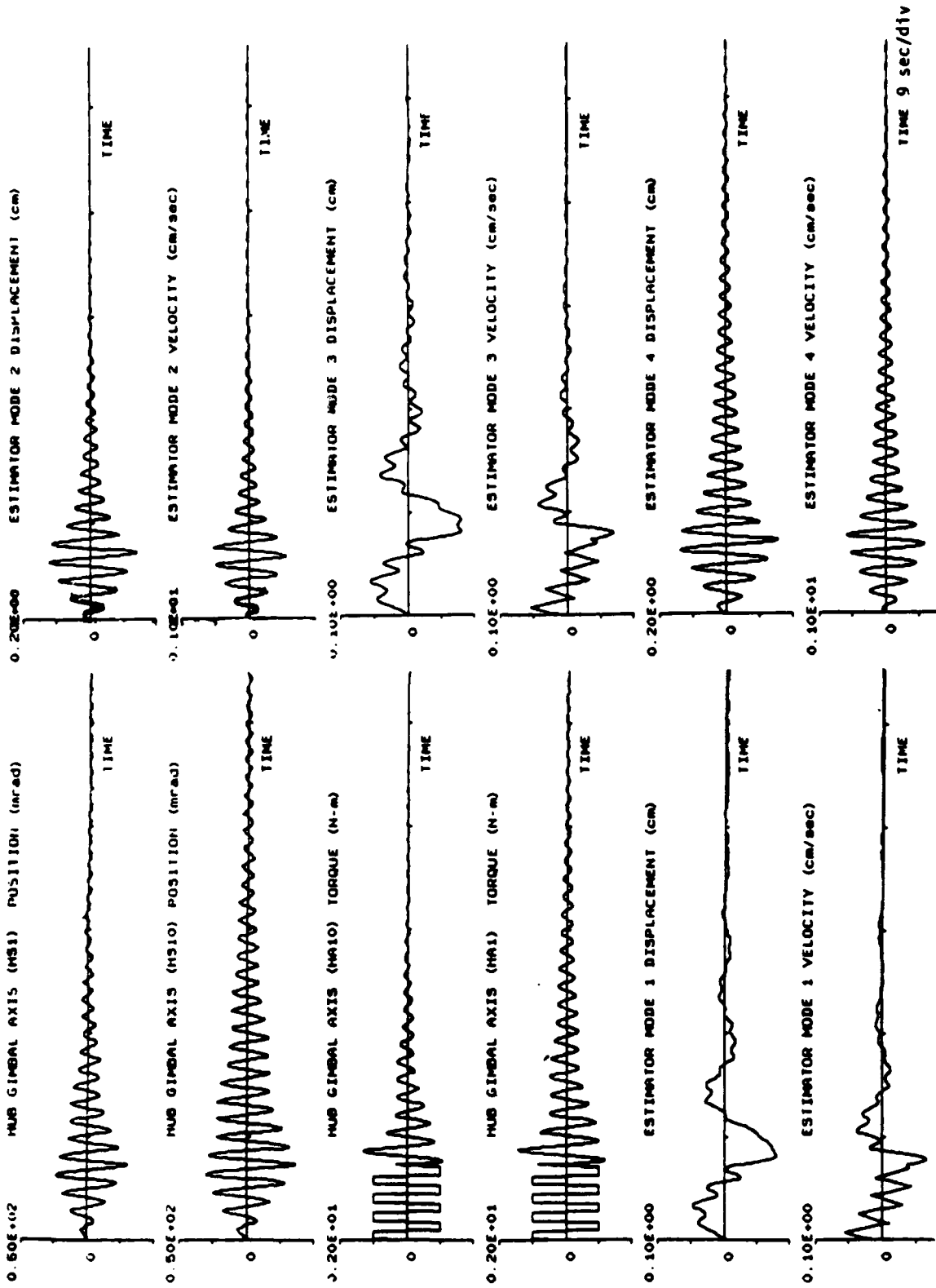


Figure 5.1-14 Time History Plots of Case 1 Controller with Analytic Model under Input Pattern 2

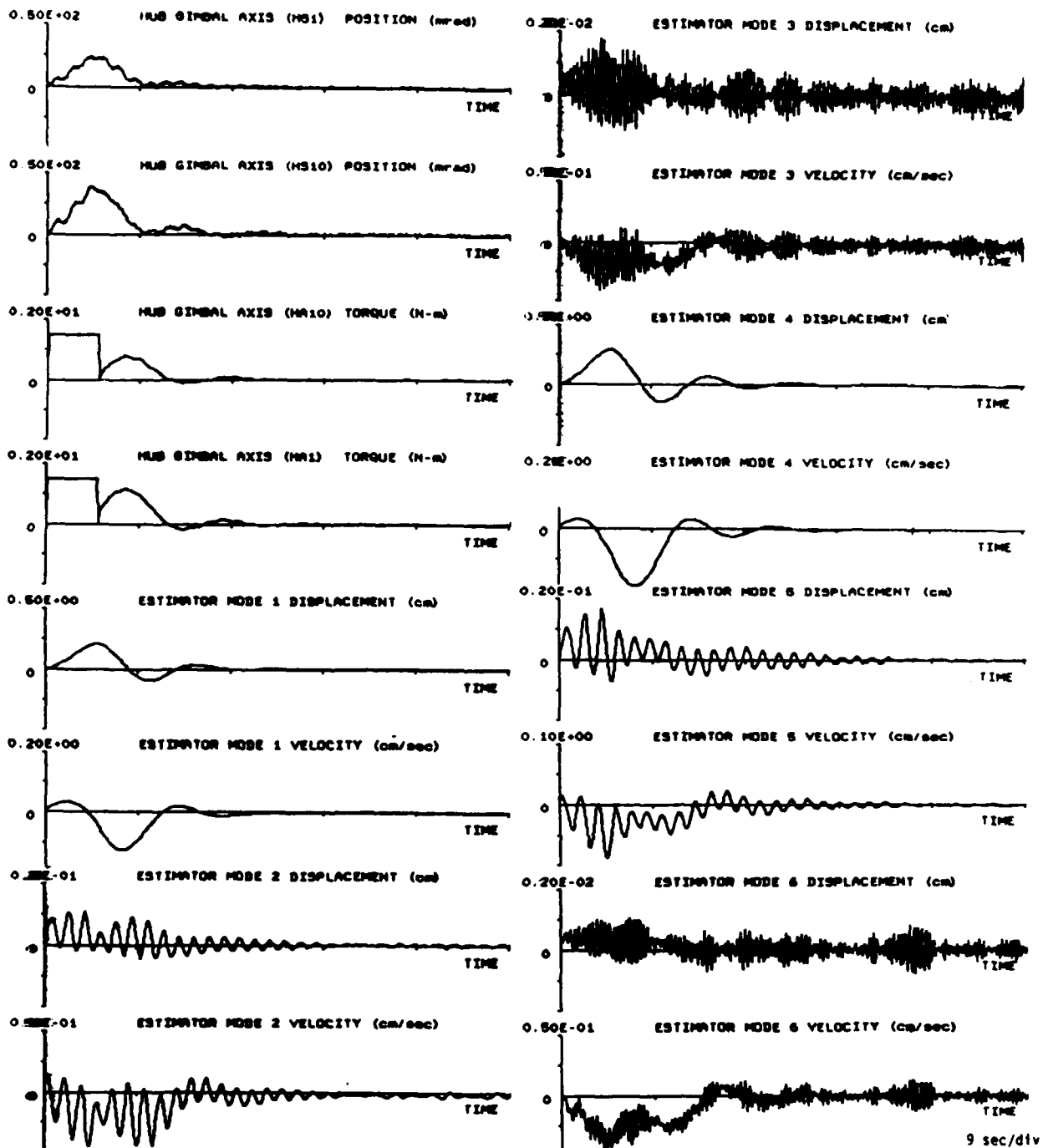


Figure 5.1-15 Time History Plots of Case 2 Controller with Analytic Model under Input Pattern 1

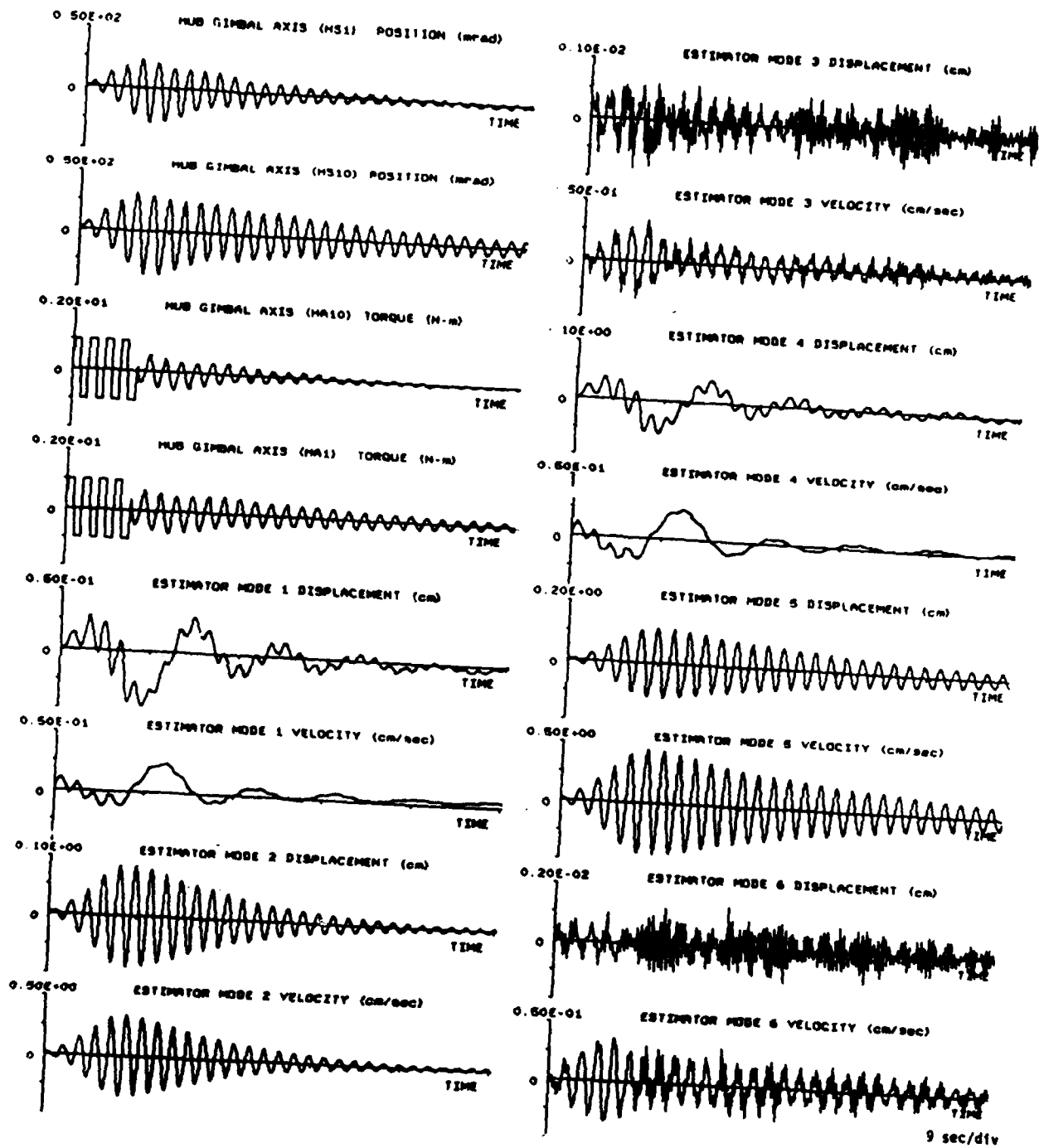


Figure 5.1-16 Time History Plots of Case 2 Controller with Analytic Model under Input Pattern 2



controller Case 2 with excitation Pattern 1 and controller Case 1 with excitation Pattern 2. The reason for the discrepancy between Cases 1 and 2 is likely to be the different accuracies of the first two modes in the analytic model. The analytic model is more accurate in the first mode (the pendulum mode); therefore, larger weightings in Case 2 produce the corresponding better performance when the first mode is predominantly excited. On the other hand, the second mode is not known as accurately; hence, higher gain may even contribute to a degradation of performance. This is seen with the excitation Pattern 2.

The controllers based on the first identified model have much larger damping ratios in the first two modes. Therefore, in order to see the impact of the control action, the weighting parameters must be increased. In general, the performance of these controllers is very good for excitation Pattern 1 and poor for excitation Pattern 2. In fact, when high performance is demanded (same as in Case 2, but  $m_2$ , the loop transfer recovery coefficient, is doubled to 1E8 or the hub angle penalty weighting increased to .1), the structure becomes unstable. The model based on the crude identification appears to be even worse off than the analytic model so far as controller design is concerned. Case 2 controller applies the LTR modification. Since the error is mainly in the modal frequencies and damping ratios, LTR was not expected and indeed did not make a significant difference. The time responses are shown in Figures 5.1-17 - 5.1-19. The specific performance for the representative cases is listed below:

| Case 1        |                         |                         |                        |                          |
|---------------|-------------------------|-------------------------|------------------------|--------------------------|
| Input pattern | Maximum overshoot(mrad) |                         | 10% settling time(sec) |                          |
| 1             | <u>HS1</u><br>3.1(77%)  | <u>HS10</u><br>5.8(79%) | <u>HS1</u><br>8.8(78%) | <u>HS10</u><br>17.0(67%) |
| 2             | 26.9                    | 34.6                    | 41.5                   | > 90                     |

| Case 2        |                   |                     |                    |                     |
|---------------|-------------------|---------------------|--------------------|---------------------|
| Input pattern | Maximum overshoot |                     | 10% settling time  |                     |
| 2             | <u>HS1</u><br>25  | <u>HS10</u><br>34.6 | <u>HS1</u><br>35.4 | <u>HS10</u><br>84.2 |

Table 5.1-12 Performance of First Identified Model Based Controller

The second identified model is more refined than the first identified model since the ID technique is slightly more sophisticated. Many cases were run based on this model. The performance with respect to excitation Pattern 1 is consistently worse than the analytical model based controllers. The performance with respect to excitation Pattern 2 is on a par with the analytical model based controllers. When the controllers are designed without any robustness enhancement, the performance, as given in the table below, is considerably worse than the analytical model case. The time

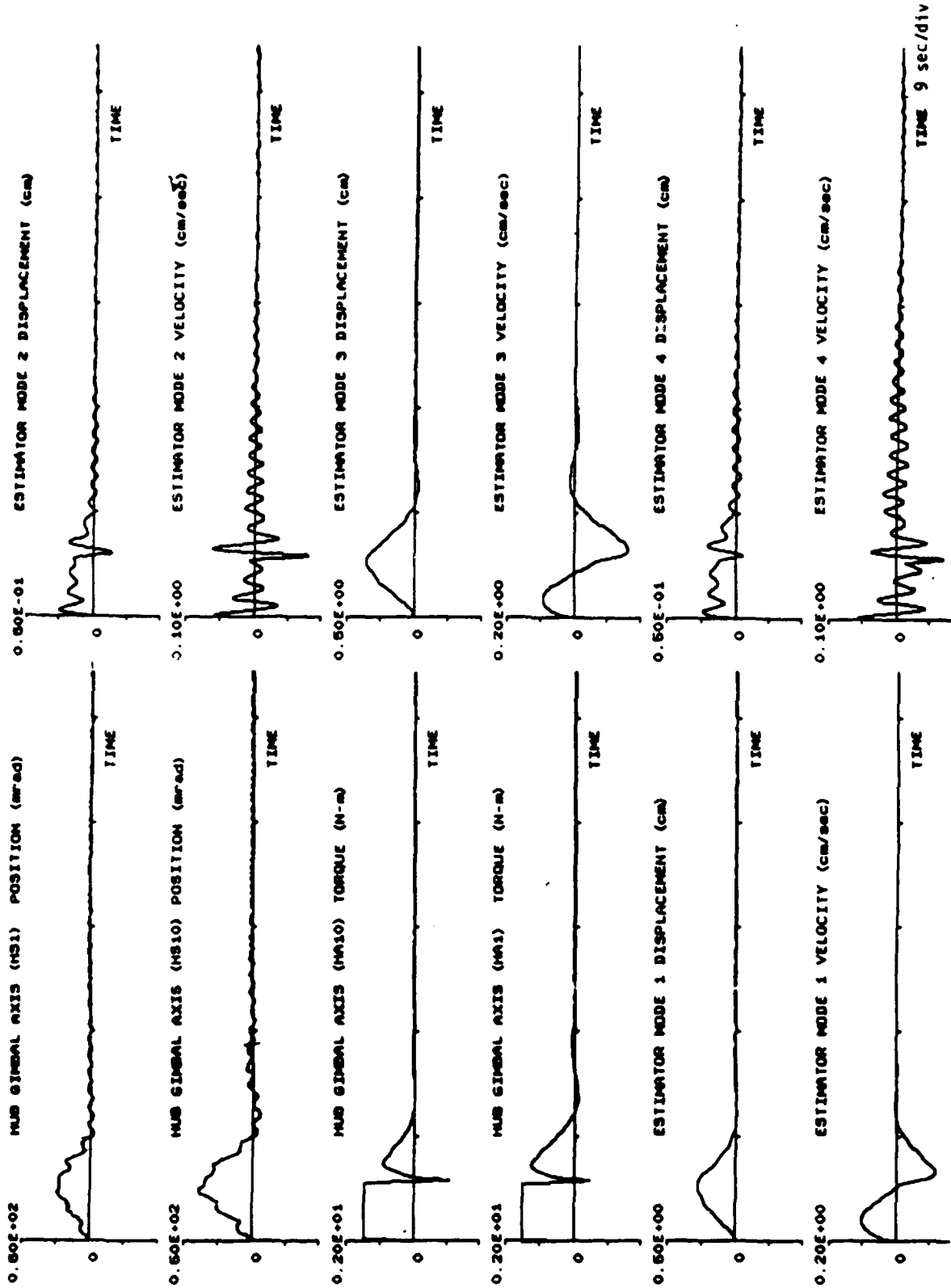


Figure 5.1-17 Time History Plots of Case 1 Controller with First Identified Model under Input Pattern 1

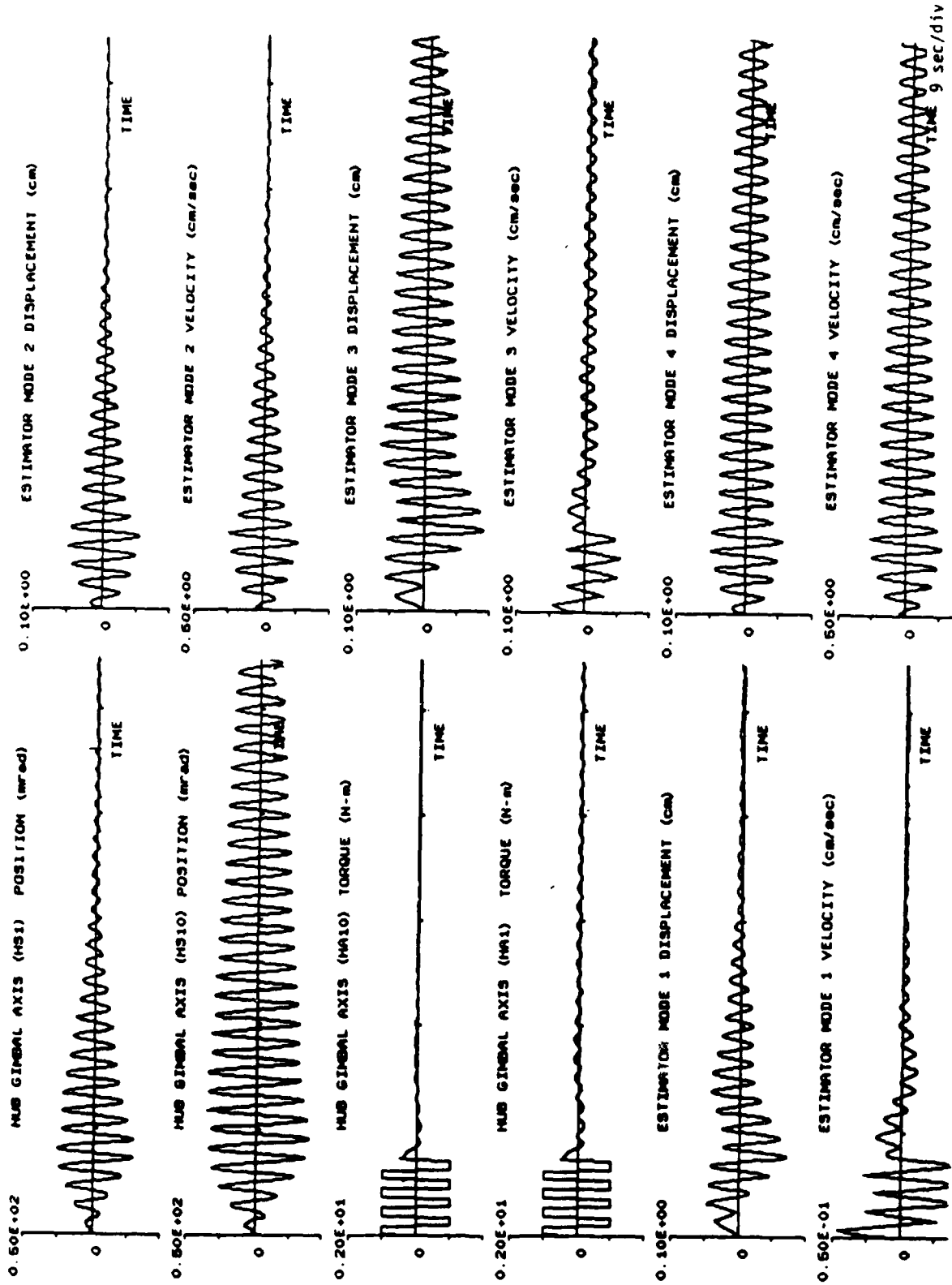


Figure 5.1-18 Time History Plots of Case 1 Controller with First Identified Model under Input Pattern 2

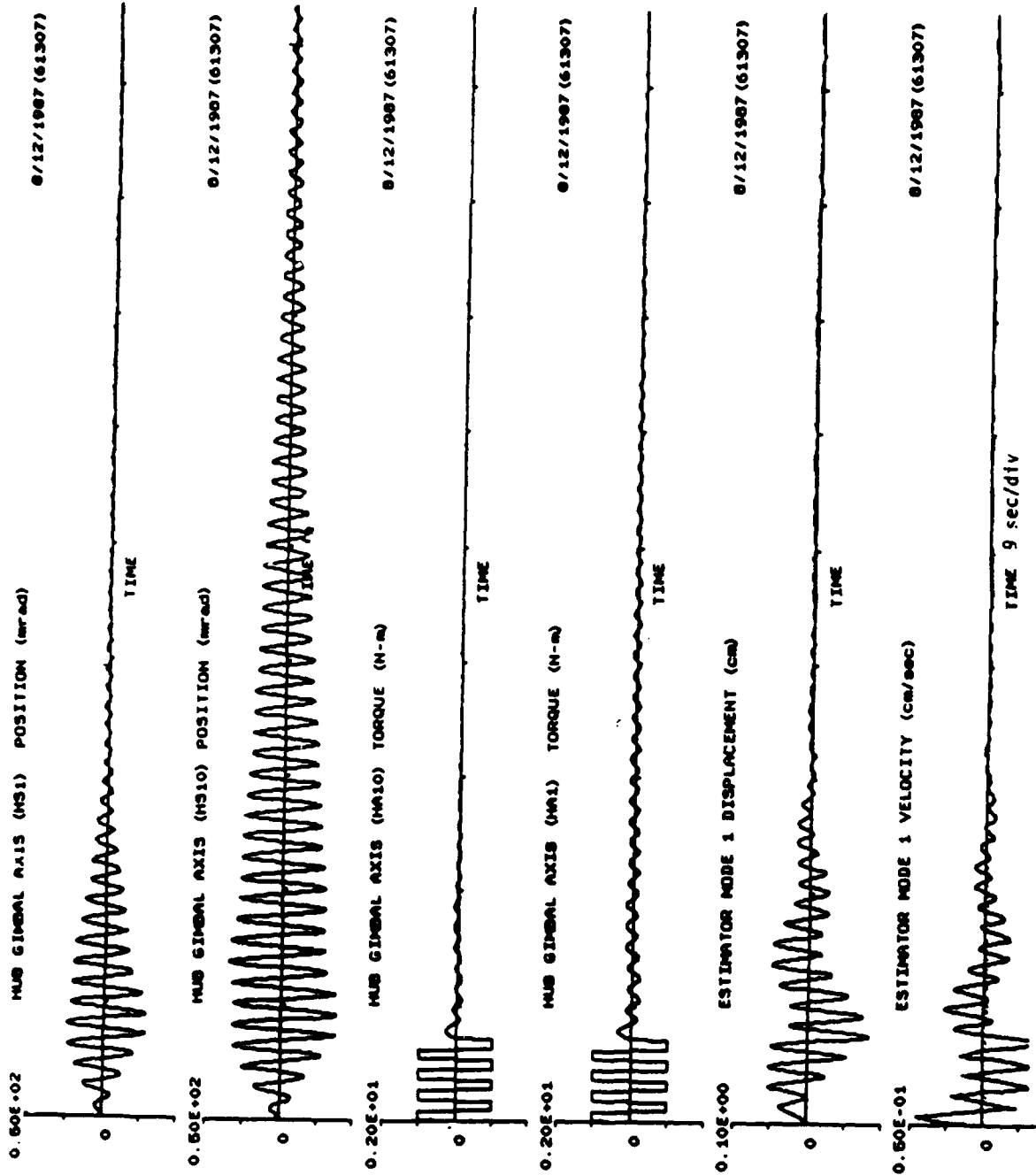


Figure 5.1-19 Time History Plots of Case 2 Controller with First Identified Model under Input Pattern 2

history plots are shown in Figures 5.1-20 - 5.1-22. The three-mode controller (Case 2) showed instability in the third mode (see the estimated Mode 3 displacement and velocity) which is likely caused by the inaccuracy in the model of the third mode.

Case 1

| Input pattern | Maximum overshoot |             | 10% settling time |             |
|---------------|-------------------|-------------|-------------------|-------------|
|               | <u>HS1</u>        | <u>HS10</u> | <u>HS1</u>        | <u>HS10</u> |
| 1             | 5.8(57%)          | 10.4(61%)   | 15.1(40%)         | 21.3(55%)   |
| 2             | 18.5(20%)         | 26.9(18%)   | 30.3(13%)         | 48.6(38%)   |

Case 2

| Input pattern | Maximum overshoot |             | 10% settling time |             |
|---------------|-------------------|-------------|-------------------|-------------|
|               | <u>HS1</u>        | <u>HS10</u> | <u>HS1</u>        | <u>HS10</u> |
| 2             | 19.2(17%)         | 26.9(18%)   | 32(7%)            | 40.5(50)    |

Table 5.1-13 Performance of Second Identified Model Based Controller (Cases 1 - 2)

Simultaneously enhanced performance and robustness were attempted next by using the idea based on the positive realness concept in Section 5.1.2. This is represented by Cases 3-5; Cases 3-4 are used in the controller design and Case 5 is used for the estimator design. The modified control design involves subtracting a lower bound of uncertainty from the system Matrix A and using it in the design. Furthermore, Q and M are modified according to the rule stated in Section 5.1.2. Since most of the uncertainty is suspected to be due to Mode 2, the above modification pertains to the uncertain modal frequency and damping of Mode 2 in particular. The effect of robustness enhancement modification puts additional emphasis on Mode 2, hence the performance with respect to excitation Pattern 2 is improved from Cases 1 and 2. Compared with the analytical model based controller, the performance is slightly better, also. The controller gain corresponding to the first mode becomes too small, due largely to the high damping in the model, and the response with respect to excitation Pattern 1 is therefore very poor. Time history plots of these cases are shown in Figures 5.1-23 - 5.1-26. The performances of these cases are summarized below:

Case 3

| Input pattern | Maximum overshoot |             | 10% settling time |             |
|---------------|-------------------|-------------|-------------------|-------------|
|               | <u>HS1</u>        | <u>HS10</u> | <u>HS1</u>        | <u>HS10</u> |
| 1             | 13.5(0%)          | 28.1        | 25.7              | 40.5(3%)    |
| 2             | 19.2(17%)         | 26.9(18%)   | 32.9(3%)          | 39.2(52%)   |

Table 5.1-14 Performance of Second Identified Model Based Controller (Cases 3 - 4)

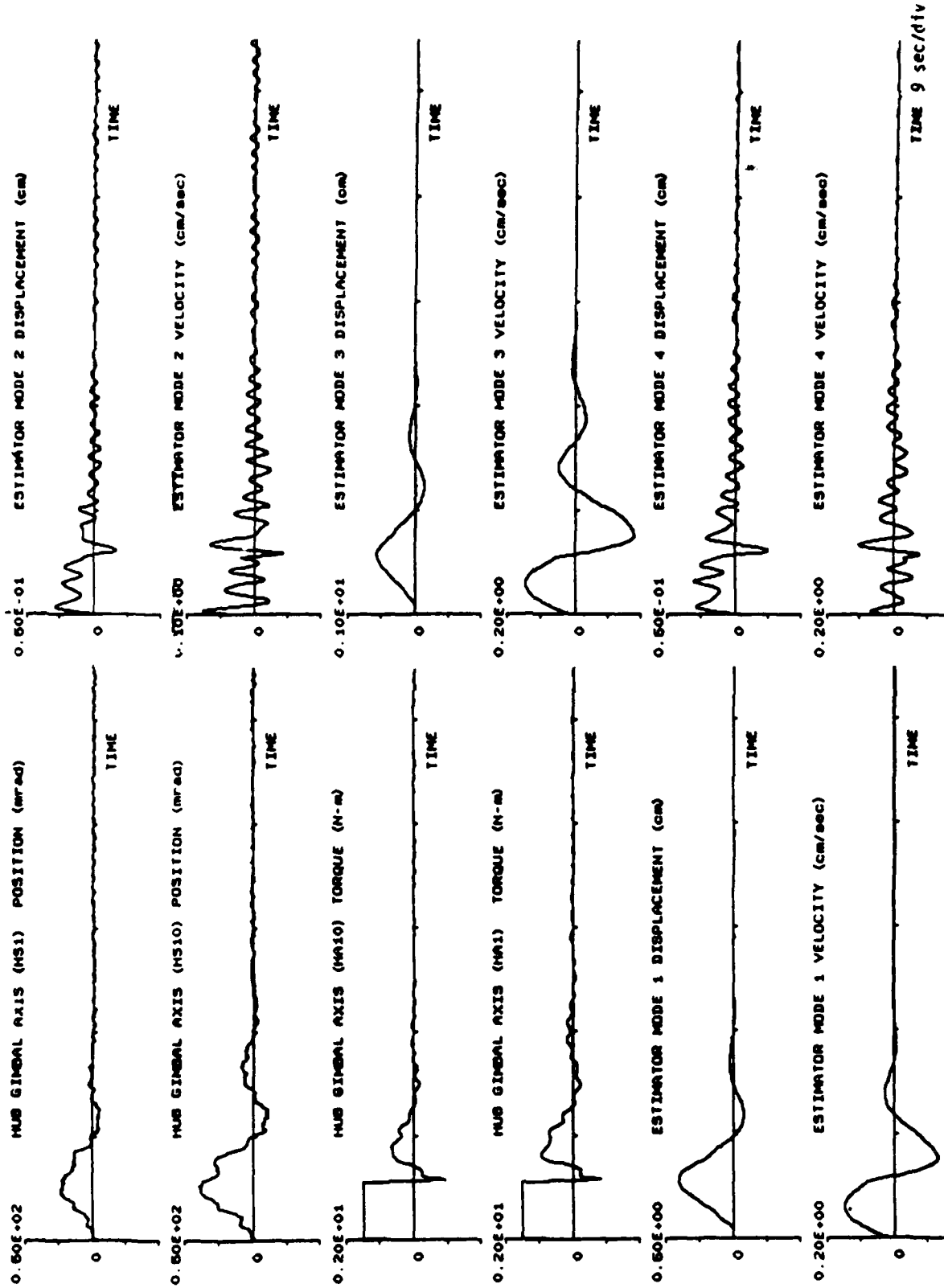


Figure 5.1-20 Time History Plots of Case 1 Controller with Second Identified Model under Input Pattern 1

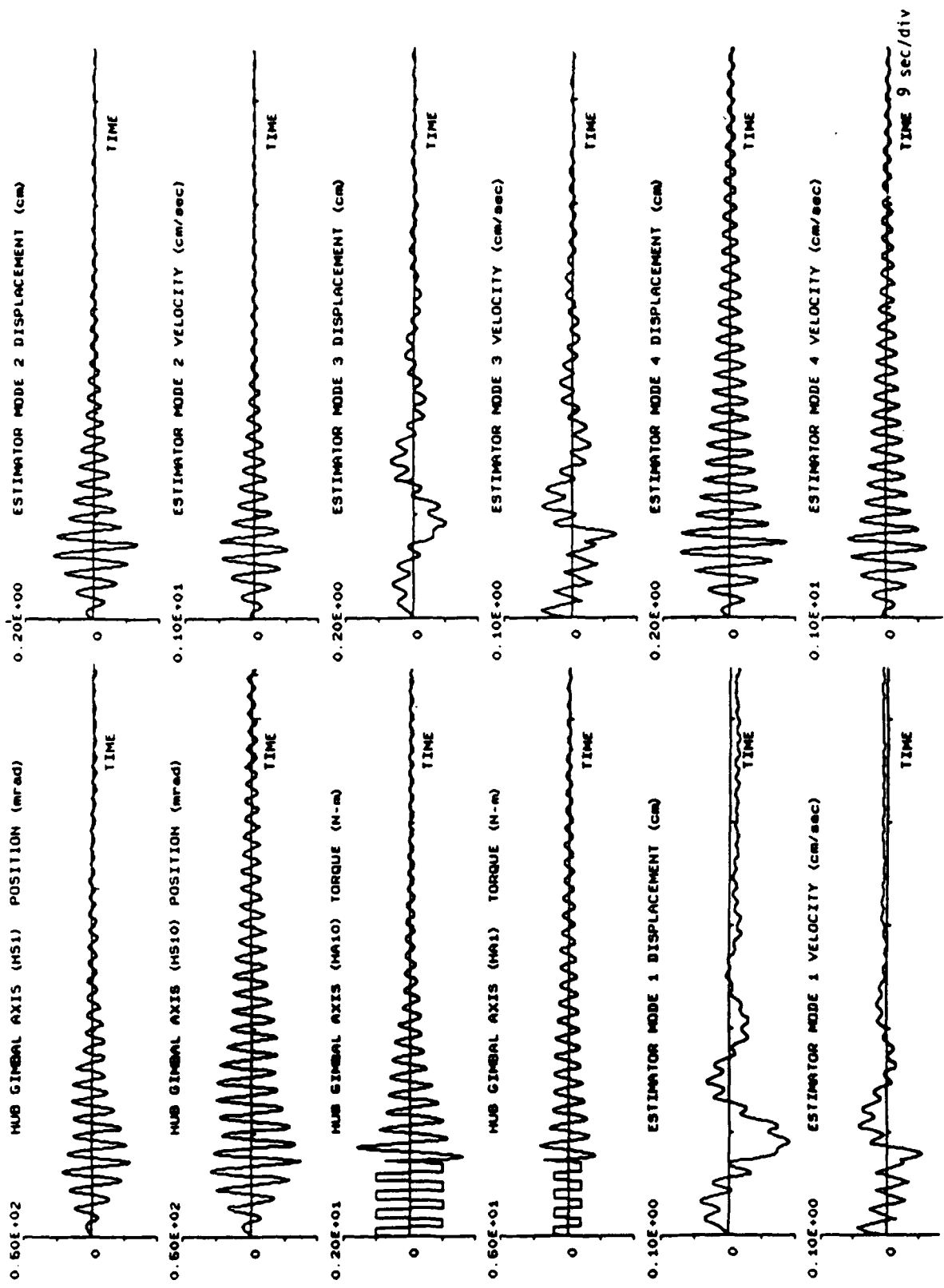


Figure 5.1-21 Time History Plots of Case 1 Controller with Second Identified Model under Input Pattern 2

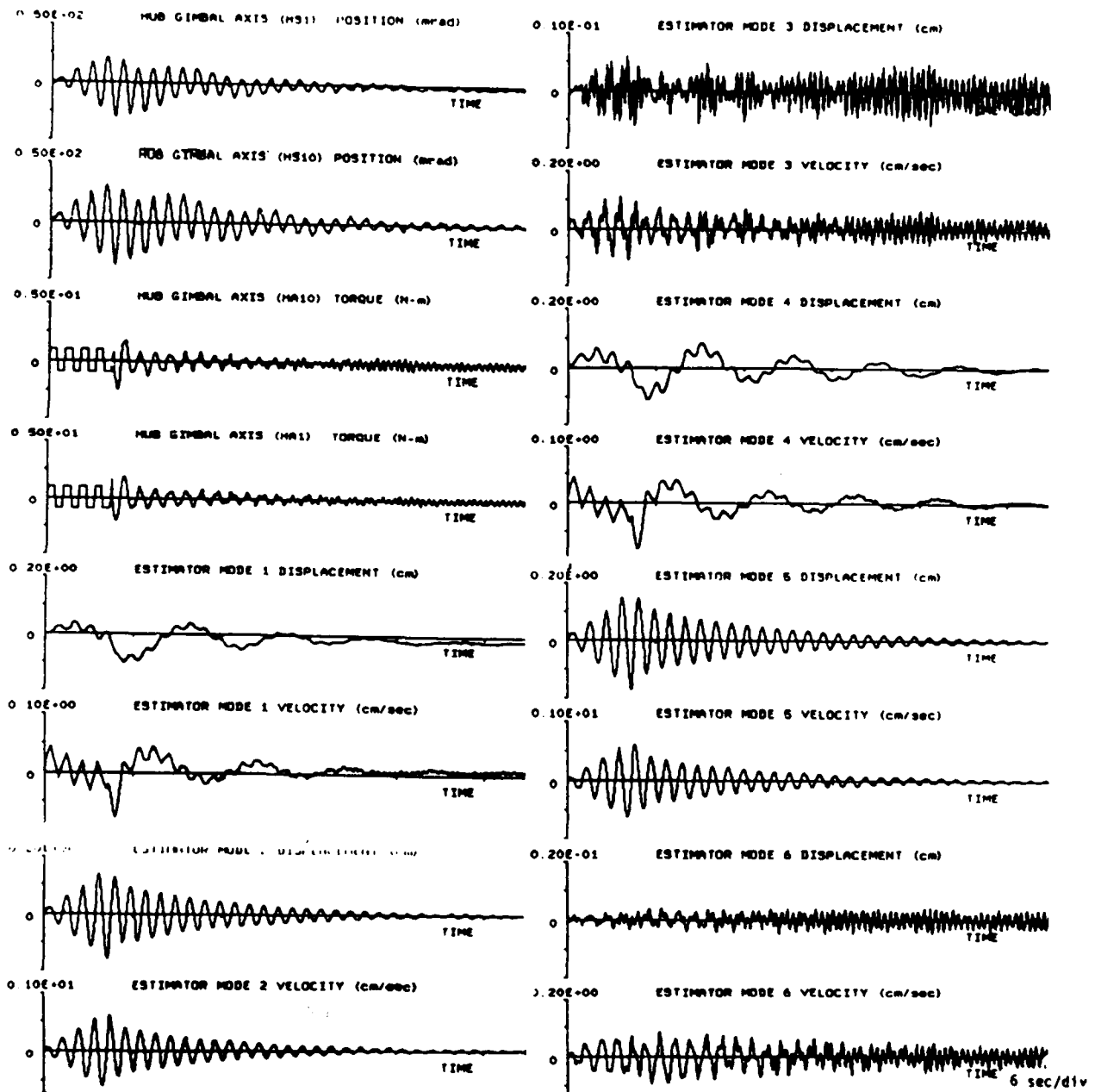


Figure 5.1-22 Time History Plots of Case 2 Controller with  
Second Identified Model under Input Pattern 2



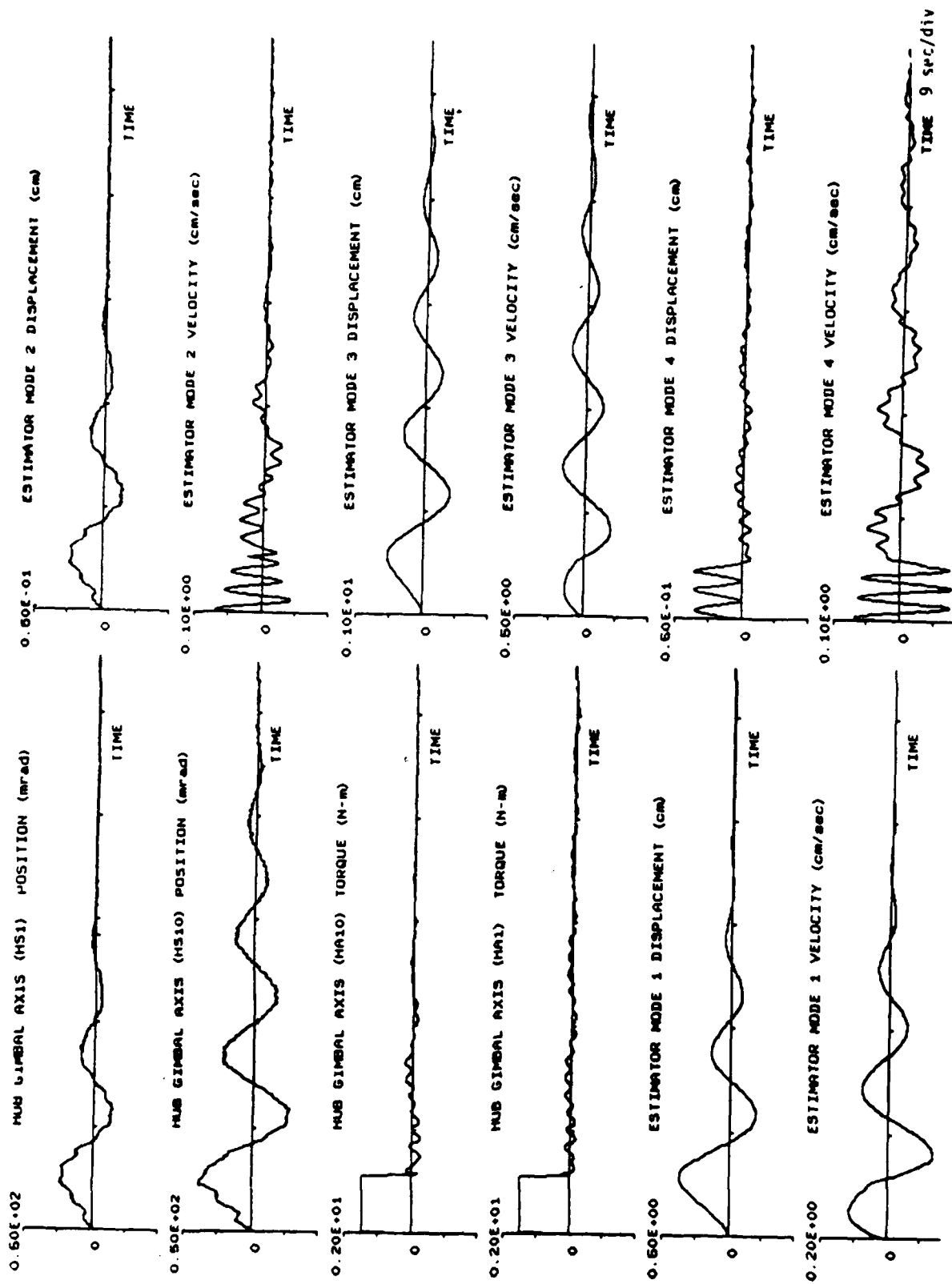


Figure 5.1-23 Time History Plots of Case 3 Controller with Second Identified Model under Input Pattern 1

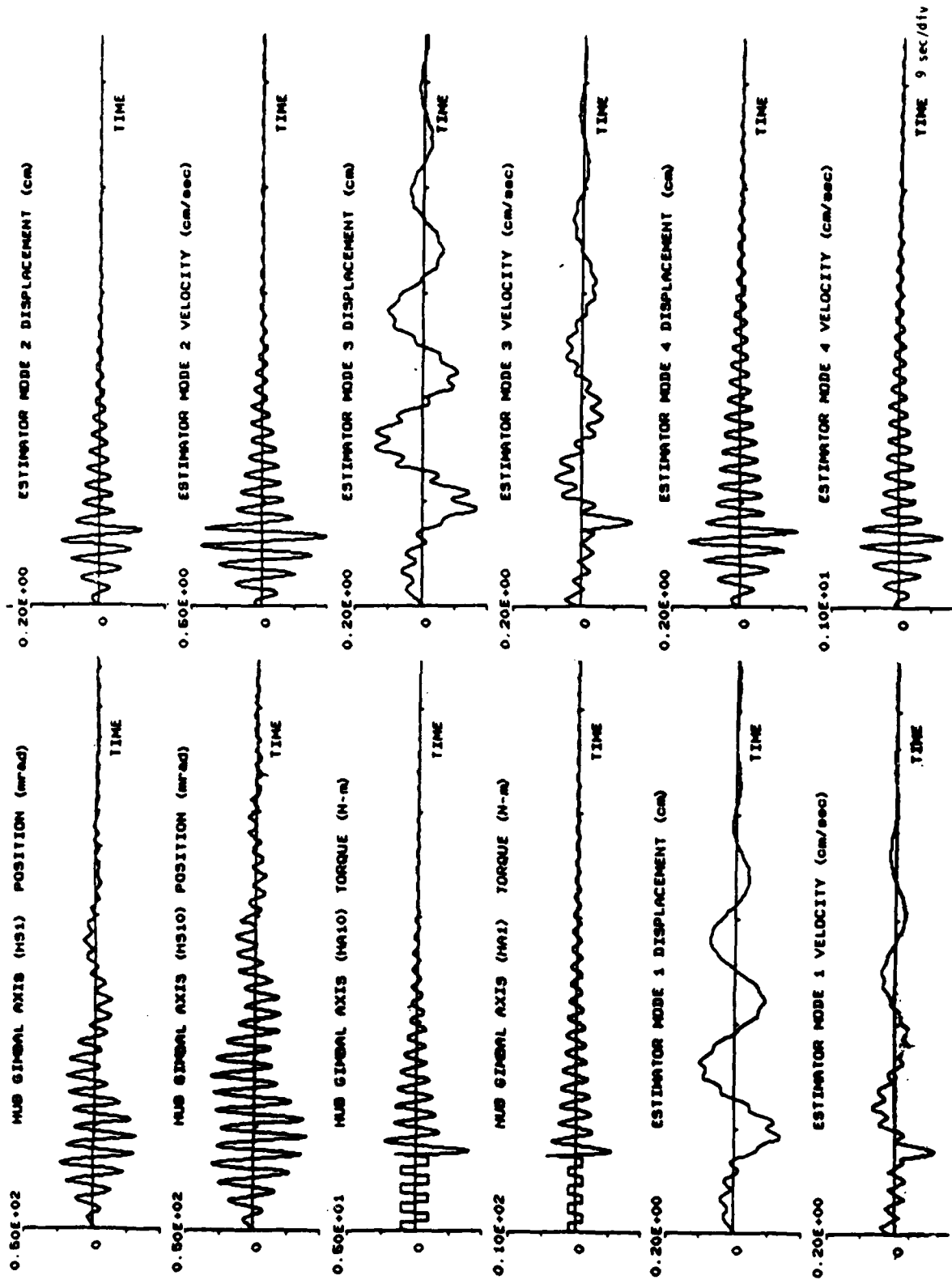


Figure 5.1-24 Time History Plots of Case 3 Controller with Second Identified Model under Input Pattern 2

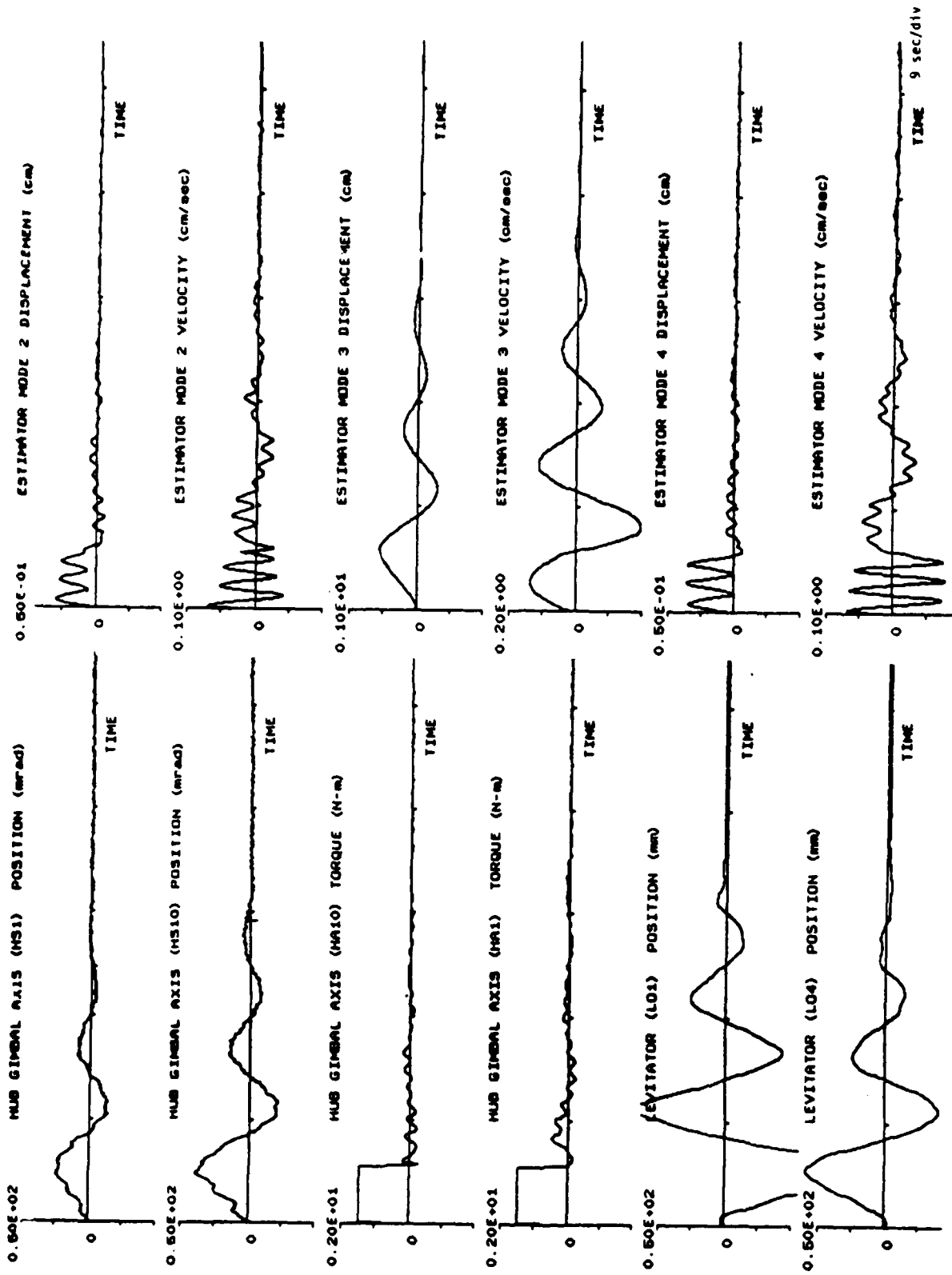


Figure 5.1-25 Time History Plots of Case 4 Controller with Second Identified Model under Input Pattern 1

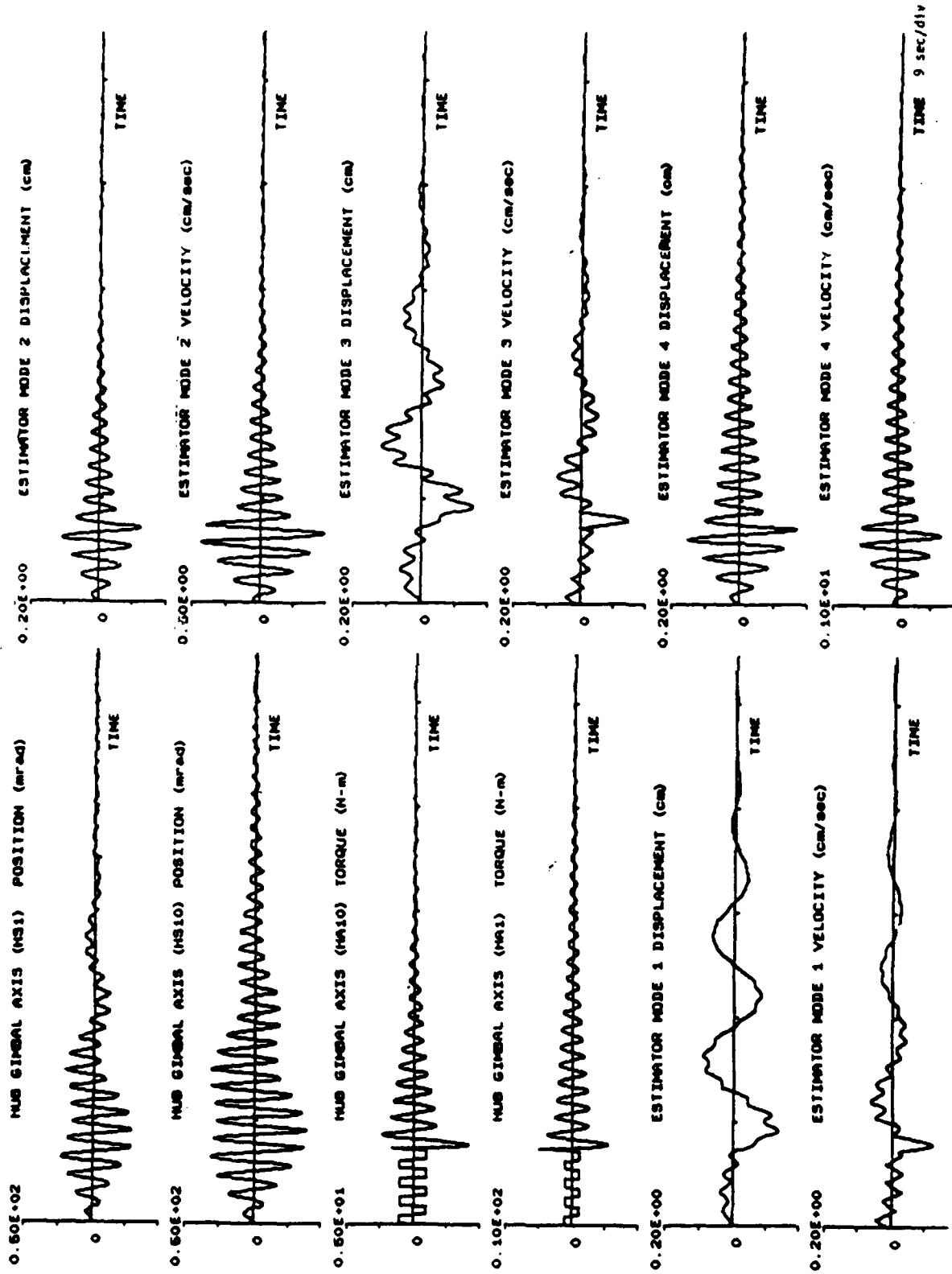


Figure 5.1-26 Time History Plots of Case 4 Controller with Second Identified Model under Input Pattern 2

Case 4

| Input pattern | Maximum overshoot |             | 10% settling time |             |
|---------------|-------------------|-------------|-------------------|-------------|
|               | <u>HS1</u>        | <u>HS10</u> | <u>HS1</u>        | <u>HS10</u> |
| 1             | 13.5(0%)          | 23.1(14%)   | 22.3              | 26.2(42%)   |
| 2             | 19.2(17%)         | 28.8(12%)   | 31.5(8%)          | 37.1(55%)   |

Table 5.1-14 Performance of Second Identified Model Based Controller (Cases 3 - 4) Continued

It is interesting to note that when the LTR parameter  $m_2$  is increased to  $1E7$  or when  $\alpha$  is increased to .2, performance deteriorates rapidly. When both are increased, instability results (with excitation Pattern 2). This phenomenon is not surprising since high performance control based on an uncertain model tends to degrade performance.

Since the lower gain with respect to Mode 1 is one of the suspected causes of poor performance with Excitation 1, performance requirements are increased by introducing a larger hub angle penalty and state error penalty. Many cases were run with performances under Excitation 1 remaining poor even though the gains associated with Mode 1 were increased. A representative illustration is Case 6, the time history plots of which are shown in Figure 5.1-27. The results suggest that low gain in Mode 1 alone did not contribute to poor performance. The performance is summarized below:

Case 6

| Input pattern | Maximum overshoot |             | 10% settling time |             |
|---------------|-------------------|-------------|-------------------|-------------|
|               | <u>HS1</u>        | <u>HS10</u> | <u>HS1</u>        | <u>HS10</u> |
| 1             | 14.9              | 19.7(27%)   | 22.3              | 24.2(47%)   |

Table 5.1-15 Performance of Second Identified Model Based Controller (Case 6)

To see if performance can be improved even under an ill-known model (as demonstrated by some of the cases above), the performance requirement is increased while scaling down the input matrix to guard against instability due to saturation. A set that yields good performance in simulation is Cases 7-8. The relation between input scale down and robustness enhancement in the input channel is based on the result stated in Section 5.1.2. A small  $\sigma$  is chosen to avoid controller saturation while other performance weightings are increased. The time history plots of these cases are shown in Figures 5.1-28-5.1-30. When these control laws are applied to the actual structure, the following performance is obtained:

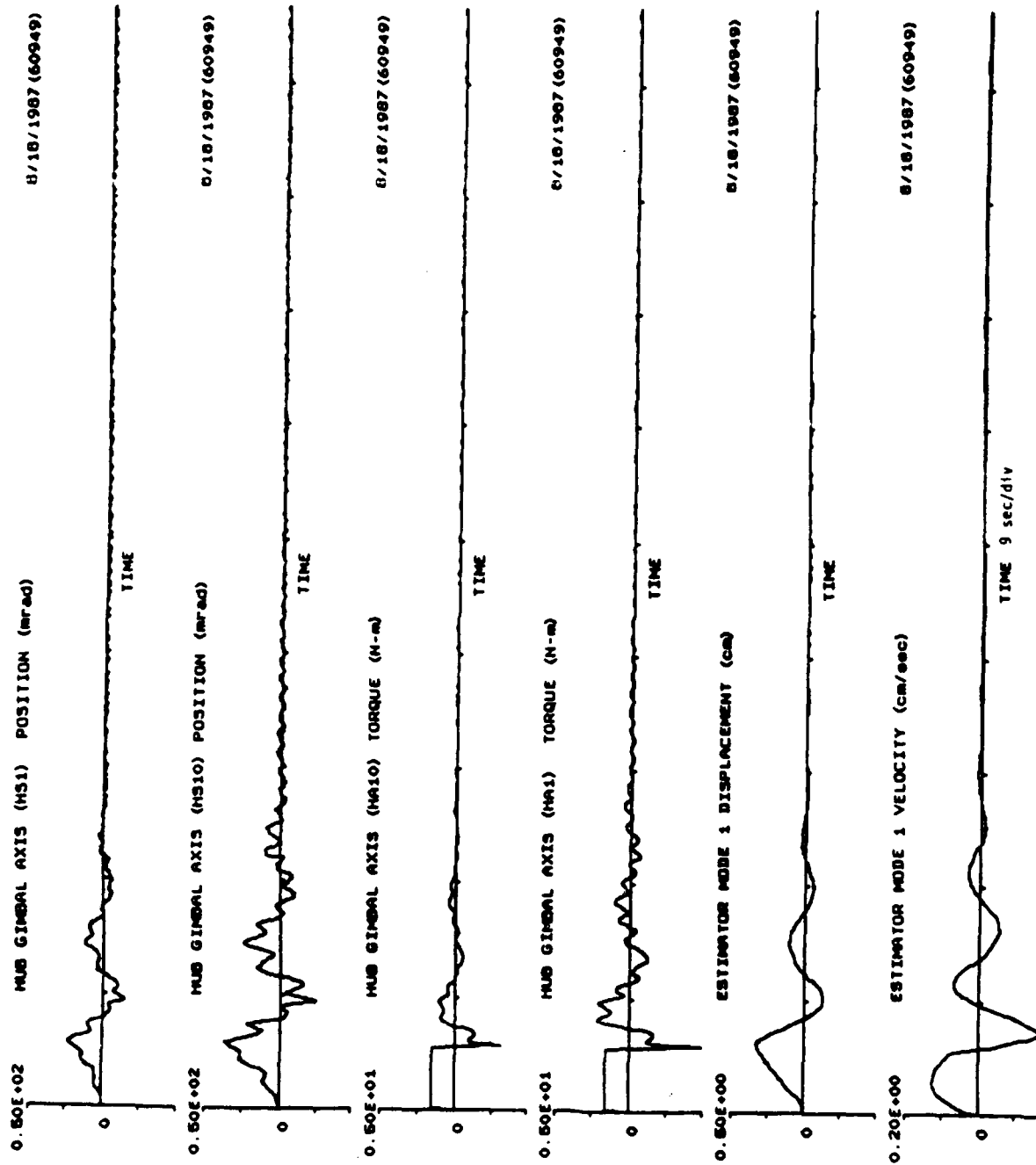


Figure 5.1-27 Time History Plots of Case 6 Controller with Second Identified Model under Input Pattern 1

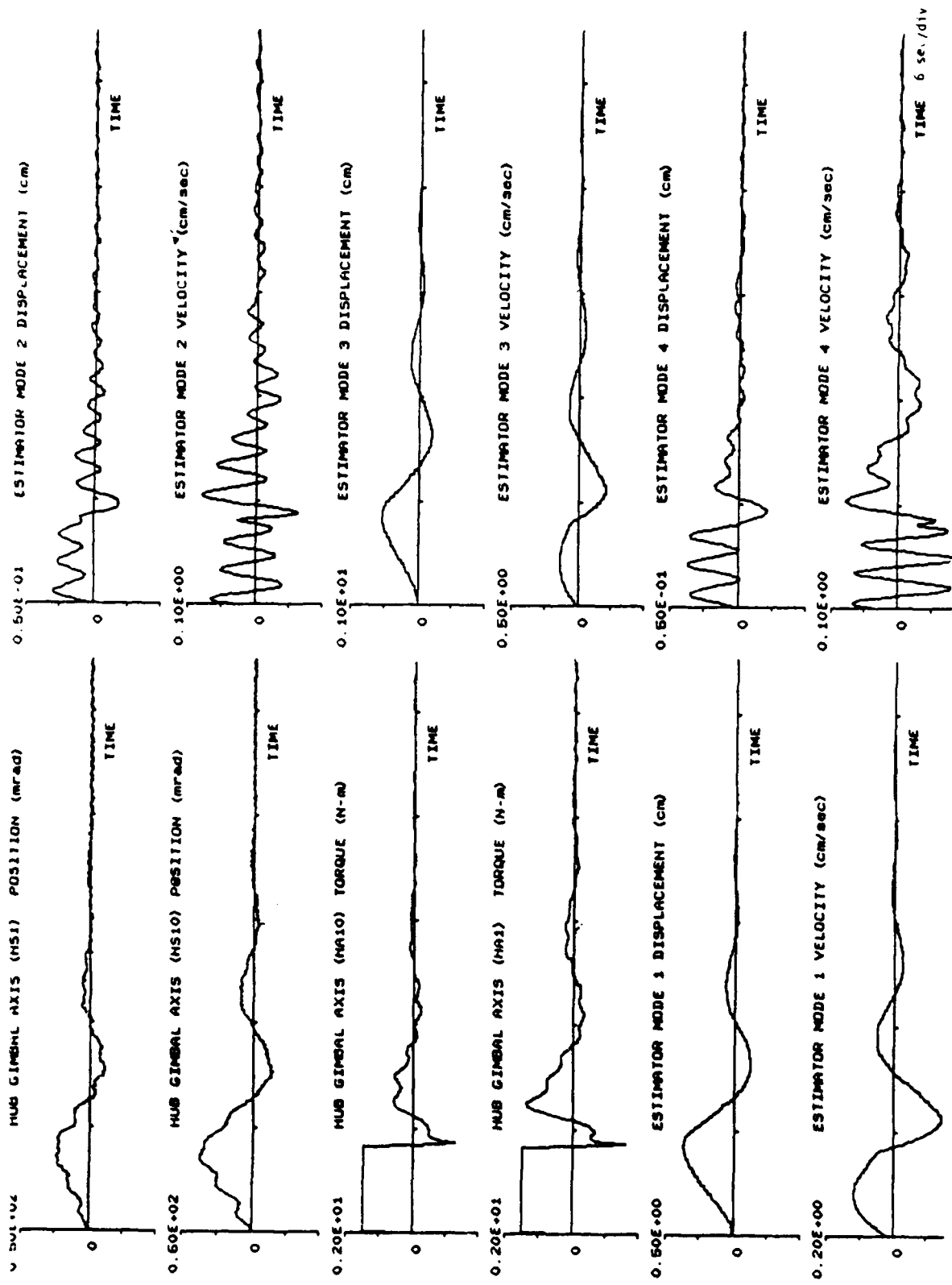


Figure 5.1-28 Time History Plots of Case 7 Controller with Second Identified Model under Input Pattern 1

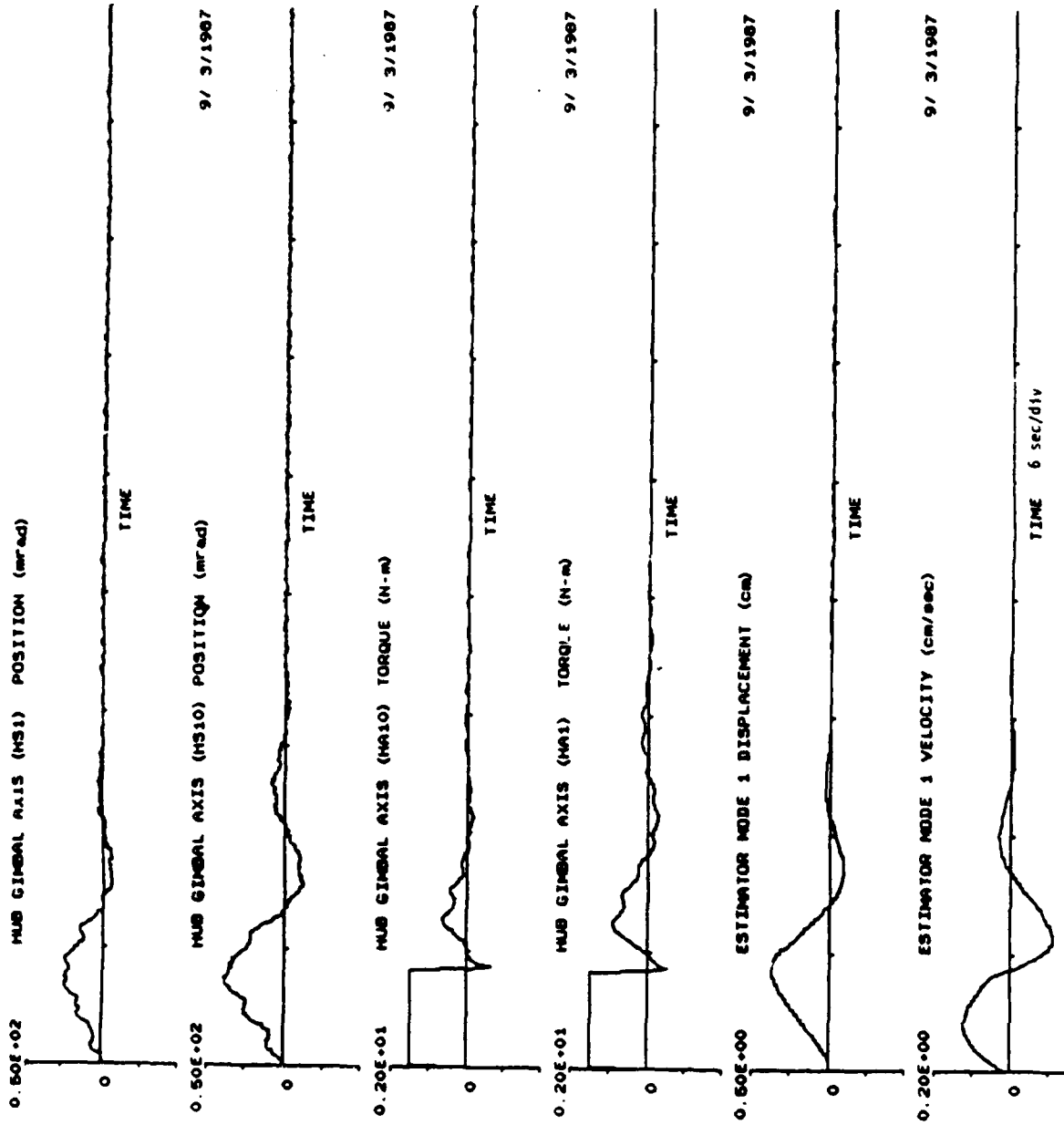


Figure 5.1-29 Time History Plots of Case 8 Controller with Second Identified Model under Input Pattern 1



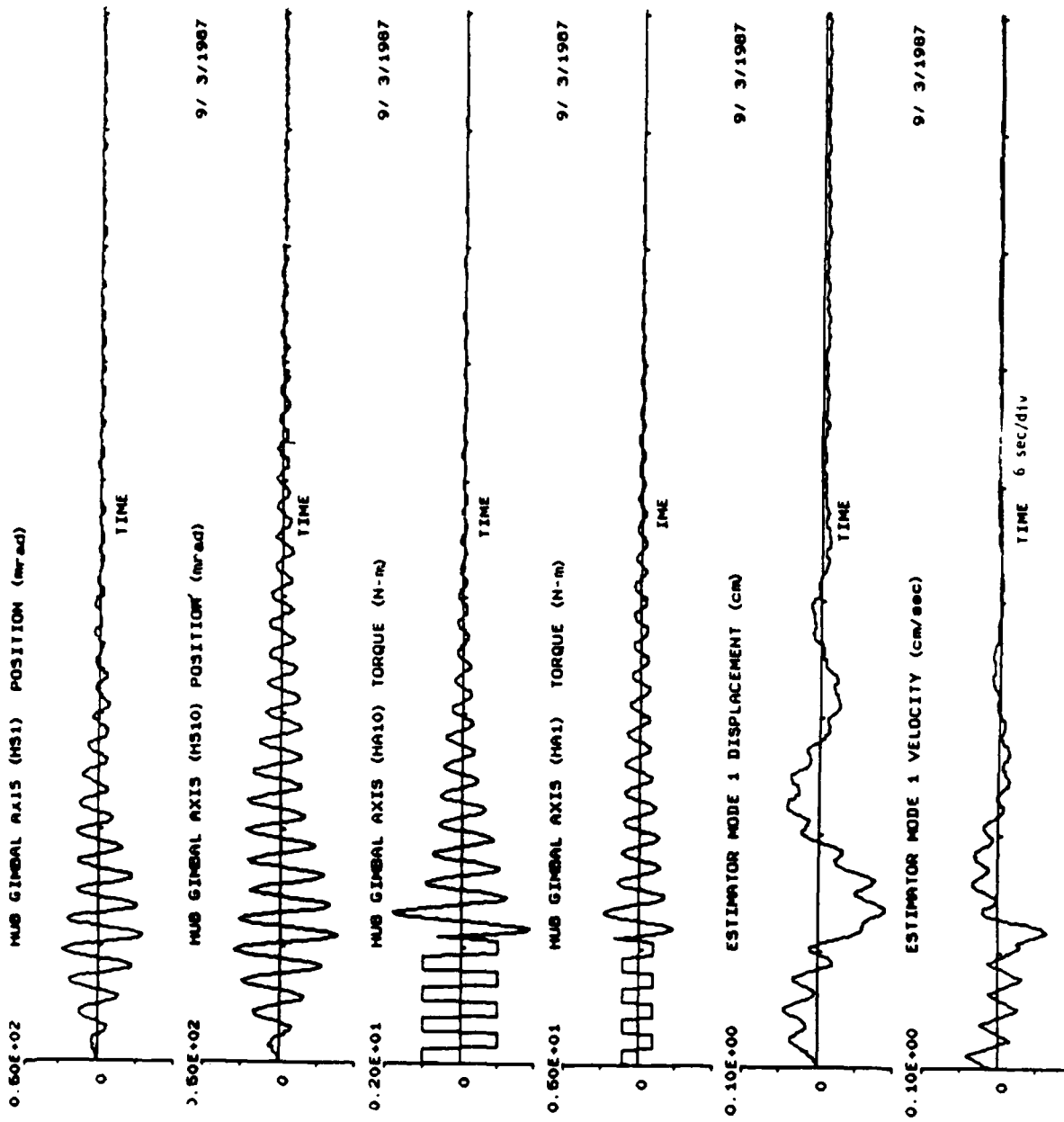


Figure 5.1-30 Time History Plots of Case 8 Controller with Second Identified Model under Input Pattern 2

Case 7

| Input pattern | Maximum overshoot       |                          | 10% settling time       |                          |
|---------------|-------------------------|--------------------------|-------------------------|--------------------------|
| 1             | <u>HS1</u><br>11.5(15%) | <u>HS10</u><br>15.4(43%) | <u>HS1</u><br>15.9(36%) | <u>HS10</u><br>17.8(65%) |

Case 8

| Input pattern | Maximum overshoot      |                          | 10% settling time       |                          |
|---------------|------------------------|--------------------------|-------------------------|--------------------------|
| 1             | <u>HS1</u><br>6.9(49%) | <u>HS10</u><br>11.5(57%) | <u>HS1</u><br>11.2(63%) | <u>HS10</u><br>16.4(69%) |
| 2             | 20(13%)                | 26.9(18%)                | 29.1(17%)               | 32(63%)                  |

Table 5.1-16 Performance of Second Identified Model Based Controller (Cases 7 - 8)

Case 7 yields settling time comparable to the analytic model cases but the overshoot is much larger. The situation improves slightly in Case 8, but the overshoot is still quite large.

In order to achieve further performance improvement, it is necessary to find out whether the controller or the estimator in the analytic model based controller has caused the difference in performance. First the controller from Case 1 in Model 1 is used in conjunction with the estimator from Case 7. Then, the estimator from Case 1 in Model 1 is used together with the controllers from Cases 7-8. The time history plots are shown in Figures 5.1-31 - 5.1-35. The performances are listed below:

Case 1, Model 1 controller with Case 7 estimator

| Input pattern | Maximum overshoot      |                          | 10% settling time       |                          |
|---------------|------------------------|--------------------------|-------------------------|--------------------------|
| 1             | <u>HS1</u><br>7.7(43%) | <u>HS10</u><br>15.4(43%) | <u>HS1</u><br>16.5(32%) | <u>HS10</u><br>16.2(69%) |

Table 5.1-17 Performance of Analytic Model Based Controller and Second Identified Model Based Estimator

Case 1, Model 1 estimator with Case 7 controller

| Input pattern | Maximum overshoot      |                         | 10% settling time       |                          |
|---------------|------------------------|-------------------------|-------------------------|--------------------------|
| 1             | <u>HS1</u><br>6.9(49%) | <u>HS10</u><br>7.7(71%) | <u>HS1</u><br>14.4(44%) | <u>HS10</u><br>14.9(73%) |
| 2             | 19.2(17%)              | 23.1(29%)               | 21.0(47%)               | 25.2(72%)                |

Table 5.1-18 Performance of Second Identified Model Based Controller and Analytic Model Based Estimator

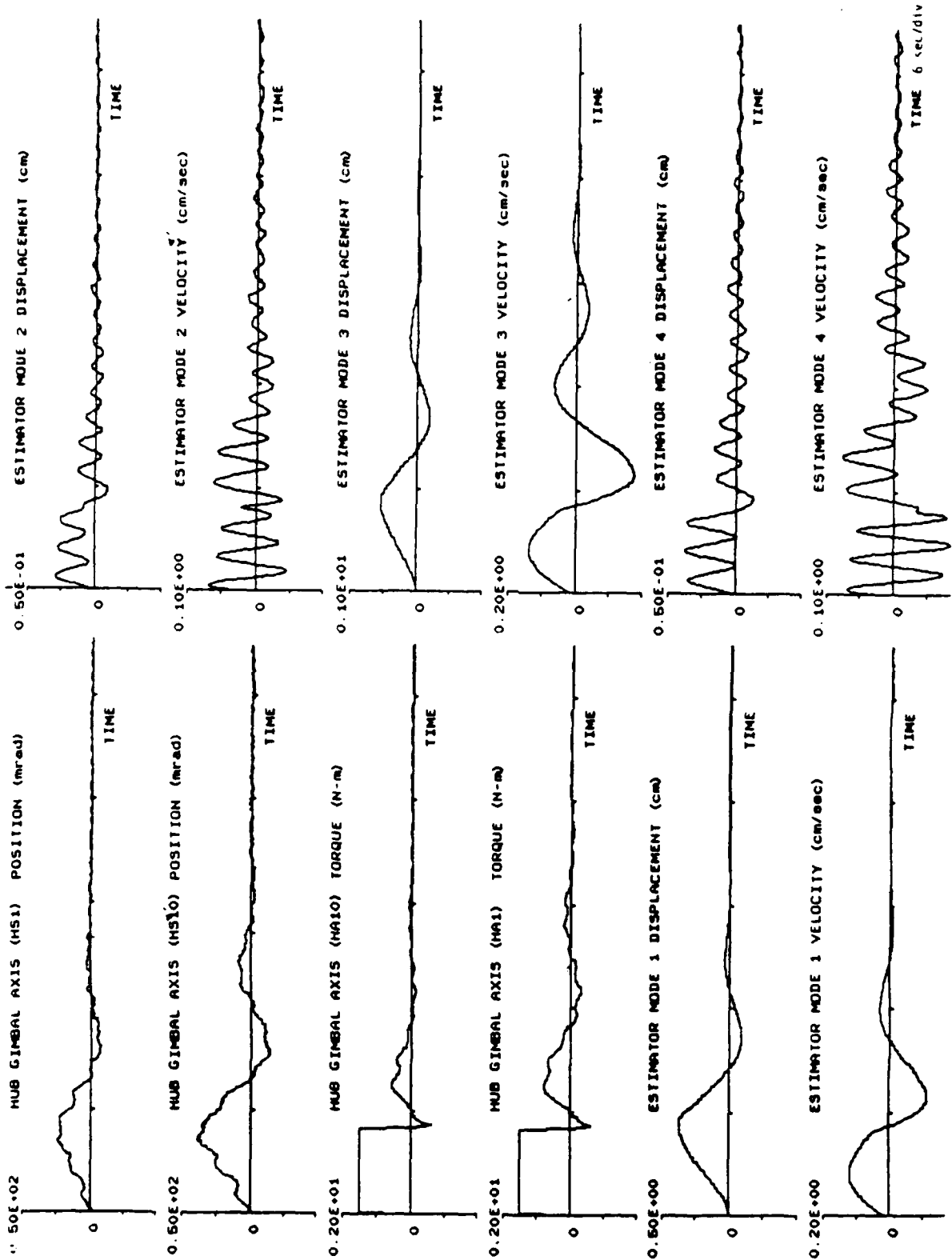


Figure 5.1-31 Time History Plots of Case 1 Controller with Analytic Model and Case 7 Estimator with Second Identified Model under Input Pattern 1

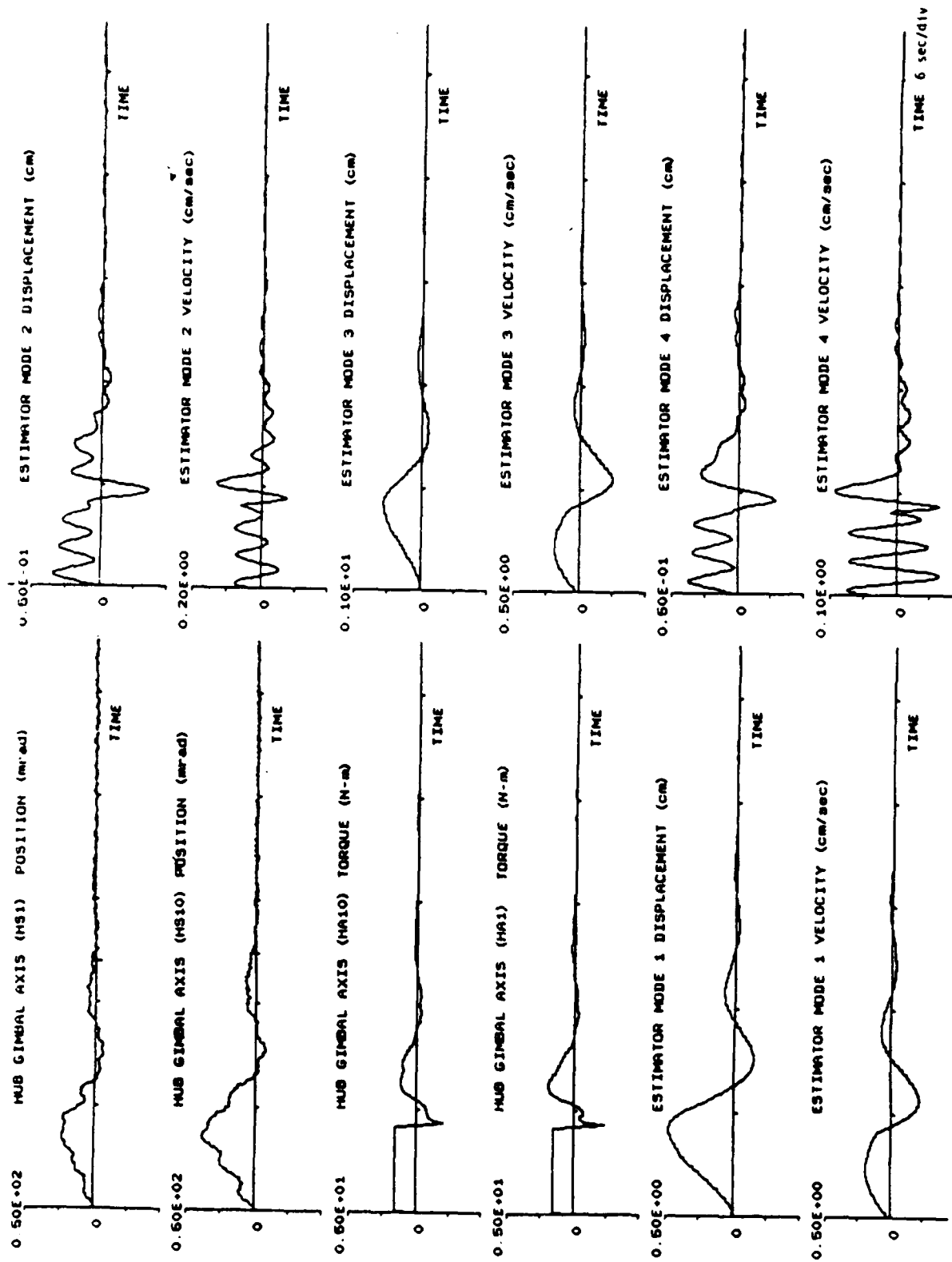


Figure 5.1-32 Time History Plots of Case 7 Controller with Second Identified Model and Case 1 Estimator with Analytic Model under Input Pattern 1

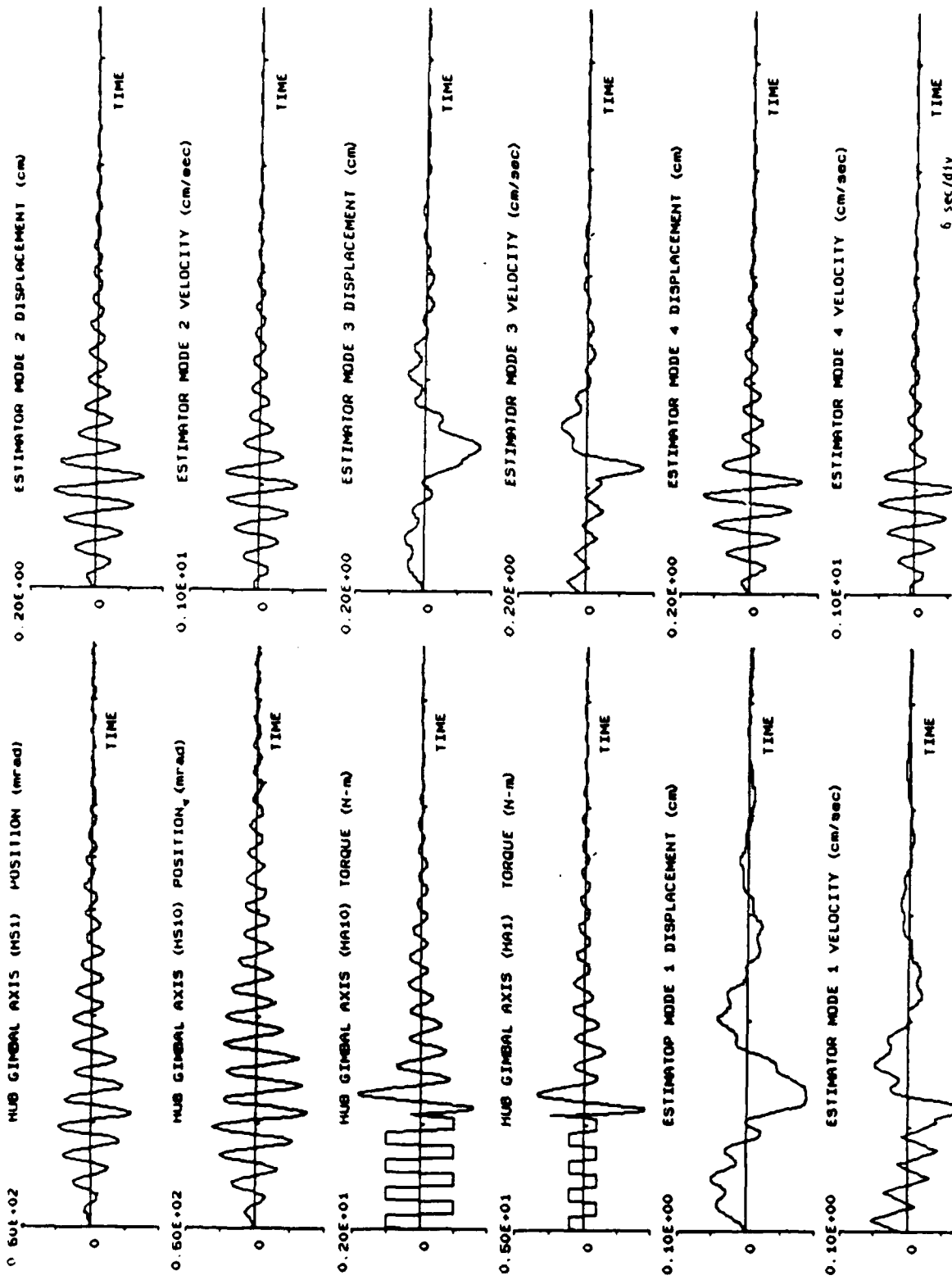


Figure 5.1-33 Time History Plots of Case 7 Controller with Second Identified Model and Case 1 Estimator with Analytic Model under Input Pattern 2

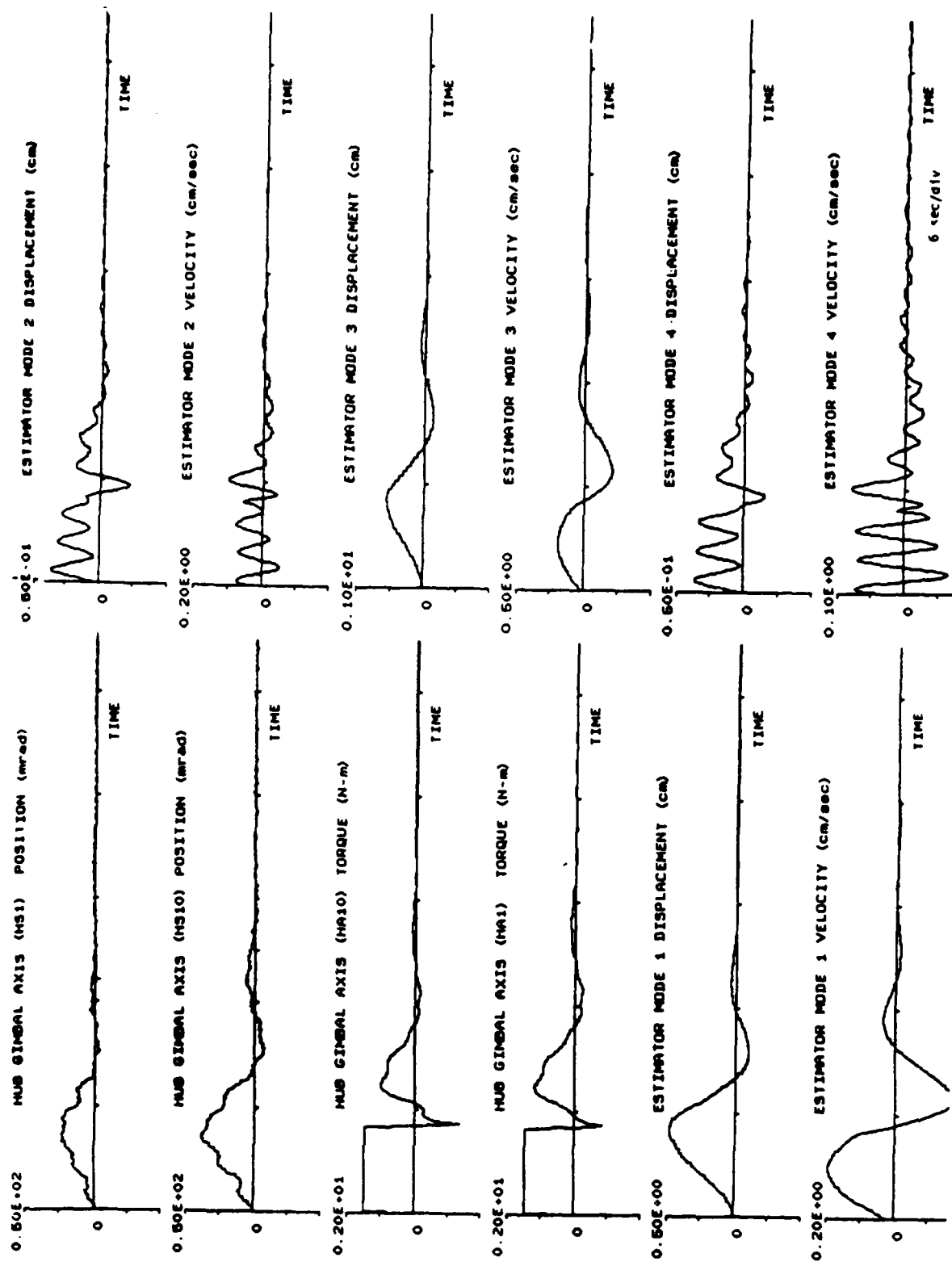


Figure 5.1-34 Time History Plots of Case 8 Controller with Second Identified Model and Case 1 Estimator with Analytic Model under Input Pattern 1

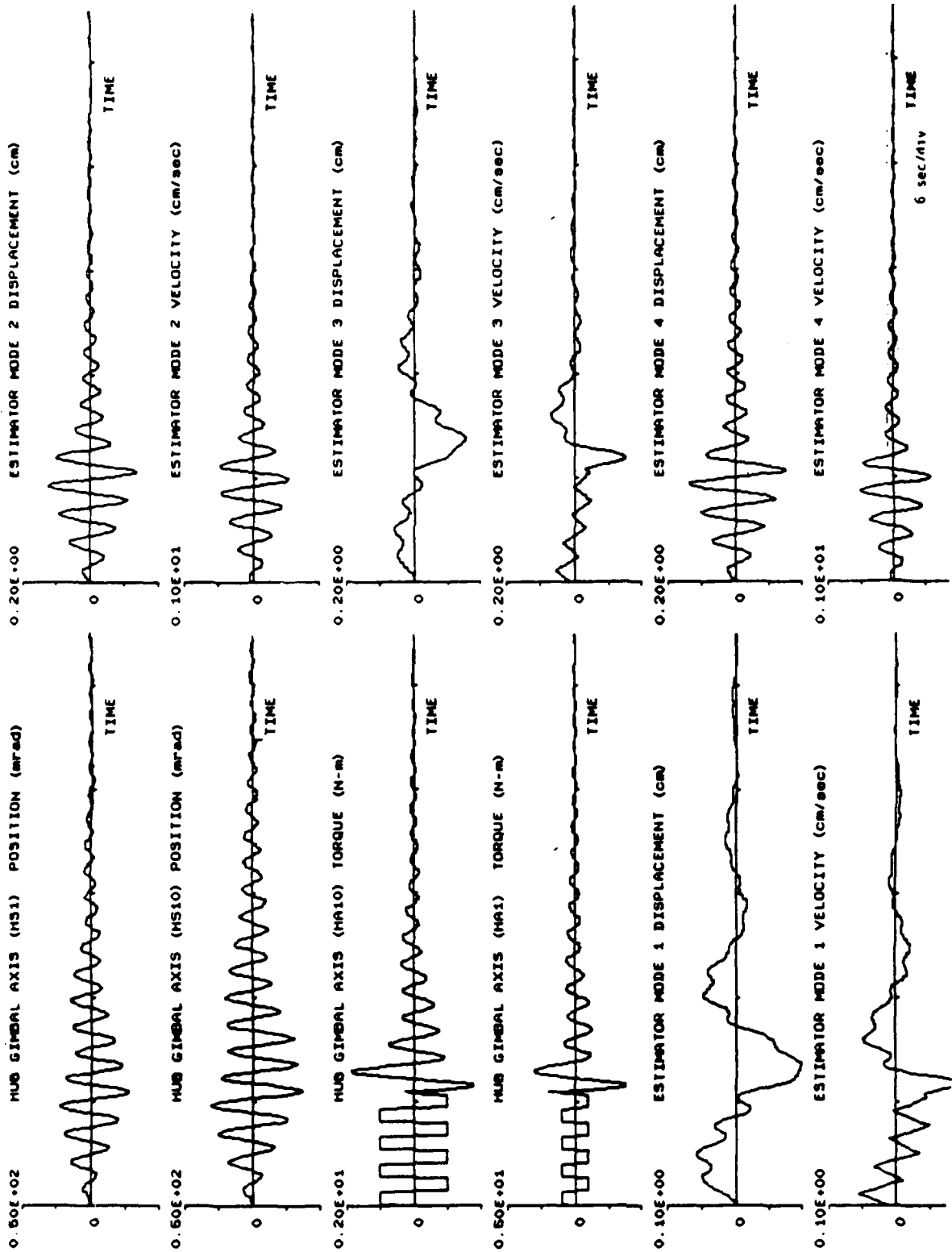


Figure 5.1-35 Time History Plots of Case 8 Controller with Second Identified Model and Case 1 Estimator with Analytic Model under Input Pattern 2

Case 1, Model 1 Estimator with Case 8 Controller

| Input pattern | Maximum overshoot |             | 10% settling time |             |
|---------------|-------------------|-------------|-------------------|-------------|
|               | <u>HS1</u>        | <u>HS10</u> | <u>HS1</u>        | <u>HS10</u> |
| 1             | 3.8(72%)          | 7.7(71%)    | 13.2(51%)         | 15.0(73%)   |
| 2             | 17.3(25%)         | 26.9(18%)   | 25.5(30%)         | 26.9(70%)   |

Table 5.1-18 Performance of Second Identified Model Based Controller and Analytic Model Based Estimator (Continued)

In the first case, improvement is obtained, but the most dramatic difference occurs when the estimator based on Case 1, Model 1 is used with the higher performance controller based on the updated model. This result suggests that the estimator is the critical component in terms of performance. Further fine tuning of the model is necessary for a faster converging estimator and improved performance. Closer examination of the estimated states of Mode 1 reveal that the "good" cases have earlier zero crossover in the estimated Mode 1 velocity, thus allowing the corrective control action to kick in faster. The first modal frequency of the identified model is too low and consequently large overshoots result.

After fine tuning the model, the estimator based on the same parameter set as in Case 1, Model 1, is used. The controller is designed based on the same parameter set as in Case 8, Model 3. The performance, as expected, is the best among all of the cases that were run. The time history plots are shown in Figures 5.1-36 - 5.1-37.

| Input pattern | Maximum overshoot |             | 10% settling time |             |
|---------------|-------------------|-------------|-------------------|-------------|
|               | <u>HS1</u>        | <u>HS10</u> | <u>HS1</u>        | <u>HS10</u> |
| 1             | 1.2(91%)          | 8.5(69%)    | 8.7(78%)          | 13.2(78%)   |
| 2             | 19.2(17%)         | 26.9(18%)   | 19.2(53%)         | 23.2(75%)   |

Table 5.1-19 Performance of Third Identified Model Based Controller

5.1.4. Conclusions

The Phase 1 dynamic control experiment demonstrated the efficacy of the LQG-based control laws in the control of flexible structures. The results in Phase 1 indicate that stability and improved closed loop performance (over the open loop response) can be achieved even with very crude models. However, when the performance requirement is increased beyond a certain point a well identified model is essential. In fact, a number of experiments showed that a high performance controller based on an imprecise model can cause more damage than good. It is expected that with a more refined model, (scheduled for availability in December, 1987), better performance can be attained. Most of



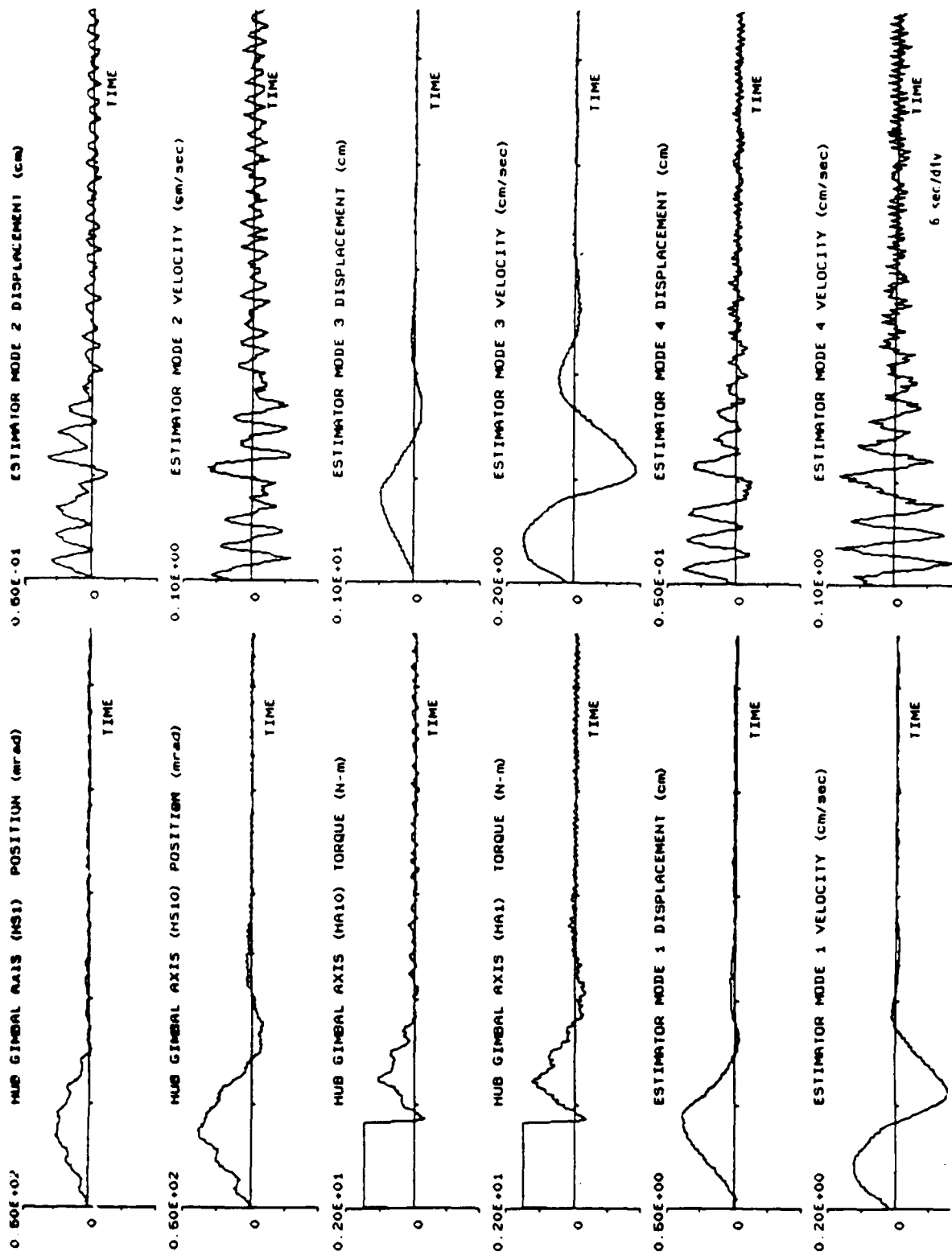


Figure 5.1-36 Time History Plots of Case 8 Controller with Third Identified Model under Input Pattern 1

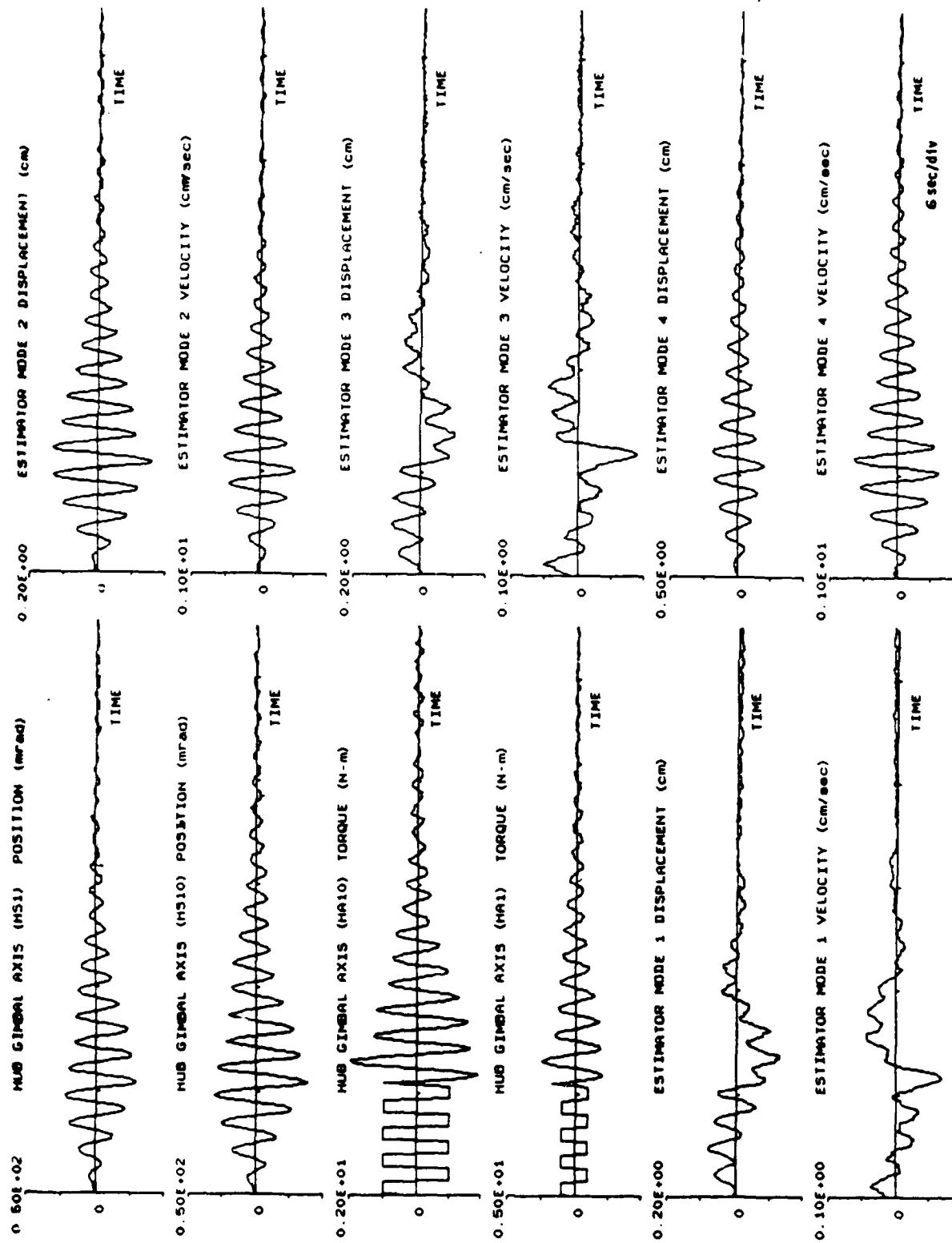


Figure 5.1-37 Time History Plots of Case 8 Controller with Third Identified Model under Input Pattern 2

the controllers tested were designed based on a pair of uncoupled two-mode models. Indeed, the third mode is known so poorly that when its model was used in the controller design, the closed loop performance sometimes became unstable. A better identified model will significantly help investigation of the behavior of higher frequency modes. The Phase 1 experiment also shows the viability of the robust design approach as suggested in Section 5.1.2. In most of the cases involving robustness enhancement (provided performance demand does not exceed the actuator capacity and sampling constraint), not only stability is preserved but performance is also increased as compared to the nominal controllers. However, in order to achieve a significant improvement in performance, fine tuning of the model is still needed. A more systematic study of the robust controller issue is slated for future phases.

#### References

- [1] Ljung, L. and T. Soderstrom, Theory and Practice of Recursive Identification, The MIT Press, Cambridge, Mass., 1983.
- [2] Scheid, R., Jr., "The use of cyclic symmetry in the distributed model of a large dish antenna," JPL Engineering Memo #347-83-146 (Internal Document), 1983.
- [3] Wen, J., "Derivation of the analytical JPL/AFRPL antenna model," JPL Engineering Memo #347-86-187 (Internal Document), 1986.
- [4] Eldred, D., Y. Yam, D. Boussalis and S.J. Wang, "Large flexible structure control technology experiment and facility design," Fourth IFAC Symposium on Control of Distributed Parameter Systems, Los Angeles, June, 1986.
- [5] Yam, Y., "System model for the RPL/JPL ground test facility," JPL Engineering Memo #347-86-191 (Internal Document), 1986.
- [6] Mingori, D.L., J.S. Gibson, P.A. Belloch and A. Adamian, "Final report on unified control/structure design and modeling research," Jan, 1986.
- [7] Balakrishnan, A.V., Applied Functional Analysis, 2nd Ed., Springer-Verlag, New York, 1981.
- [8] Curtain, R.F. and A.J. Pritchard, Infinite Dimensional Linear System Theory, Lecture Notes in Contr. and Info. Sc., 8, Springer-Verlag, Berlin, 1978.
- [9] Gibson, J.S., "The Riccati integral equations for optimal control problems on Hilbert Spaces," SIAM J. Contr. & Opt., 17, 1979. pp. 537-565.
- [10] Doyle, J.C. and G. Stein, "Multivariable feedback design: concepts for a classical/modern synthesis," IEEE Trans. Automat. Contr., 26, 1981. pp.4-16.
- [11] Desoer, C.A. and M. Vidyasagar, Feedback Systems: Input-Output Properties, Academic press, New York, 1975.

- [12] Wen, J., "Unified controller analysis and design for distributed parameter systems in Hilbert Space based on the positive realness concept, Parts I, II," JPL Engineering Memo #347-86-193, 347-87-208 (Internal Documents), 1986, 1987.
- [13] Kwakernaak, H. and R. Sivan, Linear Optimal Control Systems, John Wiley, New York, 1972.
- [14] Joshi, S.M., "Stability of multiloop LQ regulators with nonlinearities - Part I: regions of attraction, Part II: regions of ultimate boundedness," IEEE Trans. Automat. Contr., 31, 1986. pp. 364-370.
- [15] Belloch, P.A. and D.L. Mingori, "Modified LTR robust control for flexible structures," Proc. AIAA Guidance, Navig. & Contr. Conf., Williamsburg, Va., 1986.

## 5.2 ADAPTIVE CONTROL EXPERIMENTS

### 5.2.1 Experiment Description

The objective for the adaptive control experiments for FY'87-89 is to validate and demonstrate the autonomous direct Model Reference Adaptive Control (MRAC) methodology for the control of large flexible space structural systems with a physical structure and actual control hardware. Specifically, a control subsystem capability will be demonstrated in stages with increasing complexity for which the controller will be adaptive to significant dynamical uncertainties, hardware saturation, actuator time delays, and reconfiguration. The relevance of such capabilities lies in the fact that future space systems are to be controlled under uncertain and changing environments.

The objective for Phase I is to demonstrate the effectiveness of Model Reference Adaptive Control techniques for compensation of parameter errors and model truncation through transient and initial deflection regulation utilizing a small set of sensors and actuators. These proof-of-concept technology validation experiments establish baseline performance as a foundation for the future development and demonstration of more complex configurations which use additional sets of sensors and actuators to accommodate more challenging environmental conditions.

The instrumentation used for control purposes in Phase I experiments includes 2-axis hub torquers (HA1 and HA10)\* and 2-axis hub angle sensors (HS1 and HS10). The HS1 sensor measures the angle of rotation about rib 1-7 axis excited by the HA10 torquer mounted on rib 10. The HS10 sensor measures the angle of rotation about rib 4-10 axis excited by the HA1 torquer mounted on rib 1. Unfortunately, the hub angle measurements include biases which cannot be eliminated through mechanical adjustment, and they vary slightly from day to day. Thus, prior to running the experiments, the values of these biases must be experimentally determined so that the system software can cancel them out. The symmetry assumption of the structure has been verified by John Wen [1] (See Sec. 5.1). This validates the assumption used in these experiments that excitation and control through the hub actuators excite the hub-boom modes only. The decoupling between the dynamics about 1-7 axis and 4-10 axis simplifies the structure to two single-input single-output subsystems (HA1-HS10 and HA10-HS1). The levitator displacement sensors are also utilized, but the data are used for performance evaluation only.

The basic idea of the specific Model Reference Adaptive Control technique considered here is to design a reference model whose output reflects the desired system performance and then, through the adaptive controller to drive the plant output to asymptotically track the model output. The main virtue of this technique is that it allows the reference model to be of low-order while the actual system order is infinite or high, and in the process of controller design, relatively little knowledge about the system is assumed.

There are three experiments performed in Phase I, as described in the following paragraphs:

---

\*See Fig. 2.2-2

### Exp. 1 Quiescent Control Experiment

This experiment serves as a test preceding the two regulation experiments. The experiment starts with the structure at rest. No disturbances are applied. After the controller is turned on, the system should stay at quiescent state throughout the experiment period. The detailed operational procedure is:

- (1) Set the system at quiescent state.
- (2) Activate the system software.
- (3) Set the length of experiment period through the system software.
- (4) Select Experiment #1.
- (5) Activate the adaptive control experiment software.

### Exp. 2 Transient Regulation Experiment

In this experiment, the reference model is in a quiescent state, i e., it has zero input commands and zero initial conditions. The disturbances are introduced through the hub torquers to excite the system. The adaptive controller is then turned on to suppress the resulting vibration by commanding the system to track the zero reference model outputs. The detailed operational procedure is:

- (1) Activate the system software.
- (2) Set the length of experiment period through the system software.
- (3) Select experiment conditions including excitation intensity and duration for each actuator.
- (4) Select Experiment #2.
- (5) Activate the adaptive control experiment software.
- (6) Repeat the experiment with different gains and parameters.

Three excitation patterns are used to excite both axes 1-7 and 4-10.

- i) Single pulse with 1.5 N-m amplitude for 1 sec
- ii) Single pulse with 1.5 N-m amplitude for 2 sec
- iii) Single pulse with 1.5 N-m amplitude for 3 sec

### Exp. 3 Initial Deflection Regulation Experiment

In this experiment, the system is given an initial deflection by tilting the structure from its resting position. The reference model consists of two modes corresponding to the first mode of each subsystem. However, they are set 50% and 100% off the nominal values of the modal frequencies and mode shapes of the structure, respectively. The reference model still has zero inputs but nonzero initial condition and high damping (damping ratio  $\zeta=1.0$ ). The adaptive controller is activated when the structure is released from its deflected position, forcing the system outputs to track the highly damped reference model outputs to suppress the vibrations. The detailed operational procedure is:

- (1) Activate the system software.
- (2) Set the length of experiment period through the system software.

- (3) Manually tilt the structure from its resting position, and release it at time 0.
- (4) Select Experiment #3.
- (5) Activate the adaptive control experiment software.
- (6) Repeat the experiment with different gains and parameters.

The sampling rate is set at 20 Hz (50 ms sampling period) for all experiments in Phase I since it provides ample time for control algorithm computation and it is fast enough to keep the discretized algorithm stable.

The experimental parameters are stored in the data file named PFILE.DAT which is an ASCII file and can be modified by the VAX text editor. The parameters which need to be modified from experiment to experiment include gain weighting matrices, leakage factors for integral and proportional gains and time constants for the branch filter. A typical PFILE.DAT is shown below:

```

[.IH]LP.dat ;Proportional input gain weighting file name
[.IH]TP.dat ;Proportional output gain weighting file name
[.IH]LI.dat ;Integral input gain weighting file name
[.IH]TI.dat ;Integral output gain weighting file name
[.IH]W2M.dat ;Reference model eigenvalue matrix file name
[.IH]EVECS.dat ;Reference model eigenvector matrix file name
[.IH]B.dat ;Control influence matrix file name
[.IH]C.dat ;Measurement distribution matrix file name
[.IH]EG.dat ;Estimator gain file name
[.IH]CP.dat ;Matrix C multiplied by eigenvector matrix PHI
2 ;Number of modes of reference model
0 0 0 0 ;Initial condition of reference model states
55 ;Number of save variables
2 ;Number of input and output for plant and model
0.5 ;Leakage factor for integral gain
21.99 ;Leakage factor for proportional gain
1.5 1.5 ;Maximum actuator signal levels (N-m)
-1.5 -1.5 ;Minimum actuator signal levels (N-m)
2.0 ;Convergence criterion (mrad)
21.99 ;Time constant for the first-order branch filter
1.0 1.0 ;Modal damping ratios of the reference model
0.2 ;Weighting factor of position vs. rate measurement
0.05 ;Sampling period
0 0 ;Initial values for integral gains
2 ;Number of decoupled subsystems
4 4 ;Vector containing size of subsystem estimators
0 0 0 0 0 0 0 ;Estimator initial condition
1 1 ;Vector containing size of subsystem output vectors
1 1 ;Vector containing size of subsystem input vectors
0. ;Threshold for the estimated rate

```

Besides the sensor and actuator readings, the data saved for post-experiment analysis are the reference model outputs, plant outputs, output errors, filtered output errors, proportional and integral gains, and the estimated angular rates.

## 5.2.2 Algorithm Description

5.2.2.1 Problem Formulation. The flexible structure, or the controlled plant can be represented by the following state space equations:

$$\dot{x}_p(t) = A_p x_p(t) + B_p u_p(t) \quad (5.2.1a)$$

$$y_p(t) = C_p x_p(t) \quad (5.2.1b)$$

where  $x_p \in \mathbb{R}^{N_p}$ ,  $u_p \in \mathbb{R}^M$ ,  $y_p \in \mathbb{R}^M$  and  $A_p$ ,  $B_p$ ,  $C_p$  are of appropriate dimensions. It is assumed that  $(A_p, B_p)$  is controllable,  $(A_p, C_p)$  is observable, and that the number of inputs equals the number of outputs. The output  $y_p$  is a combination of position and rate measurements with a measurement weighting factor  $\alpha$  defined as the position to rate ratio.  $\alpha$  is a small positive number which means that the rate measurement dominates for this adaptive algorithm.

A stable reference model which specifies the desired performance of the plant is described by the following state space representation,

$$\dot{x}_m(t) = A_m x_m(t) + B_m u_m(t) \quad (5.2.2a)$$

$$y_m(t) = C_m x_m(t) \quad (5.2.2b)$$

where  $x_m \in \mathbb{R}^{N_m}$ ,  $u_m \in \mathbb{R}^M$ ,  $y_m \in \mathbb{R}^M$  and  $A_m$ ,  $B_m$ ,  $C_m$  are of appropriate dimensions.

For practical application to flexible structures, the following condition is necessary for any adaptive algorithms:

$$N_p \gg N_m \quad (5.2.3)$$

Define the output error between the plant and the model as

$$e_y(t) = y_m(t) - y_p(t) \quad (5.2.4)$$

Since the reference model specifies the desired performance of the plant (flexible structure), the objective is then, without assuming complete knowledge of the plant, to design an adaptation mechanism to generate a suitable plant control input  $u_p(t)$ , so that the plant output tracks the model output asymptotically, i.e.,

$$\lim_{t \rightarrow \infty} e_y(t) = 0 \quad (5.2.5)$$

5.2.2.2 Adaptive Control Algorithm. Employing the Command Generator Tracker (CGT) theory [2], an ideal plant trajectory  $x_p^*$  is assumed to exist such that

$$C_p x_p^* = C_m x_m \quad (5.2.6)$$

$$\dot{x}_p^* = A_p x_p^* + B_p u_p^* \quad (5.2.7)$$



Assuming that  $u_m$  is a step function, then there exist constant matrices  $S_{11}$ ,  $S_{12}$ ,  $S_{21}$  and  $S_{22}$  such that,

$$x_p^* = S_{11}x_m + S_{12}u_m \quad (5.2.8a)$$

$$u_p^* = S_{21}x_m + S_{22}u_m \quad (5.2.8b)$$

The assumption that  $u_m$  is a step function is not overly restrictive since the reference model can be appropriately augmented to internally produce any command signal which can be described as the solution to a linear constant coefficient differential equation with step input.

Define the plant state error  $e_x \triangleq x_p^* - x_p$ . Using Eqs. (5.2.1) and (5.2.7) one has

$$\dot{e}_x = A_p e_x + B_p [u_p^* - u_p] \quad (5.2.9)$$

It is required that the adaptive control algorithm to be described subsequently must ensure global stability of the error equation (5.2.9).

The algorithm employed here, due originally to Sobel, Kaufman and Mabius [2], has found important application to large space structures specifically due to its inherent robustness to unmodelled dynamics and the extendibility to multiple-input multiple-output (MIMO) systems. Several important modifications of this basic adaptive algorithm have been made at JPL. In particular, the use of a low gain inner loop, as put forth in [3], eliminated the destabilizing effect of the rigid body dynamics, and the use of input gain weighting, proposed in [4], was found necessary to effectively distribute control energy to key structural locations. The theory and application of introducing a branch filter into the adaptive controller to effectively suppress measurement noise, while insuring global stability of the adaptive algorithm, was developed in [5]. The new algorithm is depicted in Fig. 5.2-1 and summarized below.

The plant control is written as

$$u_p = K\bar{r} \quad (5.2.10)$$

where  $\bar{r}^T = [\bar{e}_y^T, x_m^T, u_m^T]^T \quad (5.2.11)$

$$K = [K_e, K_x, K_u] \quad (5.2.12)$$

and  $\bar{e}_y$  is the output of the branch filter  $F_B$

$$\bar{e}_y = F_B(e_y) \quad (5.2.13)$$

The gain  $K$  in (5.2.12) is chosen as the sum of a proportional component  $K_p$  and an integral component  $K_I$  so that,

$$K = K_p + K_I \quad (5.2.14)$$

The adaptive laws contain filtering effects of their own and utilize both the filtered and unfiltered branches of the output error as follows,

$$\dot{X}_1 = A_1 X_1 + B_1 L e_y \bar{r}^T \quad (5.2.15a)$$

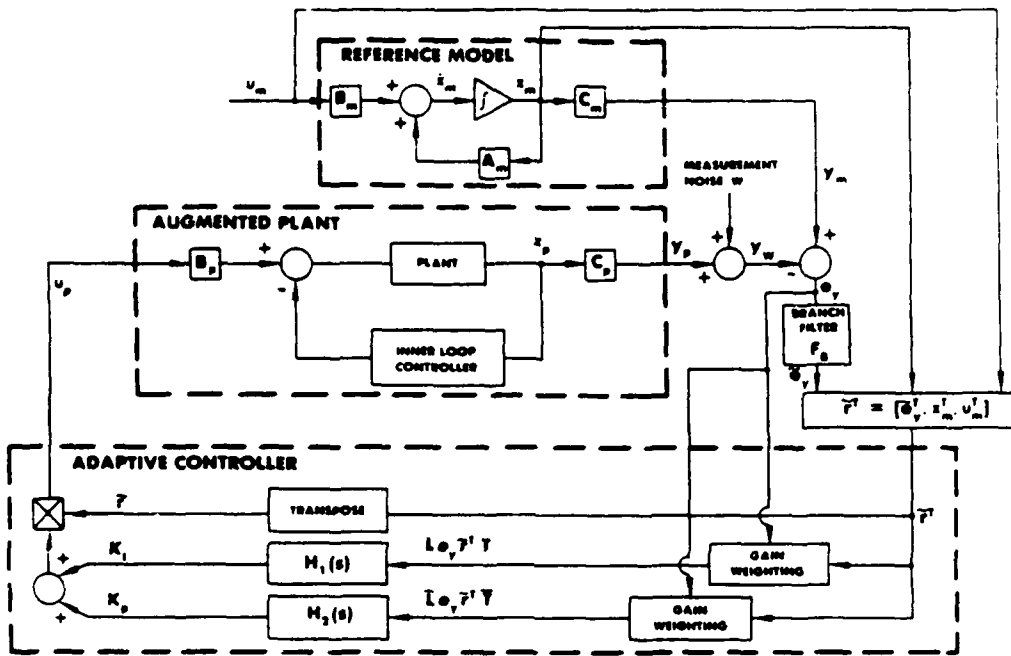


Figure 5.2-1 Adaptive Control System Block Diagram

$$K_I = C_1 X_1 \quad (5.2.15b)$$

$$\dot{X}_2 = A_2 X_2 + B_2 \bar{L} e_y \bar{r}^T \quad (5.2.16a)$$

$$K_P = C_2 X_2 \quad (5.2.16b)$$

Here,  $X_1 \in \mathbb{R}^{\eta_1 \times (2M+N_m)}$ ,  $X_2 \in \mathbb{R}^{\eta_2 \times (2M+N_m)}$  are time varying matrices satisfying the above state equations, where  $\eta_1$  and  $\eta_2$  are arbitrary. Sufficient conditions for global stability are derived in [5] and summarized as follows:

- (1)  $T, \bar{T}, L, \bar{L} > 0$
- (2) there exists a  $P = P^T > 0$  such that
  - (a)  $P B_p = C_p^T$
  - (b)  $P A_p + A_p^T P < 0$
- (3)  $\bar{H}_1(s)$  and  $\bar{H}_2(s)$  are strictly positive real (SPR), where
 
$$\bar{H}_1(s) = C_1 (sI - A_1)^{-1} B_1 L$$

$$\bar{H}_2(s) = C_2 (sI - A_2)^{-1} B_2 \bar{L}$$
- (4)  $F_B(\cdot)$  is any stable linear or nonlinear filter
- (5)  $\text{rank} \{ [C_1 : C_2] \} = M$

Condition (2) is equivalent to the assumption that the open-loop plant transfer function matrix  $Z(s) = C_p (sI - A_p)^{-1} B_p$  is SPR. This condition can be satisfied, for instance, by a flexible structure with collocated sensors and actuators, having small but non-zero intrinsic damping, and low-gain inner-loop compensation. There is no loss of generality of condition (5) since it can be satisfied, for example, by any filters  $H_1$  and  $H_2$  with non-redundant outputs (i.e.,  $\text{Rank} \{C_1\} = \text{Rank} \{C_2\} = M$ ).

A specific set of Eqs. (5.2.13), (5.2.15) and (5.2.16) was implemented for the experiment,

$$\dot{K}_I = -\sigma_1 K_I + L e_y \bar{r}^T \quad (5.2.17)$$

$$\dot{K}_P = -\sigma_2 K_P + \bar{L} e_y \bar{r}^T \quad (5.2.18)$$

$$\dot{\bar{e}}_y = (e_y - \bar{e}_y) \gamma \quad \text{Branch Filter} \quad (5.2.19)$$

The introduction of  $L$  and  $\bar{L}$  in the adaptive law allows the designer to selectively increase the control effort in specified locations on the structure. The reason for branch filtering is explained as follows. The most natural place to introduce a noise filter  $F(s)$  (Fig. 5.2-1) is directly after the measurement noise enters, i.e., as an output filter in cascade with the plant. However, in this case global stability of the adaptive algorithm would require that the cascade transfer function  $C_p (sI - A_p)^{-1} B_p F(s)$  be strictly positive real (SPR). This condition is very difficult to satisfy in practice

since the phase lag of the output filter adds to that of the plant. This destabilizing effect is demonstrated in [5]. The branch filter concept avoids the cascade SPR condition by filtering only a single branch of the output error which feeds into the adaptive law. This has successfully eliminated the bias caused by the noise squaring problem, and requires only that the open-loop plant  $C_p(sI-A_p)^{-1}B_p$  be SPR. In addition, the noise on the remaining branch of the output error is attenuated by the filtering action of the adaptive gain generator itself (Eqs. (5.2.17) and (5.2.18)). For this purpose, it is useful to introduce filtering action on  $K_p$  in (5.2.18) to avoid direct transmission of noise. For practical purposes, the proportional gain filtering is chosen to be wider band than the integral gain filtering (i.e.,  $\sigma_2 > \sigma_1$ ) to preserve the relative role of the proportional and integral adaptation gains in determining adaptive performance.

For practical implementation, the above continuous adaptive control algorithm is discretized and coded using the backward differencing scheme.

### 5.2.3 Results and Evaluation

5.2.3.1 Introduction. In this subsection, the performance of the adaptive controller in the experiments described earlier is evaluated. It has been mentioned that rate information is a crucial factor for the stabilization of the adaptive control system. However, the experimental system developed to date does not have any rate sensing devices. Derived or estimated rate information must be used. At the early stage of the experiments, several approaches were tried to obtain rate information from very noisy angular position measurements. All of these methods failed to provide satisfactory rate data for the control algorithm. The resolution of this problem is discussed below.

5.2.3.2 Rate Estimation. Initially, hub angular rates were derived by differencing successive angular position measurements. The presence of excessive sensor noise made the derived rates unusable, particularly in the high frequency range. This noise and the accompanying phase shift effects feeding through the adaptive gain generator caused severe actuator saturation and eventually drove the system unstable. A moving window average differencing method was then implemented with various window sizes ranging from 2-10 sampling periods. However, even for a window size of 5 sampling periods, the noise effects were not significantly attenuated, and a window size of 10 sampling periods caused serious time lag--both resulting in unsatisfactory controller performance. Neither a simple first or second order filter could reduce the high frequency noise effects. The phase delays associated with the filters, combined with the inherent delays in the data acquisition system, system software and algorithmic computation are the main source of the problem.

Finally, a minimum variance type of state estimator (Kalman filter) used by Wen [1] was implemented for generating estimated hub angular rates based on position measurements. For the continuous case, the estimated state  $x$  is generated by the state estimator equation:

$$\hat{\dot{x}}_p = A_p \hat{x}_p + B_p u_p + K(y_p - C_p \hat{x}_p) \quad (5.2.20)$$

where the filter gain matrix  $K$  is given by

$$K = HC_p^T N^{-1} \quad (5.2.21)$$

and  $H$  is the solution of the Riccati equation

$$A_p H + H A_p^T + M - HC_p^T N^{-1} C_p H = 0 \quad (5.2.22)$$

It can be shown that provided  $(A_p, C_p)$  is observable, and  $(A_p, B_p)$ ,  $(A_p, M^T)$  are controllable, the Riccati equation has a unique positive solution.

The discretized state estimator equation is given by

$$\hat{x}_{n+1} = \Phi \hat{x}_n + \Gamma_1 u_n + \Gamma_2 y_n \quad (5.2.23)$$

where  $y_n$  is the position measurement,  $\hat{x}_n$  is the estimated state, and the values of  $\Phi, \Gamma_1$  and  $\Gamma_2$  are determined by the sampling period. Because of computational loading constraints, only two boom modes (with frequencies of 0.09 Hz and 0.62 Hz) were included in the estimator. In this case,  $x_n$  is given by

$$\hat{x}_n^T = [\hat{x}_1 \quad \dot{\hat{x}}_1 \quad \hat{x}_2 \quad \dot{\hat{x}}_2]^T \quad (5.2.24)$$

and since the estimated position output is

$$\hat{y}_n = C \hat{x}_n \quad (5.2.25)$$

where

$$C = [C_{1n} \quad 0 \quad C_{2n} \quad 0] \quad (5.2.26)$$

by defining

$$\tilde{C} = [0 \quad C_{1n} \quad 0 \quad C_{2n}] \quad (5.2.27)$$

we can obtain the estimated angular rate  $\dot{\hat{y}}_n$  by

$$\dot{\hat{y}}_n = \tilde{C} \hat{x}_n \quad (5.2.28)$$

It turned out that the minimum variance rate estimates obtained this way were sufficiently accurate to stabilize the adaptive controller and allow excellent overall performance. It is noted that in an adaptive context, the minimum variance estimator (which is plant dependent) must properly be considered as an emulator for a rate sensor in the system hardware rather than as part of the adaptive algorithm. As such, it was used in all of the experiments described below.

**5.2.3.3 Quiescent Control Experiment.** As mentioned before, this experiment served as a test of the algorithm and software. No initial deflection or excitation was given. As shown in Fig. 5.2-2, with the controller on, the hub angle sensors stay at the same values (zero) throughout the experiment as expected.

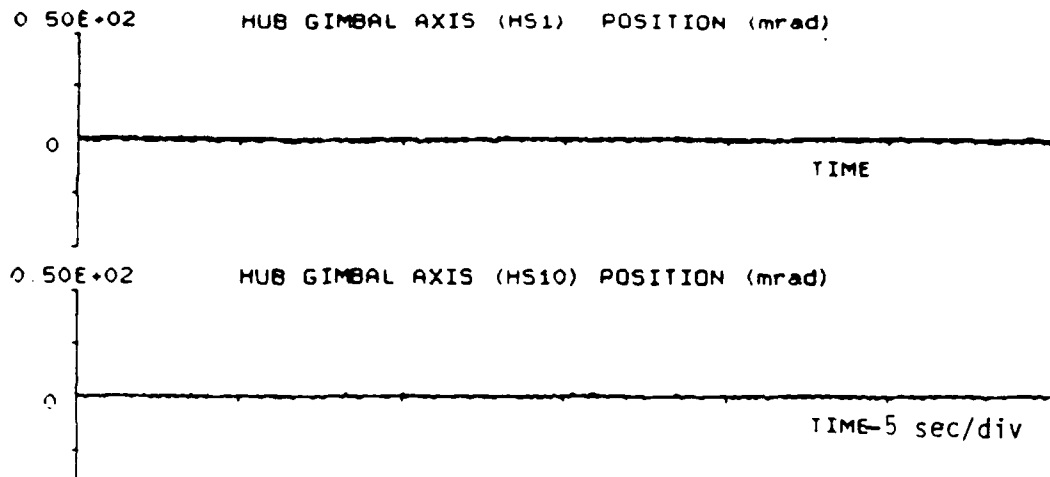


Figure 5.2-2 Quiescent Control Response

5.2.3.4 Transient Regulation Experiment. For all of the regulation experiments, the open-loop responses are discussed first, then compared with the corresponding closed-loop responses. The comparison between the two is based on three figures of merit:

- (1) Maximum overshoot
- (2) Settling time (with convergence criterion of 2.0 mrad)
- (3) Root-mean-square (RMS) error (over the range of 0 - 30 sec).

Starting with the case of a 2-sec 1.5 N-m single pulse excitation, the open-loop responses are plotted in Fig. 5.2-3. As can be seen, the HA1-HS10 axis is much more susceptible to disturbances and has lower damping than the HA10-HS1 axis (Fig. 5.2-3 (a) and (b)):

|      | Maximum<br>Overshoot<br>(m rad) | Settling<br>Time<br>(sec) | RMS<br>Error<br>(m rad) |
|------|---------------------------------|---------------------------|-------------------------|
| HS1  | 17.6                            | 16.5                      | 5.417                   |
| HS10 | 23.6                            | 29.2                      | 8.598                   |

Table 5.2-1. Open-Loop Responses to 2-sec Pulse

The levitators LO1 and LO10 (Fig. 4.3-3 (m) and (n)) act accordingly. Fig. 5.2-3 (c) and (d) show the excitation pattern with no control action. The estimated hub angular rates shown in Fig. 5.2-3 (e) and (f) correlate well with the corresponding angular positions. As mentioned before, the plant output is a combination of the position and rate, with rate to position ratio of 5:1. Thus the plant output plots (Fig. 5.2-3 (g) and (h)) are fairly close to those of the rates. Also, since the estimated rates are not noisy, the output errors  $e_{y1}$  and  $e_{y2}$  are almost identical with the filtered output errors  $\bar{e}_{y1}$  and  $\bar{e}_{y1}$  (Fig. 5.2-3 (i)-(1)).

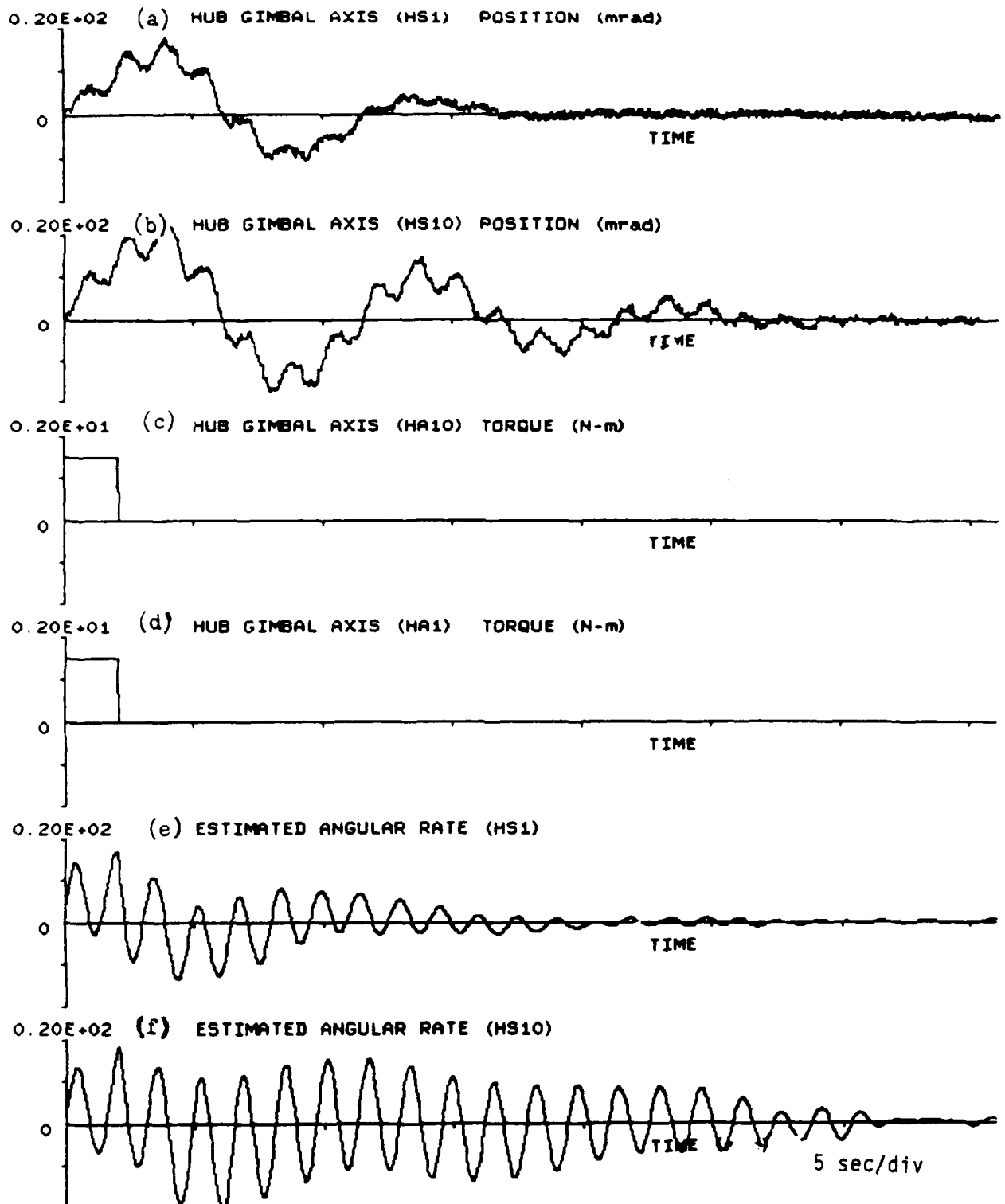


Figure 5.2-3 Open-loop Responses to 2-sec Pulse of 1.5 N-m

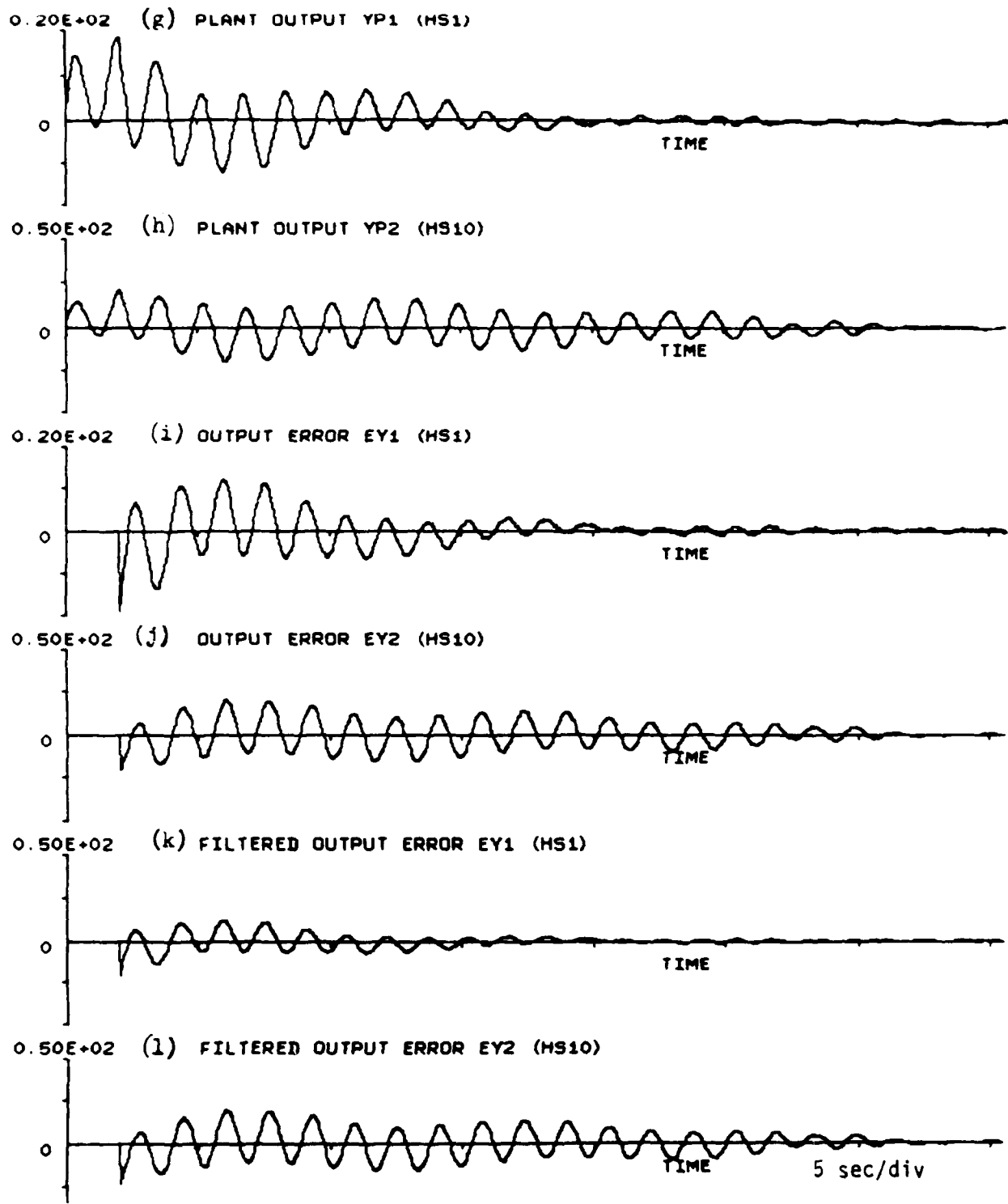


Figure 5.2-3 Open-loop Responses to 2-sec Pulse of 1.5 N-m (Cont.)



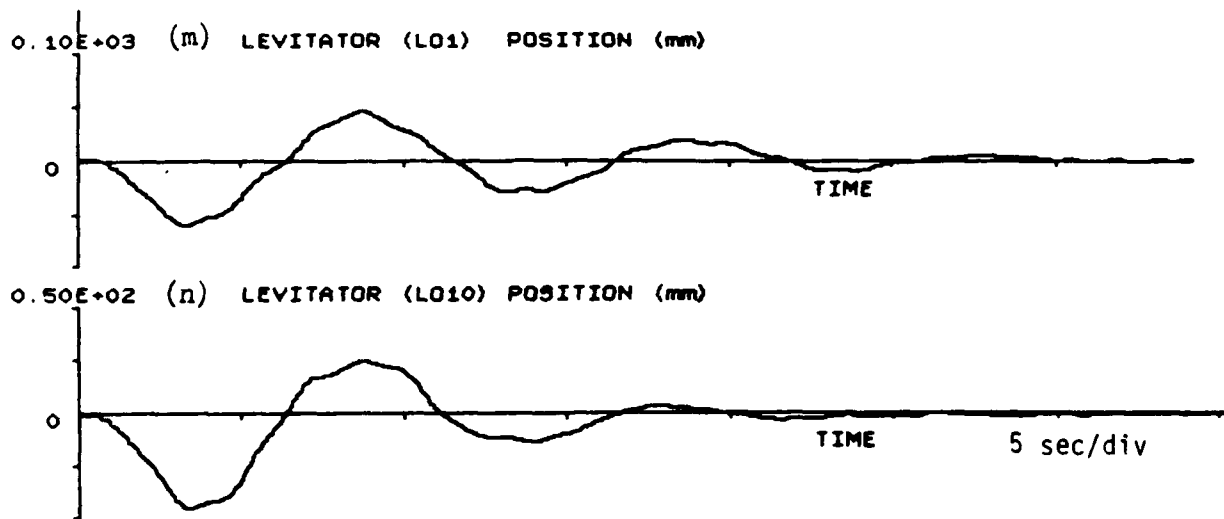


Figure 5.2-3 Open-loop Responses to 2-sec Pulse of 1.5 N-m (Cont.)

After some initial tuning, a fixed set of adaptive control design parameters was chosen for use throughout all of the transient regulation experiments. Some selected parameters are summarized below:

$$T - \bar{T} = \text{diag} (0.05, 0.05, 0.05, 0.05, 0.05, 0.05, 0.05, 0.05) \quad (5.2.29)$$

$$L - \bar{L} = \text{diag} (1, 1) \quad (5.2.30)$$

$$\sigma_1 = 0.5 \text{ (0.08 Hz integral gain bandwidth)} \quad (5.2.31)$$

$$\sigma_2 = 21.99 \text{ (3.5 Hz proportional gain bandwidth)} \quad (5.2.32)$$

$$\gamma = 21.99 \text{ (3.5 Hz branch filter bandwidth)} \quad (5.2.33)$$

The closed-loop responses are given in Fig. 5.2-4. Table 5.2-2 summarizes the features of the hub angle responses (Fig. 5.2-4 (a) and (b)):

|      | Maximum<br>Overshoot<br>(m rad) | Settling<br>Time<br>(sec) | RMS<br>Error<br>(m rad) |
|------|---------------------------------|---------------------------|-------------------------|
| HS1  | 12                              | 6.1                       | 3.195                   |
| HS10 | 16                              | 8                         | 4.612                   |

Table 5.2-2. Closed-Loop Responses to 2-sec Pulse

The closed-loop performance relative to the open-loop performance is defined as the ratio of open-loop value divided by the closed-loop value of the quantities discussed. Using Tables 5.2-1 and 5.2-2, the results are tabulated in Table 5.2-3.

|      | Maximum<br>Overshoot<br>Ratio | Settling<br>Time<br>Ratio | RMS<br>Error<br>Ratio |
|------|-------------------------------|---------------------------|-----------------------|
| HS1  | 1.467                         | 2.705                     | 1.695                 |
| HS10 | 1.475                         | 3.65                      | 1.864                 |

Table 5.2-3 Open-Loop/Closed-Loop Ratio for 2-sec Pulse Excitation

A significant 365% improvement in HS10 settling time is observed even though the adaptive controller is designed without accurate knowledge of the plant.

It is noted that there is chattering of the hub control torques (Fig. 5.2-4 (c) and (d)) during the initial stage after the controller is turned on. It is believed that this is due to complicated interaction of estimator spillover (i.e., only two modes are used in the minimum variance estimator acting as a rate sensor), noise, and hardware saturation. It was found empirically that this chattering effect can be eliminated by narrowing the branch filter bandwidth to smooth feedback signals and attenuate higher frequency noise. The broadband (i.e., 3.5 Hz) setting on the branch filter cut-off frequency used in these experiments is evidenced by the similarity of

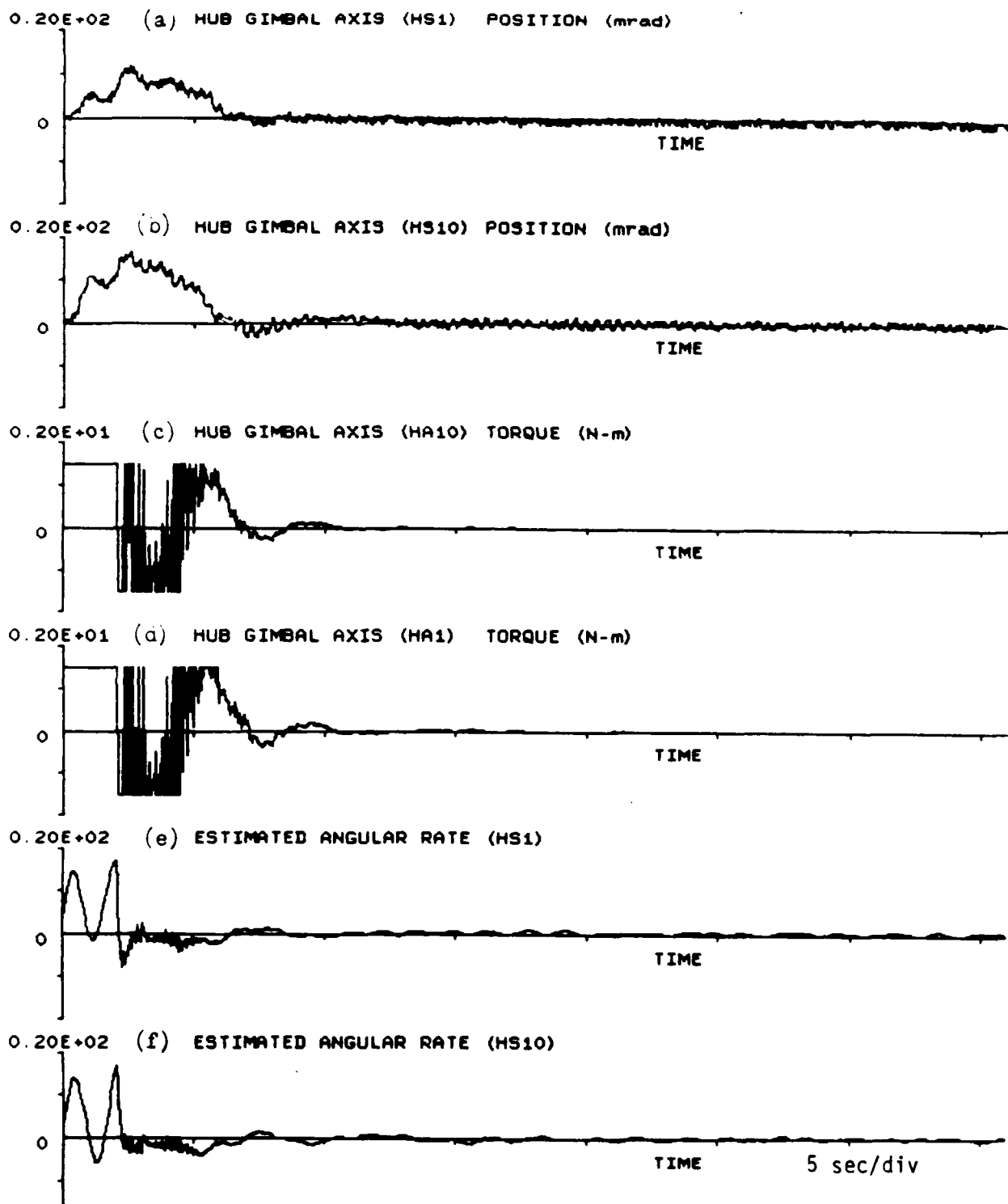


Figure 5.2-4 Closed-loop Responses to 2-sec Pulse of 1.5 N-m

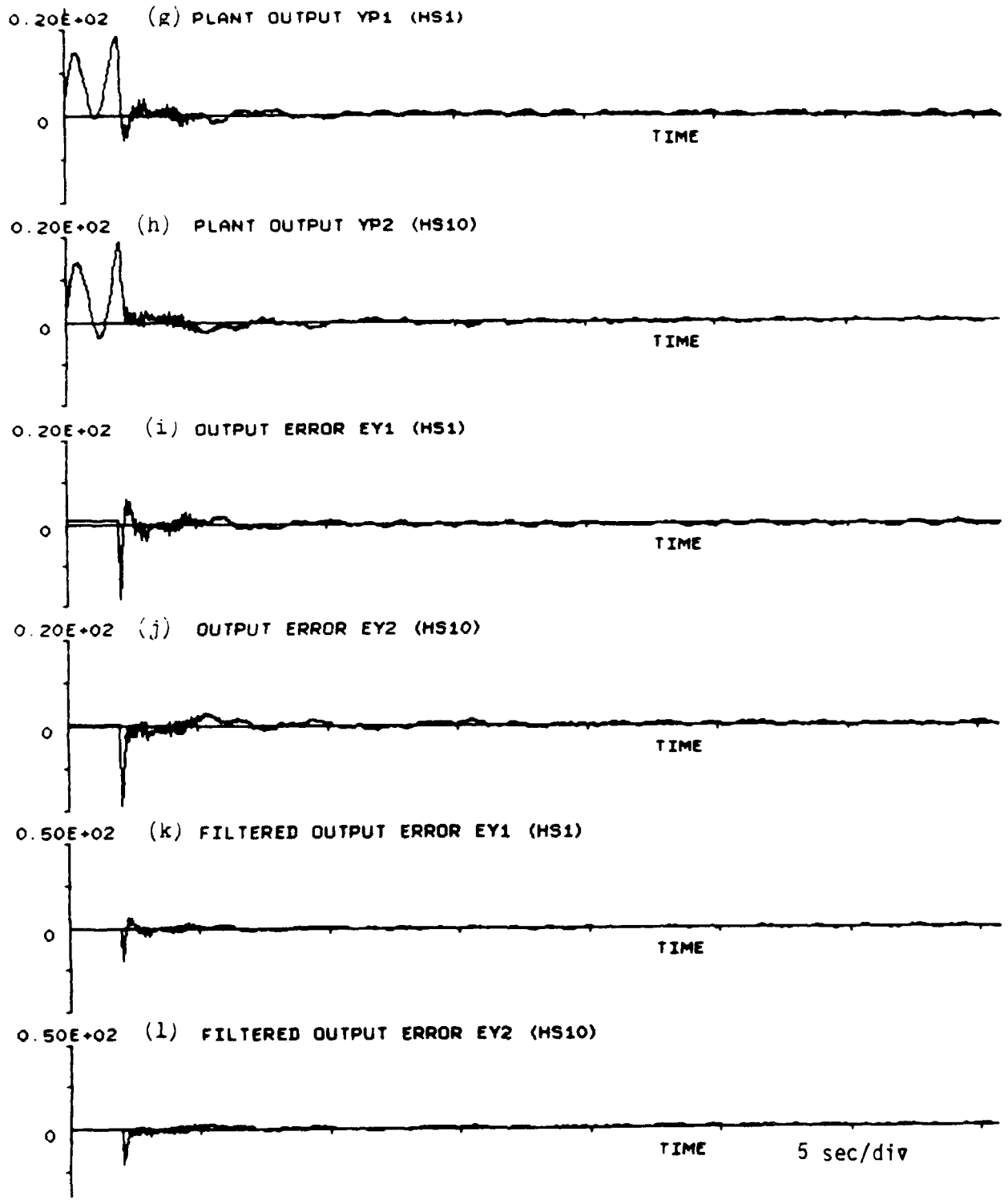


Figure 5.2-4 Closed-loop Responses to 2-sec Pulse of 1.5 N-m (Cont.)

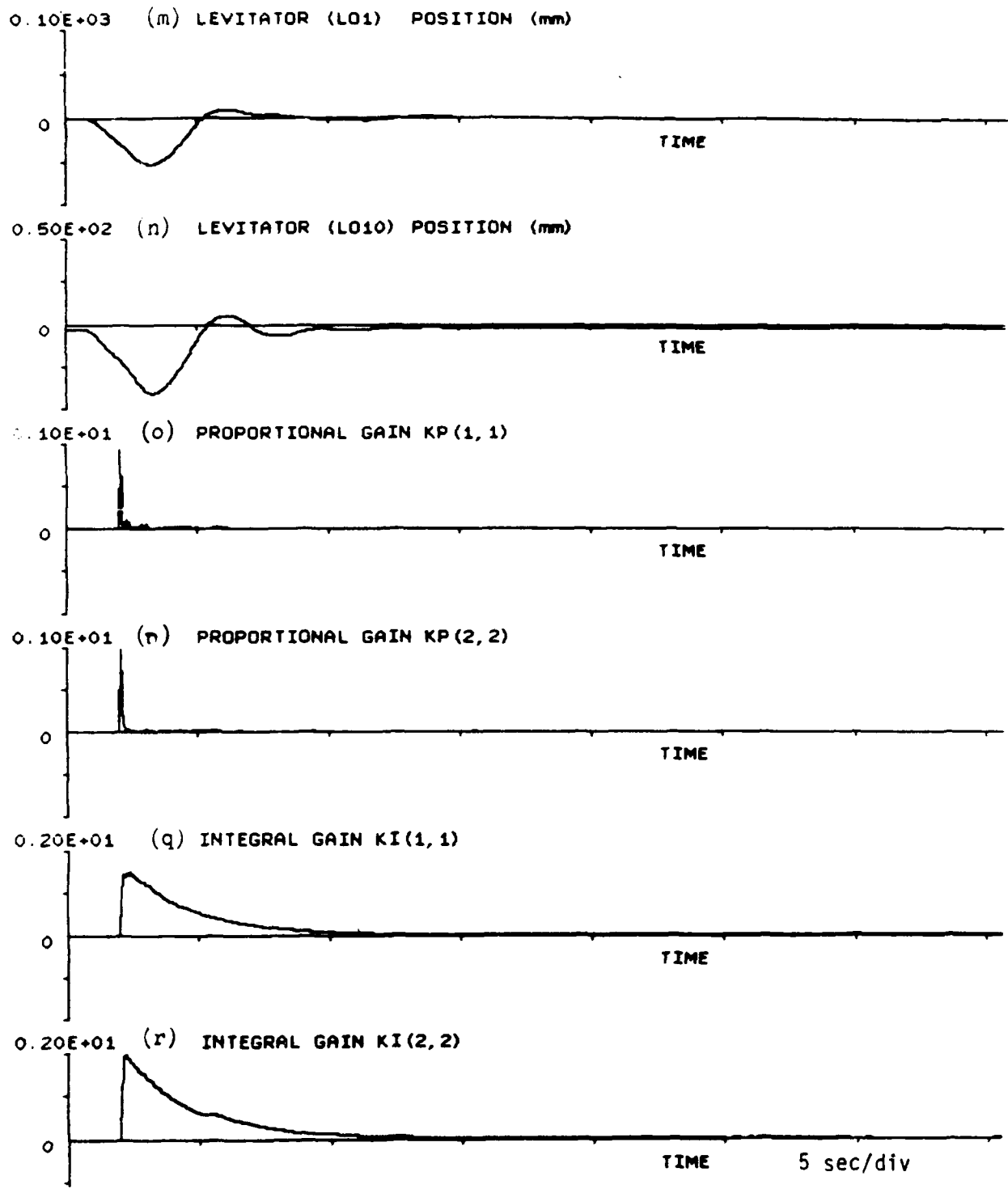


Figure 5.2-4 Closed-loop Responses to 2-sec Pulse of 1.5 N-m (Cont.)

error  $e_{y1}$  and  $e_{y2}$  plots to branch filtered error  $\bar{e}_{y1}$  and  $\bar{e}_{y2}$  plots. Significant smoothing of these error signals can be achieved by lowering branch filter bandwidth, which was used to advantage in the regulation experiments with initial deflection (cf., Subsection 5.2.3.5).

The effect of leakage terms  $-\sigma_1 K_I$  and  $-\sigma_2 K_p$  in Eqs. (5.2.17) and (5.2.18) is seen in Figs. 5.2-4 (o) ~ (r) where the integral gain  $K_I$  and proportional gain  $K_p$  decay with exponential rates corresponding to the choice of  $\sigma_1$  and  $\sigma_2$ , respectively.

The open-loop and closed loop responses for 1-sec and 3-sec 1.5N-m pulse excitations are shown in Figs. 5.2-5, 5.2-6 and Figs. 5.2-7, 5.2-8, respectively, and are discussed briefly in the following. The observations similar to those of the 2-sec pulse case are omitted. It is noted that the 1-sec pulse significantly excites the second mode (0.62 Hz) in the open-loop response relative to the earlier 2-sec pulse responses. Data extracted from Fig. 5.2-5 (a) and (b) and Fig. 5.2-6 (a) and (b), are tabulated in Tables 5.2-4, 5.2-5 and 5.2-6 below.

|      | Maximum<br>Overshoot<br>(m rad) | Settling<br>Time<br>(sec) | RMS<br>Error<br>(m rad) |
|------|---------------------------------|---------------------------|-------------------------|
| HS1  | 10                              | 10                        | 2.886                   |
| HS10 | 18.3                            | 27                        | 4.655                   |

Table 5.2-4. Open-Loop Responses to 1-sec Pulse

|      | Maximum<br>Overshoot<br>(m rad) | Settling<br>Time<br>(sec) | RMS<br>Error<br>(m rad) |
|------|---------------------------------|---------------------------|-------------------------|
| HS1  | 7.3                             | 5.5                       | 2.247                   |
| HS10 | 11.3                            | 7                         | 2.755                   |

Table 5.2-5. Closed-Loop Responses to 1-sec Pulse

|      | Maximum<br>Overshoot<br>Ratio | Settling<br>Time<br>Ratio | RMS<br>Error<br>Ratio |
|------|-------------------------------|---------------------------|-----------------------|
| HS1  | 1.370                         | 1.818                     | 1.284                 |
| HS10 | 1.619                         | 3.857                     | 1.69                  |

Table 5.2-6 Open-Loop/Closed-Loop Ratio for 1-sec Pulse Excitation

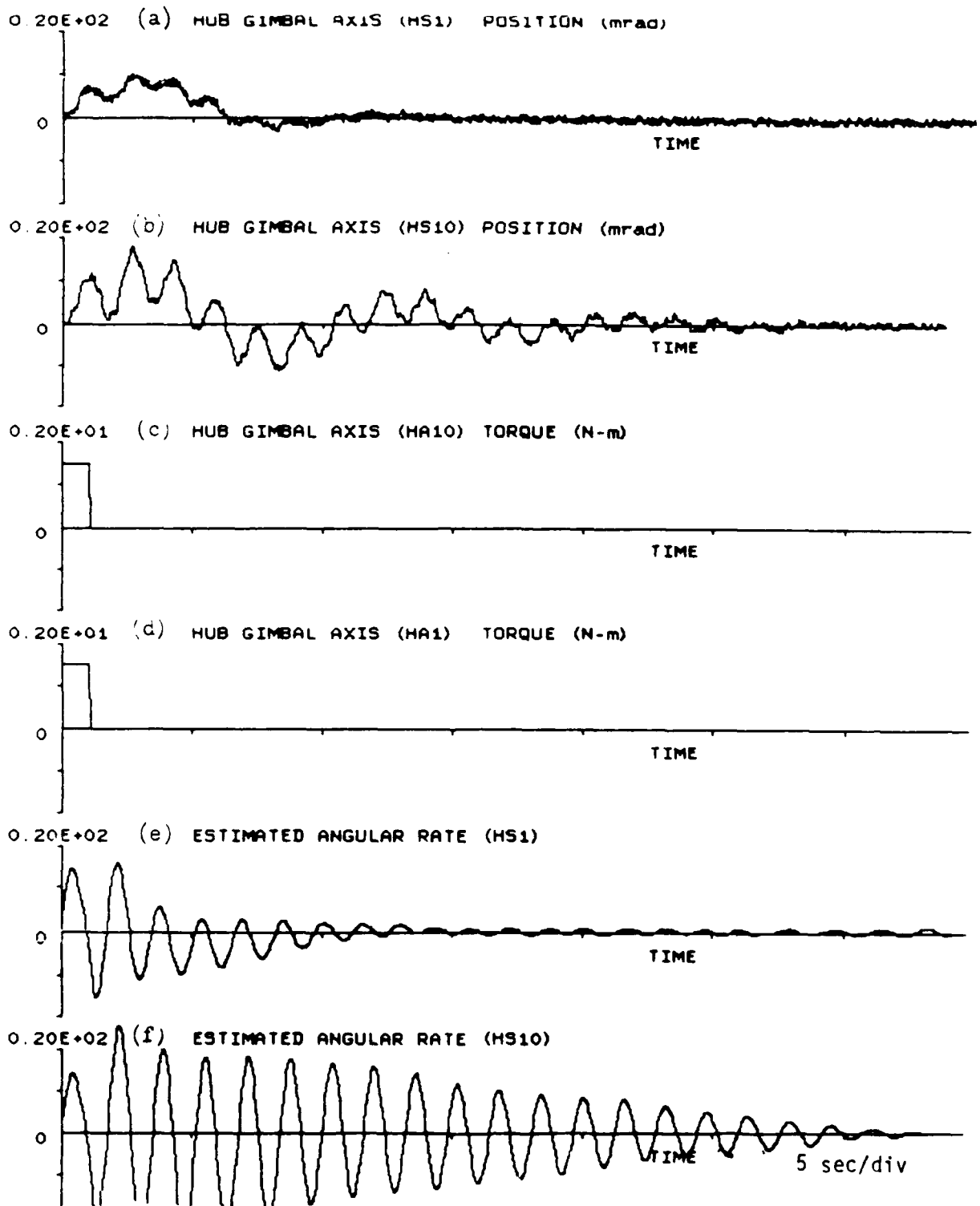


Figure 5.2-5 Open-loop Responses to 1-sec Pulse of 1.5 N-m

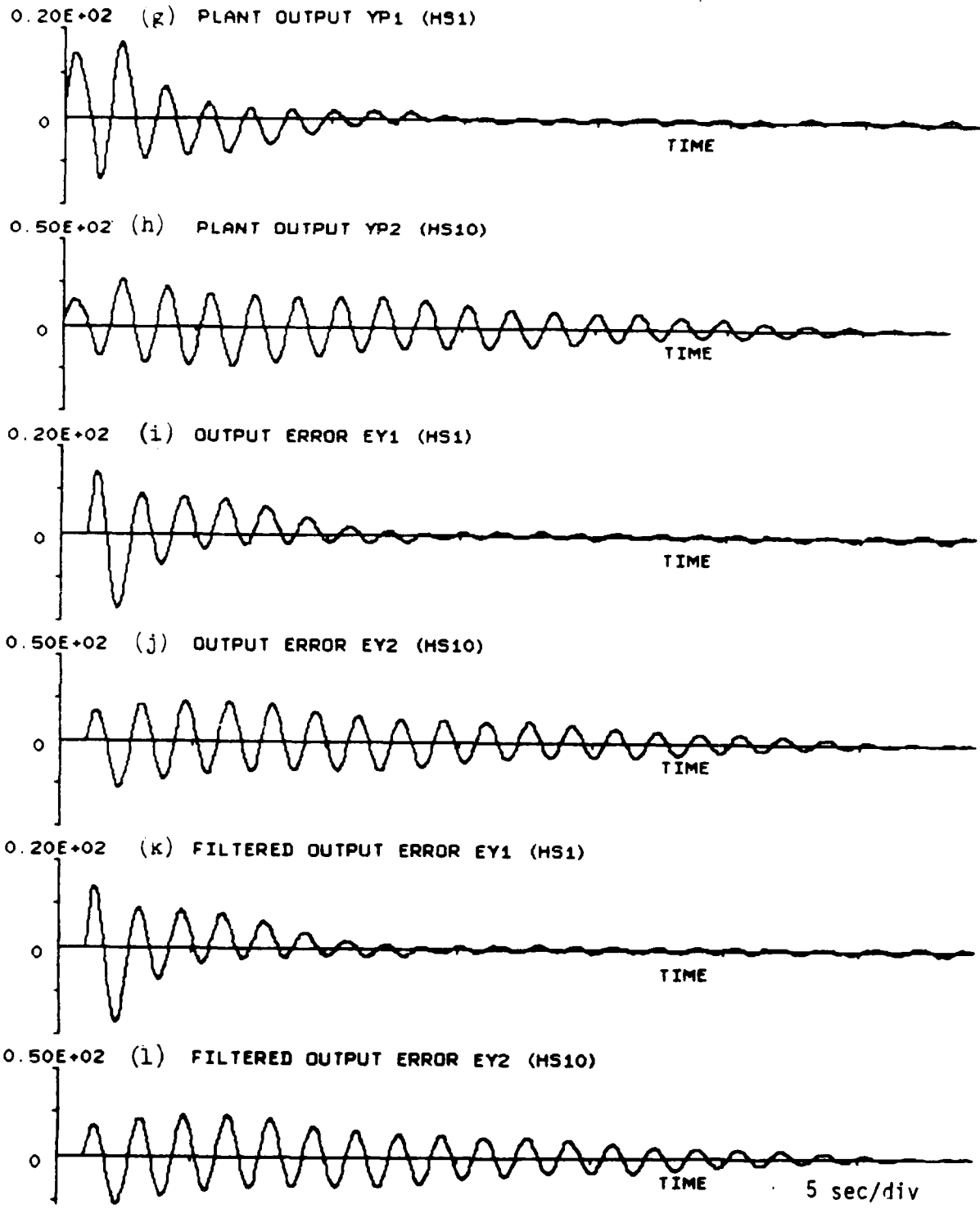


Figure 5.2-5 Open-loop Responses to 1-sec Pulse of 1.5 N-m (Cont.)



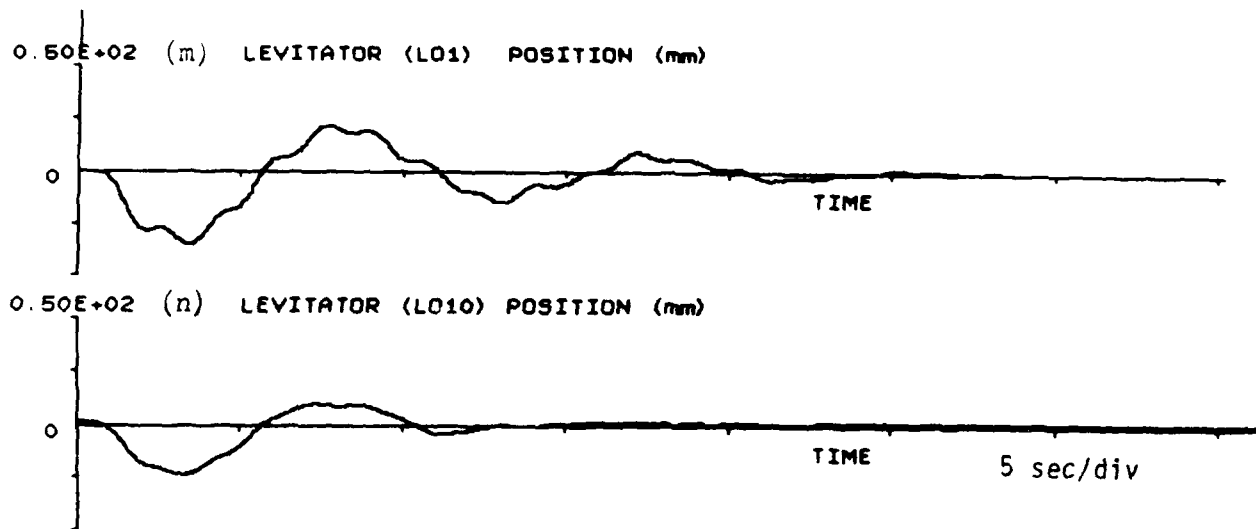


Figure 5.2-5 Open-loop Responses to 1-sec Pulse of 1.5 N-m (Cont.)

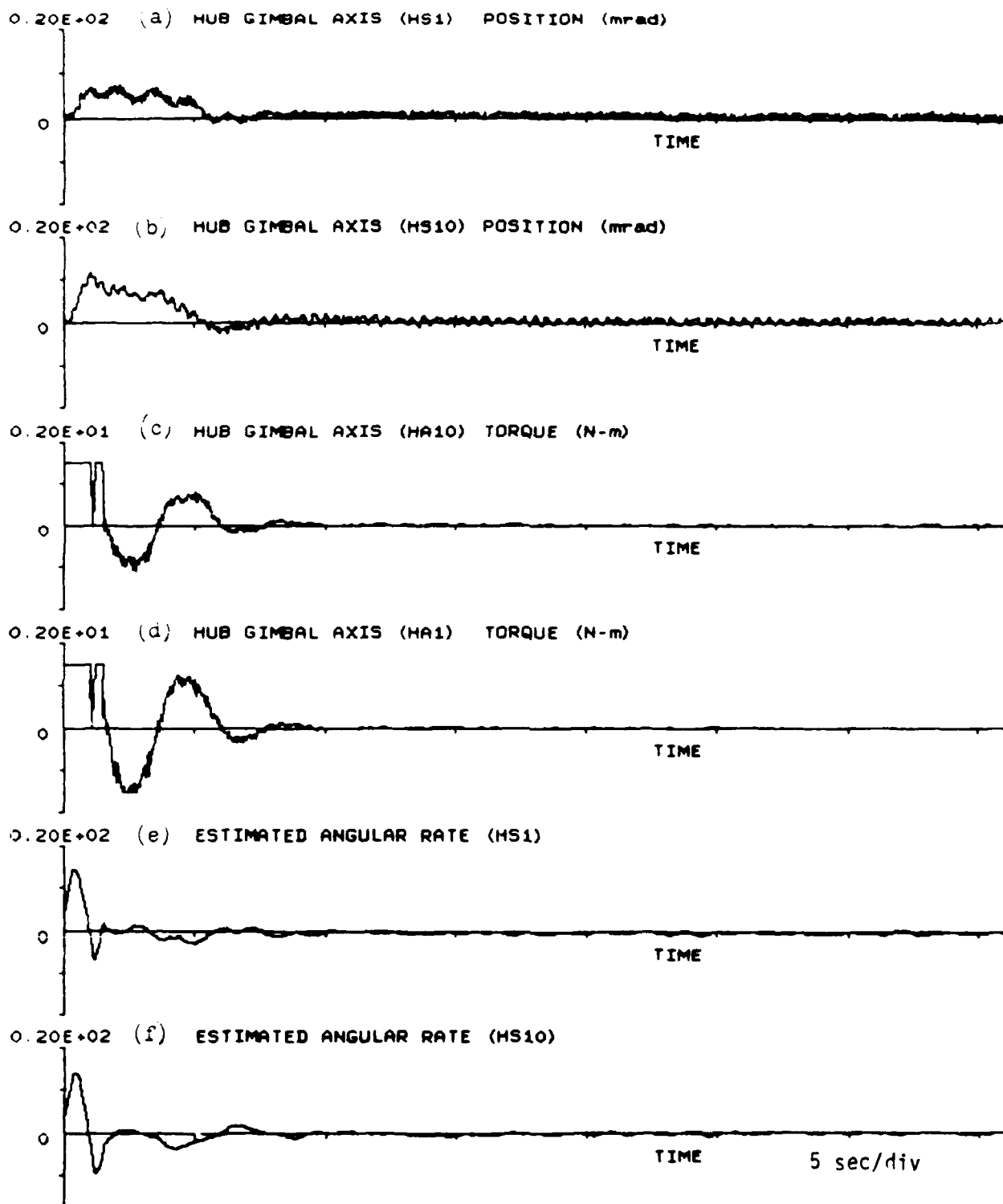


Figure 5.2-6 Closed-loop Responses to 1-sec Pulse of 1.5 N-m

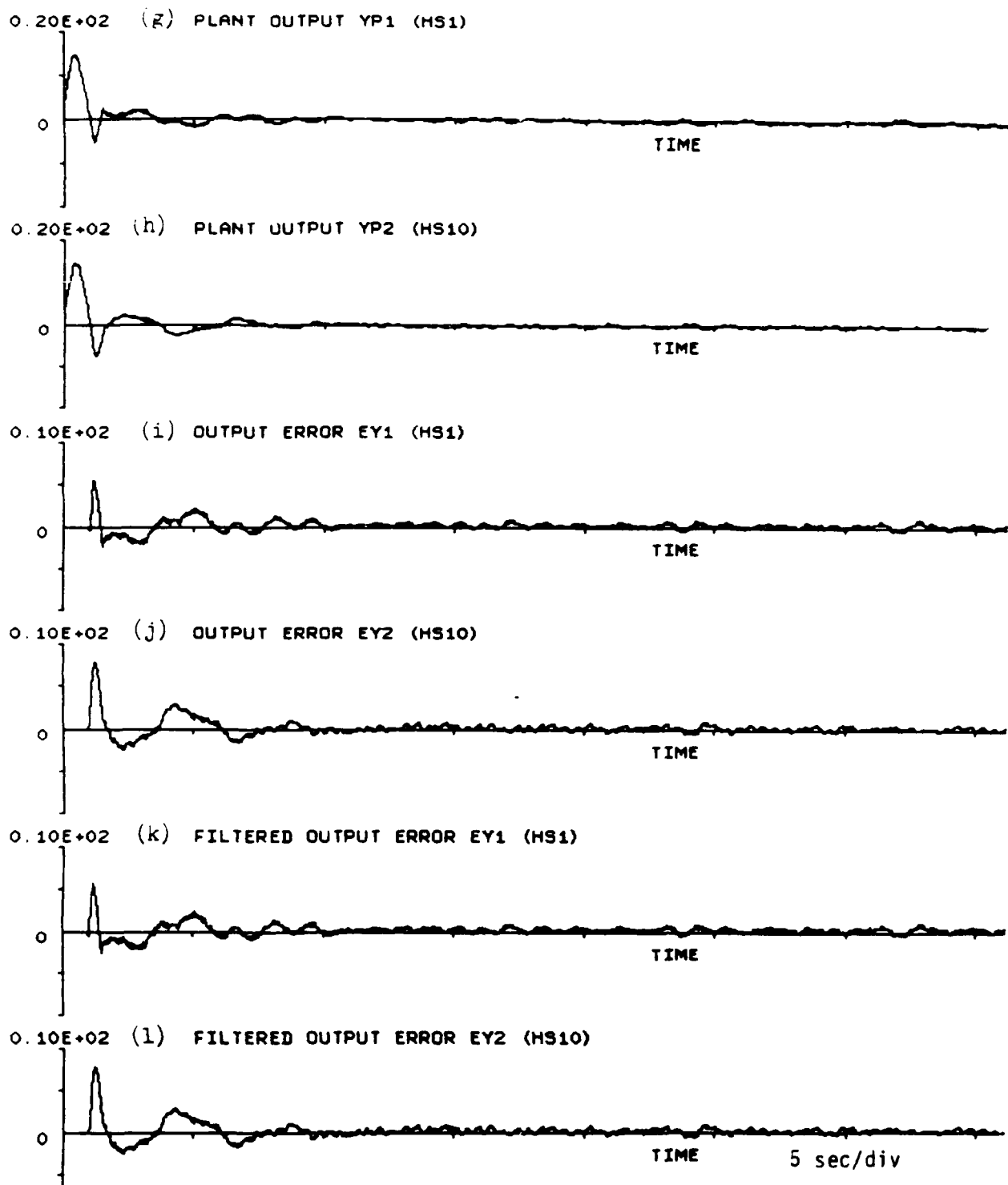


Figure 5.2-6 Closed-loop Responses to 1-sec Pulse of 1.5 N-m (Cont.)

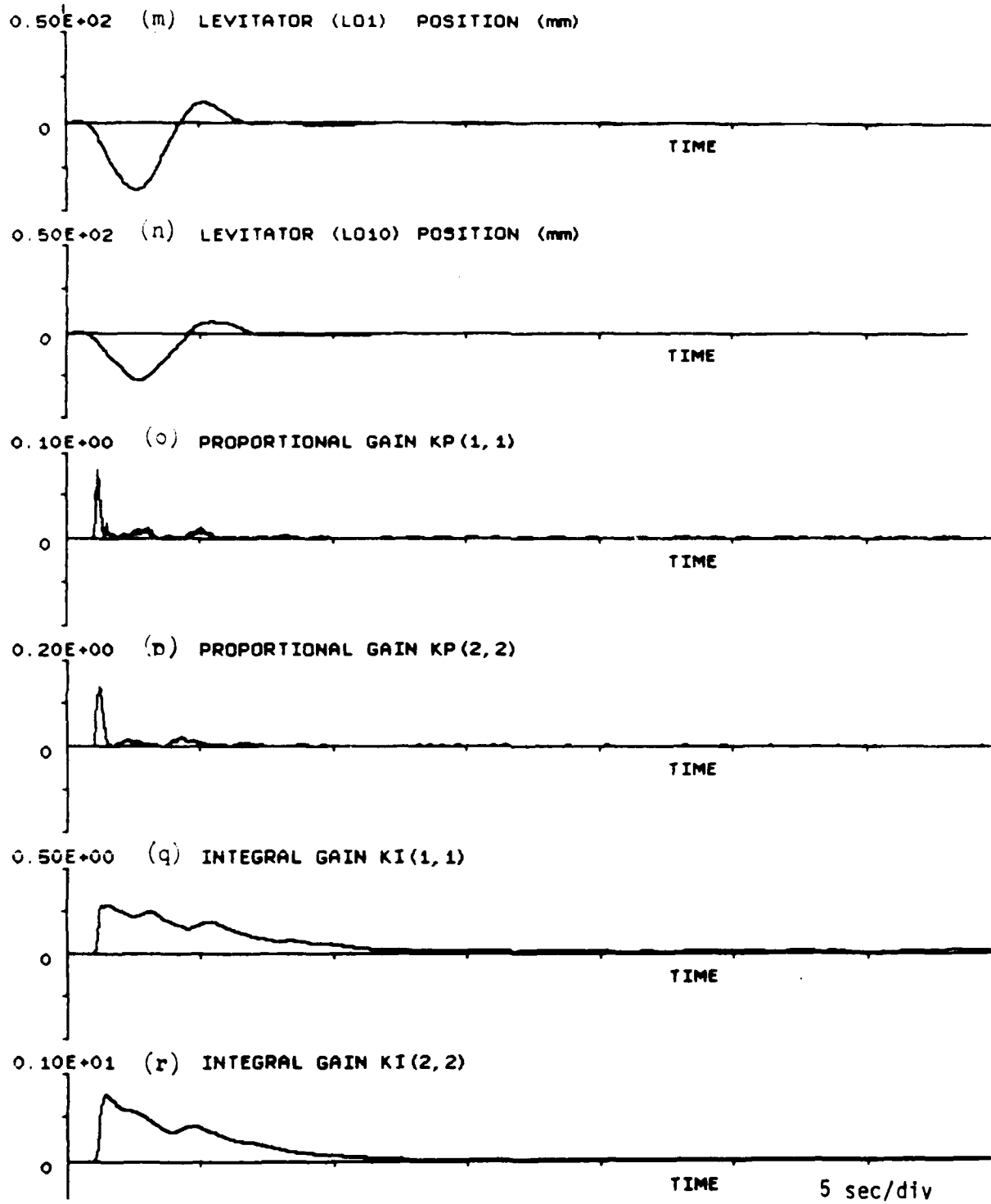


Figure 5.2-6 Closed-loop Responses to 1-sec Pulse of 1.5 N-m (Cont.)

Compared with the 2-sec pulse case, the second mode is less noticeably excited in the 3-sec pulse responses. The results based on the responses in Fig. 5.2-7 (a) and (b) and Fig. 5.2-8 (a) and (b) are tabulated in Tables 5.2-7, 5.2-8 and 5.2-9.

|      | Maximum<br>Overshoot<br>(m rad) | Settling<br>Time<br>(sec) | RMS<br>Error<br>(m rad) |
|------|---------------------------------|---------------------------|-------------------------|
| HS1  | 19.5                            | 18                        | 6.867                   |
| HS10 | 30.5                            | 30                        | 12.084                  |

Table 5.2-7. Open-Loop Responses to 3-sec Pulse

|      | Maximum<br>Overshoot<br>(m rad) | Settling<br>Time<br>(sec) | RMS<br>Error<br>(m rad) |
|------|---------------------------------|---------------------------|-------------------------|
| HS1  | 19                              | 13                        | 5.582                   |
| HS10 | 27                              | 15                        | 7.987                   |

Table 5.2-8. Closed-Loop Responses to 3-sec Pulse

|      | Maximum<br>Overshoot<br>Ratio | Settling<br>Time<br>Ratio | RMS<br>Error<br>Ratio |
|------|-------------------------------|---------------------------|-----------------------|
| HS1  | 1.026                         | 1.385                     | 1.23                  |
| HS10 | 1.13                          | 2                         | 1.513                 |

Table 5.2-9 Open-Loop/Closed-Loop Ratio for 3-sec Pulse Excitation

Comparing Tables 5.2-3, 5.2-6 and 5.2-9, it is found that the controller is less effective in the 3-sec pulse case.

5.2.3.5 Initial Deflection Regulation Experiment. As described in Subsection 5.2.1, the system output is now forced to track the highly damped reference model output (instead of zero only) to suppress the vibration. The open-loop and closed-loop responses are given in Figs. 5.2-9 and 5.2-10 respectively. Because there was a much more serious chattering and saturation of control torques than that discussed earlier in Subsection 5.2.3.4 in the first few tries (the performances were good though), the bandwidths for the branch filter and proportional gain were narrowed down to 1 Hz. This frequency was chosen commensurate with the highest frequency mode (i.e., 0.62 Hz) retained in the minimum variance rate estimator. Other parameters are the same as used in transient regulation experiment:

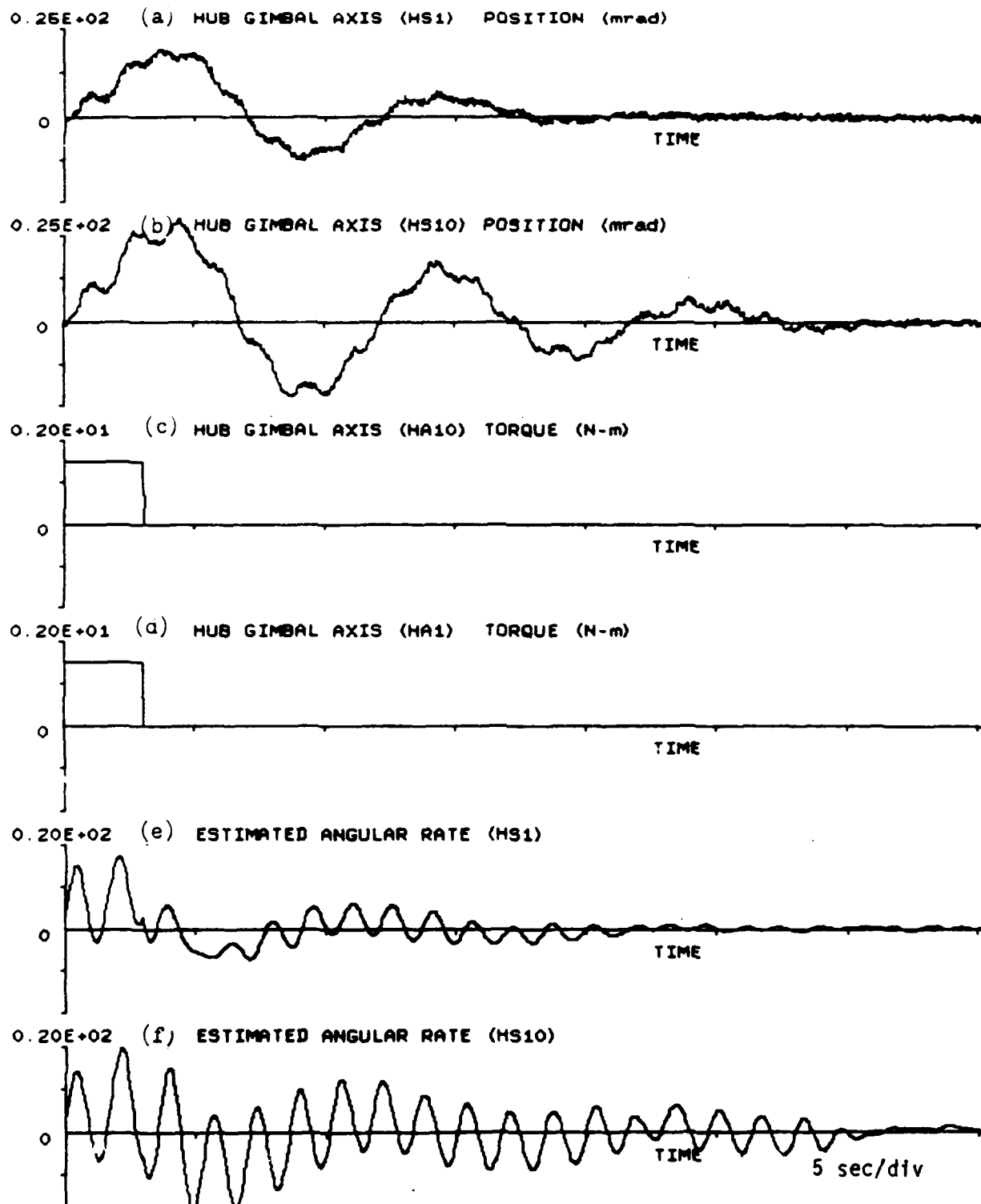


Figure 5.2-7 Open-loop Responses to 3-sec Pulse of 1.5 N-m

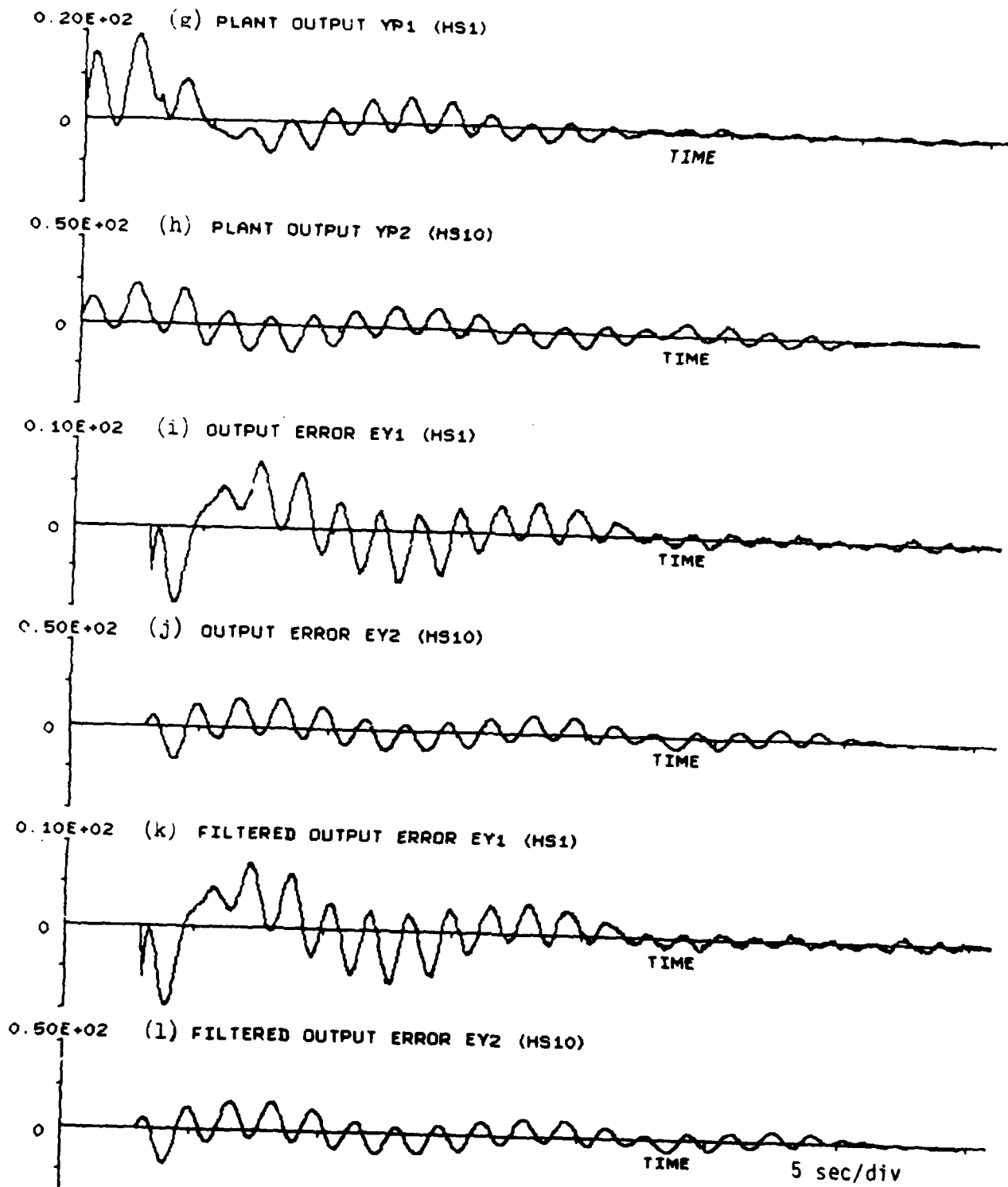


Figure 5.2-7 Open-loop Responses to 3-sec Pulse of 1.5 N-m (Cont.)

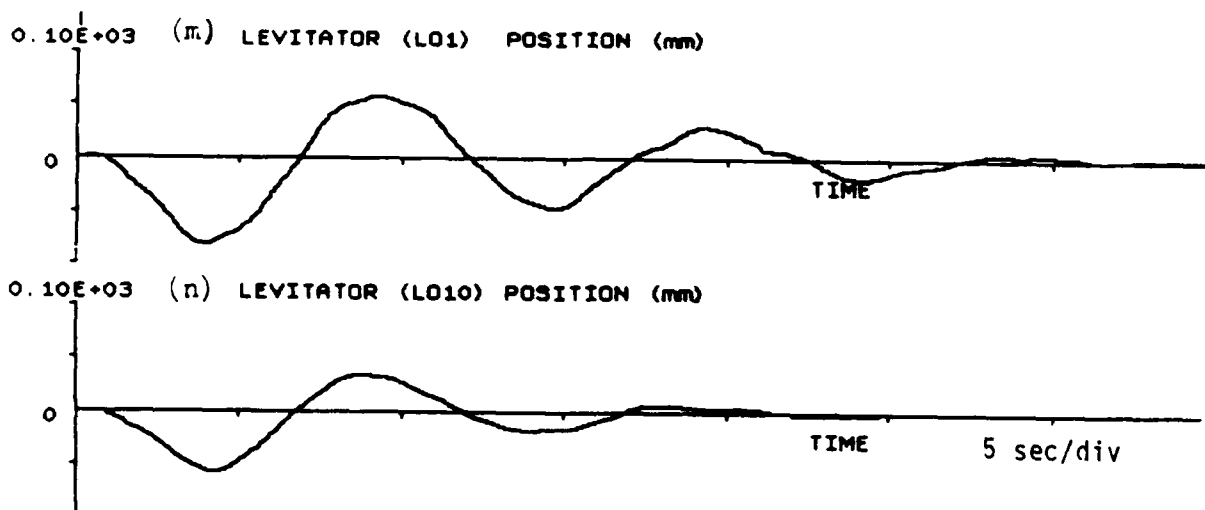


Figure 5.2-7 Open-loop Responses to 3-sec Pulse of 1.5 N-m (Cont.)



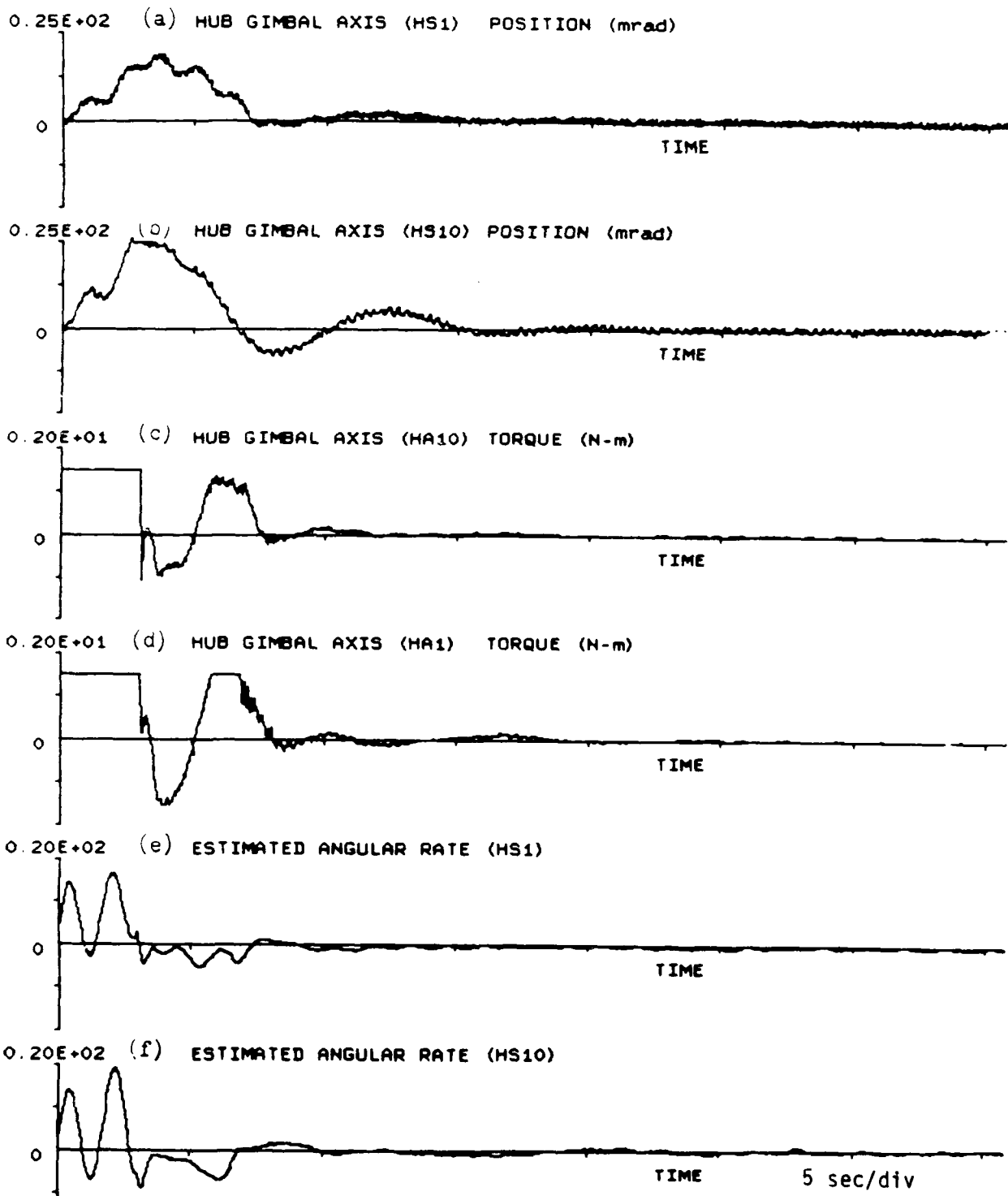


Figure 5.2-8 Closed-loop Responses to 3-sec Pulse of 1.5 N-m

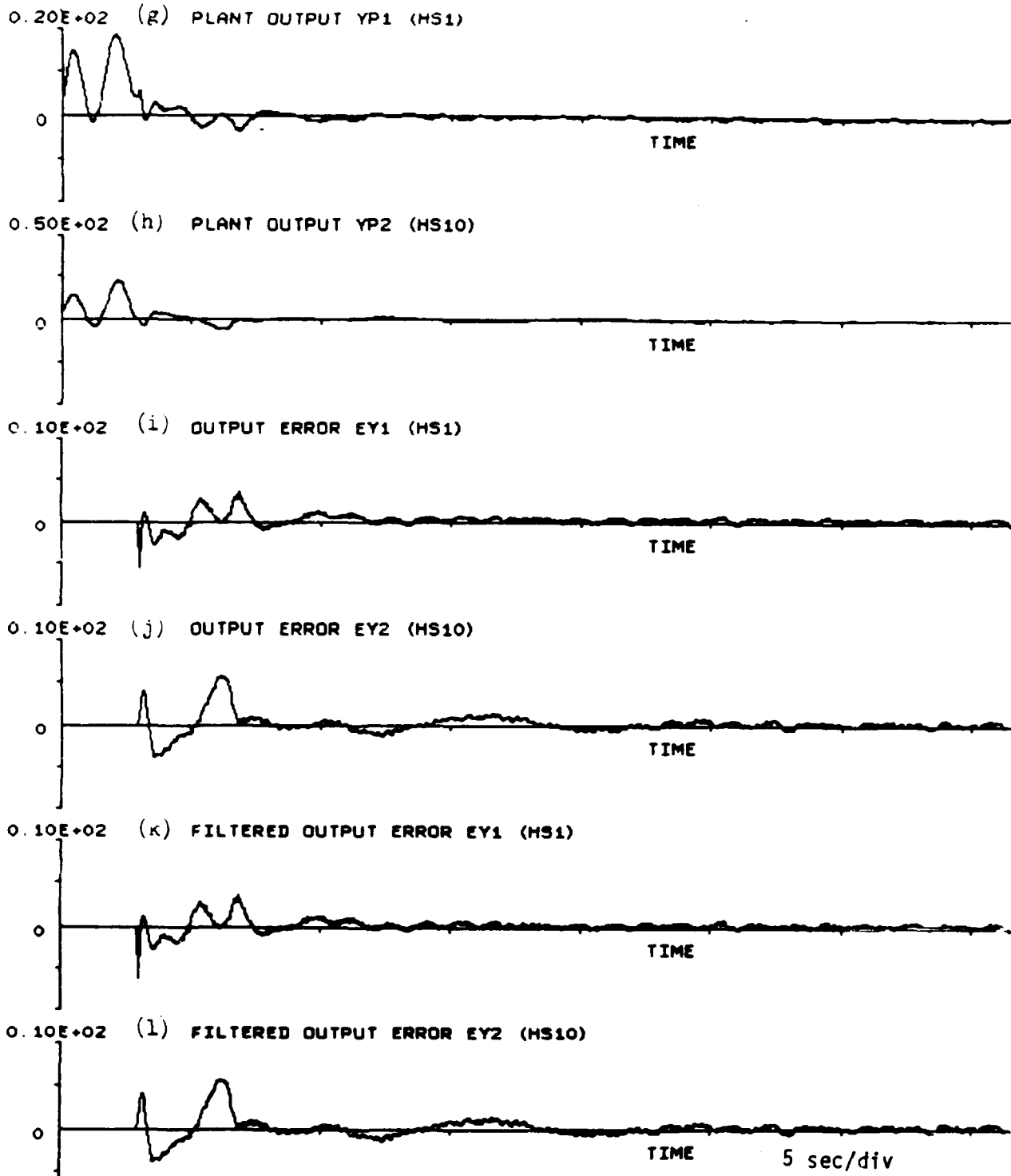


Figure 5.2-8 Closed-loop Responses to 3-sec Pulse of 1.5 N-m (Cont.)

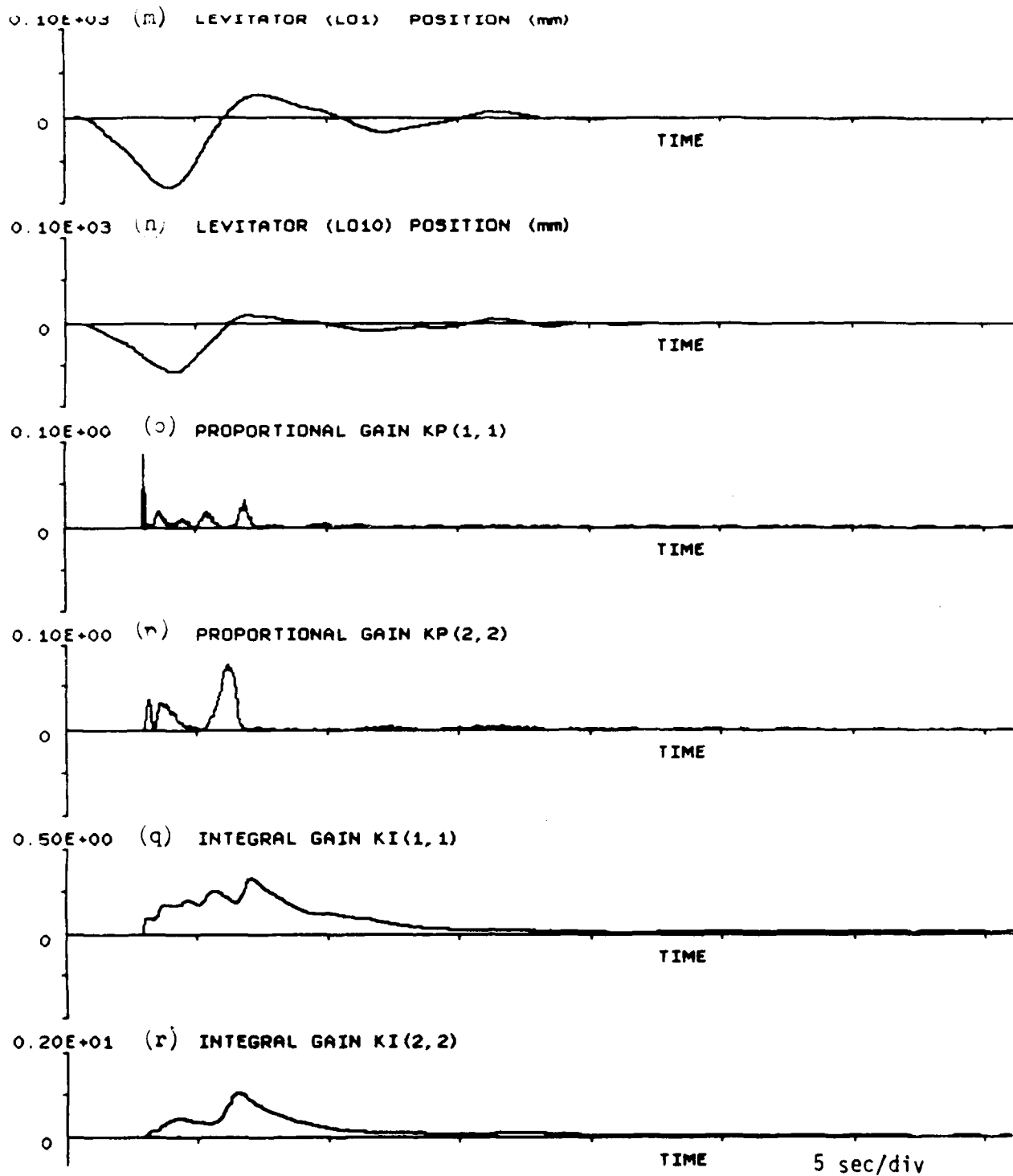


Figure 5.2-8 Closed-loop Responses to 3-sec Pulse of 1.5 N-m (Cont.)

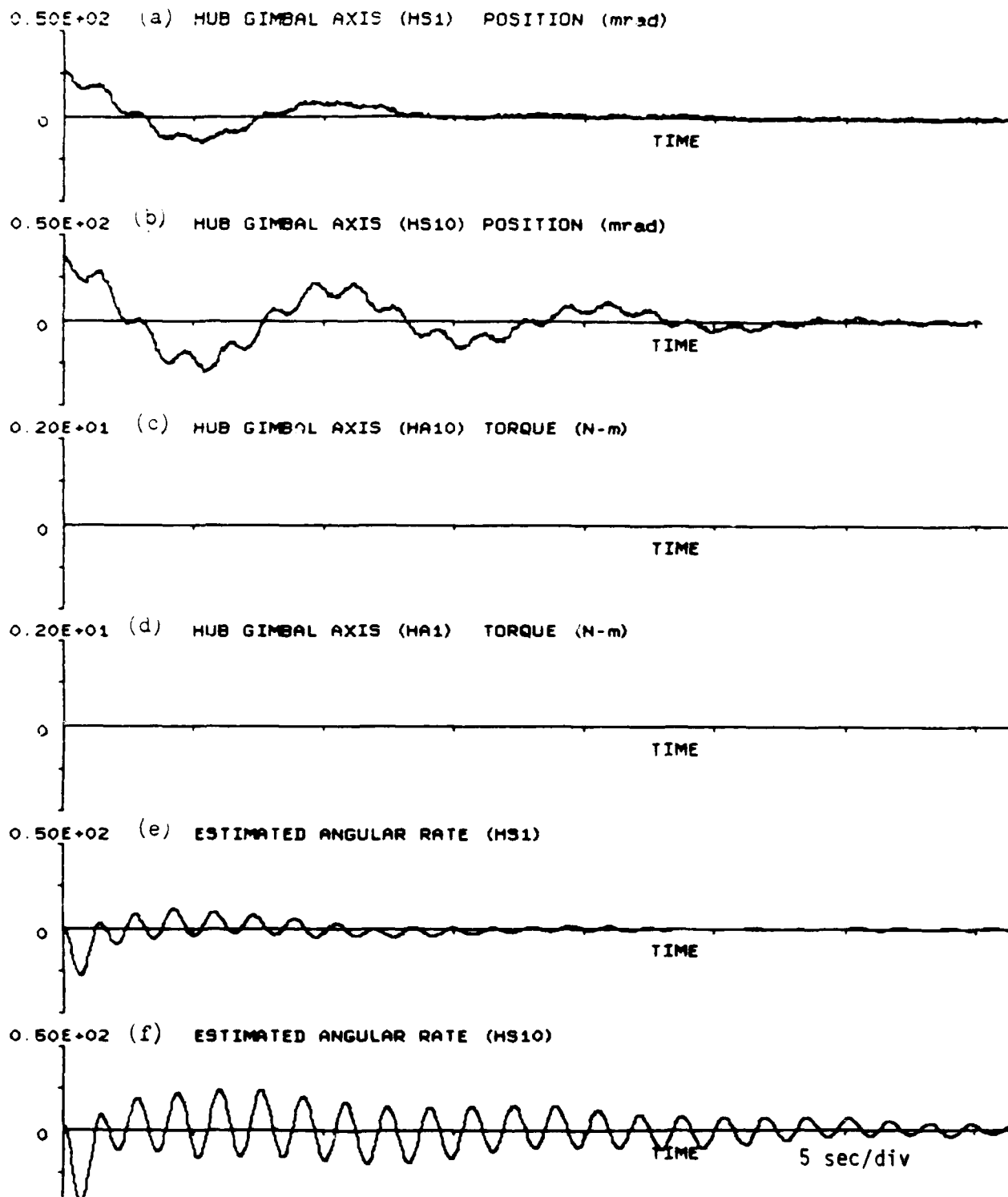


Figure 5.2-9 Open-loop Responses to Initial Deflection

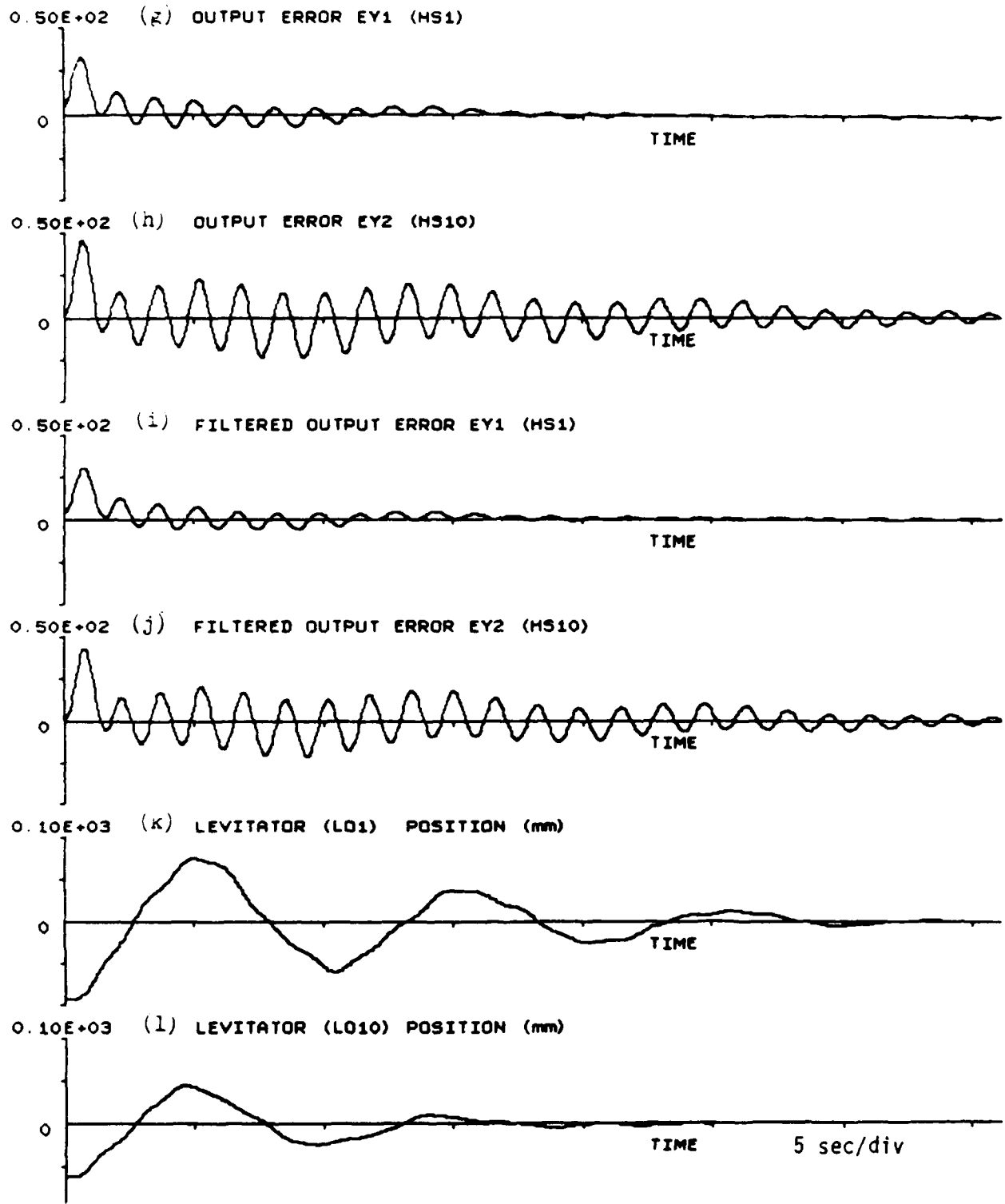


Figure 5.2-9 Open-loop Responses to Initial Deflection (Cont.)

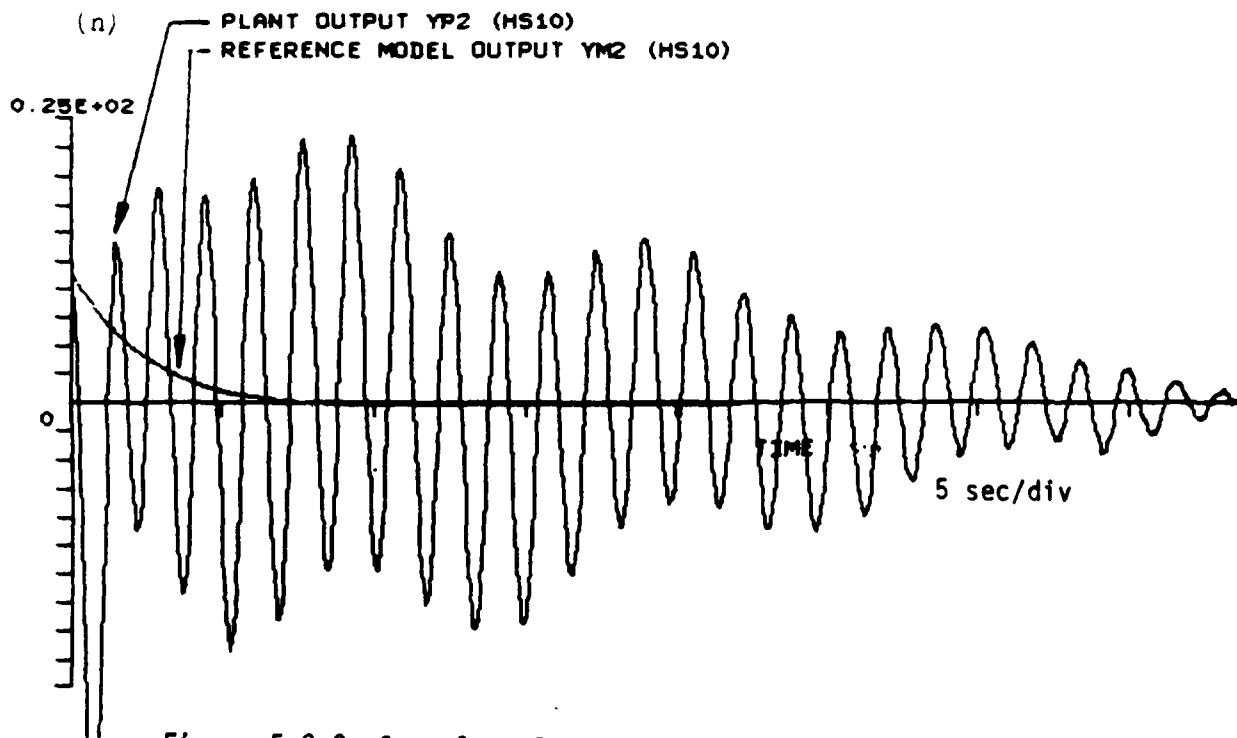
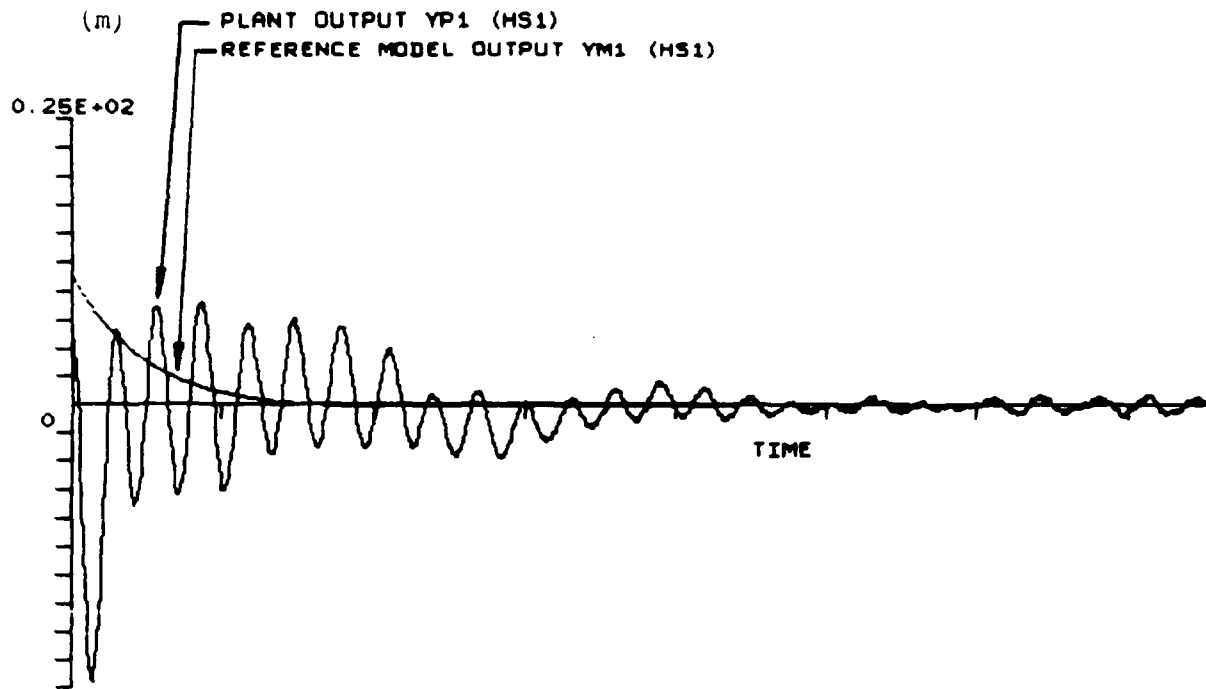


Figure 5.2-9 Open-loop Responses to Initial Deflection (Cont.)

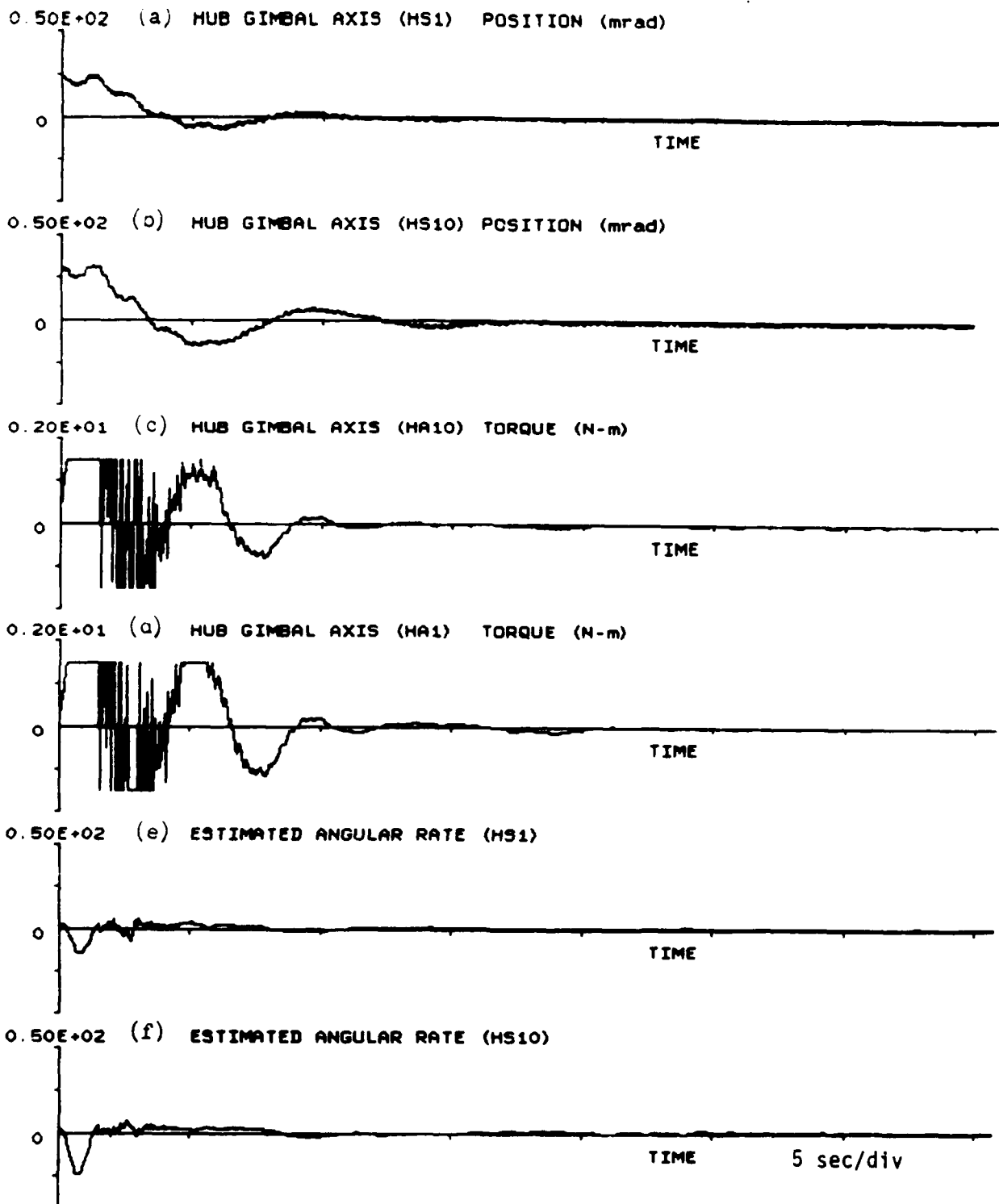


Figure 5.2-10 Closed-loop Responses to Initial Deflection

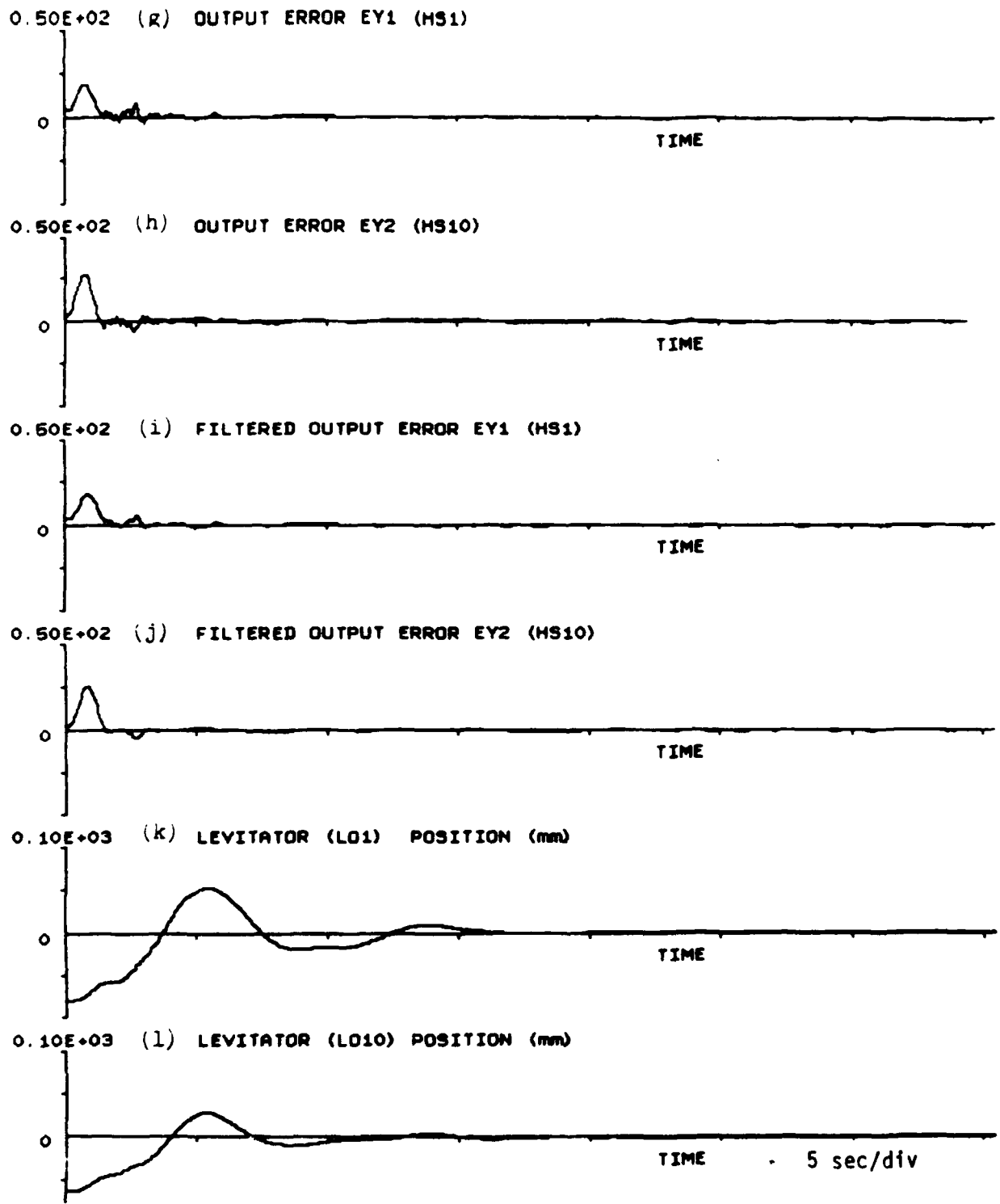


Figure 5.2-10 Closed-loop Responses to Initial Deflection (Cont.)



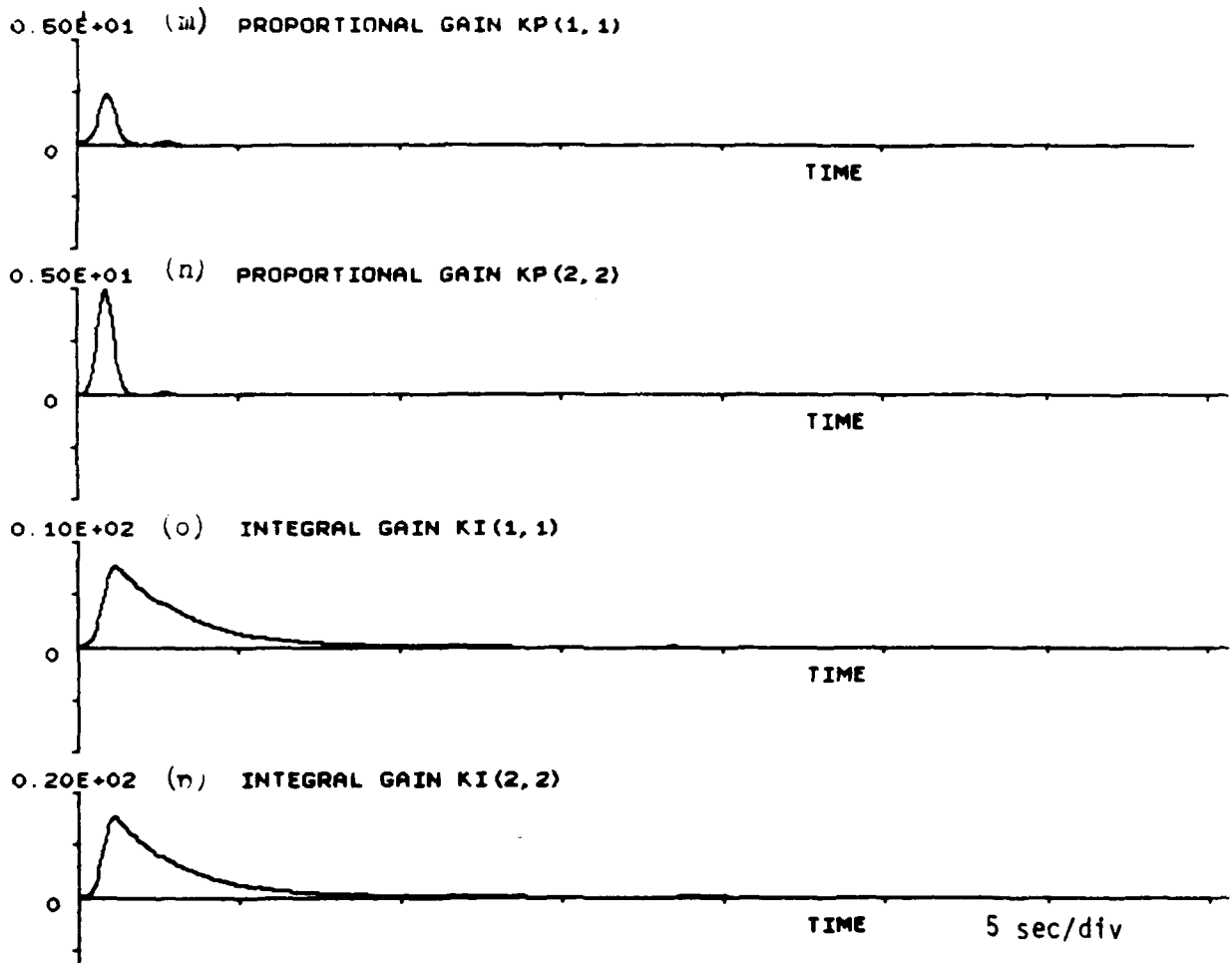


Figure 5.2-10 Closed-loop Responses to Initial Deflection (Cont.)

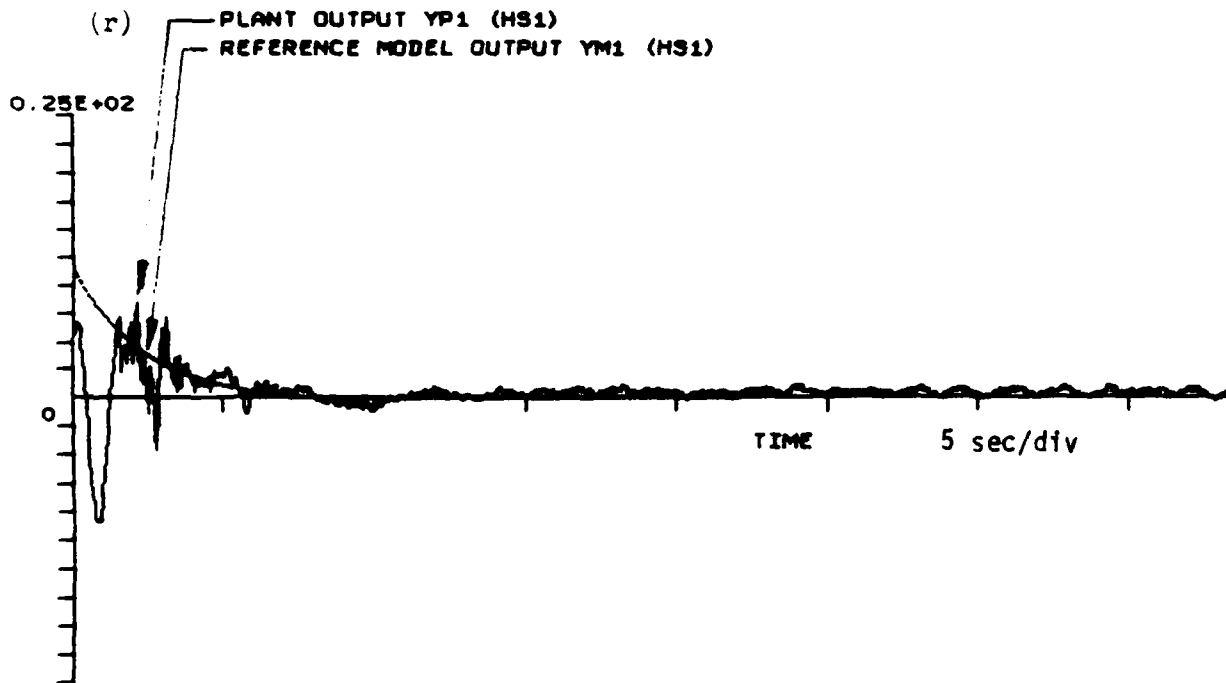
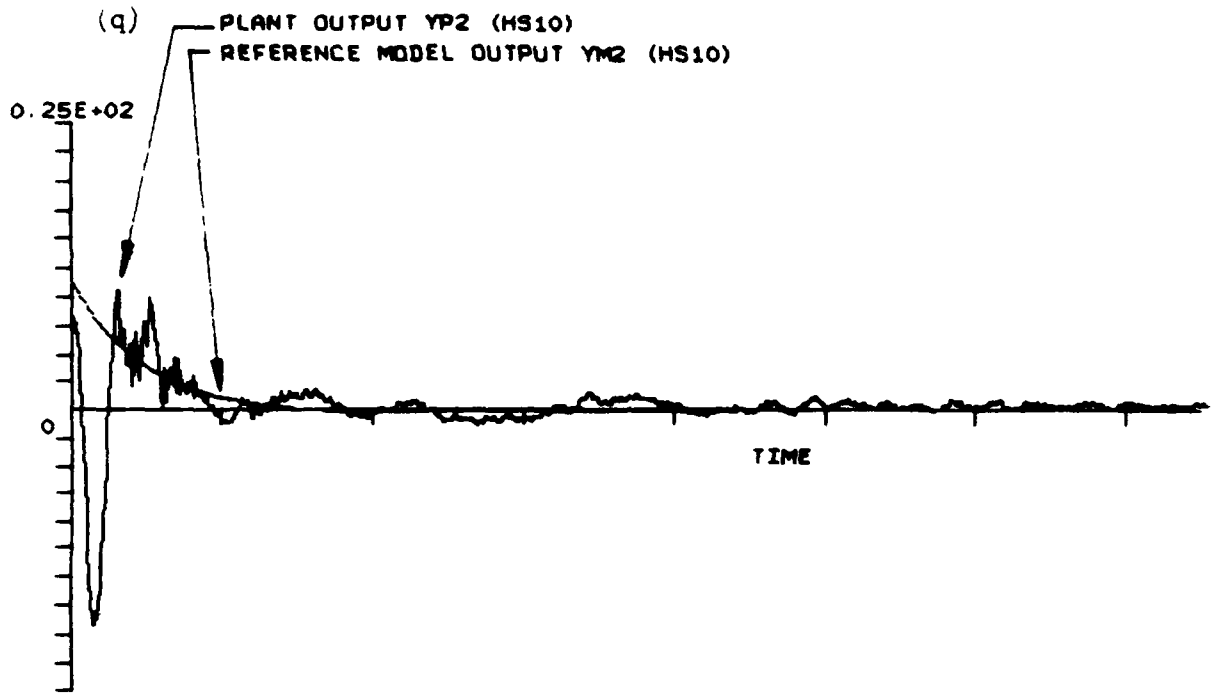


Figure 5.2-10 Closed-loop Responses to Initial Deflection (Cont.)

$$T = \bar{T} = \text{diag} (0.05, 0.05, 0.05, 0.05, 0.05, 0.05, 0.05, 0.05) \quad (5.2.34)$$

$$L = \bar{L} = \text{diag} (1, 1) \quad (5.2.35)$$

$$\sigma_1 = 0.5 \text{ (0.08 Hz integral gain bandwidth)} \quad (5.2.36)$$

$$\sigma_2 = 6.28 \text{ (1 Hz proportional gain bandwidth)} \quad (5.2.37)$$

$$\gamma = 6.28 \text{ (1 Hz branch filter bandwidth)} \quad (5.2.38)$$

Comparing the output plots 5.2-9 (m) and (n), and 5.2-10 (q) and (r), it is apparent that  $y_p$ 's track  $y_m$ 's closely and converge fast when the adaptive controller is on. Table 5.2-10 summarizes the comparison below:

|      | Open-Loop            |                        | Closed-Loop          |                        |
|------|----------------------|------------------------|----------------------|------------------------|
|      | Maximum<br>Overshoot | Settling<br>Time (sec) | Maximum<br>Overshoot | Settling<br>Time (sec) |
| HS1  | 24.9                 | 23.5                   | 10.9                 | 7                      |
| HS10 | 37.3                 | 37                     | 19.3                 | 8                      |

Table 5.2-10 Comparison of Open-Loop to Closed-Loop Outputs  $y_p$ 's for Deflection Regulation

The  $y_p$  settling time achieves 460% improvement for HS10, and 336% for HS1 while the maximum overshoot achieves 193% improvement for HS10 and 230% for HS1. Table 5.2-11 shows the open-loop angular position responses (from Fig. 5.2-9 (a) and (b)):

|      | Settling<br>Time<br>(sec) | RMS<br>Error<br>(mrad) |
|------|---------------------------|------------------------|
| HS1  | 13.5                      | 6.985                  |
| HS10 | 29                        | 12.838                 |

Table 5.2-11 Open-Loop Responses to Deflection Regulation

and from Fig. 5.2-10 (a) and (b), the closed-loop angular position responses are summarized in Table 5.2-12:

|      | Settling<br>Time<br>(sec) | RMS<br>Error<br>(mrad) |
|------|---------------------------|------------------------|
| HS1  | 10.5                      | 6.311                  |
| HS10 | 16                        | 9.597                  |

Table 5.2-12 Closed-Loop Responses to Deflection Regulation

The ratios obtained from Tables 5.2-11 and 5.2-12 are tabulated in Table 5.2-13.

|      | Settling<br>Time<br>Ratio | RMS<br>Error<br>Ratio |
|------|---------------------------|-----------------------|
| HS1  | 1.286                     | 1.107                 |
| HS10 | 1.813                     | 1.338                 |

Table 5.2-13 Open-Loop/Closed-Loop Ratio for Deflection Experiment

Because of the low branch filter bandwidth, the filtered output errors  $\bar{e}_{y1}$  and  $\bar{e}_{y2}$  are much smoother than the output errors  $e_{y1}$  and  $e_{y2}$ , as shown in Fig. 5.2-10 (g)-(j).

This subsection demonstrates model tracking, performance improvement and stability under substantial system uncertainties.

#### 5.2.4 Conclusions

Excellent results have been obtained in the Phase I adaptive control experiments. The state estimator implemented has generated satisfactory hub angular rate estimates using noisy position measurements. The adaptive controller has achieved stable transient regulation with significant improvement over the open-loop performance. The settling time has been reduced by a factor of three or better in some cases tested. In the regulation experiment with initial deflection, the system outputs followed the highly-damped reference model outputs closely and converged rapidly.

Experiments on the adaptive loop sampling rate were also conducted. No appreciable performance deterioration was observed when the sampling period was varied between 40 to 60 ms and retuning of the adaptive controller was not required in any of the cases tried.

A great deal has been learned from the experiments. Good rate measurements are crucial for the performance of this adaptive algorithm. Although a low order discrete state estimator for rate estimates has been successfully implemented, the controller performance with an actual rate sensor is still not quantified. The effects of sensor dynamics and sampling rate on the controller performance remain to be tested with actual hardware when it becomes available. In the present case where rate sensing is lacking, the effort required for tuning the adaptive controller is appreciable. The tuning process involves selection of weighting matrices, the bandwidth of the branch filter and the two adaptive gain generators which are coupled with the characteristics of the sensing devices. This effort can only be substantially reduced by developing analytical design tools, the optimization based systematic design which constitutes a major FY'88 effort.

## References

- [1] Wen, John, Final Report of "Flexible Structure Shape Determination and Control Demonstration," Sec. 5.1, Dynamic Control Experiment.
- [2] Sobel, K., H. Kaufman and L. Mabijs "Implicit Adaptive Control Systems for a Class of Multi-Input Multi-Output Systems," IEEE Trans. Aero. Elect. Syst., Vol. AES-18, No. 5, 1982, pp. 576-590.
- [3] Ih, C.C., S. J. Wang and C. T. Leondes, "An Investigation of Adaptive Control Techniques for Space Stations," Proc. 1985 American Control Conference, Boston, MA, June, 1985, pp. 81-94.
- [4] Ih, C.C., D.S. Bayard, and S. J. Wang, "Space Station Adaptive Payload Articulation Control," Proc. of 4th IFAC Symposium on Control of Distributed Parameter Systems, Los Angeles, CA, July, 1986.
- [5] Bayard, D.S., C.H.C. Ih and S. J. Wang, "Adaptive Control for Flexible Space Structures with Measurement Noise." Proc. of 1987 American Control Conference, June 10-12, 1987, Minneapolis, Minnesota.

7

.

.

(

### 5.3 STATIC SHAPE DETERMINATION AND CONTROL

A number of important emerging applications in the technology of large space structures can be appropriately analyzed as static distributed systems. This approach is applicable to systems where the time-dependent effects are negligible and where the control forces can be applied without significantly exciting dynamic behavior in the system. More generally, one can consider problem settings where the stiffness properties dominate the mass properties in determining the energy balances. Then a static response of the structure defines a reference configuration about which motions can be resolved with greater accuracy. In this context one can include applications where the time-varying effects of the model are changing slowly with respect to the scale on which control operations must be carried out. These quasi-static disturbances may, for example, include gravitational and thermal effects. In some applications the control hardware may be designed to carry out a local temporal averaging of the resulting quasi-static effects.

The introduction of statistical model errors allows the smearing of effects which have been ignored in the modeling or which occur on too fine a scale to be adequately modeled. This treatment of the so-called spillover distinguishes our approach from purely dynamic treatments of the problem. As a result, the observational data can be statistically referenced to a plant, and questions regarding the validity of the estimates can be treated in a statistical framework which includes modeling errors as well as observational errors. This connection is crucial if one wishes to develop a methodology for choosing basis functions in the approximation of the state and the parameter spaces.

Important applications include many future space system designs which are based on the assembly and joining of discrete modules. This construction will result in a configuration which is a large scale composite of many structural elements whose static and dynamic characteristics cannot be adequately modeled in advance. In fact, any modeling will require periodic updating as the structural properties of the elements slowly change over the lifetime of the system.

Of particular interest are the many proposed large space antenna systems. Performance requirements in communications and radiometry call for antennas which have diameters tens of meters or larger and which have surface error requirements far beyond current capabilities.

Minimization of the surface error is crucial for the maintenance of electromagnetic performance requirements. Current technology is based on a calibration process whereby measurements taken by a technician using a theodolite are processed to give a least-squares fit of the data to an idealized parabolic surface. This procedure is unworkable not only because of the stringent performance requirements but also because the nature of the application precludes such a re-calibration after deployment.

#### 5.3.1 Experiment Description

The problem of static shape estimation is fundamental to the long-range methodology for static structural experiments and must be resolved adequately before it is possible to execute experiments in static control and

identification. Thus the Phase 1 objectives focus on the implementation and evaluation of algorithms designed to estimate the shape of the dish which has been deformed by static loads produced by test masses hung at various locations on the structure. Another Phase 1 objective is to evaluate the performance and utility of the SHAPES sensor in an operational environment.

5.3.1.1 Experiment procedure. The experiment structure is operated at the floor position to perform the static determination experiments. With the structure at the floor level, the experiment time on the facility is greatly reduced since the SHAPES sensors and hanging masses can be repositioned between experiment runs with much less difficulty. Also, the hub must be fixed before calibration since the goal in Phase 1 is to estimate the shape of the deformed dish without considering the modeling and estimation of rigid body modes.

For the purposes of providing a convenient framework for the analysis of the experiment, a Critical Point Directory is employed which labels each point of the structure which can be used as a point of actuation, sensing, or model error in an experiment trial (See Figure 5.3-1). In the discussion of the results, the nth critical point is designated by the notation CPn.

Actuation consists of hanging masses at any of the critical points plus electrical excitation of the force-calibrated rib-root actuators located at the first critical point of each rib (CP1, CP11, CP21, ..., CP121). Sensing consists of position displacement measurements from the twenty-four levitators (CP4, CP8, CP14, CP28, ..., CP114, CP118) plus the four sensors collocated with selected rib-root actuators (CP4, CP34, CP64, CP94), plus up to fourteen SHAPES targets located at any of the critical points. Model errors are treated as disturbing forces in the state equation (cf. 5.3.1a,b); these disturbances are represented in the estimators either as global constant forces or as discrete point-forces at any of the critical points.

After the initial calibration of the sensors, a static deformation is created by the actuation described above. The shape of the dish is estimated by means of a minimum variance estimator which is based on the finite element model (see Section 4). A reference model such as a least squares scheme which fits the measurements to a geometric model is also implemented. Measurements taken using position sensing devices are processed by the estimator to synthesize the state estimates and the corresponding covariances. Comparison of the estimators leads to the specification of a goodness-of-fit model for use in subsequent experiments.

5.3.1.2 Experiment software. In designing static shape experiment software interface specifications, future experiments have been kept in mind so as to minimize future software alterations. The experimental software consists of a single subroutine named STATIC\_SHAPE\_DET. The form of the subroutine call is

```
SUBROUTINE STATIC_SHAPE_DET(INITIALIZE, IC, PARAM_FILE_NAME,
PARAM, SENSOR, ACTUATOR, SAVE_STATE, STATUS)
```

where the declaration in the system software is



|              |                  |
|--------------|------------------|
| LOGICAL*1    | INITIALIZE       |
| REAL*4       | IC(100)          |
| CHARACTER*20 | PARAM_FILE_NAME  |
| REAL*4       | PARAM(100)       |
| REAL*4       | SENSOR(50)       |
| REAL*4       | ACTUATOR(20)     |
| REAL*4       | SAVE_STATE(2741) |
| LOGICAL*1    | STATUS(100)      |

Upon selecting the static identification experiment in the system level menu, the experiment level menu is displayed :

- 0 - Exit
- 1 - Initialization Control
- 2 - Parameter File Name
- 3 - Number of Sampling Intervals
- 4 - Mode of Operation
- 5 - Shape Estimate Resolution
- 6 - Create Data Save Files
- 7 - Force Metering Control

The response to each selection is summarized below

- 0 - Exit back to the system level menu.
- 1 - The experimental software updates the parameter values based on the current parameter file.
- 2 - The indicator box displays the current parameter file name in the first slot. The user is prompted for the new parameter file name (maximum 20 characters ).
- 3 - The user is prompted for the number of sampling units that the sensor data should be averaged over (for mode of operation 2, "collect and average sensor data").
- 4 - The indicator box now displays the current mode of operation and the meaning of each. The modes are defined as:
  - 1 - Activate rib root actuators
  - 2 - Collect and average sensor data
  - 3 - Control law to compute actuator inputs
  - 4 - Compute shape estimates
  - 5 - Turn off the actuators

The user is prompted for the mode of operation.

- 5 - The user is prompted for the number of points to be plotted per rib in system plotting features. The maximum resolution is one hundred points per rib.
- 6 - The user is prompted to select which input and output files are written to disk for future analysis.

- 7 - The user is prompted to specify system parameters which determine rates for rib-root actuation hardware so as to avoid unwanted dynamic excitation.

As stated above, the indicator box maintains a default display of the error statuses (returned from STATIC\_SHAPE\_DET) and changes its display for different menu selections. The specific requirement of each menu option is now stated below:

- Item #
- 0 - Return to system level menu.
  - 1 - Set INITIALIZE = true.  
Call STATIC\_SHAPE\_DET.  
Set INITIALIZE = false.  
Return to experiment level menu.
  - 2 - Store the new parameter file name in PARAM\_FILE\_NAME.  
Return to experiment level menu.
  - 3 - Store the window size (# of sampling units) in PARAM(2).
  - 4 - Store the mode of operation code in PARAM(1).
  - 5 - Store the number of points to be plotted per rib in PARAM(3).
  - 6 - Writes selected input and output files to disk under the directory [.SAV2].
  - 7 - Updates system parameters to specify the number of increments and the time for implementation for commands to the rib-root actuators.

The parameter file is an ASCII file that can be modified by the regular text editor on the VAX. The organization of the file is given below. The comments at the end of the line have been made part of the file so as to facilitate data changes; the "[.DEE]" before each file name is required by the MicroVAX system software since all of the static shape determination software is stored in the ".DEE" directory:

```
[.DEE]GLOBALLOCAL_ERROR ; Global & Local Model Uncertainty File
[.DEE]OBS_ERROR ; Observational Uncertainty File Name
[.DEE]LOCATION_CRIT_PTS ; Loc. of Crit. Pts. for Est. File Name
[.DEE]HANGMASS_LOCATION ; Hanging Mass Locations File Name
[.DEE]HANGMASS_VALUES ; Hanging Mass Values File Name
[.DEE]SENSOR_LOCATION ; Sensor location file name
[.DEE]SENSOR_USAGE ; Sensor usage file name
[.DEE]SHAPEEST_CONTROL ; Shape Estimate File Name
[.DEE]SHAPEDES_CONTROL ; Desired Shape File Name
[.DEE]CONTROL_GAIN ; Control Gain File Name
[.DEE]STATE_SPACE_INFO ; State Space Information File Name
[.DEE]RRACT_VALUE ; Rib Root Actuator Values File Name
[.DEE]RRACT_USAGE ; Rib Root Actuator Usage File Name
[.DEE]SHAPE_FUNCTION ; Shape Function File Name
[.DEE]SENSOR_PLOT_USE ; Sensor Plotting Information File Name
[.DEE]LOC_CP_SHP_FCTN ; Location of C.P.'s for Shape Functions
24 ; Total Number of C.P.'s Catalogued
61 ; Dimension of Spatial Uncertainty Set
40 ; Dimension of Sensor Set
```

```

20 ; Number of Total State Space Elements
16 ; Number of SHAPES Sensors Used
12 ; Number of Hanging Masses
12 ; Number of Rib Root Actuators Used
2741 ; Number of Save State Variables
40 ; Number of Outputs for Estimator
2 ; Type of Geometric Fit
1 1 1 1 1 1 1 1 1 1 1 1 1 1 ; Max. Actuator Amount (N)
-1 -1 -1 -1 -1 -1 -1 -1 -1 -1 -1 -1 -1 -1 ; Min. Actuator Amount (N)

```

The uncertainty files, critical point file, hanging mass files, sensor files, shape estimate file, desired shape file, control gain file, state space info file, rib root actuator files, shape function file, sensor plotting information file, and critical point location file are also ASCII text files that can be modified by any VAX editor. The data are stored in matrix column form according to the appropriate dimensions. Comments in these files must be placed at the end of the files after all of the data values.

Error estimate, shape estimate, and geometric fit values stored in the SAVE\_STATE may be plotted at the system level. For STATIC\_SHAPE\_DET the plotting options are specified via a system level menu that provides the following:

- 0 - Exit (return to system level menu)
- 1 - Specify ribs to be plotted (1-12)
- 2 - Plot shape estimate only
- 3 - Plot shape estimate & geometric fit only
- 4 - Plot shape estimate & sensors used/not used
- 5 - Plot shape estimate, geometric fit, & sensors used/not used

An example of the plotting capabilities is shown in Figure 5.3-2.

### 5.3.2 Algorithm Description

In this section, the basic analysis which supports the static shape determination algorithms is summarized. This approach to shape estimation is part of an integrated methodology which combines the techniques of modeling, identification, and estimation for static control of distributed systems which are characterized by infinite-dimensional state and parameter spaces. A more complete discussion is given in [2]. These techniques are appropriate for systems where the time-dependent effects are negligible and where the control forces can be applied without significantly exciting dynamic behavior.

Let the state variable be given by  $u$ . The models considered have the general form

$$A(\theta) u(\theta) = B(\theta)\omega + C(\theta) f \quad (5.3.1a)$$

$$y(\theta) = H(\theta) u(\theta) + F(\theta)\eta. \quad (5.3.1b)$$

Here  $A$  is an invertible self-adjoint elliptic differential operator defined over the spatial domain  $\Omega$ ; the integral operator  $\Phi$  is related to  $A$  by

$$A \Phi - I \quad (5.3.2)$$

where  $I$  is the identity. The parameter  $\theta$  is possibly infinite-dimensional. For simplicity, attention is generally confined to cases where the  $\theta$ -dependence is restricted to the operator  $A$  and where that dependence is linear. This corresponds to important applications where  $\theta$  represents physically relevant stiffness parameters of a static system characterized by the equations of linear elasticity. This corresponds to the case

$$\begin{aligned} A(\theta) &= D^*[\theta D] \\ \langle D^*u, v \rangle_2 &= \langle u, Dv \rangle_2, \end{aligned} \quad (5.3.3)$$

where  $D$  is a partial differential operator with formal adjoint  $D^*$  with respect to the state-space inner product.

$H$  is an operator which characterizes the state-to-observation map, and  $C$  is an operator that models the relevant deterministic forces including controls. It is assumed that the observation space has dimension  $N_s$  which corresponds to a finite-dimensional sensing scheme and that the control space has dimension  $N_a$  which corresponds to a finite-dimensional actuation system. In some contexts it is possible to consider limiting cases which correspond to infinite-dimensional sensing and actuation spaces. The integrated form of the observation equation is given by

$$y(\theta) = H(\theta)\Phi(\theta)C(\theta)f + H(\theta)\Phi(\theta)B(\theta)\omega + F(\theta)\eta. \quad (5.3.4)$$

There are three Hilbert spaces of primary interest: the input space  $S_1$  to which the process error  $\omega$  and the deterministic input  $f$  belong; the state space  $S_2$  containing the state  $u$ ; and the measurement space  $S_3$  where the data  $y$  and the observation error  $\eta$  belong. The inner product between two arbitrary elements  $u$  and  $v$  in the space  $S_1$  is denoted by  $\langle u, v \rangle_1$  or by the simpler notation  $u^*v = \langle u, v \rangle_1$ . Similarly,  $uv^*$  denotes a Hilbert space outer product. The corresponding norms are given by  $\|\cdot\|_1$  or, when the context is clear, by the simpler notation  $\|\cdot\|$ .

The appropriately dimensioned operators,  $B(\theta)$  and  $F(\theta)$ , model the statistical influence of the process error and the measurement error; these errors,  $\omega$  and  $\eta$ , form the model error vector

$$\epsilon = (\omega, \eta) \quad (5.3.6)$$

which represents spatial white noise and is characterized by the covariance operator

$$E(\epsilon \epsilon^*) = I. \quad (5.3.6)$$

More precisely, we have  $x_1 \in S_1$  and  $x_3 \in S_3$

$$\begin{aligned} E[\omega] &= 0 & E[\langle x_1, \omega \rangle_1 \omega] &= x_1 \\ E[\eta] &= 0 & E[\langle x_3, \eta \rangle_3 \eta] &= x_3 \end{aligned} \quad (5.3.7)$$

The limiting cases,  $\|B\| \rightarrow 0$  and  $\|F\| \rightarrow 0$ , respectively represent the assumptions of perfect modeling and perfect measurements. For a given

experiment trial these operators are determined by the contents of the model and observational uncertainty files discussed in the previous subsection.

5.3.2.1 State estimation. The preceding assumptions lead to an appropriate framework for the analysis of minimum variance estimators of the state. Here the expected observation  $m$  is characterized by

$$m = H \Phi C f \quad (5.3.8)$$

$$E[y] = m \quad E[(y-m)(y-m)^*] = R_\omega + R_\eta$$

and the expected process and measurement covariances,  $R_\omega$  and  $R_\eta$ , are given by

$$R_\omega = \Phi B B^* \Phi^* \quad R_\eta = F F^* \quad (5.3.9)$$

The resulting formulas are analogous to what is typically derived for finite-dimensional systems (see, for example, [1]). The estimate  $u_{est}$  has the form

$$u_{est} = C f + g(y-m) \quad (5.3.10)$$

where the gain  $g$  is given by

$$g = R H^* (R_\eta + H R_\omega H^*)^{-1} \quad (5.3.11)$$

The covariance operator associated with the estimation error is given by

$$P = R_\omega - R_\omega H^* (R_\eta + H R_\omega H^*)^{-1} H R_\omega \quad (5.3.12)$$

These formulas are similar to the typical Kalman gain formulations used in the analysis of dynamic systems. One can also consider possibilities for recursive batch processing of data sets obtained by means of different sensing strategies:

$$y_1 = H_1 u + F_1 \eta_1 \quad (5.3.13)$$

$$y_2 = H_2 u + F_2 \eta_2.$$

An analysis of the second-order statistics of the related estimation error can also be conducted.

5.3.2.2 Control. After the estimation problem has been solved, it is then possible to consider the associated control problem

$$\min_{f_c} \|u_0 - \Phi C f_c\|_2^2 + \|f_c\|_2^2 \quad (5.3.14)$$

$$u_0 = u_d - u_{est}$$

Here  $u_0$  is the correction from the accepted shape estimate  $u_{est}$  to the desired shape  $u_d$ . And  $f_c$  is the control force which is constrained to be in a set which corresponds to the limits of the actuation system. The solution to this problem is given by

$$f_c = (I + C^* \Phi^* \Phi C)^{-1} C^* \Phi^* u_0. \quad (5.3.15)$$

The implementation of these algorithms requires simultaneous discretizations of the state and parameter spaces in order to make the essentially infinite-dimensional processes computationally feasible. For the experimental structure such discretizations are given by the finite element model derived in Section 4. What is common to all the algorithms considered is the large number of arithmetic operations that need to be performed. These computations primarily consist of concurrent quadratures as well as the addition and multiplication of large matrices. Most of the computations can ultimately be reduced to the parallel synthesis of a large number of vector dot products.

### 5.3.3 Preliminary Results

Although the static shape experiment is not yet fully operational, the software has been used effectively as a calibration tool and as a diagnostic device.

5.3.3.1 Calibration. After an initial verification of the input/output operations, a sequence of static loadings and measurements were carried out to calibrate the SHAPES measurements with respect to the levitator measurements. Fitting the data to Gaussian statistical parameters resulted in the calculation to within two per cent of an effective gain for transforming measurements on the facility from SHAPES units to millimeters:

$$G = -.6747 \pm .0095 \quad (\text{mm}/\text{SHAPES-units}). \quad (5.3.16)$$

5.3.3.2 Symmetry determination. Symmetry verification has been a major focus of early experiments. The results of a particular loading sequence which is representative of the results that have been obtained are described below. Positive displacements and forcings refer to the upward direction. On rib N (cf. Figure 5.3-1) a loading is prescribed as follows:

$$\begin{aligned} 3.430 \text{ Newtons at CP}(10(N-1) + 4) & \quad (350 \text{ grams}) \\ -1.176 \text{ Newtons at CP}(10(N-1) + 9) & \quad (120 \text{ grams}). \end{aligned} \quad (5.3.17)$$

The outer levitator measurement on the Nth rib is denoted by  $L_N$ . The outer levitator measurements for ribs (N+1) and (N-1) are denoted respectively by  $L_{N+}$  and  $L_{N-}$ . To measure the local symmetry about rib N we define the dimensionless quantity  $S_N$ :

$$S_N = 2(L_{N+} - L_{N-}) / (L_{N+} + L_{N-}). \quad (5.3.18)$$

The results for a sequence of trials covering each rib are given in Figure 5.3-3. The resolution of the levitator measurements is taken to be 0.26 mm in accordance with the system hardware specifications (see Subsection 3.1). The error estimate for  $S_N$  was derived by assuming absolute errors in  $L_{N+}$  and  $L_{N-}$  of 0.26 mm about the nominal value 6.3 mm. The data show a particular lack of symmetry about ribs one and three with a moderate loss of symmetry about ribs six, ten, eleven. This lack of symmetry may be the

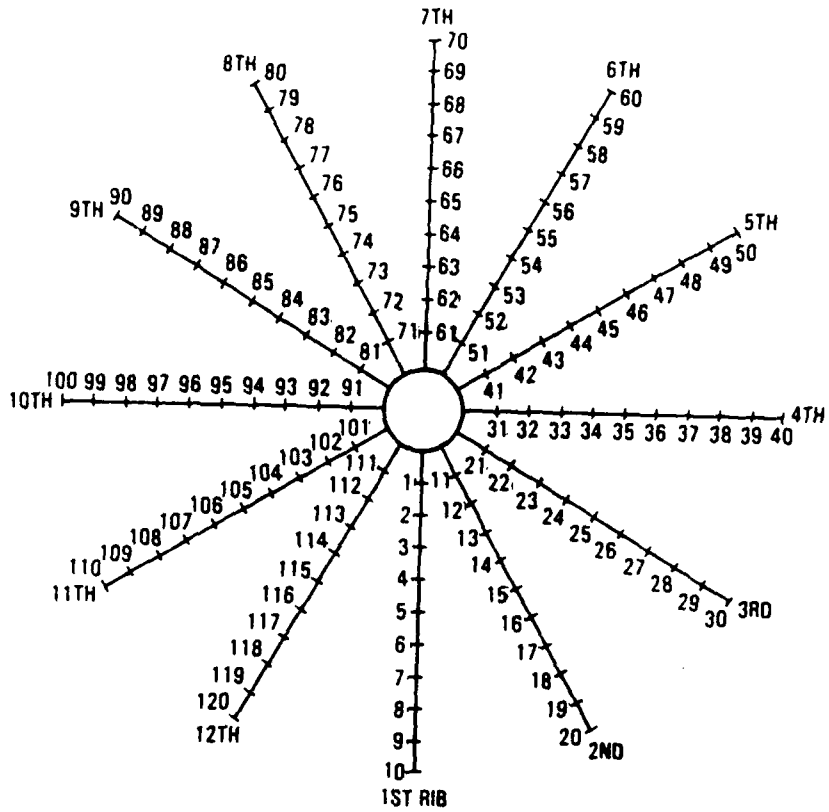


Figure 5.3-1 Critical Point Directory

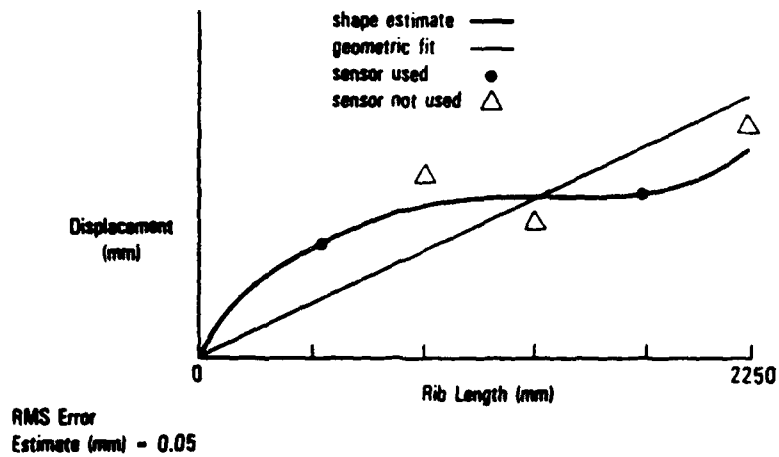


Figure 5.3-2 Rib No. 3 Profile

| WEIGHTED<br>RIB<br>(N) | $L_N$<br>( $\pm 0.26$ mm) | $L_N^-$<br>( $\pm 0.26$ mm) | $L_N^+$<br>( $\pm 0.26$ mm) | $S_N$<br>( $\pm 0.08$ ) |
|------------------------|---------------------------|-----------------------------|-----------------------------|-------------------------|
| 1                      | -36.4                     | -6.9                        | -5.6                        | -0.21                   |
| 2                      | -36.7                     | -6.4                        | -6.6                        | 0.03                    |
| 3                      | -35.4                     | -4.3                        | -5.9                        | 0.31                    |
| 4                      | -36.4                     | -6.1                        | -6.4                        | 0.05                    |
| 5                      | -37.5                     | -6.4                        | -6.4                        | 0.00                    |
| 6                      | -33.8                     | -5.1                        | -5.6                        | 0.09                    |
| 7                      | -37.2                     | -6.7                        | -6.9                        | 0.03                    |
| 8                      | -36.7                     | -6.4                        | -6.1                        | 0.05                    |
| 9                      | -36.2                     | -5.9                        | -5.9                        | 0.00                    |
| 10                     | -36.4                     | -6.1                        | -6.7                        | 0.09                    |
| 11                     | -36.4                     | -6.7                        | -7.4                        | 0.10                    |
| 12                     | -37.2                     | -6.9                        | -6.7                        | -0.03                   |

AVERAGE VALUE FOR  $L_N$ : -36.4 mm

SAMPLE STANDARD DEVIATION: 1.0 mm

AVERAGE VALUE FOR  $L_N^+$  AND  $L_N^-$ : -6.3 mm

SAMPLE STANDARD DEVIATION: 0.7 mm

Figure 5.3-3 Symmetry Analysis (9/21/87)

| WEIGHTED<br>RIB<br>(N) | $S_N$ (7/16/87)<br>( $\pm 0.08$ ) | $S_N$ (9/15/87)<br>( $\pm 0.08$ ) | $S_N$ (9/21/87)<br>( $\pm 0.08$ ) |
|------------------------|-----------------------------------|-----------------------------------|-----------------------------------|
| 1                      | -0.22                             | -0.33                             | -0.21                             |
| 4                      | 0.00                              | 0.00                              | 0.05                              |
| 7                      | 0.05                              | 0.05                              | 0.03                              |
| 10                     | 0.21                              | 0.12                              | 0.09                              |

Figure 5.3-4 Symmetry Shifts Over Time



result of errors in the tensions of the coupling wires since the consistency to within a few per cent of the major deflection  $L_N$  suggests that the ribs have been adequately modeled. Possible problems with the coupling wires may also explain the results of Figure 5.3-4 which compares the results for the same loadings (5.3.17) on selected ribs over an interval of approximately two months. Another possible source of error is the static friction associated with the levitator systems. Additional tests are currently being designed to further refine the calibration of the facility. The static shape determination methodologies are particularly well-suited for this type of diagnostic analysis since both the size and the resolution of the sensing and actuation sets are greater than what is generally available in dynamic analysis.

5.3.3.3 Conclusions. The problem of shape estimation is fundamental to the ultimate goals of optimization and control for static distributed systems. A major difficulty encountered is that disturbance effects can occur on various scales which cannot be simultaneously modeled using current technologies. And, likewise, one can expect that no single sensing system will adequately resolve all static distortions of the system.

The approach developed here leads to a framework which is suitable for combining a variety of models, both geometric and structural, together with a variety of sensing systems, both mechanical and electro-optical. The preliminary results represent the first step towards this necessary integration. First, the calibration work makes possible the combining of mechanical and electro-optical sensing technologies in a unified framework for estimation. And, secondly, the symmetry analysis represents the necessary validation of basic geometric models which must be justified before the more detailed structural models can be implemented.

The successful integration of SHAPES sensing significantly enhances the capabilities for future experiments at the facility. This technology will make static shape control possible in a larger class of space applications.

#### References

- [1] A. E. Bryson and Y.-C. Ho, Applied Optimal Control, Washington, D.C.:Hemisphere Publishing Company, 1975.
- [2] G. Rodriguez and R. E. Scheid, Jr., "An Integrated Approach to Modeling, Identification, Estimation, and Control for Static Distributed Systems", Fourth IFAC Symposium on the Control of Distributed Parameter Systems, Los Angeles, CA, June 1987